Unconventional Superconductivity and Quantum-Criticality in the Heavy-Fermion Metal CeIrIn$_5$

by

Hamideh Shakeripour

A thesis submitted to the physics department in
accordance with the requirements of the degree of
Doctor of Philosophy in the Faculty of Science.

FACULTÉ DES SCIENCES
UNIVERSITÉ DE SHERBROOKE

Sherbrooke, Québec, Canada, 16th July 2008

Referees

Le ——————————————, *le jury a accepté le mémoire de Hamideh Shakeripour dans sa version finale.*

Prof. Serg Jandl
Département de physique
Président-rapporteur

Prof. Louis Taillefer
Département de physique
Directeur de recherche

Prof. David Sénéchal
Département de physique

Prof. Kamran Behnia
UPR5- Laboratoire de Physique Quantique,
Ecole Supérieure de Physique et de Chimie Industrielles,
France

to those who love peace and make efforts to create a peaceful world
and to my family

Abstract

The thermal conductivity and electrical resistivity of single crystals of CeIrIn$_5$, one of the members of the CeMIn$_5$ family (M = Co, Ir or Rh), were measured as a function of temperature, magnetic field, doping and current orientation with respect to the crystal axes, to investigate the superconducting and normal states of this compound. In particular the aim of this study was to determine the gap symmetry of CeIrIn$_5$, a heavy-fermion superconductor with T_c=0.4K.

Comparison of the in-plane, κ_a, and inter-plane, κ_c, thermal conductivity of high-purity CeIrIn$_5$ crystals as $T \rightarrow 0$ revealed a large anisotropy of the superconducting gap, which suggested a hybrid E_g gap symmetry for this compound. Our doping and magnetic field studies support this suggestion. The doping study with light substitution of Ce with La reveals universal heat transport in the plane and non-universal heat transport along the tetragonal axis. This is the first observation of universal heat transport in a heavy fermion system. In the magnetic field study, measurements of the overall temperature and magnetic field dependence of the inter-plane thermal conductivity, κ_c, in the mixed state show a clear anomaly at low temperature. This anomaly is most pronounced in the highest purity samples and for the magnetic field applied in the ab plane. The resulting $H - T$ phase diagram suggests the existence of a new phase inside the superconducting state, which may confirm the existence of a two-component order parameter in this material.

Finally, electrical resistivity measurements reveal an anomalous $T^{4/3}$ power law resistivity, $\rho(T) = \rho_0 + AT^{4/3}$, in the high field non-Fermi liquid regime of inter-plane transport. This suggests the presence of *ferromagnetic* spin fluctuations in this compound, beyond the well-known antiferromagnetic spin fluctuations in the 115 family. These ferromagnetic spin fluctuations are lead to a quantum phase transition at high fields in CeIrIn$_5$.

Sommaire

La conductivité thermique et la résistivité électrique de mono-cristaux de CeIrIn$_5$, un des membres de la famille de composés du type CeMIn$_5$ (M = Co, Ir ou Rh), ont été mesurées en fonction de la température, du champ magnétique, du dopage et de la direction du courrant appliqué par rapport aux axes cristallographiques, dans le but d'étudier l'état normal et supraconducteur de ce matériau. L'objectif principal de cette étude est de déterminer la symétrie du gap supraconducteur de CeIrIn$_5$, un fermion lourd devenant supraconducteur en dessous de T_c=0.4K.

La comparaison de la conductivité thermique lorsque $T \rightarrow 0$, dans le plan, κ_a, avec celle perpendiculaire aux plans, κ_c dans des mono-cristaux de grandes puretés de CeIrIn$_5$ revèle une grande anisotropie du gap supraconducteur, suggérant ainsi une symmétrie hybride pour le gap E_g de ce composé. De plus une étude en fonction du dopage, réalisée en substituant des atomes de Ce par des atomes de La, révèle l'universalité du transport thermique dans le plan, alors qu'il est non-universel le long de l'axe tétragonal. Ceci constitue la première observation de transport thermique universel dans un système à fermions lourds.

Les mesures de la dépendance en champ magnétique et en température de la conducivité thermique inter-plan, κ_c, dans l'état mixte, révèle une anomalie très claire à basse température. Le diagramme de phase $H - T$ extrait de ces mesures suggère l'existence d'une nouvelle phase à l'intérieur même de l'état supraconducteur, pouvant ainsi confirmer l'existence d'un paramètre d'ordre à deux composantes dans ce matériau.

Enfin, les mesures de résistivité électriques hors plan à haut champ magnétique, dans le régime non-liquide de Fermi, révèlent une dépendance en température anormale, telle que $\rho(T) = \rho_0 + AT^{4/3}$. Ceci suggère la présence de fluctuations de spin ferromagnétiques, contrairement aux fluctuations de spin antiferromagnétiques observées dans la famille 115. Les fluctuations ferromagnétiques de spin mènent alors à une transition de phase quantique à haut champ magnétique dans CeIrIn$_5$.

Statement of Originality

The discovery of superconductivity in heavy-fermion materials and copper oxides has attracted considerable attention in the past thirty years. One of the main questions is what causes high and low T_c in these two compounds which show proximity to or coexistence with AFM order in their phase diagram. In this regard the first essential step is to determine the symmetry of the order parameter. In this respect, much effort has been focused on the CeMIn$_5$ (M=Co, Ir, Rh) compounds, which exhibit unconventional superconductivity in the vicinity of a quantum critical point, most likely magnetic.

While the superconducting state in CeCoIn$_5$ with $T_c = 2.3$ K is generally thought to have d-wave symmetry (although with some controversy as to whether it is $d_{x^2-y^2}$ or d_{xy}), much less is known about the related material CeIrIn$_5$ with $T_c = 0.4$ K. Thus, the study presented in this thesis provides the *first* directional study of the gap in CeIrIn$_5$, using heat transport measurements on the purest single crystals ever studied, to shed light on the mechanism of superconductivity in these systems.

The novelty of the present work resides in the extensive investigation of the superconducting and normal states as a function of crystal orientation, temperature, field and doping. Our main findings are:

- *Determination of gap symmetry in CeIrIn$_5$.*

  Using the anisotropy of thermal conductivity at very low temperatures we suggest a hybrid E_g gap in tetragonal point group symmetry for CeIrIn$_5$. We were the first to report two distinct gap symmetries in the closely related compounds CeCoIn$_5$ and CeIrIn$_5$.

- *The first observation of universal thermal conductivity in heavy fermion systems.*

  Response to doping provides an efficient way to study the superconducting pairing mechanism in superconductors. Universal behaviour, a constancy of the electronic residual thermal conductivity with variation of impurity density, was observed experimentally in cuprates and Sr$_2$RuO$_4$, but never in any of heavy fermion superconductors. Measuring pure and doped single crystals CeIrIn$_5$ we found universal transport in the plane and non-universal transport along the tetragonal axis, which both consistent with hybrid E_g gap structure.

- *The first observation of multi-phase superconductivity in 115 family.*

  The highly pure $c-$axis crystal under application of magnetic field in the ab plane shows a very low temperature anomaly in the thermal conductivity data. The anomalies in various fields delineate a new phase in the superconducting state. Comparing with theoretical models and a recent measurement we suggest the gap symmetry of each phase.

- *A resistivity of $\rho(T) = \rho_0 + AT^{4/3}$ in the presence of a high magnetic field for a large temperature range.*

  The quadratic exponent associated with a Fermi-liquid behaviour is observed at low temperatures and at low fields. This item which is the most significant result of this study may define the presence of *ferromagnetic* spin fluctuations in 115 family which lead to a ferromagnetic quantum phase transition in CeIrIn$_5$.

All preparation, characterization and measurements of CeIrIn$_5$ samples reported here were performed by myself, initially with the assistance of Shiyan Li, who helped me to learn fridge running.

Makariy Tanatar also assisted with preparation and measurement of the c-axis CeRhIn$_5$ crystal, measurement of 20%La-doped CeIrIn$_5$ samples and preparation of samples for μSR measurements (results in Appendix A, B and C), in the last year of my PhD. The μSR measurements were performed by myself in TRIUMF, Canada with the assistance of G.J. Macdougall, J.A. Rodriguez, A. Aczel and J.P. Carlo. The amazingly pure crystals in this study were grown by our collaborator Cedomir Petrovic in Brookhaven National Laboratory. Definitely without these highly-purity crystals we were unable to obtain these new results.

The major achievements of this thesis are presented in the following papers:

1. "Hybrid gap structure in the heavy-fermion superconductor CeIrIn$_5$"
H. Shakeripour, M. A. Tanatar, S. Y. Li, C. Petrovic, and Louis Taillefer,
Phys. Rev. Lett. **99**, 1877004 (2007).
2. "Universal heat transport in a heavy-fermion superconductor"
H. Shakeripour, M. A. Tanatar, C. Petrovic, and Louis Taillefer,
(preprint, to be submitted).
3. "Multi-phase superconductivity in heavy-fermion superconductor CeIrIn$_5$"
H. Shakeripour, M. A. Tanatar, C. Petrovic, and Louis Taillefer,
(manuscript in preparation).
4. "Ferromagnetic quantum phase transition in a spin-singlet superconductor CeIrIn$_5$"
H. Shakeripour, M. A. Tanatar, C. Petrovic, and Louis Taillefer,
(manuscript in preparation).
The papers were written primarily by myself, Makariy Tanatar and Louis Taillefer.

Acknowledgements

Last, but not least, I thank my husband Peyman and my daughter Zahra for their support, patience and sympathy during my measurements in the days and midnights.

And finally I thank my parents who taught me valuable lessons about humanity, life, world, and for their unconditional support and continuous encouragement during the whole period of my studies.

<div align="right">

Hamideh Shakeripour
Sherbrooke
Spring 2008

</div>

Contents

List of Tables

List of Figures

Chapter 1

Introduction

1.1 Motivation

The discovery of magnetically-mediated superconductivity in the heavy-fermion material $CeIn_3$ [139] has attracted considerable attention as a possible archetype for unconventional pairing in a variety of superconductors. However, in order to make progress, it is essential to determine the symmetry of the order parameter, something which is very difficult to do in $CeIn_3$ because its superconductivity exists only under high pressure. In this respect, the closely related family of $CeMIn_5$ (M=Co, Ir, Rh) compounds offers an ideal testing ground, as two members of this family show superconducting order at ambient pressure.

In spite of there are a few studies that have already aimed at elucidating the gap structure of $CeCoIn_5$ [94, 13, 217, 182], the closely related cousin of $CeIrIn_5$, but still the order parameter and gap structure of $CeCoIn_5$ are far from solidly established. While most measurements agree to the presence of nodes in the gap, there is a lively controversy as to the actual order parameter (whether $d_{x^2-y^2}$ or d_{xy}, for example) and the origin of uncondensed electrons [217] (whether due to gapless regions [26], multi-band scenario [217] or quantum criticality [242]). As regards $CeIrIn_5$, several recent studies [153, 105] suggest that it may actually support a different superconducting state. Until now, this suggestion has been based on indirect evidence, e.g. a comparison of magnetic fluctuation spectra (assumed to cause superconductivity) and phase diagram vs. alloying or pressure.

One of the main conclusion of this manuscript, the existence of pronounced anisotropy in transport incompatible with a d-wave gap, as believed to be realized in closely related $CeCoIn_5$, and more compatible with a hybrid gap, is robust against details of the Fermi

surface, because it comes from the asymptotic $(T \to 0)$ behaviour. As demonstrated by Graf et al. [74], the asymptotic behaviour of the thermal conductivity reveals the symmetry of the superconducting order parameter independently of details of the Fermi surface. To date this is the *first* observation of different superconducting symmetries in two closely related compounds with the same Fermi surface.

Further information was provided by our impurity and magnetic field studies: the first observation of universal thermal conductivity in a heavy fermion compound, multi-component/multi-phase superconductivity, and more importantly discovery of ferromagnetic quantum phase transition in $CeIrIn_5$ are all new results presented in this thesis.

The significance of our report is that it provides direct information on the gap structure of $CeIrIn_5$ and its potential difference with respect to that of $CeCoIn_5$. This could be of prime importance for the whole field of magnetically-mediated superconductivity, by providing an ideal (and unprecedented) test case for the relation between magnetic fluctuations and superconducting order parameter, via the comparison of two closely related materials (with the same crystal structure and nearly identical Fermi surfaces). The present findings in $CeIrIn_5$ have the potential to transform the field of heavy-fermion superconductivity by revealing the intrinsic anisotropy of the underlying electron interactions.

In this Chapter we review the major historical developments which have laid the groundwork for the study of unconventional superconductivity in $CeMIn_5$ compound which we undertake in Chapters 5, 6, 7, 8 and 9.

1.2 Conventional superconductivity

Superconductivity was discovered in 1911 by Heike Kamerlingh Onnes, who was studying the resistance of solid mercury at cryogenic temperatures using the recently-discovered liquid helium as a refrigerant. The next important finding occurred in 1933, when Meissner and Ochsenfeld discovered that superconductors expelled applied magnetic fields, a phenomenon which is known as the Meissner effect. In 1935, F. London proposed a relation between the current density and electromagnetic vector potential in a superconducting metal, known as the London equation, $\mathbf{j} = -\frac{n_s e^2}{m_e c}\mathbf{A}$. Here n_s is the density of superconducting electrons, e the electron charge, m_e the electron mass, and c the speed of light. According to the London theory, the magnetic field can only penetrate a distance into the superconductor, with λ_L given by $\lambda_L = \sqrt{n_s e^2/m_e c^2}$ [18].

The phenomenological Ginzburg-Landau theory of superconductivity was devised by Landau and Ginzburg in 1950 [66]. This theory had great success in explaining the macroscopic properties of superconductors by adding the important concept of a super-conducting wave function or order parameter. In particular, Abrikosov [1] showed that Ginzburg-Landau theory predicts two categories of superconductors referred to as type I and type II. He proposed that materials in which $k = \lambda_L/\xi$ is greater than $1/\sqrt{2}$ would exhibit type II superconductivity ($\xi(T)$ is the coherence length or the size of a Cooper pair).

Also in 1950, Maxwell and Reynolds found a direct relation between the critical temperature of a superconductor and the isotopic mass of the constituent element, $T_c \propto M^{-\alpha}$, where M is the ionic mass and $\alpha \approx 1/2$. This important discovery pointed to the electron-phonon interaction as the microscopic mechanism responsible for superconductivity [18].

The complete microscopic theory of superconductivity was finally proposed in 1957 by Bardeen, Cooper, and Schrieffer [24]. BCS theory explained the superconducting current as a superfluid of Cooper pairs, pairs of electrons interacting through the exchange of phonons. [1] In this theory a macroscopic wave function is considered for superconducting electrons as

$$|\Psi\rangle = \prod_k (u_k + v_k b_k^+)|0\rangle \tag{1.1}$$

where b_k^+ creates an electron pair ($k \uparrow$, $-k \downarrow$) and $|0\rangle$ is the filled Fermi sea ground state. Based on this wave function, Cooper and Schrieffer found that the excitation spectrum exhibits quasiparticles of energy E_k with an energy gap Δ which plays an essential role in the properties of superconductors. The BCS theory predicts a second-order phase transition at a critical temperature, T_c, a specific heat jump at the transition temperature, a complete diamagnetic effect, and a quantized magnetic flux.

In 1962, Josephson [96] predicted that a supercurrent can flow between two pieces of superconductor separated by a thin layer of insulator, with a magnitude of $I_s = I_c \sin(\Delta\phi)$, where $\Delta\phi$ is the difference in the phase of the order parameter in the two superconductors. This prediction shows the importance of the phase of the order parameter. This phenomenon, called the Josephson effect, is applied in superconducting

---

[1]BCS theory relies on an earlier discovery by Cooper (1956), who showed that the ground state of a material is unstable with respect to pairs of 'bound' electrons. These pairs are known as Cooper pairs. The formation of Cooper pairs is supported by the fact that BCS and the Ginzburg-Landau theories predict the charge and mass of the supercurrent particle to be $2e$ and $2m_e$ respectively [18].

devices such as SQUIDs.

In brief, there are two specific properties for conventional superconductivity. The electron pair has *s*-wave symmetry which means the two electrons with opposite spin and momentum are effectively paired (spin singlet state). These cooper pairs form a condensate state that can be described by a single quantum-mechanical phase, leading to long-range macroscopic phase coherence. The gap is isotropic in the momentum space, independent of the directions at the Fermi surface. Moreover, the microscopic mechanism of conventional superconductivity is based on the electron-phonon interaction. These two are not valid for unconventional superconductors which we discuss them as follows.

1.3   Unconventional superconductivity

Until 1986, it was believed that BCS theory forbade superconductivity at temperatures above 30 K. In that year, Bednorz and Müller [29] discovered superconductivity with a transition temperature of 35 K. Shortly after a high critical temperature 92 K was found in YBCO cuprate. Many other cuprate superconductors have since been discovered, and the theory of superconductivity in these materials is one of the major outstanding challenges of condensed matter physics.

Unconventional superconductivity means that the symmetry of the superconducting gap function is lower than the symmetry of the underlying Fermi surface. Experimental evidence for this is provided by the power-law temperature dependence of the electronic excitation spectrum below T_c, instead of exponential behaviour expected in conventional superconductivity, indicating presence of point nodes and/or line nodes in the gap. The superconducting condensate is formed by Cooper pairs with non-zero angular momentum.

Unconventional superconductivity, or the study of superconductors with anisotropic order parameter, began in 1979 with the discovery of superconductivity in the heavy-fermion (HF) $CeCu_2Si_2$ [199] and then in organic compound and High-T_c cuprates. These superconductors have many unusual properties that are difficult to understand in terms of standard BCS theory, in particular symmetry and e-ph mechanism.

Moreover, in recent years other unconventional superconductors have been discovered. These include some that do not superconduct at high temperatures, such as $SrRu_2O_4$ with $T_c = 1.5K$ [130] and superconductors with high values of T_c, like MgB_2 with T_c=39 K, which may be extreme examples of conventional superconductors.

In the following we will briefly discuss two examples of unconventional superconduc-

tivity: cuprate and heavy-fermion materials. Then, we introduce shortly the classification of unconventional superconductors so far identified.

1.3.1 High-T_c cuprate superconductors

High temperature superconductors are the class of unconventional superconductors which had for sure the highest impact on the development of concepts and understanding of the whole field. The first unconventional singlet d-wave superconductor was discovered in LaBaCuO by Bednorz and Müller in 1986 with a T_c nearly 35 K. This was well above the highest critical temperature known at the time (T_c=23 K) and thus the new family of materials were called high-temperature superconductors.

Following the discovery, one of the most challenges in condensed-matter physics is the question of the symmetry of the pairing state and thus pairing mechanism in the high-temperature superconductor. The determination of the order-parameter symmetry is a crucial first step in identifying the pairing mechanism and in the development of a microscopic theory for high-temperature superconductivity [222]. A growing list of theoretical calculations and experiments have suggested a d-wave (or more precisely, $d_{x^2-y^2}$-wave) superconductivity in cuprates, with gap function $\Delta(\mathbf{k}) = \Delta_0 \cos(2\phi)$, where ϕ is the angle of the quasiparticle momentum in the ab plane and Δ_0 the maximal value of the energy gap [219]. The gap has a strongly anisotropic magnitude with nodes along the (110) direction in k space and a sign change in the order parameter between the lobes in the k_x and k_y directions.

There are two key properties for d-wave state. First, it exhibits nodes in the energy gap vs ϕ that lead to zero temperature excitations. The presence of such excitations is based on angle-resolved photoemission spectroscopy (ARPES) measurements and the low temperature power law behaviour in some physical quantities. Second, the d-wave symmetry is implied by a number of possible superconducting pairing mechanisms, particularly those involving magnetic interactions (antiferromagnetic spin fluctuations) (for a review see [222] and [45]). The motivation for this thinking is the proximity of the superconducting state to an antiferromagnetic state in the phase diagram. The antiferromagnetic state has a relatively high Neel temperature of 600 K, and the unusually high T_N and T_c suggest some common origin for their properties.

1.3.2 Heavy fermion superconductors
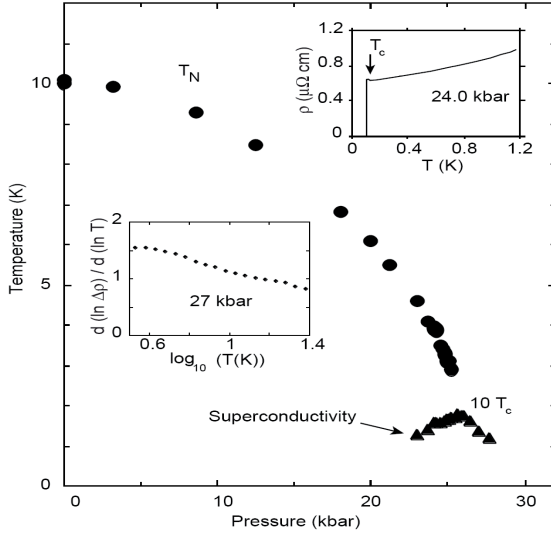
Superconductivity, which was one of the best understood many-body problems in physics, became again a challenging problem when a new kind of superconductivity was discovered in the heavy fermion material $CeCu_2Si_2$ [199]. This discovery seemed to opposite existing wisdom that magnetism destroys superconductivity.

Since this discovery, heavy fermion superconductivity has been observed in several Ce, U, Pr, and recently Pu-based compounds [235]. Multi-phase diagrams in heavy fermion UPt_3 [200,201,79] and $U(Be_{1-x}Th_x)_{13}$ [197,159] indicate superconductivity with multi-component order parameter. UPd_2Al_3 and UNi_2Al_3 [63,64] show superconductivity coexisting with the AF phase. Furthermore, pressure-induced superconductivity has been reported in AFM metals $CeCu_2Ge_2$ [95], $CePd_2Si_2$ [76,139], $CeRh_2Si_2$ [149], $CeNi_2Ge_2$ [119], and $CeIn_3$ [139,230].

Quite recently, several kinds of new heavy-fermion superconductors have been discovered. One is a family of $CeMIn_5$ (M=Co, Rh, and Ir) [81,173,174] which the phase diagram shows the coexistence of different ground states, such as SC and AFM. Another is the coexistence of superconductivity and ferromagnetism in UGe_2 at high pressure and URhGe at ambient pressure [188,12]. These materials have attracted much attention, since it is believed that a triplet pairing state coexists with the ferromagnetic phase. Moreover, other new superconductors, including neither Ce nor U atom, have been discovered. In $PrOs_4Sb_{12}$ (T_c=1.85 K), the possibility of a double transition has been indicated [27,92]. In the Pu-based compound $PuCoGa_5$ [183] with the same crystal structure as a family of $CeMIn_5$, an unusually high transition temperature T_c=18.5 K has been reported.

Heavy fermion behaviour has been found at low temperatures in a variety of states, including metallic and superconducting states. The compounds involve at least one element containing outer shell f electrons, which are believed to be the electrons that are responsible for the superconductivity. The common factor in heavy fermion materials is a large effective mass and electronic specific heat coefficient, γ. The huge effective mass is related to the strong correlation between the localized f electrons and the conduction electrons.

Most of the properties of heavy fermion systems can be explained by the competition of the on-site Kondo interaction (an antiferromagnetic interaction between the localized moments and the spins of the conduction electrons) and the inter-site RKKY exchange interaction. At high temperatures the RKKY interaction dominates, which leads to lo-

FIGURE 1.1: $T - P$ phase diagram of CeIn$_3$ (from [139]).

calized moments; therefore the magnetic susceptibility, for instance, near room temperature follows a Curie-Weiss like temperature dependence as expected for local moments, $\chi \propto \frac{1}{T - \theta_{CW}}$, where θ_{CW} is the Curie-Weiss temperature. The resistivity is dominated by incoherent scattering of the conduction electrons off the local moments. On the other hand, when the temperature is low enough the Kondo process dominates, which leads to the local singlet ground state (Kondo effect). This screening effect prevents the local moments seen at room temperature from forming a long-range ordered state at low temperature. Instead, below some coherence temperature, T_K, local moment behaviour is lost. With decreasing temperature the resistivity shows a peak followed by a drop, which is interpreted as an onset of coherent scattering. Below T_K, the magnetic susceptibility saturates and becomes Pauli-like (temperature independent), corresponding to itinerant moments [235].

The unconventional nature of heavy fermion superconductivity can be observed by the following properties.

First, the power law temperature dependence of resistivity, specific heat, sound attenuation, NMR spin lattice relaxation, and thermal conductivity below T_c support the existence of the nodes in the superconducting gap or anisotropic pairing [142].

Second, introducing non-magnetic impurity to these systems efficiently breaks the Cooper pair (see [97]). In contrast to conventional superconductors where dilute concentrations of non-magnetic impurities have little effect on the superconductivity. Non-

magnetic impurities strongly affect the pair breaking like a magnetic impurity in *s*-wave superconductors. This has been interpreted as evidence for non-*s*-wave pairing.

While the pairing mechanism in heavy fermion superconductivity is not understood yet, there are several reports that the superconducting pairing is mediated by magnetic interactions. This has been suggested from the pressure induced superconductivity in $CeIn_3$ and $CePd_2Si_2$, which occurs with suppression of magnetism with increasing pressure by enhancing hybridization between conduction electrons and local moments (Fig. 1.1) [139].

In brief, heavy-fermion superconductors show a variety of ground states and offer rich examples to investigate unconventional superconductivity in strongly correlated electron systems. However, superconductivity has not been explained from the microscopic point of view in these compounds, mainly due to the complicated band structures and strong correlations.

1.4 Gap symmetry and classification of order parameters

Classification of the superconducting state depends on whether we have spin-singlet or -triplet.

The general classification for the superconducting order parameter is based on its behaviour under symmetry transformations. The full symmetry group O of the crystal contains the gauge group $U(1)$, crystal point group G, spin rotation group $SU(2)$, and time reversal symmetry group τ [142],

$$O = U(1) \otimes G \otimes SU(2) \otimes \tau. \tag{1.2}$$

In conventional superconductors only gauge symmetry $U(1)$ is broken below T_c, while additional symmetries are broken at the phase transition in unconventional superconductors. The conventional superconducting state has full point symmetry of the crystal lattice. For the rest of superconducting states, the point symmetry properties are broken. An important consequence of the broken point group symmetry is the existence of zeroes in the order parameter, so called nodes, *i.e.* the order parameter vanishes at points or lines on the Fermi surface. This leads to gapless excitation spectrum which alters the low temperature behaviour of many physical properties in the superconducting
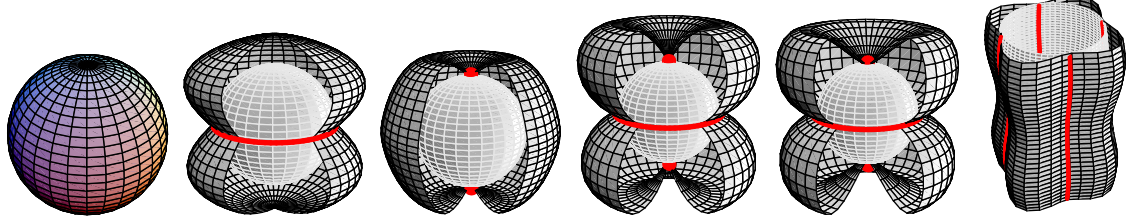
FIGURE 1.2: Some examples of the gap symmetry. The isotropic gap with A_{1g} symmetry (s-wave), polar (line node), axial (point node), E_g (hybrid), E_{2u} (hybrid II) (both with point and line nodes) and d-wave gap symmetries are shown from left to right.

state. In particular, power laws $\propto T^n$ are observed instead of an exponential temperature dependence, and the exponent n is determined by the topology of the nodes [142]. Some examples for the gap symmetries and the corresponding nodal structures are shown in Fig. 1.2. In this Figure, the conventional s-wave gap is finite everywhere, while the polar gap has a line of zeros in the basal plane. The axial gap vanishes along points nodes at the poles. The hybrid gap has line of zeros in the basal plane and point nodes at the poles and d-wave gap has four vertical line nodes.

The superconducting order parameter is proportional to the gap function $\Delta_{\mathbf{s}_1,\mathbf{s}_2}^L(\mathbf{k})$, which is proportional to the amplitude of the wave function for the Cooper pair $\Psi_{\mathbf{s}_1,\mathbf{s}_2}^L(\mathbf{k}) = \langle \psi_{\mathbf{k},\mathbf{s}_1} \psi_{-\mathbf{k},\mathbf{s}_2} \rangle$. Because only those electrons which are located near the Fermi surface are involved, $\mathbf{k}$, the quasiparticle momentum, is considered near Fermi surface. $\mathbf{s}_i$ is the electron spin, and ψ is the single electron wave function.

Pauli exclusion principle for fermions requires that the gap function to be antisymmetric with respect to the permutation of two particles: $\Delta_{\mathbf{s}_1,\mathbf{s}_2}^L(\mathbf{k}) = -\Delta_{\mathbf{s}_2,\mathbf{s}_1}^L(-\mathbf{k})$. In the case of weak spin-orbit interaction, the total angular momentum $\mathbf{L}$ and total spin $\mathbf{S} = \mathbf{s}_1 + \mathbf{s}_2$ are good quantum numbres, and $\Delta_{\mathbf{s}_1,\mathbf{s}_2}(\mathbf{k})$ can be written as a product of orbital and spin parts,

$$\Delta_{\mathbf{s}_1,\mathbf{s}_2}^L(\mathbf{k}) = g_L(\mathbf{k})\chi_s(\mathbf{s}_1, \mathbf{s}_2). \tag{1.3}$$

The orbital part of the order parameter, $g_L(\mathbf{k})$ can be decomposed in a linear combination of spherical harmonics $Y_{Lm}(\mathbf{k})$, with the orbital angular momentum L and its z-projection m,

$$g_L(\mathbf{k}) = \sum_{m=-L}^{L} a_{Lm} Y_{Lm}(\hat{\mathbf{k}}). \tag{1.4}$$

So, L determines the type of pairing; $g_L(\mathbf{k})$ is even for even values of L and odd for odd values of L, $g_L(\mathbf{k}) = (-1)^L g_L(-\mathbf{k})$, and superconductors with $L=0$, 1, 2, 3, 4,... are labelled as having s, p, d, f, g, ...-wave gap, respectively. This classification is useful for isotropic systems [2].

The spin part of the order parameter, $\chi_s(\mathbf{s}_1, \mathbf{s}_2)$, is a product of the two spins for the two electrons in the Cooper pair. Thus the gap function is a 2×2 matrix in spin space. For singlet pairing, S=0, the spin part of the wave function is $|\uparrow\downarrow\rangle$ - $|\downarrow\uparrow\rangle$, and therefore the gap function is given by

$$\mathbf{\Delta}(\mathbf{k}) = \Delta g_L(\mathbf{k}) i\sigma_y \quad , \tag{1.5}$$

where L is even and σ_y is the Pauli matrix. The energy of single particle excitations is

$$E_k = \sqrt{\xi_k^2 + \Delta^2 |g(\mathbf{k})|^2} \quad , \tag{1.6}$$

where ξ_k is the band energy relative to the chemical potential. For superconductors with an isotropic $\Delta(\mathbf{k})$ the excitations have a finite energy gap everywhere at the Fermi surface, while for anisotropic pairing the gap amplitude depends to the component of $g(\mathbf{k})$.

In the case triplet pairing (S=1), the wave function has three components corresponding to the three different spin projections, S^z: $|\uparrow\uparrow\rangle$, $|\uparrow\downarrow\rangle + |\downarrow\uparrow\rangle$ and $|\downarrow\downarrow\rangle$. Consequently, we can write the order parameter as

$$\mathbf{\Delta}(\mathbf{k}) = i(\mathbf{d}(\mathbf{k}).\vec{\sigma})\sigma_y = (d_x(\mathbf{k})\sigma_x + d_y(\mathbf{k})\sigma_y + d_z(\mathbf{k})\sigma_z)i\sigma_y$$

$$= \begin{pmatrix} -d_x(\mathbf{k}) + id_y(\mathbf{k}) & d_z(\mathbf{k}) \\ d_z(\mathbf{k}) & d_x(\mathbf{k}) + id_y(\mathbf{k}) \end{pmatrix} \tag{1.7}$$

The components $(g_1 = -d_x + id_y)$, $g_2 = d_z$ and $(g_3 = d_x + id_y)$ are the orbital parts of spin up $|\uparrow\uparrow\rangle$, spin zero $|\uparrow\downarrow\rangle + |\downarrow\uparrow\rangle$, and spin down $|\downarrow\downarrow\rangle$ pairing state, respectively. The

---

[2]When crystal anisotropy is present, the spherical harmonics in Eq. (1.4) have to be replaced by the basis functions of the different irreducible representations Γ of the point group of the crystal symmetry. Now, Eq. (1.4) for both spin singlet and spin triplet gap symmetry transform to: $g(\mathbf{k}) = \sum_{i=1}^{d_\Gamma} \eta_i \psi_i^{\Gamma_g}(\hat{\mathbf{k}})$ and $\mathbf{d}(\mathbf{k}) = \sum_{i=1}^{d_\Gamma} \eta_i \psi_i^{\Gamma_u}(\hat{\mathbf{k}})$, where the subscript g and u refer to even and odd basis functions respectively. $\psi_i^{\Gamma_g}(\hat{\mathbf{k}})$ and $\psi_i^{\Gamma_u}(\hat{\mathbf{k}})$ are the basis functions of irreducible representations Γ of group G with dimensionality d_Γ [142]. One then invokes group theoretical arguments to decompose the point group symmetry into its irreducible representations. This procedure has been carried out by many authors in the case of strong spin-orbit coupling [197, 227] and weak spin-orbit coupling [160]

excitation energy for this case is

$$E_k = \sqrt{\xi_k^2 + \Delta^2 |\mathbf{d}(\mathbf{k})|^2} \; . \tag{1.8}$$

In the presence of strong spin-orbit coupling only the total angular momentum $\mathbf{J}=\mathbf{L}+\mathbf{S}$ is a good quantum number (only the total angular momentum is conserved), and the classification according to the physical electron spin is not possible [142]. Parity therefore provides a useful classification scheme as pointed out by Anderson. Even and odd-parity states are the counterpart of the singlet and triplet states mentioned above.

After this classification we introduce in brief the symmetry of the order parameter of hybrid gaps, E_g and E_{2u}. E_g is the suggested gap symmetry for CeIrIn$_5$ compound in this thesis.

1.4.1 Hybrid gap (E_g)

In a tetragonal crystal structure with point group symmetry D_{4h} for spin-singlet even-parity pairing, there are four one-dimensional (A_{1g}, A_{2g}, B_{1g} and B_{2g}) and three possible two-dimensional representations (E_g). The famous reported d_{x2-y2} model in high-T_c superconductors belongs to the B$_{1g}$ representation. The 2D $E_g(1, i)$ representation with the basis function $k_z(k_x + ik_y)$ is called *hybrid E_g* gap. The nodal structure is characterized by two linear point nodes, $|\Delta(\theta)| \propto \mu_{point}\Delta_0(|\theta|)$, where μ_{point} is the slope or curvature of the gap at the node in a spherical coordinate system, in the c direction and a line node in the basal plane.

1.4.2 Hybrid II gap (E_{2u})

The corresponding basis function is $k_z(k_x+ik_y)^2$. It belongs to hexagonal crystal structure with point group symmetry D_{6h} with spin-triplet parity pairing. The nodal structure is characterized by quadratic point nodes, $|\Delta(\theta)| \propto \mu'_{point}\Delta_0(|\theta|)^2$, in the c direction and a line node in the basal plane. The crucial difference between the E_g and E_{2u} states lies in the opening of the gap with angle θ at the polar point nodes, as shown in Fig. 1.3.

The proposed model for the order parameter in the low-temperature phase of HF SC UPt$_3$ is the odd parity E_{2u} state.
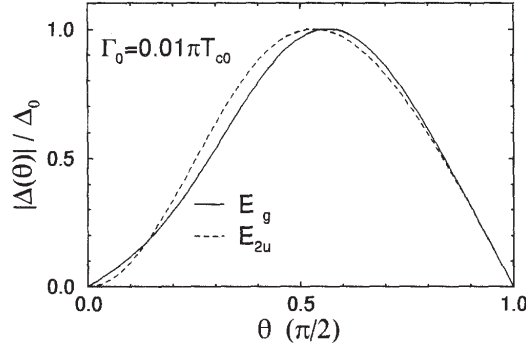
FIGURE 1.3: The normalized excitation gap at $T = 0$ for two states E_g and E_{2u} as a function of the polar angle θ (from [72]).

1.4.3 Experimental probes of gap symmetry

As we mentioned above, classification of superconductors into singlet and triplet pairing needs information on the parity and spin state of the pairing state. This information can be accessed through measurements in a magnetic field due to the different response of pairs with S=0 and S=1 to an applied magnetic field. The Knight shift of the nuclear magnetic resonance (NMR) frequency, muon spin rotation (μSR), or the magnetic properties such as the Pauli limit can be used for studying the spin state. The Knight shift is linear in the electron spin susceptibility χ_s, and therefore is a direct measure of the spin polarization in the superconducting state. In a spin singlet superconductor the spin contribution to the Knight shift falls rapidly on cooling through the transition. In contrast, in a triplet superconductor the Knight shift remains unchanged below T_c [140].

Angle-resolved photoemission spectroscopy (ARPES) is a direct measurement that reflects the symmetry of the paired state. The asymptotic behaviour of the thermal conductivity in different direction of crystal axes is one of the best transport measurements that can detect the symmetry of the order parameter [74]. Energy gap measurements such as specific heat, penetration depth, superfluid density, point contact spectroscopy, scanning tunnelling spectroscopy (STS), and ultrasound attenuation, are usually used to determine the quasiparticle density of states especially from their low temperature behaviour. Although, they may be misleading by the impurity scattering effect that changes the superconducting state dramatically in which will lead to so-called gapless superconductivity. Therefore theses measurements should be performed in highly pure single crystals.

Phase sensitive phenomena can be used to determine the change of phase along dif-

ferent directions. Phase information is usually probed by the Josephson effect which is based on pair tunnelling. For more information the reader is referred to [68].

1.5   Review of thesis

In Chapter 2, an introduction to the basic theoretical concepts about the thermal conductivity in both conventional and unconventional superconductors in zero and applied magnetic field is given. A review of the current set of theoretical and experimental ideas on the physical properties of heavy-fermion $CeMIn_5$ family, mostly on $CeIrIn_5$, is presented in Chapter 3. Providing an explanation of the experimental techniques used in this study in Chapter 4, we will present our main experimental results in Chapters 5, 6, 7, 8 and 9.

In Chapter 5 we present zero field thermal conductivity results taken on highly pure single crystals $CeIrIn_5$. We suggest that E_g gap symmetry is the only candidate for gap structure of this material among the all candidate gap symmetries in the tetragonal spin singlet D_{4h} point group symmetry. By adding non-magnetic La ions to the crystals, we investigate the impurity effect on the residual linear term of thermal conductivity at zero temperature in the superconducting state in Chapter 6. We found universal thermal conductivity for the in-plane and non-universality for the inter-plane heat transport, consistent with hybrid E_g gap symmetry proposed in the previous chapter. The effect of magnetic field on the phase diagram of $CeIrIn_5$ has been probed in Chapter 7. We observed a phase transition inside of the superconductivity state; in another words, a multi-component/multi-phase superconductivity has been detected. In Chapter 8, we searched for quantum criticality near H_{c2} in this compound, comparing to the closely related material $CeCoIn_5$ that shows a quantum critical point (QCP) at the upper superconducting transition field, H_{c2}. We found no criticality at H_{c2} for a- and c-axis heat current directions in $CeIrIn_5$. However, we found fascinating evidence for ferromagnetic spin fluctuations which lead to quantum phase transition at much higher fields in $CeIrIn_5$, shown in Chapter 9. Further measurements and related results on $CeIrIn_5$ and antiferromagnetic $CeRhIn_5$ are presented in Appendices.

A summary of thesis was made in the Chapter conclusion and possible further studies were also pointed out at the end.

Chapter 2

Basic Theoretical Concepts on Heat Transport

Heat transport is a directional probe for investigating the gap structure of superconductors. Tensorial character of the transport properties allows the measurement of several independent components at the same time. This is very useful in the studies of highly correlated systems, which are very anisotropic. Comparison of the behaviour of independent components of a transport property gives important information about the gap symmetry. Besides the electron carries, phonons and magnons can also carry heat, as well as scatter the electrons. Therefore for interpretation of heat transport data one must take into account all the different carriers and their associated scattering mechanisms. The main weakness of the technique is that it is often difficult to separate these contributions. Fortunately in the case of high-quality metallic crystals of heavy fermion metals because of high concentration of conduction electrons, only electrons are effective to carry heat at low temperatures.

In this chapter we provide some background theoretical concepts regarding the interpretation of heat transport first in metals and then in conventional and unconventional superconductors.

2.1 Electron conduction in metals

Metals conduct electricity via delocalised electrons within the metal lattice. The simplest way of explaining conductivity in a metal is by using the Drude model (1900). Only a few years after Thomson discovered the electron, Drude put forward his theory of electrical

and thermal conductivity based on the idea that conduction electrons in metals behave like atoms of gas. Although Drude's original model did not include quantum mechanics, his formula for the conductivity of metals remains correct even in the modern quantum theory of metals. Later, Drude's theory was refined within a theory based on the laws of quantum mechanics by Sommerfeld (1927) who also started from the free electron gas but took into account the Pauli Exclusion Principle by using Fermi-Dirac statistic.

2.1.1 Electrical conductivity

Here we discuss low temperature aspects of the electrical conductivity of mainly simple metals. Concerning transition metals we make a brief remark on them. In these metals not only s-electrons but also d-electrons are present in the conduction band. Although the density of states of d-electrons at the Fermi energy exceeds that of s-electrons they hardly contribute to conduction because of their low mobility. This poor mobility is mainly due to the high effective mass of the electrons in the narrow bands. In transition metals the mobility of the s-electrons is generally lower than in simple metals. This reduction is caused by the scattering of s-electrons into d-band states. As a result, the conductivity of transition metals is, in general, smaller than that of simple metals although both *s*- and *d*-band electrons are present [56].

In the Fermi gas description of metals the electrical conductivity, σ, is given by the Drude theory as:

$$\sigma = \frac{ne^2\tau}{m^*} \tag{2.1}$$

where n is the density of electrons (in a relation of the density of states at the Fermi surface, $N(E_F) = \frac{3n}{2E_F}$), m^* the effective mass of the conduction electrons, -*e* the electron charge and τ is the average life time for free motion of the electrons between collisions with impurities or other electrons.

This equation shows that the electrical conductivity depends on temperature mainly via the different scattering processes which enter into the scattering life time τ. In a typical metal there are three main scattering processes, scattering by impurities, electron-electron scattering and electron-phonon scattering. These are independent processes, and so a total effective scattering rate is a sum of these scattering rates. This empirical

relationship is known as Matthiessen's rule:

$$\tau^{-1} = \tau^{-1}_{e-imp} + \tau^{-1}_{e-e} + \tau^{-1}_{e-ph} \tag{2.2}$$

where τ^{-1}_{e-imp} is the scattering rate by impurities, τ^{-1}_{e-e} the electron-electron scattering rate and τ^{-1}_{e-ph} the electron-phonon scattering rate. This leads to the total resistivity $\rho = 1/\sigma$ that is a sum of independent contributions from each of these different scattering processes. Each of these scattering life times is a characteristic function of temperature. The impurity scattering rate, is essentially independent of temperature, at least for the case of non magnetic impurities [1]. The electron-electron scattering rate, is proportional to $\tau^{-1}_{e-e} \propto T^2$. At low temperature, well below the phonon Deby temperature, the electron-phonon scattering rate is proportional to $\tau^{-1}_{e-ph} \propto T^5$. Therefore we should expect that resistivity of a metal is of the form

$$\rho = \rho_0 + AT^2 + ... \tag{2.3}$$

at very low temperature. The zero temperature resistivity, the residual resistivity, ρ_0, depends only on the concentration of impurities and therefore on purity and quality of the sample. For most metals the resistivity indeed behaves as the Eq. (2.3) at low temperatures [11].

2.1.2 Thermal conductivity

Thermal conductivity, κ, is a property of a material that indicates its ability to conduct heat. It is defined as the coefficient of proportionality between a heat current $\mathbf{j}_Q$ and an applied temperature gradient ∇T, $\mathbf{j}_Q = -\kappa \nabla T$.

In typical metals, heat is mainly transported by electrons and phonons. Thus the total thermal conductivity is the sum of the conductivities of these heat carriers, $\kappa = \kappa_e + \kappa_{ph}$, where κ_e and κ_{ph} are thermal conductivity due to electrons and phonons, respectively (In insulating solids, only phonons carry heat. Also in alloys or metals with high impurity content electrons are strongly scattered by impurities and defects. Then their contribution to the heat transport is heavily reduced and the phonon contribution becomes dominant). However, in highly pure metals and at low temperatures, electrons

---

[1]For magnetic impurities the conduction electrons will tend to screen the spins of the impurities as a results of Kondo effect, leading to a logarithmic increase of scattering with decreasing temperature.
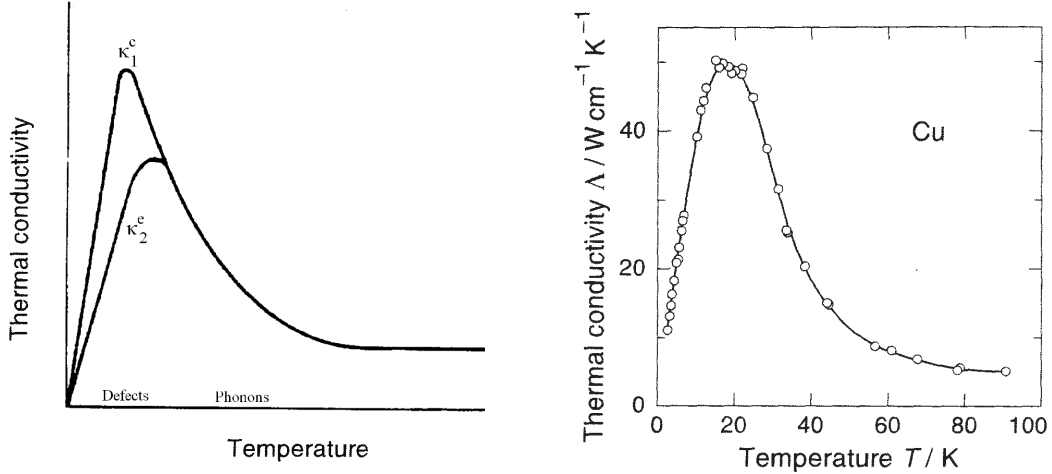
FIGURE 2.1: (Left) A schematic of the thermal conductivity in a conventional metal. The dominant scatterers are impurities at low temperatures and phonons at higher temperatures. The higher curves are for purer samples; adapted from [31]. (Right) Thermal conductivity copper as a function of temperature [56].

are more effective for carrying heat because the number of electrons able to carry heat is always much larger than the number of excited phonons. This can be seen also from the temperature dependence of the specific heat; the electronic specific heat increases linearly with temperature, while the lattice contribution increases proportional to T^3, as we will see it below.

Electronic thermal conductivity

Following the derivation of Ashcroft and Mermin using the free electron Drude's model, we get [18]:

$$\kappa_e = \frac{1}{3}C_e v_F^2 \tau_e = \frac{1}{3}C_e v_F l_e \tag{2.4}$$

where C_e is the electronic specific heat, v_F is the electron velocity and l_e is the electron mean free path, $l = v\tau$.

At low temperature the specific heat, C can be expressed as,

$$C = \frac{1}{T}\int_{-\infty}^{\infty} dE(-\frac{\partial f}{\partial E})N(E)E^2 \tag{2.5}$$

Electron scattering mechanisms	$\rho(T)$	$\kappa_e(T)$
impurities	T^0	T
electron-phonon ($T < 0.1\theta_D$)	T^5	T^{-2}
electron-phonon ($T > 0.7\theta_D$)	T	T^0
electron-electron	T^2	T^{-1}
Kondo effect	$-\ln T$	-

TABLEAU 2.1: Temperature dependence of the electrical resistivity, ρ, and the electronic thermal conductivity, κ_e, in the presence of various electron scattering mechanisms in a metal. θ_D is the Debye temperature of the metal (after [31]).

where f is the Fermi function. Then, the temperature dependence of the specific heat is directly related to the energy dependence of the density of states of electrons. The prediction of a linear temperature dependence of electronic specific heat for normal metals,

$$C_e = \frac{\pi^2}{3} k_B^2 N(E_F) T \quad , \tag{2.6}$$

is one of the most important consequence of Fermi-Dirac statistic. $N(E_F)$ is the density of states at the Fermi surface. Thus, the linear coefficient in the electronic specific heat ($\gamma = \frac{C_e}{T} \propto N(E_F)$) is just proportional to the density of quasiparticles. Later in the superconducting part, we will see that the generic form of $N(E)$ at low temperatures depends only on the topology of the surface where the excitation gap is zero. A surface of gap zeros will lead to a constant density of states, a line of nodes leads to a linear density of states and a point node leads to a quadratic dependence.

Qualitatively, the temperature variation of the thermal conductivity of a metal can be explained by considering just the electronic contribution. Fig. 2.1 displays the thermal conductivity of a metal as a function of temperature along with the electron-scattering mechanisms responsible for the shape of the curve. At very low temperatures, electrons are predominantly scattered by impurities or imperfections in the lattice, resulting in a constant electron mean free path. In this case, the linear temperature dependence of the specific heat gives rise to a linear increase of the thermal conductivity, $\kappa_{e-impurity} \propto T$. With increasing temperature, the electron-phonon interaction becomes more and more important, because of the growing number of high-frequency thermal phonons. The electron mean free path decreases rapidly, with a scattering time for electron-phonon processes proportional to T^{-3}, more than compensating for the rise that is caused by the

linear specific heat, and thus the thermal conductivity falls (in a typical metal $\kappa_{e-phonon} \propto 1/T^2$). At higher temperatures, the dominant scattering centers are phonons those with the Debye frequency. Their density rises linearly with temperature, leading to a electronic mean free path inversely proportional to temperature, $l \propto 1/T$. Thus, the temperature dependence of the specific heat and the mean free path cancel each other, and the thermal conductivity becomes almost constant, $\kappa_{e-phonon} \propto$ constant [56] (See Table 2.1).

Except for these electron scattering mechanisms that can cause resistance to the electronic heat flow, also electron-electron scattering process is dominant in perfect metallic crystals. This gives rise to a T^2 dependence of scattering cross-section, a thermal conductivity proportional to $1/T$, $\kappa \propto 1/T$, and an electrical resistivity proportional to T^2, $\rho \propto T^2$. In heavy fermion compounds, the electron-electron cross section is enhanced by the large effective masses and becomes very significant.

The Wiedemann-Franz law

Those metals which are the best electrical conductors are also the best thermal conductors. At a given temperature, the thermal and electrical conductivities of metals are proportional. This behaviour is quantified in the Wiedemann-Franz Law (WF law):

$$\frac{\kappa}{\sigma T} = \frac{\pi^2}{3}(\frac{k_B}{e})^2 \equiv L_0 = 2.45 \times 10^{-8} W\Omega K^{-2} \tag{2.7}$$

where the constant L_0 is the Sommerfeld value of the Lorenz number. Qualitatively, this relationship is based upon the fact that the heat and electrical transport both involve the same free electrons in the metal [18].

This law is very general and is valid if the electronic mean free path determining the electrical and heat conductivities is limited by the same process. At high temperature, namely for $T > \theta_D$, scattering processes with large momentum transfer (like Umklapp processes) limit both the electrical and the thermal conductivity. Therefore the Widemannn-Franz law is valid. At moderately low temperatures, processes with small momentum change dominate. These processes cause the energy to change but the momentum is hardly altered. This leads to a greater degradation of the thermal current than the electrical current. Consequently, the ratio $\frac{\kappa}{\sigma T}$ decreases and differs from Lorenz number L_0 (see more explanation in [162]). Finally at very low temperatures, elastic impurity scattering dominates both electrical and thermal transport and the WF law is valid [56].

Historically, this law was first reported experimentally by Wiedemann and Franz in 1852. They found that the Lorenz number was the same for many metals at room temperature. This law is extremely robust as has been demonstrated both experimentally and theoretically. Experimentally as $T \to 0$, this law has been verified in numerous materials; in simple metals, in strongly correlated systems like heavy fermion systems and HTCS, quasi two-dimensional systems or even in quasi one dimensional organic conductor, and in systems in the proximity of a quantum critical point. However, recently for the first time a new and unexpected anisotropic violation of the WF law in the normal state of heavy fermion metallic compound $CeCoIn_5$ at $T \to 0$ has been reported [215].

Lattice thermal conductivity

Here we make a few remarks on the contribution of phonons to the thermal conductivity of metals. For phonons in the same way as electrons, from simple kinetic theory the conductivity of phonons is given by [39]:

$$\kappa_{ph} = \frac{1}{3} C_{ph} v_{ph} l_{ph} \tag{2.8}$$

where C_{ph} is the lattice specific heat, v_{ph} is the phonon velocity that assumed to be temperature independent and l_{ph} is the phonon mean free path.

The Debye theory predicts a T^3 dependence for the lattice specific heat at low temperatures, $T < \theta_D$, [18]:

$$C_{ph} = \frac{12\pi^4}{5} n k_B (\frac{T}{\theta_D})^3 \tag{2.9}$$

This leads to a $\kappa_{ph-boundary} \propto T^3$ if the phonon mean free path is temperature independent. This happens when there are no electrons to scatter the phonons at low temperature and only grain size or sample boundary becomes the dominant scattering process. In this case, l_{ph} becomes temperature independent, given by nearly the cross-sectional area A of the sample: $l_{ph} = 2\sqrt{A/\pi}$.

In the case of heavy fermion materials where there is high concentration of conduction electrons, conductivity of phonons are limited by electrons. This leads a scattering rate with a linear temperature dependence, $l \propto 1/T$, leading to a $\kappa_{ph-e} \propto T^2$. This type of scattering is also important in the vortex state of a superconductor, so that vortices are electronic in nature and can scatter phonons strongly. There are other types of
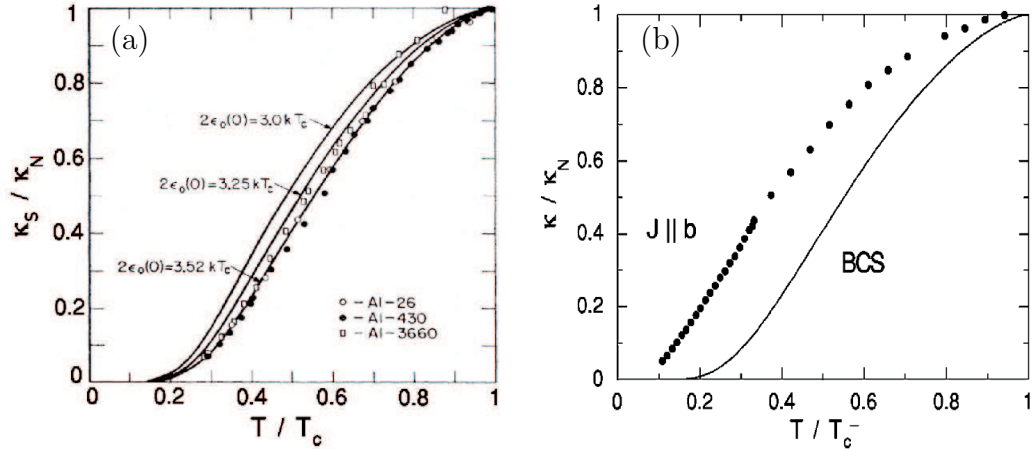
FIGURE 2.2: (a) Ratio of superconducting to normal state thermal conductivity of aluminum for different purities indicated by the residual resistivity ratio, RRR=$\rho(Room)/\rho(1.2K)$ [186]. The thermal conductivity calculated for *s*-wave superconductor in BRT theory (solid lines) fits data very well. (b) A comparison between the behaviour of κ of BCS theory and an unconventional superconductor, UPt$_3$ [97].

scattering that limit the lattice conductivity, like phonon-phonon scattering and different types of defects (like point defects, dislocations, etc). For a complete review on phonon conductivity see e.g. [31, 36].

2.2 Thermal conductivity in superconductors

Thermal conductivity is a fascinating probe for investigating bulk superconductivity. It does not vanish in the superconducting state, unlike electrical resistivity. Cooper pairs do not carry entropy and therefore do not contribute to the thermal transport. Thus, the thermal conductivity probes the delocalized low energy quasiparticles.

2.2.1 Thermal conductivity in conventional superconductors

The presence of gap in the spectra of *s*-wave superconductors leads to exponential behaviour, $\propto e^{\Delta_0/T}$, of all thermodynamic and kinetic quantities at low temperature.

Bardeen, Rickayzen, and Tewordt (1959) calculated the electronic contribution to the thermal conductivity of a *s*-wave superconductor, when the dominant scatterers are impurities. They found an expression for thermal conductivity in superconducting state, $\kappa_{es} \propto N(E)v^2\tau$, which is exactly equivalent to the normal state expression except for the

gap $\Delta(T)$ in the quasiparticle spectrum [25]:

$$\kappa_{es}(T)/\kappa_{eN} = \frac{\int_{\Delta(T)}^{\infty} dE \; E^2 \frac{\partial f}{\partial E}}{\int_0^{\infty} dE \; E^2 \frac{\partial f}{\partial E}}, \tag{2.10}$$

where $f(E) = (1 + e^{E/k_B T})^{-1}$. For $T << T_c$ this expression reduces to

$$\kappa_{es}/\kappa_{eN} \propto \left(\frac{\Delta_0}{k_B T}\right)^2 e^{-\Delta_0/k_B T}. \tag{2.11}$$

These calculations agree well with measurements on a variety of conventional super-conductors; see one example in Fig. 2.2(a). In this figure, BRT theory with the standard BCS value for the gap with $2\Delta(0) = 3.52 k_B T_c$ provides an excellent agreement with the experimental data of three samples of varying impurity concentration [186]. κ_{es} rises exponentialy and has only 1-2 % of its normal-state value at 0.2 T_c (Fig. 2.2(a)).

Here it is instructive to compare the BRT theory with the thermal conductivity of an unconventional superconductor UPt$_3$, displayed in Fig. 2.2(b), where κ_b, the in-plane heat transport, is plotted vs reduced temperature T_c^-. Because the theory does not include any inelastic scattering, the comparison should be made in the elastic regime below about $T_c/4$ [97]. In that regime, obviously there is no consistency between data and the theory.

2.2.2 Thermal conductivity in unconventional superconductors

The presence of nodes in the spectrum of elementary excitations leads to considerable changes in the thermodynamic properties of superconductors at low temperature. On the contrary to conventional superconductors, in superconductors with the gap nodes at the Fermi surface, the temperature dependence of thermal conductivity and other thermodynamic quantities follow a power law. Table 2.2 shows the power law dependence of some physical quantities in an unconventional superconductor.

In the mid-1980s, several authors generalized the standard BRT theory to apply it to unconventional order parameters [85, 190, 17, 16]. They neglected inelastic electron-electron scattering and assumed isotropic (s-wave) scattering off impurities, which is treated either in the Born limit of weak scattering (scattering phase shift [2] $\delta = 0$) or in the unitarity limit of strong scattering ($\delta = \pi/2$). Two types of calculations were

---

[2]The phase shift between the incoming and scattered electronic waves.

	Line node	Point node
Specific heat C_V	T^2	T^3
NMR relaxation rate $1/T_1$	T^3	T^5
Thermal conductivity κ	T^2	T^3
Penetration depth $1/\lambda_\parallel^2$	T^3	T^2
Penetration depth $1/\lambda_\perp^2$	T	T^4

TABLEAU 2.2: Power-law dependences for various quantities in low temperature regime. These laws hold for a clean superconductor with linear dispersion of the gap at the nodes [97].

performed: self-consistent calculations which include the pair-breaking effect of impurity scattering [85,190] and those which neglect this effect [16,17]. The effect of pair breaking shows up at temperatures below an energy scale γ, called the impurity bandwidth, which depends on the normal-state scattering rate, Γ. The value of γ depends strongly on the phase shift; it is highest for unitarity scattering, $\gamma = \sqrt{\hbar\Gamma k_B T_c}$. The main feature of that regime, which is called gapless regime, is the presence of a residual normal fluid of zero-energy quasiparticles at $T = 0$.

Much of the discussion of the results in this work will focus on low and zero temperature results where $k_B T << \gamma$, and γ is the dominant energy scale. This is defined as the *dirty* limit, and the case where $k_B T >> \gamma$ as the corresponding *clean* limit (see Fig. 2.5(a) in this regard).

Here, before moving to look at the thermal transport theories in detail, we take 2D d-wave gap as our basis for the following formalism introduced by Lee (1993) [118]. When the gap approaches to zero at the Fermi surface, we can only concentrate on the nodal region where the density of sates is finite and neglect the structure Δ_k away from the node. In other words, this is allowed to linearize the gap spectrum around the node. Quasiparticle excitations is then described by the Dirac spectrum:

$$E_k = \sqrt{\xi_k^2 + \Delta_k^2} = \hbar\sqrt{(v_F k_1)^2 + (v_2 k_2)^2} \tag{2.12}$$

where $\hat{\mathbf{k}}_1$ is perpendicular to the Fermi surface and $\hat{\mathbf{k}}_2$ is tangential to it. v_F is the Fermi velocity and v_2 is the second velocity that emerges as the slope of the gap at the node, $S = \frac{d\Delta}{dk} = \hbar k_F v_2$. For a d-wave gap this slope is given by $S = \Delta_0/2$. Thus the quasiparticle energies are confined to a cone.

In the clean limit ($T > \gamma$) and dirty limit ($T < \gamma$) the expressions for the density of

	$N(E)$
Full gap	0
Surface of zeros	constant
Line node	E
Quadratic point node	E
Linear point node	E^2

TABLEAU 2.3: Low temperature dependence of the density of states, $N(E)$ in superconductors.

states are given by:

$$N_s(E) = \frac{2}{\pi\hbar^2}\frac{E}{v_F v_2} \propto E \qquad (T > \gamma) \tag{2.13}$$

and

$$N_s(E) = \frac{\gamma}{\pi^2\hbar v_F v_2} \qquad (T < \gamma) \ , \tag{2.14}$$

respectively. It has been predicted the finite density of sates at zero temperature in the dirty limit, Eq. (2.14), leads to universal charge transport, which is given by:

$$\sigma_0 = \frac{e^2}{\pi^2\hbar}\frac{v_F}{v_2} \cong e^2 N_F v_F^2 \tau_\Delta \ , \tag{2.15}$$

with the universal scattering time $\tau_\Delta \cong \frac{\hbar}{\pi\Delta_0}$. This universal charge transport is a consequence of the d-wave gap being linear at the node and is independent of the scattering rate of quasiparticle excitations.

The linear energy dependence of density of states in the superconducting state, Eq. (2.13), leads to power law dependence of many physical properties instead of activated behaviour for s-wave superconductors. For instance, this relation provides an electronic specific heat $C_{es} \propto T^2$. The linear energy dependence of density of states is obtained for line node and quadratic point nodes; $N_s(E) \propto E$. For linear point nodes we have $N_s(E) \propto E^2$ (see Table 2.3 for a summary).

Returning back to our discussion on thermal conductivity, neglecting the pair-breaking effect of impurities and assuming isotropic scattering, Arfi and Pethick (1988) calculated the two components of κ, namely, $\kappa_{zz} \equiv \kappa_c$ and $\kappa_{xx} \equiv \kappa_a = \kappa_b$, for three generic gap structures: the polar ($\Delta(\theta) \propto \cos\theta$), the axial ($\Delta(\theta) \propto \sin\theta$), and the so-called "$d$-wave"
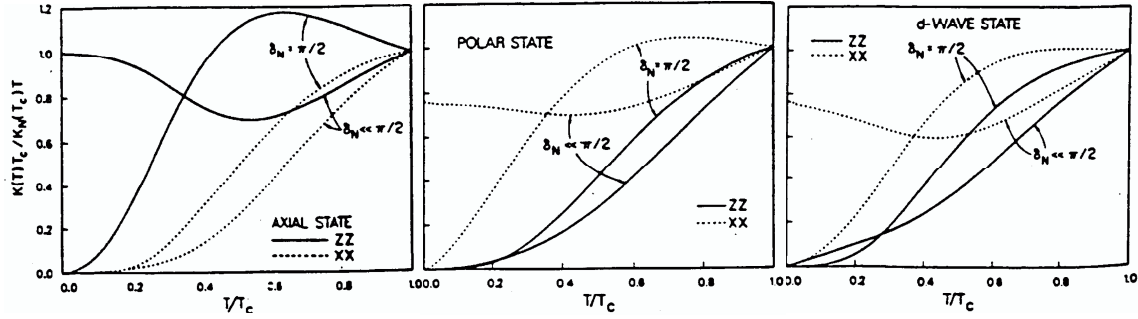
FIGURE 2.3: Normalized thermal conductivity along (ZZ) and perpendicular (XX) to the *c*-axis in the Born and unitarity limit for axial, polar and hybrid gap symmetries [17].

gap ($\Delta(\theta) \propto \sin\theta\cos\theta$) (this is *hybrid gap* that was introduced in the introduction chapter), on a single spherical Fermi surface for a scattering phase shift close to 0 up to $\pi/2$. Their results are shown in Fig. 2.3. Two basic features emerge: (1) heat conduction is always much better along the direction of nodes and (2) qualitative agreement with experimental data is not possible in the Born approximation, which is seen to lead to large values of κ/T at $T \to 0$ in the nodal directions, comparable in magnitude to the normal-state value. The necessity of large phase shifts, close to $\pi/2$, was first predicted by Pethick and Pines (1986) [172] [3]. It has since become an assumption in the description of superconducting properties in all strongly correlated electron systems. In a later work, Arfi *et al.* [16] investigated the effect of an arbitrary phase shift on the thermal conductivity. The motivation for this justification was that an impurity added to the system is replaced for a magnetic or non-magnetic atom. So this gives a large or near zero phase shift. Thus an intermediate phase shift might be expected. The result for hybrid gap symmetry is given in Fig. 2.4.

For the gap symmetries considered in Fig. 2.3 and Fig. 2.4, the heat anisotropy is strong. For example, the ratio of heat conduction parallel and perpendicular to the *c* axis, κ_{zz}/κ_{xx}, goes to zero for a polar gap and to infinity for an axial gap, as $T \to 0$. This implies that a measurement of transport anisotropy can be a powerful way of

---

[3]It was shown [172] multiple interactions of a quasiparticle with an impurity, which corresponds to a large phase shift in the normal state, leads to a good agreement between temperature dependence of the transport coefficients in the superconducting state with the experimental data. The motivation for the large phase shifts arises from the fact the f electrons of Ce or U atoms in the heavy fermion materials, are thought to be responsible for the heavy electron behaviour. When non-magnetic impurities are introduced, it is possible to replace an f electron atom. The impurity then corresponds to the absence of a magnetic site, and thus it gives rise to a phase shift close to $\pi/2$. In the case when the impurity replaces one of the other atoms, the phase shift is likely to be small.
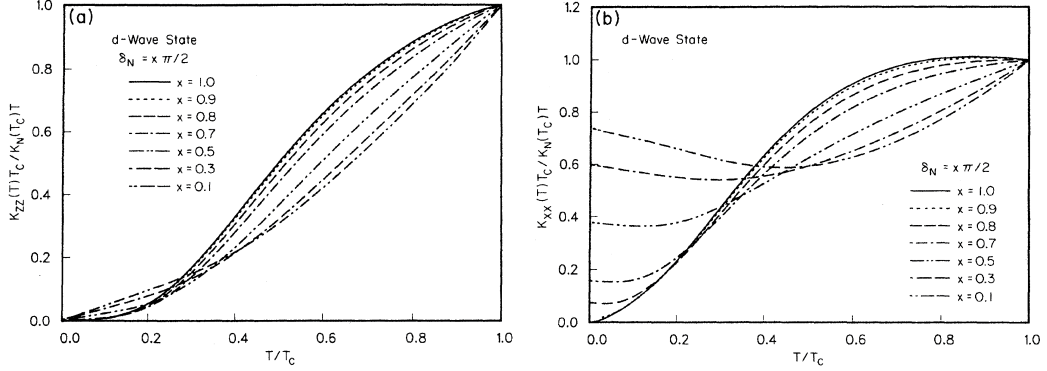
FIGURE 2.4: Normalized thermal conductivity vs reduced temperature for different phase shifts for the *c*-axis (ZZ) and *ab*-plane (XX) current directions of hybrid gap, E_g [16].

distinguishing between candidate gap structures.

The lack of self-consistency, neglecting anisotropy of the Fermi surface and inelastic scattering in Arfi's calculations, which are known to be important for a comparison with experiment, motivated further calculations, which were performed by Fledderjohann and Hirschfeld [60], Norman and Hirschfeld [155], Graf et al. [72, 74], and Hirschfeld and Putikka [87].

Fledderjohann and Hirschfeld (1995) [60] considered the self-consistent treatment of impurity scattering and found a gapless behaviour for E_{1g} (hybrid gap), absent in the theory of Arfi [16]. They showed that there is a distinct difference between the two hybrid gaps E_{1g} and E_{2u} symmetries. Indeed, while the anisotropy ratio tends to zero as $T \to 0$ for the former, it remains finite for the latter (it is indeed unchanged below T_c for a spherical Fermi surface) (see Table 2.4 in this regard). This is a consequence of the difference in the gap at the point node between the two structures, namely, $\Delta(\theta) \propto \theta$ vs θ^2 [which leads to $N_s(E) \propto E^2$ vs E]. It appears that no other physical property is as sensitive to that topological difference [97]. In Chapter 5, we make a comparison with this theory and our experimental data.

In general, $\kappa(T)$ is expected to depend on the complex topology of the Fermi surface and one must go beyond a model with a spherical Fermi surface. However, as argued by Graf, et al. [72] and Barash and Svidzinsky [23, 22], at sufficiently low temperature only a knowledge of the topology of the gap at the nodes is needed, and the low energy spectrum can be determined accurately, without complete knowledge of the Fermi surface. Norman and Hirschfeld [155] and Graf, et al. [72] have performed this and found an excellent agreement with experiment at low temperatures. However, because the theory is

Gap	Nodes	States	κ_c/κ_b
S wave	None	A_{1g}	0
Axial I	LP	$E_{1u}(1,i)$	∞
Axial II	QP	$E_{2g}(1,i)$	∞
Polar	Line	A_{1u}	0
Hybrid	Line + LP	$E_g(1,i)$	0
Hybrid I	Line + LP	$E_{1g}(1,i)$	0
Hybrid II	Line + QP	$E_{2u}(1,i)$	1

TABLEAU 2.4: The gap structure of a few uniaxial states (for strong spin-orbit coupling and ellipsoidal Fermi surface), and the limiting value of the anisotropy ratio κ_c/κ_b expected as $T \to 0$, in the absence of gapless behaviour. The nodal structures include a gap going to zero at a point along the c axis, either with a linear (LP) or a quadratic (QP) k dependence, and along a line in the basal plane [127, 60, 187].

simplified in its treatment of electron-electron scattering, the comparison with experiment should be done only in the elastic regime. A direct comparison with Graf findings and our experimental data will be provided in Chapter 5.

In a brief, in spite of lots of work and efforts on calculation of thermal conductivity in unconventional superconductors, but still there is no good agreement between theory and experiment, especially on heavy fermion compound, may be because of their complicated band structure.

2.3 Disorder effects in unconventional superconductors

Adding of non-magnetic impurities in a nodal superconductor strongly affects the low energy transport and thermodynamic properties. In contrast, in conventional superconductors the nonmagnetic impurities have no influence on physical properties (Anderson's theorem [9]) and also the critical temperature is independent of the concentration of non-magnetic impurities. In s-wave superconductors superconductivity is suppressed only by magnetic impurity scattering, which destroys the coherence of the electron spin states and leads to a gapless superconductor [3, 132]. In a nodal superconductor, a finite concentration of non-magnetic impurities leads to Andreev states with a bandwidth, $\gamma << \Delta_0$, deep in the superconducting state, below which the density of states is non-zero and almost constant, as shown in Fig. 2.5(a). This is only true for unitary scattering. In
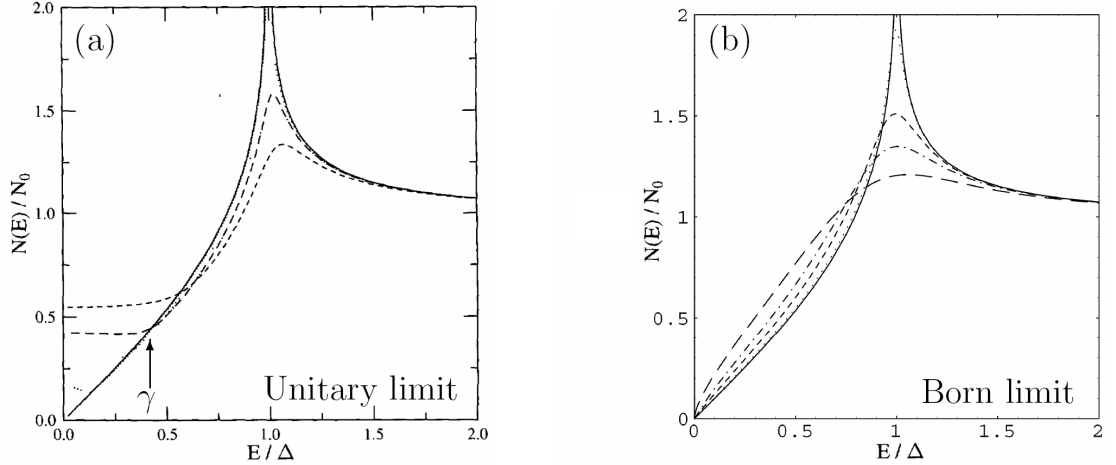
FIGURE 2.5: The effect of impurities on the density of states of a d-wave superconductor (a) in unitary and (b) Born scattering limits [136,178]. In unitary scattering, the density of state at zero energy increases as impurities are added. In Born scattering, the linear density of state, $N(E) \propto E$ slightly changes slope. γ denotes the energy scale at which the density of states becomes constant in energy. Solid lines are for scattering rate $\Gamma/\Delta = 0$.

this figure, even a small amount of impurities creates significant low-energy excitations and decreases the peak normally observed at $E = \Delta$. The results obtained for a d-wave superconductor are similar to recently reported calculations for nodal heavy fermion PrOs$_4$Sb$_{12}$ [171] and E_{2u} gap symmetry [236].

Universal heat transport

This novel metallic band, deep in the superconducting phase, can exhibit universal values for the transport coefficients at very low temperature, $k_B T << \gamma$, *i.e.*, independent of the impurity density or scattering phase shift. This universality can be understood as the cancellation of an increase in $N_s(0) \propto \Gamma$ induced by adding disorder and a decrease in the scattering time, $\tau \propto 1/\Gamma$, by the same disorder, so that $\frac{\kappa_0}{T} \sim \frac{N_s(0)}{\Gamma} \sim constant$.

Universality in the thermal transport at the temperatures approaching zero has been predicted by Graf et al. [74] for certain gap topologies (Later Durst and Lee calculated it for d-wave superconductors [53]). For line nodes, it is given by:

$$\frac{\kappa_{0\parallel}}{T} = \frac{\pi^2}{3} k_B^2 N_F v_F^2 \frac{a\hbar}{2\mu\Delta_0} \tag{2.16}$$

and for quadratic point nodes, a gap opening up quadraticaly with angle at the position
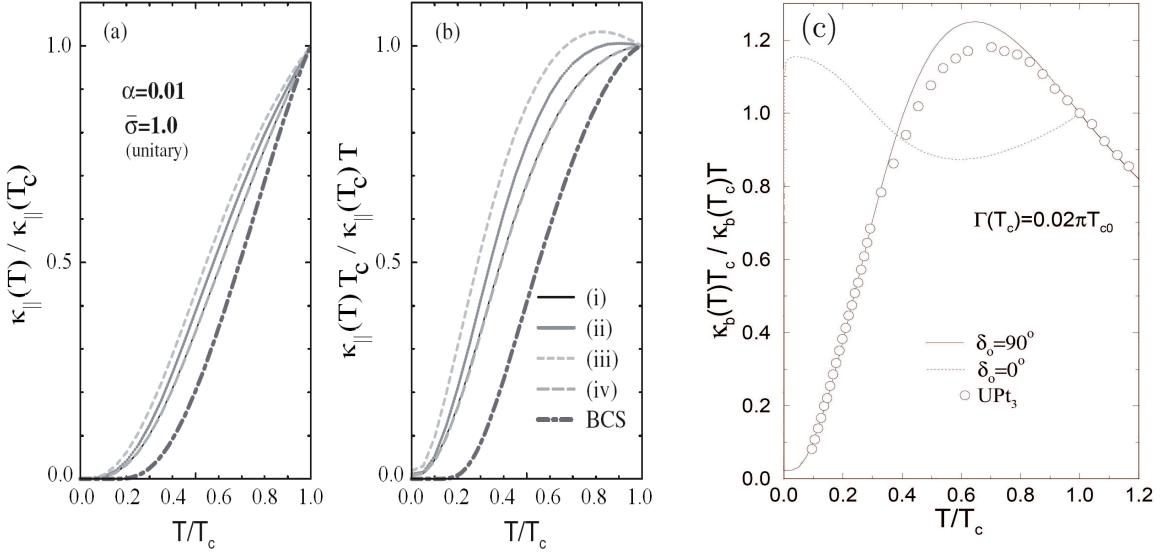
FIGURE 2.6: (a,b) The in-plane thermal conductivity vs temperature for unconventional superconductors in the unitary limit ($\bar{\sigma} = 1$) with a dimensionless scattering rate $\alpha = \frac{1}{2\pi T_{c0}\tau_{c0}} = 0.01$. The different pairing states are: (i) $d_{x^2-y^2}$ (ii) polar (iii) hybrid I, and (iv) hybrid II state. For comparison the result for an isotropic BCS superconductor is shown (adapted from [68]). Note the finite intercept of κ/T for the unconventional pairing states (i) - (iv) [74]. (c) A comparison between normalized thermal conductivity of UPt$_3$ and calculated ones for E_{2u}-state with a scattering rate $\Gamma(T_c) = 0.02\pi T_{c0}$, in resonant and Born scattering limits [72].

of the point nodes, $\Delta(\theta) \propto \mu_{point}^{`}\Delta_0\theta^2$ (*e.g.*, in hybrid II) is given by :

$$\frac{\kappa_{0\perp}}{T} = \frac{\pi^2}{3}k_B^2 N_F v_F^2 \frac{\hbar}{2\mu_{point}^{`}\Delta_0} \quad , \tag{2.17}$$

where $\kappa_{0\parallel}/T$ ($\kappa_{0\perp}/T$) is the residual in-plane (inter-plane) conductivity in the universal impurity scattering limit $k_B T < \gamma << \Delta_0$, N_F is the density of state in the normal state, v_F is the Fermi velocity, Δ_0 is the maximum value of gap, μ ($\mu_{point}^{`}$) is the slope parameter of the gap at the line node (quadratic point node) and a is a coefficient of the order of unity which depends on the gap symmetry. Fig. 2.6(a,b) shows the results of the in-plane thermal conductivity for four pairing states in the resonant scattering limit. All curves show an identical residual linear term. Fig. 2.6(c) shows a comparison between the Graf's calculation and an experimental work on unconventional SC UPt$_3$. It looks this theory agrees well with the experiments.

Experimentally for the first time universal heat transport was confirmed in the high-

T_c cuprate $YBa_2Cu_3O_7$ by Taillefer, et al. [210] and later in the triplet superconductor $SrRu_2O_4$ [209], as shown in Fig. 2.7(a).

The linear point node, where the gap opens up linearly with angle at the position of the point nodes, $\Delta(\theta) \propto \mu_{point}\Delta_0\theta$ (*e.g.,* in hybrid gap) does not show universality [74] (κ_0 shows an impurity concentration dependence),

$$\frac{\kappa_{0\perp}}{T} = \frac{\pi^2}{3}k_B^2 N_F v_F^2 \ \frac{\hbar\gamma}{\mu_{point}^2\Delta_0^2} \quad . \tag{2.18}$$

The magntiude is generally much less than $\kappa_{0\|}$ (Eq. (2.17)) by a factor of order $(\frac{\gamma}{\Delta_0})$ [4]. Therefore in the case of hybrid gap symmetry, increasing of impurity density would increase the zero temperature thermal conductivity at the poles, which has been observed in $CeIrIn_5$, as shown in Chapter 6.

Although Graf assumed a cylindrical or isotropic Fermi surface in his calculations, the results have been proposed to be more general [74]. Thus, experiments on unconventional superconductors with controlled impurity concentrations might allow distinguishing various order-parameter scenarios, depending on whether or not they approach a universal limit [74].

Further effect of impurities, is the dependence of transition temperature to the impurity scattering rate, $T_c(\Gamma)$. $T_c(\Gamma)$ is found by calculating the well-known Abrikosov-Gorkov equation [3]:

$$ln(\frac{T_{c0}}{T_c}) = \Psi(\frac{1}{2} + \frac{\hbar\Gamma}{k_B T_{c0}}) - \Psi(\frac{1}{2}) \tag{2.19}$$

where $\Psi(x)$ is the digamma function and T_{c0} is the maximum T_c for the disorder free material. The critical impurity scattering rate, Γ_c, is given by $0.88T_{c0}$ [207].

Furthermore, note that adding a large amount of impurities will actually destroy the superconductivity, and the thermal conductivity will also deviate from the universal constant at large values of Γ. This has been calculated by Sun and Maki [207] and shown in Fig. 2.7(b). In this figure, κ is shown normalized to the zero disorder limit as a function of scattering rate.

The impurity effects on T_c and upper critical field of UPt_3 compound were stud-

---

[4]Quite recently Vorontsov et al. [229] have calculated the thermal conductivity for a hybrid gap symmetry, considering an *open* Fermi surface. Then the non universality for zero temperature inter-plane thermal conductivity obtained as $\frac{\kappa_{0\perp}}{T} \propto (\frac{\gamma}{\Delta_0})^2 \frac{\kappa_{0\|}}{T}$.
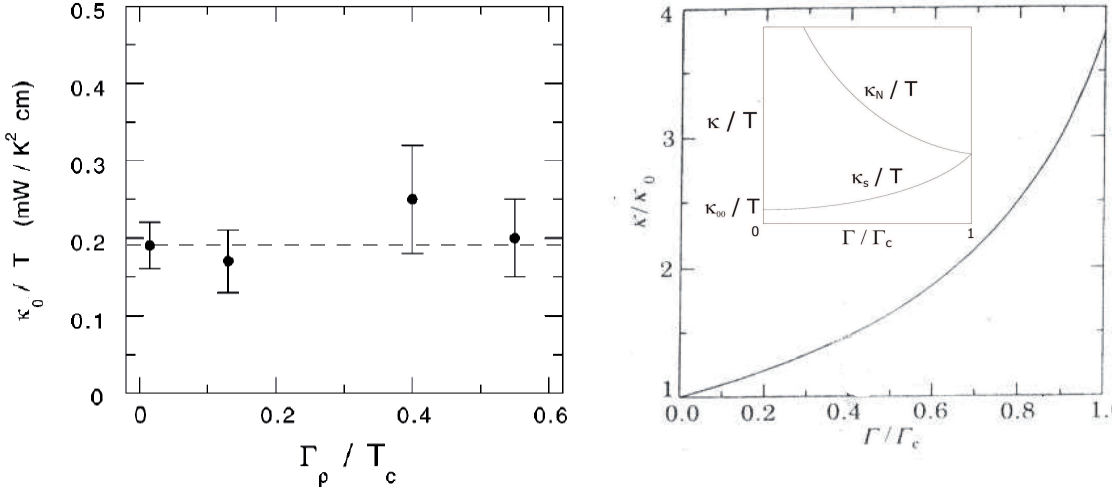
FIGURE 2.7: (a) Universal thermal conductivity in a *d*-wave superconductor YBCO. The residual thermal conductivity κ_0/T plotted as a function of scattering rate Γ [210]. (b) The correction to the universal thermal conductivity with disorder where $\hbar\Gamma_c = 0.88 k_B T_c$, where Γ_c is the critical scattering rate needed to suppress superconductivity completely (after [207]). The inset shows a schematic of the same graph with the normal state thermal conductivity.

ied [117, 204]. Suderow *et al.* found that the crossing point of the upper critical field between $H\|c$ and $H\perp c$ in UPt$_3$ moves to the lower temperature with increasing impurity concentration, which is consistent with the theoretical prediction [43].

Gapless regime - Low temperature corrections

Using the quasiclassical theory, Graf *et al.* [74] considered finite-temperature corrections to the transport coefficients and calculated κ in the gapless regime ($k_B T < \gamma$). The behaviour for in-plane transport is given by:

$$\frac{\kappa(T)}{T} = \frac{\kappa_0}{T}[1 + \frac{7\pi^2}{15}a^2(\frac{k_B T}{\gamma})^2] \quad , \tag{2.20}$$

where κ_0 is the residual linear term. The coefficient a is strongly dependent on the phase shift. For resonant scattering $a = 1/2$, independent of the specific pairing state. They found $\kappa/T \propto T^2$ for *a*- and *c*- heat current directions in hybrid I and II gap symmetries [72].

2.4 Thermal conductivity in a magnetic field

2.4.1 s-wave superconductors

The study of the magnetic-field dependence of thermal conductivity is another way to test the order-parameter symmetry in superconductors. The usefulness of the magnetic field as a probe relies on an important difference between the properties of the vortex state in nodal superconductors compared to s-wave superconductors. While the DOS and the entropy at low fields, $H << H_{c2}$, are determined by the localized states in the vortex cores in the s-wave case, in the superconductors with nodes they are dominated by the delocalized quasiparticle states, which exist close to the nodal directions in momentum space. A qualitative behaviour of the thermal conductivity at low temperatures as a function of magnetic field for an s-wave and a d-wave superconductor is shown in Fig. 2.8.

In s-wave superconductors the only quasiparticle states present at $T << T_c$ are those associated with vortices. At low fields where the vortices are far apart, these states are bound to the vortex core and are therefore localized and unable to transport heat; the thermal conductivity shows an exponential behaviour with very slow growth with H. At high fields near H_{c2} when the vortices are close to each other, tunnelling of quasiparticle excitations from core-to-core becomes possible, which leads to a large enhancement of the quasiparticle mean free path and thermal conductivity. Such a field dependence of the thermal conductivity is observed in Nb and V_3Si [122, 102].

2.4.2 Unconventional superconductors

In contrast, in d-wave superconductors, the quasiparticle heat conduction, due to near nodal states, grow rapidly as soon as the field exceeds H_{c1}. As pointed out by Volovik [226], the quasiparticles spreaded outside the vortex cores can participate in the heat transport at fields just above H_{c1} because of the Doppler shift (as explained below) of the quasiparticle energy spectrum. This leads to immediate increase of κ at low fields, which is proportional to the density of states $N(E = 0, H) \propto \sqrt{H}$ for $H_{c1} < H << H_{c2}$. Thus we may expect an increase in $\kappa(H)$ almost proportional to $\sqrt{H}$, as observed in several unconventional superconductors [42].

Doppler shift energy

A most remarkable effect of the magnetic field on a nodal superconductor is the
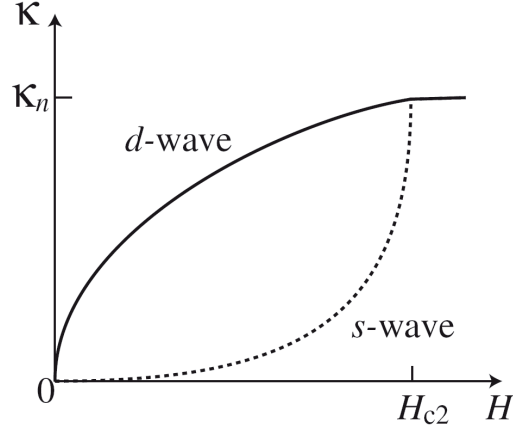
FIGURE 2.8: A schematic of general field dependence of the thermal conductivity κ for s and d-wave superconductors. In s-wave superconductors, the thermal conductivity shows an exponential behaviour with very slow growth with H [122,102]. In contrast, in d-wave superconductors, the quasiparticle conduction grows rapidly as soon as the field exceeds H_{c1}. The slope of $\kappa(H)$ at H_{c2} depends on purity (from [140]).

Doppler shift of the quasiparticle spectrum [226]. In the presence of a supercurrent with velocity $\mathbf{v}_s$ the energy of a quasiparticle with momentum $\mathbf{k}$ is Doppler shifted relative to the superconducting condensate by

$$\epsilon(\mathbf{k}) \longrightarrow \epsilon(\mathbf{k}) - \hbar \mathbf{k}.\mathbf{v_s} \ . \tag{2.21}$$

To estimate the characteristic energy scale of the Doppler shift we can approximate the velocity field by that around a single vortex, $v_s = \hbar\hat{\phi}/2mr$, where r is the distance from the centre of the vortex and $\hat{\phi}$ is a unit vector along the circulating current. This expression is valid outside the vortex core and up to a cut-off of the order $\min\{R, \lambda_L\}$, where $R = a\sqrt{\Phi_0/\pi H}$ is the intervortex distance, Φ_0 is the flux quantum and a is a geometric constant. This energy shift, E_H, is calculated by integrating over a unit cell of vortex lattice with lattice parameter a :

$$E_H = \langle|\mathbf{v}_s.\mathbf{p}|\rangle = \int_{|\mathbf{r}|<R} \frac{d^2\mathbf{r}}{\pi R^2} |\mathbf{p}.\mathbf{v}_s| \propto \frac{4}{a\pi}\hbar v_F \sqrt{\frac{H}{\Phi_0}}. \tag{2.22}$$

Recalling the linear in E dependence of $N(E)$ in the clean limit (Eq. (2.13)), the Volovik effect naturally leads to $N(E = 0, H) \propto E_H \propto \sqrt{H}$. The $\sqrt{H}$ dependence of $N(H)$ leads to a $\sqrt{H}$ dependence of specific heat coefficient. Experimentally the Volovik model was

confirmed in the specific heat studies [145, 146, 58, 233] (In fully gapped superconductors, this shifted energy is typically very small compared to Δ_0 and thus negligible.).

Note that in the Doppler shift model only the quasiparticle energy is shifted, so that the quasiparticle scattering rate is not directly affected by the presence of the vortices. In the self-consistent T-matrix approximation, the magnetic field does affect the lifetime indirectly, by modifying the density of states available for scattering [115, 116]. Hence the Doppler shift method does not include the scattering of the quasiparticles on vortices, which is important most away from the zero temperature.

In reality, the behaviour of the thermal conductivity is more complex especially at higher temperatures. While the magnetic field enhances the density of states, it also leads to suppression in the transport life time both via the impurity scattering and Andreev scattering off the vortices. In spite of lots of efforts has been done in this regard [223, 115, 224, 229, 23, 22, 61, 239, 19], the complete picture is not still developed. In general, at low temperatures-low fields the enhancement of density of states plays the dominant role, and the thermal conductivity increases with field. At higher temperatures and low fields, the effect of scattering by vortices also come in. Consequently, the thermal conductivity initially decreases with field, and goes through a minimum at a finite H [224]. This behaviour has been observed in high T_c cuprates [114] and also in other systems, like $CeCoIn_5$, UPd_2Al_3 and $SrRu_2O_4$ [94, 232, 93].

In conclusion, we have reviewed the behaviour of the thermal conductivity in metals and superconductors. The thermal conductivity of conventional and unconventional superconductors was reviewed for $H = 0$ and in a magnetic field. A review on the effect of non-magnetic impurity on thermal conductivity of nodal superconductors was given.
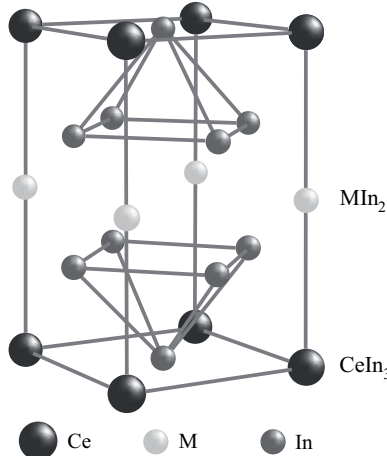
Chapter 3

Heavy Fermion CeMIn$_5$ (115 Family)

3.1 General physical properties

After discovery of pressure induced superconductivity in antiferromagnetic CeIn$_3$ with T_N=10K, lots of effort have been done to understand the mechanism of superconductivity in this compound. On this road, quickly another pressure induced superconductivity in the antiferromagnet tetragonal version of CeIn$_3$ compound, CeRhIn$_5$ was reported. These findings suggested that the mechanism forming Cooper pairs can be magnetic in origin. Following the initial report on CeRhIn$_5$ [81], further investigations have revealed the existence of superconductivity in the isostructural, ambient-pressure superconductors CeIrIn$_5$ and CeCoIn$_5$. The most striking thing about CeMIn$_5$ compound is the rich variety of ground states, proximity or coexistence of superconducting and magnetic ground states, similar to the high-T_c cuprate. Here a summary of a few physical properties of CeMIn$_5$ is given.

The family of Ce-based heavy fermion compounds CeMIn$_5$ in which M is a transition metal, M=Co, Rh or Ir [173], crystallizes in the tetragonal HoCoGa$_5$ structure consisting of the conducting CeIn$_3$ layers separated by MIn$_2$ layers stacked sequentially along the tetragonal c-axis (Fig. 3.1). The parent compound of this family, CeIn$_3$, has cubic crystal structure. At ambient pressure, it is an antiferromagnet with an ordering vector Q=(0.5,0.5,0.5), while at the critical pressure P_c=2.55 GPa, it becomes superconducting with $T_c \approx 0.2$K [139]. Recently, the unconventional nature of superconductivity in this compound has been confirmed from the lack of the coherence peak in the ^{115}In-NQR

FIGURE 3.1: Crystal structure of CeMIn$_5$.

measurement [1] [104]. The related material CeRhIn$_5$ is quasi 2D and has relatively high $T_c = 2.1$K, under pressure. This comparison indicates that the dimensionality is one of the important factors for the occurrence of unconventional superconductivity [235]. Effect of dimensionality on T_c has been already discussed for the spin-fluctuation mediated superconductivity. Both in the phenomenological models [152, 147] and in the microscopic calculations [213], it has been shown that the magnitude of T_c is higher in quasi 2D systems than in 3D systems[2]. It seems the relation between T_c and ratio c/a in 115 family obeys the above model (see Fig. 3.2), although it is still not clear that what role dimensionality plays in determining the varying ground states in this material. Lattice parameters and ratio c/a of CeMIn$_5$ compound through the transition metal series are $a = 4.614, 4.652, 4.6662$ $\mathring{A}$, $c = 7.552, 7.542, 7.5168$ $\mathring{A}$ so that $c/a = 1.637, 1.621, 1.610$ for $M =$ Co, Rh and Ir, respectively.

Consistent with the layered description of the crystal structure, electronic structure calculations reveal a quasi two dimensional (open along the c-axis) character of the Fermi surface that has been confirmed by de Haas-van Alphen (dHvA) measurements [129, 78]. While the 115 materials show small anisotropy nearly 2-3 in the electrical resistivity, much more isotropic than, *e.g.*, high-T_c cuprate, they show a dominant warped cylindrical Fermi surface, with significant f-electron weight, in their band structure. A representative

---

[1]an anomalous temperature dependencies of the electrical resistivity already has been reported [139].

[2]In fluctuation models it has been predicted with increasing three-dimensionality on the energy dispersion, the AF phase is stabilized owing to the suppression of the fluctuation, and the SC phase shrinks. Moreover, the total weight of the spin fluctuations decreases with increasing the dimensionality [152, 147, 213].
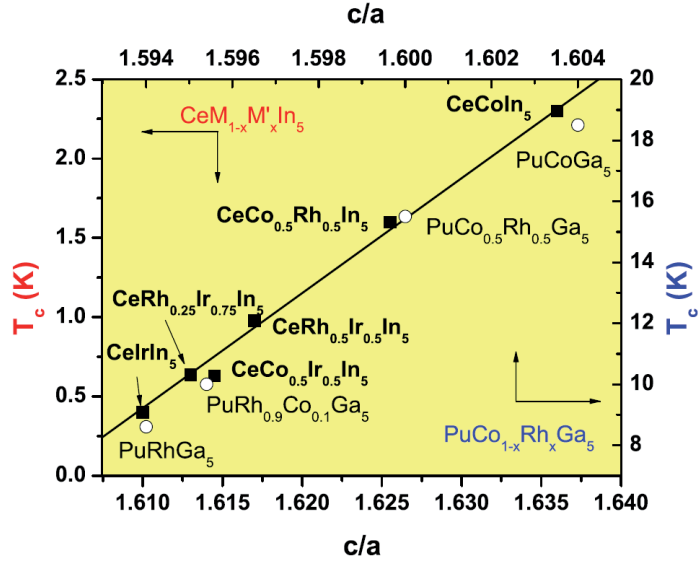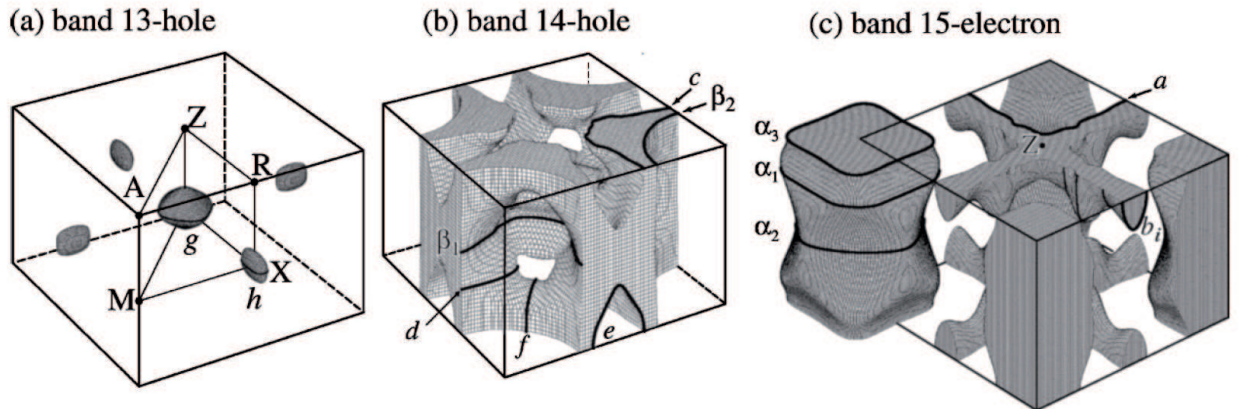
FIGURE 3.2: Superconducting transition temperatures as a function of tetragonal lattice parameters c/a for various Ce- and Pu-members of the CeMIn$_5$ and PuMGa$_5$ families. The relative dependence of T_c on c/a is nearly identical for both families [184].

calculation of the Fermi surface of CeIrIn$_5$ is shown in Fig. 3.3 [78]. Calculation using the relativistic linear augmented plane wave method (FLAPW) within the local-density approximation in the itinerant $4f$ electron band model have reported an almost identical Fermi surface for CeCoIn$_5$ and CeIrIn$_5$ [129]. This study conclude that any difference between these two compounds must arise on a small energy scale that would not affect the band structure calculation. Although, it is generally accepted that the Fermi surface in CeMIn$_5$ has several cylindrical 2D and spherical 3D sheets, as shown in Fig. 3.3, associated with three to four bands crossing the Fermi surface [78]. The multiband effects may appear in physical properties, *e.g.* in the superconducting state.

In the case of CeRhIn$_5$, the reported band structure compared to the angular dependence of various dHvA frequencies has shown a similar Fermi surface to ones for the non-magnetic compound LaRhIn$_5$ (no f electron). This suggests that the f-electrons in CeRhIn$_5$ are localized, in contrast to their itinerant behaviour in CeCoIn$_5$ and CeIrIn$_5$ [195, 8].

The electronic specific-heat coefficient γ of CeMIn$_5$ compound is large which confirms heavy fermion behaviour of this family. This coefficient increases through the transition metal series from $\gamma(T_c)$ =350 mJ/molK^2 for M=Co [241] over $\gamma(T_N) \sim$ 420 mJ/molK^2 for M=Rh [81] to $\gamma(T_c)$ =720 mJ/molK^2 for M=Ir [173]. In contrast, the La analogues

(a) band 13-hole   (b) band 14-hole   (c) band 15-electron

FIGURE 3.3:   Fermi surfaces of CeIrIn$_5$ [78].

are Pauli paramagnets with γ of about 5 mJ/molK^2 [173].

CeIrIn$_5$ and CeCoIn$_5$ are superconductor at ambient pressure with transition temperatures $T_c = 0.4$K [173] and 2.3K [174] respectively. A strange behaviour is observed in CeIrIn$_5$. As shown in Fig. 3.4 the resistivity drops to zero at about $T_{c\ \rho} = 1.2$K $\sim 3T_{c\ bulk}$, while the thermodynamic and magnetic signatures of superconductivity appear at much lower temperature. The origin of this observation still is not clear though filamentary superconductivity was suggested [34] [3].

In the normal state of CeIrIn$_5$ C/T weakly increases as temperature approaches T_c, which could be consistent with Fermi-liquid behaviour; however, in this temperature range, the electrical resistivity in not quadratic in temperature, as expected for a Landau Fermi liquid, but increases as $\rho_a \propto T^{1.25}$ [173]. Furthermore, in a high magnetic field much larger than $H_{c2}(0)$, C/T tends to approach a logarithmic divergence at low temperatures [38]. This study of the field dependence of C/T suggests that there should be a field induced quantum critical point near $H = 25$T, which is where a metamagnetic transition [108] in CeIrIn$_5$ also extrapolates to $T = 0$.

The third member of this family CeRhIn$_5$, is an antiferromagnet with ordering temperature $T_N = 3.8$K [81,21]. Small magnetic Ce moments ($0.26\mu_B$ at 1.4K) form a helical spiral along the c-axis and are antiparallel for nearest-neighbour pairs in the tetragonal

---

[3]Josephson effect has been investigated on an SNS'-type weak link with S=CeIrIn$_5$, N=Cu and S'=Nb [206] in order to shed more light on the peculiar behaviour of the resistivity in comparison with bulk superconductivity. Indeed, a Josephson critical current I_c was observed below the temperature $T_{c\ \rho}$, where the resistivity of the sample drops to zero, *i.e.*, well above bulk $T_{c\ bulk}$. The result confirms the presence of a superconducting state above $T_{c\ bulk}$ and possible phase coherence between CeIrIn$_5$ and Nb, at least at the surface of CeIrIn$_5$ [68].
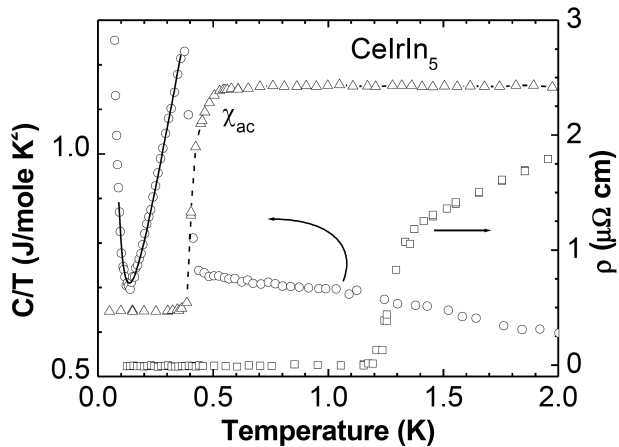
FIGURE 3.4: Specific heat divided by temperature C/T (circles, left ordinate), ac suscep-tibility χ_{ac} (triangles, arbitrary units), and electrical resistivity ρ (squares, right ordinate) of CeIrIn$_5$ as a function of temperature (from [173]).

basal plane [21].

Recently superconductivity with a transition temperature above 18K was reported in isostructural Pu compounds, PuCoGa$_5$ [183, 185] (The related compound PuRhGa$_5$ has $T_c = 8.6$K [231]). Inspite of the structural similarity with the Ce-based compounds, PuCoGa$_5$ exhibits only a modest quasiparticle mass enhancement, indicated by specific heat measurements [28]. Furthermore, in both Co compounds the electrical resistivity shows non-Fermi-liquid behaviour with a $T^{1.35}$ power law for PuCoGa$_5$ and a nearly linear behaviour for CeCoIn$_5$. The origin of superconductivity with relatively high transition temperature in this compound is still not clear. However, it has been argued that it might be attributed to increased hybridization of the Pu $5f$ electrons compared to the more localized Ce $4f$ electrons, and that the superconductivity is most likely spin-fluctuation mediated [183].

In the following we review published studies of the order-parameter symmetry in superconductors CeCoIn$_5$ and CeIrIn$_5$.

3.2 Gap symmetry

3.2.1 Nodal structure

Specific heat
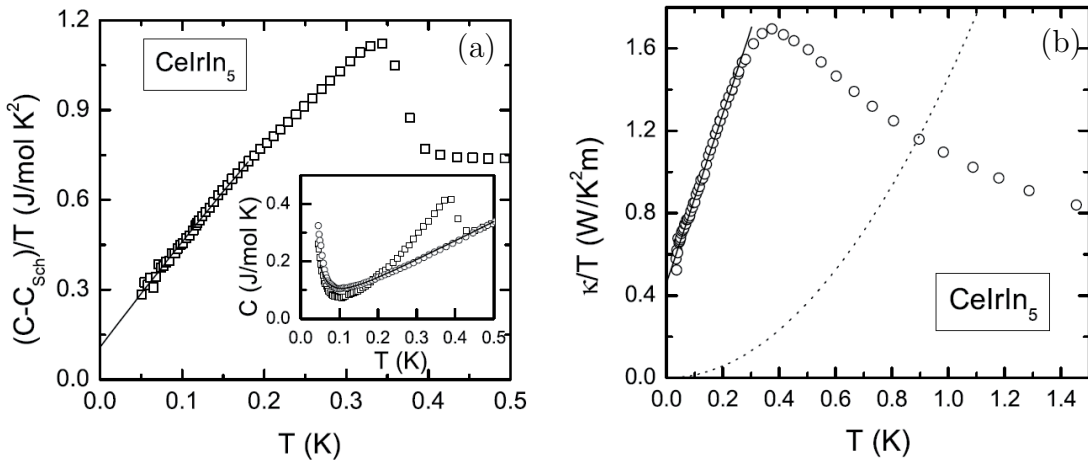
FIGURE 3.5: (a) Electronic specific heat and (b) thermal conductivity of CeIrIn$_5$ measured by Movshovich et al. [150].

Specific-heat measurements reveal $C(T) \propto T^2$ for both compounds, down to low temperature (below $T_c/3$) [173, 174, 89, 150]. The T^2 electronic specific heat is an indication of the presence of line nodes in the superconducting gap. In addition, a residual linear-T contribution in CeIrIn$_5$ and CeCoIn$_5$ was attributed to an impurity band that form the nodes (see Fig. 3.5(a)).

Thermal conductivity

There are a few thermal conductivity studies for CeCoIn$_5$ but so far *only* one in-plane thermal conductivity study reported on CeIrIn$_5$ [4] [150, 94, 217]. For both compounds a residual κ/T for $T \to 0$ have been reported. Based on the existence of power law behaviour in $\kappa(T)$ in the superconducting state, the presence of line nodes in both compounds was reported. Further information on the nodal structure of CeCoIn$_5$ by field-angle dependent thermal-conductivity measurements show fourfold symmetry consistent with nodes along the $(\pm\pi, \pm\pi)$ positions [94]. Field-angle dependent measurements of the specific heat aslo support a fourfold symmetry but disagree on the location of the nodes [13]. Recent theoretical analysis suggested that, when the redistribution of the spectral density due to the vortex scattering is accounted for, the specific heat is also consistent with the

---

[4]During doing corrections on my thesis, Kasahara *et al.* [100] measured in-plane thermal conductivity of CeIrIn$_5$ down to temperature 0.15K. The temperature dependency and the residual linear term are nearly in agreement with our data. Later we make a complete comparison between their data and ours in Chapter 7.
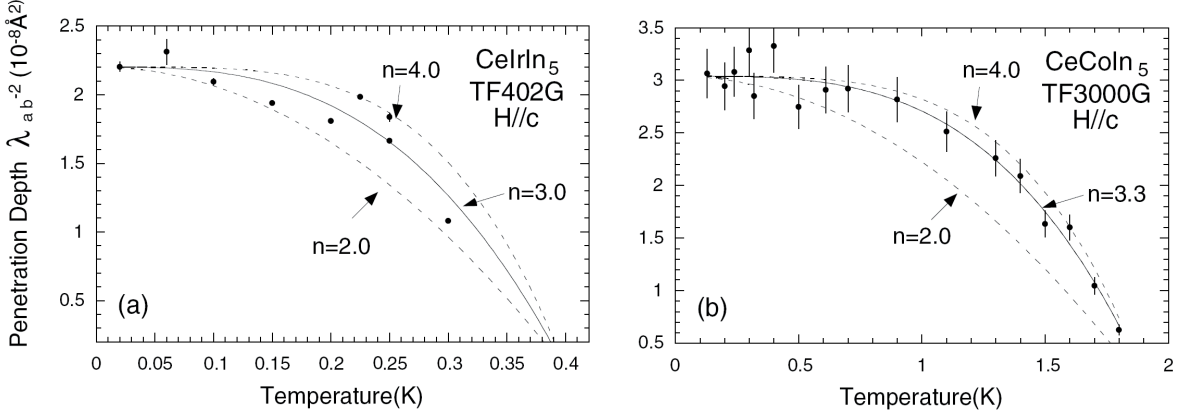
FIGURE 3.6: Temperature dependence of $1/\lambda_{ab}^2$ in (a) CeIrIn$_5$ and (b) CeCoIn$_5$. Solid lines indicate the power-law relation determined by fitting and dashed lines indicate the cases $n = 2$ (line-node with impurities scattering) and $n = 4$ (BCS case) [84]

$d_{x^2-y^2}$ gap [229].

Recent thermal conductivity measurements on CeCoIn$_5$ show also the presence of uncondensed electrons in the superconducting state [217].

Penetration-depth

Penetration depth measurements have been performed by several groups either by μSR [84] or microwave measurements [158, 161, 41]. The magnetic penetration depth λ_{ab} and its temperature dependence was deduced by transverse field μSR measurements with field applied parallel to the c-axis. For CeIrIn$_5$ a magnetic penetration depth $\lambda_{ab} \cong 6700A^0$ was estimated, similar to that for CeCoIn$_5$ with $\lambda_{ab} \cong 5500A^0$. A power law temperature dependence of $\Delta\lambda_{ab}^{-2} = \lambda_{ab}^{-2}(0) - \lambda_{ab}^{-2}(T)$ with exponents $n = 3 \pm 0.4$ for CeIrIn$_5$ and $n = 3.3 \pm 0.4$ for CeCoIn$_5$ was seen. The exponents deviate from the T^4 and T behaviours expected for an isotropic s-wave superconductor and for an order parameter with line nodes in the clean limit, respectively [234]. It was argued that impurity scattering [169] can cause the deviations from the linear dependence of the superfluid density at low temperature, although the impurity effect changes the linear-T dependence only into a T^2 dependence (see Fig. 3.6) [68].

3.2.2 Parity and spin state

Upper critical fields

Upper critical field measurements can probe the spin state of the Cooper pairs. The
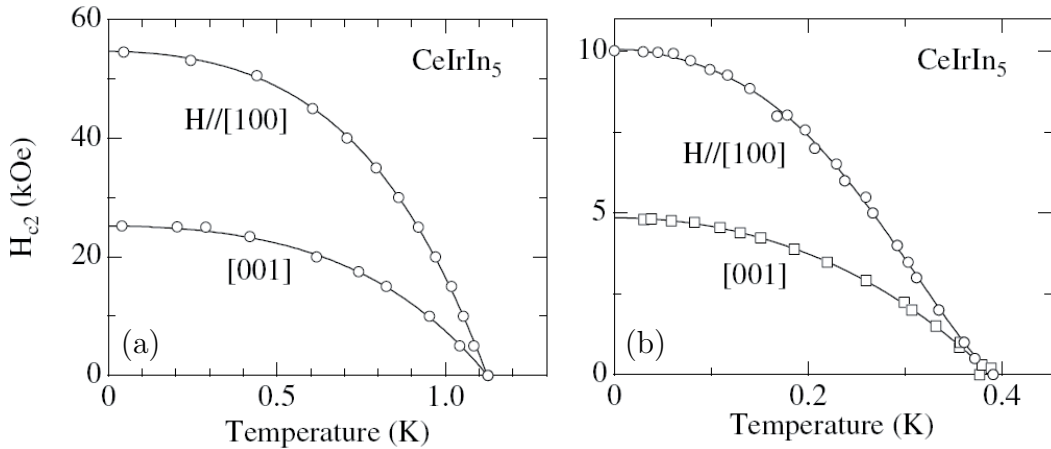
FIGURE 3.7: Temperature dependence of H_{c2} measured in CeIrIn$_5$ by (a) resistivity and (b) magnetic susceptibility [195].

upper critical field of CeCoIn$_5$ has been determined by measurements of the specific heat and thermal expansion. Both indicate a change from a second-order transition at H_{c2} at fields below 4.7 T to a first-order transition [35], as can be revealed by a step in the H dependence of the thermal conductivity, magnetization and specific heat [94,218,35]. It was interpreted that the first-order superconducting phase transition is due to Pauli limiting [218]. The observation of Pauli paramagnetic limit is a direct evidence of a spin singlet pairing [68] [5].

Regarding CeIrIn$_5$, the upper critical field H_{c2} was measured only by temperature and field dependence of the electrical resistivity and ac susceptibility (see Fig. 3.7) [195,173]. The factor nearly 2 anisotropy of H_{c2} with respect to field orientation has been attributed to the anisotropy in the electronic system [195].

Nuclear spin resonance

Nuclear quadrupolar resonance (NQR) measurements show no Hebel-Slichter peak just below T_c in either compound, consistent with unconventional superconductivity [112, 243, 47]. Below T_c the spin susceptibility is suppressed, indicating singlet pairing. For CeIrIn$_5$ the nuclear relaxation rate follows a $1/T_1 \propto T^3$ down to 50mK [112] (see Fig. 3.8) compatible with a line-node gap [243]. As we showed in previous chapter, the linear increase in energy of the density of states, $N(E) \propto E$, gives rise to the T^3 variation of

---

[5]The first order transition at low temperatures has also been linked to the possible presence of a Fulde-Ferrel-Larkin-Ovchinnikov (FFLO) phase [32].
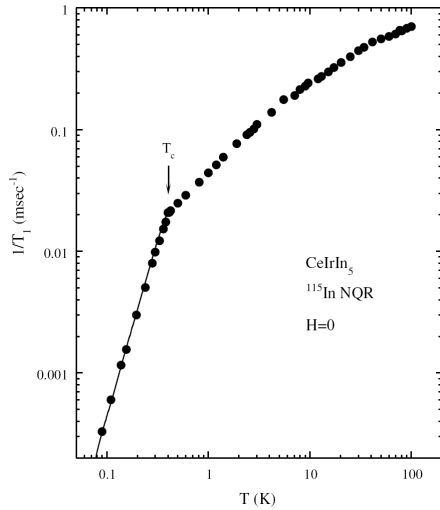
FIGURE 3.8: Temperature dependence of the [115]In nuclear spin-lattice relaxation rate of CeIrIn₅. The solid line is a calculation assuming the gap model $\Delta(\phi) = \Delta_0 \cos(\phi)$ with $2\Delta_0 = 5.0 k_B T_c$ and the BCS temperature dependence of the gap (from [243]).

$1/T_1$ at low T. However, NQR measurements on CeCoIn₅ [112] do not show the T^3 low-temperature behaviour; instead $1/T_1$ saturates below 0.3K probably due to paramagnetic impurities [112] or uncondensed electrons [217], which mask the intrinsic quasiparticle contribution.

3.2.3 Energy gap

Point-contact spectroscopy measurements have been performed only on CeCoIn₅ to study the order parameter symmetry through the mechanism of Andreev reflection. A d-wave order parameter, with $d_{x^2-y^2}$ symmetry [170, 68] and multi-band effects [182] have been concluded.

3.2.4 Flux line lattice

The flux-line lattice of CeCoIn₅ has been imaged using small angle neutron scattering experiments [57]. At low magnetic fields a hexagonal flux-line lattice has been reported. With increasing applied field the flux-line lattice undergoes a transition to square symmetry at about 0.6 T. This is consistent with the theoretical expectation for the $d_{x^2-y^2}$ symmetry. Theoretically, d-wave pairing is expected to stabilize a square flux-line lattice,
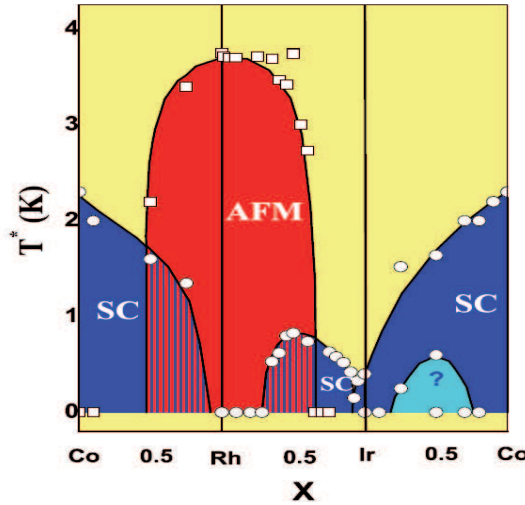
FIGURE 3.9: General phase diagram of Ce(Co, Rh, Ir)In$_5$ alloy. Hashed areas correspond to regions of coexisting AFM and SC orders. The phase labeled '?' may not be intrinsic but due to chemical phase separation. Fig taken from [184], after [167].

which was observed in the high-T_c superconductors [65] [6].

Summary

Here, we have summarized some of the evidence that points toward an unconventional pairing mechanism in CeCoIn$_5$ and CeIrIn$_5$. In spite of lots of measurements on CeCoIn$_5$, however, the order parameter and gap structure of CeCoIn$_5$ are far from solidly established. While most measurements agree to the presence of nodes in the gap, there is a lively controversy as to the actual order parameter (whether $d_{x^2-y^2}$ or d_{xy}, for example) and the origin of uncondensed electrons [217] (whether due to gapless regions [26], multi-band scenario [217] or quantum criticality [242].). An order-parameter with $d_{x^2-y^2}$ symmetry is reported as the most prominent candidate for CeCoIn$_5$ probably implying that the antiferromagnetic spin fluctuations are important for superconductivity. The angular dependence of the thermal conductivity, the power laws in various properties and the point-contact data support a d-wave order-parameter symmetry.

Regarding CeIrIn$_5$, so far there is *no direct* evidence of gap symmetry. The limited experimental situation points to a d-wave gap, the same as for the isostructural compound CeCoIn$_5$.

---

[6]However, it has been argued that the orientation of the square vortex lattice in tetragonal crystals may not serve as a conclusive test for the position of gap nodes, and that the low-field vortex lattice is consistent with d_{xy} symmetry as well [68].

3.3 More physical properties

3.3.1 Chemical tuning and phase diagrams

Pagliuso et al. [167] were the first to map out the phase diagram of single phase crystals of Ce(Rh,Ir,Co)In$_5$, revealing the rich interplay between superconductivity and magnetism in the 115 system (see Fig. 3.9).

Ir-substitution for Rh in CeRhIn$_5$ decreases the magnetism and introduces superconductivity. As shown in Fig. 3.10, antiferromagnetic order coexists with superconductivity for intermediate Ir concentrations in CeRh$_{1-x}$Ir$_x$In$_5$ compound. In this region neutron-scattering studies reveal a change in the ordered magnetic structure [120] from incommensurate antiferromagnetism in pure CeRhIn$_5$ [21, 121] to coexistence of incommensurate and commensurate antiferromagnetism in this region. In further Ir concentrations, T_c vanishes near CeRh$_{0.1}$Ir$_{0.9}$In$_5$. The observation of these two superconductivity domes, one coexisting with the AFM ground state and another far away from magnetism, suggests the possibility of two kinds of superconductivity in this family [7]. Moreover, recent NQR measurements under pressure on pure CeIrIn$_5$, as the system is away from the AFM seen in Fig. 3.10, shows T_c goes up with the pressure while the size of energy gap remains constant. The interesting point is that superconductivity emerges *without* any trace of AFM spin fluctuations [105].

Pressure study of CeRh$_{1-x}$Ir$_x$In$_5$ compound in Fig. 3.10 provides more information in this regard and helps to find the characteristic differences between CeCoIn$_5$ and CeIrIn$_5$ superconductors. Pressure further separates CeIrIn$_5$ from antiferromagnetism, or in other words, separates the two SC domes. A similar evolution from antiferromagnetism to superconductivity, occurs for CeRh$_{1-x}$Co$_x$In$_5$ [241, 156]. Fig. 3.11 shows a comparison between two materials CeRh$_{1-x}$Ir$_x$In$_5$ and CeRh$_{1-x}$Co$_x$In$_5$ [8]. These two phase diagrams

---

[7]The first observation of two dome superconductivity in heavy fermion material has been reported as a function of pressure on CeCu$_2$(Si$_{1-x}$Ge$_x$)$_2$ [240]. One dome (SC1) is formed around the antiferromagnet QCP, whereas another one (SC2) emerges under the heavy fermion state without any signature for AFM spin fluctuations. Interestingly, a maximum T_c in SC2 as the function of pressure is higher than that in SC1. Although a possible origin of SC2 is not yet known, a new type of pairing mechanism is suggested to mediate the Cooper pairs in HF systems besides AFM spin fluctuations. For instance, valence fluctuations of Ce ions may be responsible for the onset of SC2 via the increase of hybridization between conduction electrons and Ce-4f electrons [240, 157, 143, 105].

[8]The $T - x$ phase diagram for CeRh$_{1-x}$Co$_x$In$_5$ shown in Fig. 3.11(a) was determined by the neutron diffraction, specific heat and resistivity measurements [156]. The incommensurate AFM order, which is observed in the pure CeRhIn$_5$ system, appears below $x = 0.3$ and is absent at $x \geq 0.4$. The SC state is not observed down to 0.7K at $x = 0.2$, while it suddenly appears at $x \approx 0.3$. The commensurate AFM
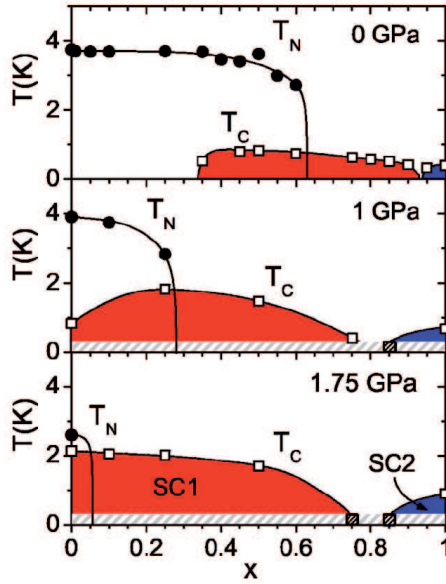
FIGURE 3.10: Evolution of the phase diagram of CeRh$_{1-x}$Ir$_x$In$_5$ with applied pressure. This evolution suggests the possibility of two superconducting (SC) phases. Taken from [184], after Nicklas et al. [153].

show some similarity: (1) simultaneous appearance of the superconductivity and AFM order at low x; (2), coexistence of superconductivity with the commensurate AFM order in the intermediate x regime. However, a significant difference also exists: while the incommensurate AFM order coexists with the superconductivity in CeRh$_{1-x}$Ir$_x$In$_5$, there is *no* intrinsic coexistence of the incommensurate AFM order with the commensurate AFM order and the superconductivity state in CeRh$_{1-x}$Co$_x$In$_5$. This leads to suggest that the superconductivity is strongly suppressed by the incommensurate AFM order in the latter system, while they coexist in the former system [156].

To compare the above results to some other experimental results on pure CeRhIn$_5$, recently specific heat measurements on pure CeRhIn$_5$ under hydrostatic pressure revealed that the incommensurate AFM order suddenly disappears above a critical pressure $p_c^* \approx 2$ GPa where a bulk SC phase sets in [110]. On the other hand, NQR experiments have revealed a magnetic transition from incommensurate to commensurate at 1.67 GPa, where superconductivity comes in. Therefore, the *absence* of any coexistence of incommensurate AFM order and superconductivity seems to be a common feature in the CeRh$_{1-x}$Co$_x$In$_5$ system and CeRhIn$_5$ under pressure [156].

---

order simultaneously appears here, and stays on the intermediate x region ($0.3 \leq x \leq 0.6$), together
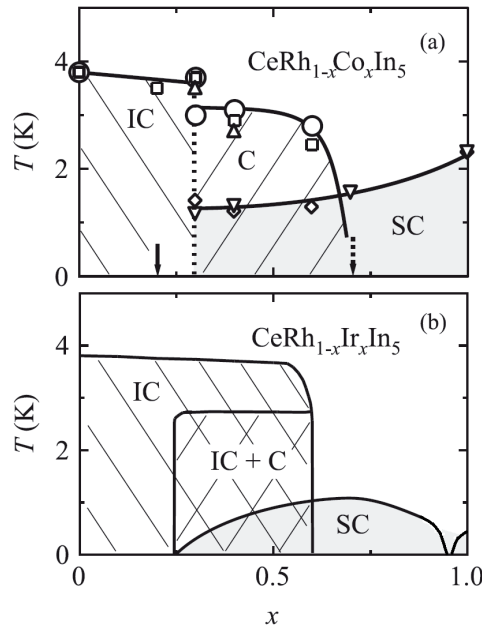
FIGURE 3.11: (a) $T-x$ phase diagram for $CeRh_{1-x}Co_xIn_5$ from the neutron diffraction, specific heat and resistivity measurements. At $x=0.2$ (solid arrow) and $x=0.7$ (dotted arrow), the superconductivity and the AFM order were not observed down to $T=0.7K$. (b) A schematic of $T-x$ phase diagram for $CeRh_{1-x}Ir_xIn_5$ reported in [120, 105]. Fig adapted from [156].

All these observations so far are consistent with a recent specific heat study of Cd-doped $CeMIn_5$ compound (see Fig. 3.12) [175]. Adding Cd on the In site, has a dramatic effect on these materials. While in $CeCoIn_5$ superconductivity is rapidly suppressed with Cd doping and an ordered antiferromagnetic state emerges in coexisiting with superconducting state, in $CeIrIn_5$ these two phases are competing. [9] This is the first example of magnetism appearing close to superconductivity in Ir115 compound, and interestingly, the magnetic ordering temperature of Cd-doped Ir115 is the highest found among the Cd-doped Ce115s, close to the T_N of the parent compound $CeIn_3$.

In Chapters 5 and 9, we will show that these evidences may support our suggestions of a different SC gap symmetry and spin fluctuations in the two systems $CeCoIn_5$ and $CeIrIn_5$.

Conclusion

As regarding $CeIrIn_5$, several recent studies suggest that it may support a different

---

with the superconductivity.

[9]The appearance of the magnetic ground state with an ordering temperature that increases with increasing Cd concentration is common to $CeRhIn_5$ as well [175].
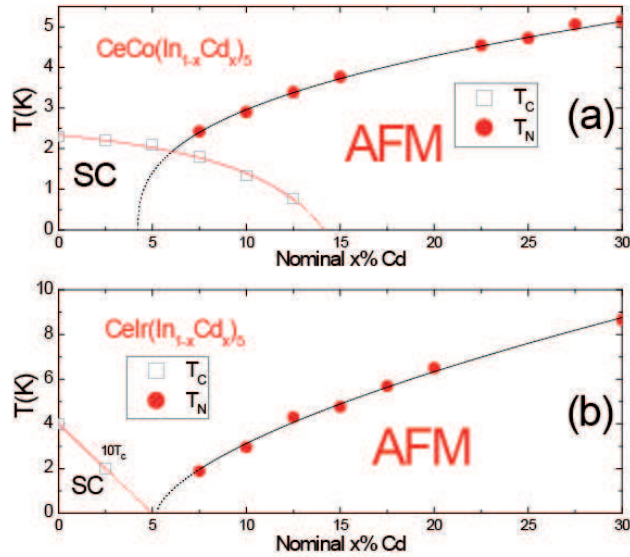
FIGURE 3.12: Dependence of superconducting transition temperatures T_c and Neel temperatures T_N on x, where x is the Cd content of crystals. (a) $CeCo(In_{1-x}Cd_x)_5$ and (b) $CeIr(In_{1-x}Cd_x)_5$. T_c and T_N were extracted from specific heat and confirmed with magnetic susceptibility and resistivity measurements. The dotted lines are smooth extrapolations to $T = 0K$ [175].

superconducting state, compared to the closely related compound $CeCoIn_5$. Until now, this suggestion has been based on indirect evidences, *e.g.* a comparison of magnetic fluctuation spectra and phase diagram vs alloying or pressure.

Chapter 4

Experimental Techniques

In this chapter a brief review on sample preparation, cryogenic techniques and experimental apparatus, the technique and our thermal conductivity mounts, is given. For comprehensive information on equipments and the cryogenic techniques developed and used in the group, please see theses of E. Boaknin and B. Lussier [36].

All measurements for this thesis were performed in a ^{4}He Dipper cryostat and an Oxford Kelvinox 300 ^{3}He-^{4}He Dilution refrigerator. The instruments were delivered in January 2004 to Sherbrooke, nearly 8 months after my arrival to Canada.

The dilution fridge can reach to nearly 8mK without heat load, but with the thermal conductivity or electrical resistivity tail can reach to below 50mK for the best conducting samples with good thermal contacts. The cryostat is equipped with a 17T superconducting magnet with a compensated region centered on the bottom plate of mixing chamber. The resistivity measurements can be done in both cryostats and cover the entire temperature range 40mK$< T <$300K, whereas the thermal conductivity measurements can be performed in the dilution fridge for 50mK$< T <$5K and in the dipper for 1.6K$< T <$100K.

All leads to the tail and the cryostat which are used for measuring simultaneously the thermal conductivity and electrical resistivity of three samples, are a 24-pin, a 26-pin and 18-pin connectors. All of the electrical leads are surrounded by a home made low pass capacitive-inductive filters located at the top of the cryostat. Usually high frequency electromagnetic waves couple to cold experimental devices via parasitic capacitance in the wires, which this cause the self heating of the thermometers at low temperatures, leading to a bad reading of temperatures. The using of the low pass filters eliminates this problem at low temperatures.

4.1   Sample preparation

One of the important steps in transport measurements especially on highly conductive 115 compound, after growing a good quality sample that definitely is very crucial step in physics experiment, is how to make a good thermal contact between sample and the electrical probe wire. Usually a bad contact on highly conductive metals leads to self heating effects in low temperature resistivity measurements and electron-phonon decoupling in low temperature thermal conductivity measurements [162]. Here a summary of sample preparation for transport experiments is given. For more details and information the reader is referred to the dissertation of J. Paglione [162].

Single crystals of 115 compound were grown in an In flux method [173]. Because of the growing method, there is excess indium on the surface of samples. For removing the excess indium from $CeCoIn_5$ material, for instance, samples are etched in HCl acid (at least for 30 minutes or until visibly free of In flux on surface) and then cleaned in a careful way [162]. Actually $CeIrIn_5$ and $CeRhIn_5$ materials show a different reaction to the acid. It seems the compound can not etch with even a high diluted acid. The best way for cleaning the surface is first, to cut sample mechanically with wire saw and second, to polish it to have the shape of parallelepiped. Samples then are washed with ethanol and immediately prepared for making contact on. It seems the surface of $CeIrIn_5$ compound is so sensitive to the oxidation in the air. Therefore making all wire-contacts in a very short time, say in 10-15 minutes, leads a good thermal contact for the thermal conductivity measurements. The typical dimensions of samples are nearly $\sim 4.5 \times 0.14 \times 0.045$ mm^3 for the a-axis and nearly $\sim 1 \times 0.15 \times 0.086$ mm^3 for the c-axis samples (In μSR measurements, the samples were cut in typical thickness 0.1$\sim$0.2mm.).

For making four-wire contacts, the same pure Ag or Au wires, with diameter either 12, 25 or 50 μm depending on sample size, soldered with silver-based alloy were used as contacts for both electrical resistivity, ρ, and thermal conductivity, κ, measurements. For Co115 samples, the Ag wires were soldered using pure Indium and a aggressive flux (Kester 2164 water soluble soldering flux) [162]. The indium could wet and attach easily to the sample surface. However, in the case Ir115 and Rh115 samples, Indium can not wet on the surface at all. Making a mixture of pure Ag and In was used to bring a good and strong contact on the surface of these metalic samples. A blue organic water soluble flux, flux No. 30, is used to improve wetting. See the description of making the soldering contacts in [162]. Then sample is put in a bath of ethanol for nearly 30

minutes to remove any residual soldering flux. Finally the sample itself is fixed to a copper plate which is screwed onto the experimental mount. The soldered contacts have typical low-temperature resistance of ~ 5 mΩ.

One of the positive point regarding using silver-based alloy rather than using pure indium comes as follows. Pure indium is a *s*-wave superconductor below 3 K (with the critical field $\sim$29.3 mT). Since a superconductor is a perfect thermal (electronic) insulator at zero temperature therefore usually it is difficult to trust zero field data at the lowest temperatures in the thermal conductivity measurement. Thus one should apply a very small field nearly 40 mT to kill superconductivity of the indium contacts. Using the new Ag-In alloy method eliminates the zero-field problem in the thermal conductivity measurements.

4.2 Cryogenic techniques

4.2.1 ^{4}He Dipper

^{4}He cryostat is the simplest form of cryogenic refrigerators, because it is easy to use and has a fast turn-around time. It is used for measuring of the electrical and thermal conductivity measurements at high temperature (above 1.6K) and at the first cooling stage in more elaborate refrigerators as described below. All measurements performed in vacuum within a sealed can. For cooling system down to 1.6K, after immersing the dipper in liquid helium and reaching to 4.2K, with continual pumping of 1K pot with a rotary pump the temperature of liquid helium inside of the pot reduced down to lowest temperature. Please see details in [36].

4.2.2 Dilution refrigerator

Here we review shortly the principles of operation of the ^{3}He-^{4}He dilution refrigerator. For more information and details see [176, 56].

When a mixture of ^{4}He and ^{3}He is cooled below 0.87K, a phase separation takes place. The concentrated phase of almost pure liquid ^{3}He floats on top of the dilute phase consisting of approximately 6% ^{3}He in superfluid ^{4}He. The ^{3}He atoms in the ^{3}He-rich phase have lower entropy than the ^{3}He atoms in the ^{4}He-rich phase. The cooling process of a dilution refrigerator takes place in the so called mixing chamber and consists of the transfer of ^{3}He atoms from the ^{3}He-rich phase into the dilute phase. In order to use this

cooling mechanism for continues operation one has to remove ^{3}He from the dilute phase in the mixing chamber and feed it back into the ^{3}He-rich phase. Therefore the ^{3}He has to be re-injected into mixing chamber.

The center part of a dilution refrigerator is the cold part of the ^{3}He/^{4}He circuit. This part of the apparatus is located in a vacuum chamber that is immersed into a ^{4}He bath. It essentially consists of the mixing chamber, the still, counter flow heat exchanger and 1K pot. The circulation of the ^{3}He/^{4}He mixture is driven by pumping the still. The ^{3}He is pumped out of the lower phase by pumping the still with a power full roots blower. The still is heated to about 0.7K to increase the efficiency of the pumping. [1] Because of its higher vapour pressure, ^{3}He predominantly is evaporated from the liquid. Once it has been pumped, the ^{3}He is cleaned outside the cryostat in a nitrogen trap before being returned to the cryostat. Further cleaning often takes place in helium trap in the helium bath. Following this step, the ^{3}He enters the vacuum chamber in a capillary and is precooled at the 1K pot.

The pressure of the ^{3}He is maintained sufficiently high by using a flow impedance before the still so that it condenses. After the still, the ^{3}He is led into the counterflow heat exchangers and then enters the mixing chamber. The return line to the still starts in the mixing chamber below the phase boundary in the ^{4}He-rich phase. On the way back to the still, the cold mixture again flows through the heat exchangers and in this way precools the incoming ^{3}He. Pumping the sill results in a concentration gradient and, in turn, to an osmotic pressure that causes ^{3}He to flow from the mixing chamber to the still. This is, of course, only possible if ^{3}He atoms cross the phase boundary in the mixing chamber, which leads to cooling. With this method, typically a temperature of about 5mK can be produced [56].

For measuring temperature a principal Germanium thermometer (model GR-200A-30) from Lakeshore is used, which is calibrated from 50mK up to 5K. A ruthenium oxide, RuO_2, thick film resistor calibrated by Oxford was used for lower temperatures, down to 20mK. For taking data at high temperatures for the electrical resistivity measurements, for instance, while the system is cooling from room temperature, a Cernox thermometer is used. Temperature controlling was done using a Lakeshore model 370 AC temperature controller. All controlling thermometers were well attached on the bottom plate of the

---

[1]Typical operational temperatures of the still are in the range between 0.6K and 0.7K. Increasing the temperature much above 0.7K results in an enhanced fraction of ^{4}He in the gas phase and therefore ^{4}He has to be circulate as well. The important point is that the ^{4}He does not contribute to the cooling process itself [56].
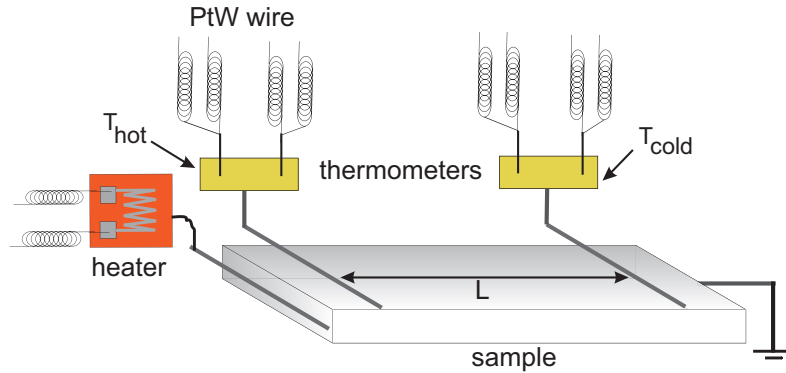
FIGURE 4.1: Schematic of a four-probe thermal conductivity setup (not to scale).

mixing chamber in the field compensated area of the magnet.

Electrical current for the magnet was supplied with the PS-120-10 power supply from Oxford Instruments.

4.3 Thermal conductivity measurement

4.3.1 Basic theory

In analog to DC resistivity measurements, the thermal conductivity technique is a DC technique which uses a four-probe geometry. A current heat, $\dot{Q}$, is applied at one end of a parallepiped shaped sample and the resulting temperature drop ΔT is measured across the sample (See a schematic in Fig. 4.1). Two thermometers attached at two places along the length of the sample are used to measure the temperature gradient. The thermal conductivity is defined as $\kappa = \frac{\dot{Q}}{\alpha \Delta T}$, where $\alpha = A/L$ is the geometric factor of sample (L=length, the distance between the two voltage pads on the sample and A=the cross sectional area of the sample) and $\Delta T = T_{hot} - T_{cold}$ is the temperature gradient. Usually the typical value for $\Delta T/T$ is kept nearly 5%.

Heat losses

This steady-state longitudinal heat transport method can be used if there is no heat loss through the sample. Bad thermal contacts, for instance, result in losses of heat through the measuring electrical leads of the thermometers, or along the Kapton support structure. Furthermore, heat losses through radiation of warm parts in the cryostat [2] or

---

[2]For example, if the heater temperature is much higher than the base temperature, heat may be lost

conduction by residual gas molecules [3] and vibration are other sources of heat leaks that with considering a careful thermal conductivity experimental design have been reached to zero. Please see more details in [36].

4.3.2 Low temperature thermal conductivity mount

A schematic of the thermal conductivity measurements setup is shown in Fig. 4.1. The main components are a heating device, two thermometers and a references thermometer. The heater is a resistive element which is in the thermal contact with the sample (see details in [36]). Joule heating will produce an amount of heat equal to $\dot{Q} = RI^2$ when a DC electrical current is applied through this resistance. A heat current ranging from 0.1 to 20 μA is provided by an ultra high stability, low noise Keitley 220 or 224 constant current sources. The heaters used are strain gauges (model SR-4, Type FSM-A6306S-500-S13C) with a temperature and magnetic field independent resistance of R=5$k\Omega$ (two of them were wired in series to give a resistance of 10$k\Omega$).

The heater is carefully glued to a plate of 50-100 μm thick silver foil with GE varnish in order to have a good thermal contact. A silver wire (50 or 100mim diameter) is soldered to the silver foil with non-superconducting solder. The wire is then attached to the Ag wires attached to the sample with silver paint (Fig. 4.2 shows a schematic of heater and sample thermometer.).

The thermometers used are RuO_2 thick film resistors, which are commercially available and inexpensive. They are called surface mount chips in the electronics literature and are used in most electronic devices, because of their high reproducibility, low temperature dependence of their resistance near room temperature and having a low and well behaved magnetoresistance. [4] A proper thermometer for thermal conductivity measurement has a resistivity of 1 KΩ at room temperature and nearly 7 KΩ at 40 mK. RuO_2 chip thermometers are calibrated *in situ* against a reference Ge thermometer in *each* run.

The thermometers and heaters are suspended on thin strips of Kapton (7.5 μm thick-

---

via radiation.

[3]The only gas that can cause a problem is helium gas since all other substances are solid at the temperatures in which experiments are performed. The problem with helium is that it can liquefy and form a superfluid layer between different parts of the dilution fridge or even on the sample itself and short out the temperature gradient. The only way to prevent this problem is pumping all helium exchange gas at 4K for at least 12 hours [125].

[4]RuO_2 thick film resistors consist of a mixture of the two conductive compounds RuO_2 and Bi_2RuO_2 together with lead silica glass (PbO-B_2O_3-SiO_2). This mixture is deposited on a Al_2O_3-ceramic substrate [56].
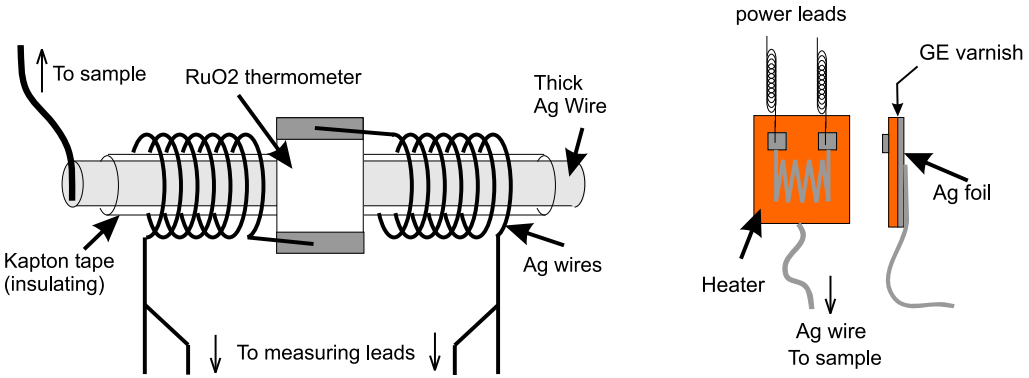
FIGURE 4.2: Schematic of thermometer and heater in our thermal conductivity setup in Dilution refrigerator [162].

ness and $\sim 100\mu$m wideness) from Dupont which are themselves supported by Vespel posts. [5]. The posts are glued to the cupper base with low temperature epoxy.

Electrical contacts to the thermometers are made with coiled 25 μm diameter PtW wire (with 92% Pt and 8% W). Each coil has an independent temperature dependence resistance of 100 Ohm. The thermometers T_{hot} and T_{cold} are measured with a 4-probe technique by using a Linear Research LR-700 Resistance Bridge operating at 16 Hz [6]. LR-700 instrument sends an ac voltage (the voltage was chosen to be very small to eliminate any self-heating of the thermometers at lowest temperatures). The voltage drop across each thermometer is detected at the excitation frequency and converted into a resistance. This procedure is repeated at each temperature with and without the heat current on. Therefore we obtain an in-situ calibration of the thermometers and use these calibrations to obtain the two temperatures T_{cold} and T_{hot} with the current on. The entire system is run under Labview program.

---

[5]In the new work for making a new thermal conductivity tail, Kelvar was suggested to use instead of Kapton, because of its very low heat transport; see laboratory report written by Carlos Paz-Soldan in Louis Taillefer group.

[6]The LR-700 Resistance Bridge was equipped with a LR-720-8 multiplexing unit, which provides the ability to measure up to eight separate four-wire resistance measurements sequentially with the same bridge. This multiplexing unit was essential in taking parallel resistivity measurements of up to six samples mounted together, and for performing parallel thermal conductivity measurements of up to three samples mounted together on the Dilution fridge.
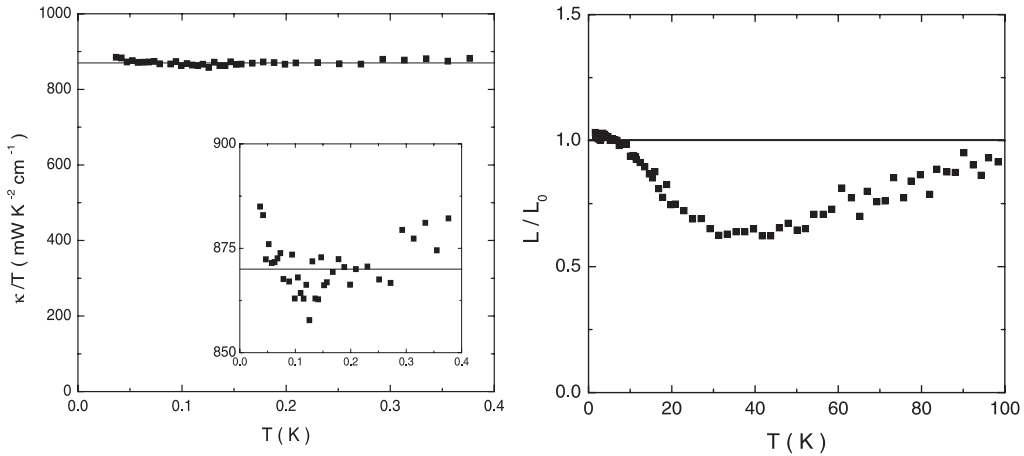
FIGURE 4.3: Test experiment of the thermal conductivity setup on pure silver wire. Inset shows the 3% scattering in the data, confirming the high precision of the thermal conductivity mount [36].

4.3.3 High temperature thermal conductivity mount ($T > 1.6\ K$)

The high temperature thermal conductivity setup has been explained in great details in [36]. Here a summary is given.

The setup is similar to the mount used for measurements in the dilution refrigerator for low temperatures. The thermal conductivity is performed between 1.6 K and 100 K in the ^{4}He cryostat. Main different on the setup is that sample thermometers (Lakeshore Cernox chips (CX-1030) with $R \sim 5k\Omega$ at T=1.5K [7]) and strain gauge heater ($R = 5k\Omega$) are suspended from a fiberglass frame by their measuring wires, which are 12μm PtW wire [8], instead of the Kapton film and Vespel posts used at low temperatures. A Cernox thermometer (CX-1050) ($R \sim 30\Omega$ at room temperature) is used as the principle thermometer for temperature control and sample thermometer calibration.

In the measuring apparatus part, a Lakeshore model DRC93 temperature controller for measuring and controlling the temperature, two Stanford research SR830 (and SR850) low frequency lock-in amplifiers for measuring of sample thermometer resistance, and a Keithley DMM-2000 digital multimeter for measuring the voltage across the strain gauge heater and thus measuring the heat current applied $\dot{Q}$, are used for the measurements. The current to heater is applied using a home-made, low noise constant-voltage source.

---

[7] The magnetoresistance of Cernox thermometers (CX-1030) is negligible at the temperatures above 7K. At lower temperatures it also relatively small, less than 10% below H=16T, but large to require a detailed calibration; maximum error was reported to be 10% [36].

[8] Each PtW measuring wire has $R \sim 30\Omega$.

4.4   Test of mount accuracy

Our thermal conductivity and experimental setup have been used for a long time and lots of work and efforts have been done for testing accuracy and reproducibility of measurements. The best method to make sure about the accuracy of the thermal conductivity setup is to test the verification of the Wiedemann-Franz law at low temperatures on a metallic sample, like gold or silver. Because the setup was designed for measuring the electrical resistivity and thermal conductivity with the same sample contacts, all uncertainty in the Lorenz number regarding the geometric factor is eliminated. The measurements on a silver wire show the high precision of the thermal conductivity setup within accuracy of 3% (see Fig. 4.3).

Chapter 5

Gap Symmetry in CeIrIn$_5$

The heavy fermion compound CeMIn$_5$ attracts a notable interest as a playground for realization and understanding of magnetically mediated superconductivity. While a number of experimental studies revealed unconventional superconductivity in two ambient pressure superconductors of the family, CeCoIn$_5$ and CeIrIn$_5$ [150, 112, 94, 243, 13, 182, 217], the symmetry of the order parameter and associated gap structure have not yet been firmly identified. In CeCoIn$_5$, the observation of a four-fold anisotropy in the thermal conductivity [94] and specific heat [13] points to a two-dimensional d-wave gap, although there is some controversy over its precise symmetry ($d_{x^2-y^2}$ vs d_{xy}) [229]. Several theoretical models propose a $d_{x^2-y^2}$ state, analogous to that realized in cuprate superconductors, mediated by antiferromagnetic spin fluctuations [212, 154, 214]. Since the calculated band structure and measured Fermi surface of both CeCoIn$_5$ and CeIrIn$_5$ are very similar, and properties like the specific heat [150] and the NQR relaxation rate [112, 243] exhibit the same temperature dependence in the superconducting state ($C/T \propto T$ and $1/T_1 \propto T^3$), it has generally been thought that the two superconductors have the same pairing state, even though their T_c differs by a factor of 6. However, recent experiments now suggest otherwise, based on the presence of two superconducting domes in the phase diagram of doped CeIrIn$_5$ materials [153] and observing notable increase in T_c of CeIrIn$_5$ with pressure, accompanied by suppression of magnetic fluctuations [105].

A powerful way to probe the gap structure and locate the position of nodes around the Fermi surface is to measure quasiparticle transport as a function of direction, at very low temperature ($T << T_c$). In this chapter, we present our thermal conductivity κ data of the heavy-fermion superconductor CeIrIn$_5$ that was taken on high purity single crystals as a function of direction, for a current parallel ($J \parallel c$) and perpendicular ($J \parallel a$)

to the tetragonal axis, down to temperatures approaching $T_c/8$. For $J \parallel a$, a sizable residual linear term κ_0/T is observed, which establishes the presence of nodes in the superconducting gap. For $J \parallel c$, on the other hand, $\kappa/T \to 0$ as $T \to 0$. The precipitous decline in the anisotropy ratio κ_c/κ_a in the superconducting state at low temperature rules out a gap structure with line nodes running along the c-axis, such as that of the usual (d_{xy} and $d_{x^2-y^2}$) two-dimensional d-wave states.

5.1 Crystal structure

As we mentioned in Chapter 3, CeIrIn$_5$ is a layered material with Lattice parameters a=4.6662 $A°$ and c=7.5168 $A°$. The presence of the cylindrical Fermi surface sheet and a ratio of $m^*_{ab}/m^*_c \approx$ 4-5 of the effective masses between the c axis and the ab planes makes CeIrIn$_5$ a moderately anisotropic system [78].

5.2 Experimental details

Two samples were used with dimensions $\sim 4.5 \times 0.14 \times 0.045$ mm^3 for the a-axis sample and $\sim 1 \times 0.15 \times 0.086$ mm^3 for the c-axis sample. Their exceptionally low residual resistivity (at $T \to 0$ and $H \to 0$), ρ_{0a} (ρ_{0c}) = 0.2 (0.5) $\mu\Omega$ cm (obtained from thermal conductivity), attests to their very high purity. Their bulk transition temperature is $T_c = 0.38 \pm 0.02$ K and their upper critical field $H_{c2} = 0.49$ T for $H \parallel c$.

Note in order to estimate the phonon contribution in our samples of pure CeIrIn$_5$, we measured the in-plane and inter-plane thermal conductivity, κ_a and κ_c, of a CeIrIn$_5$ sample doped with La impurities, named Ce$_{1-x}$La$_x$IrIn$_5$ with $x = 0.2$. This level of doping increases the residual resistivity ρ_0 by approximatelely 80 times. With such a huge increase in elastic scattering, it is reasonable to assume that inelastic scattering is negligible below 1 K, so that one expects the electronic conductivity to satisfy the WF law at very low temperature. Therefore the contribution of phonons to the thermal conductivity of our pure CeIrIn$_5$ samples is entirely negligible below 1 K (see Fig. 5.1). See more in Appendix C.
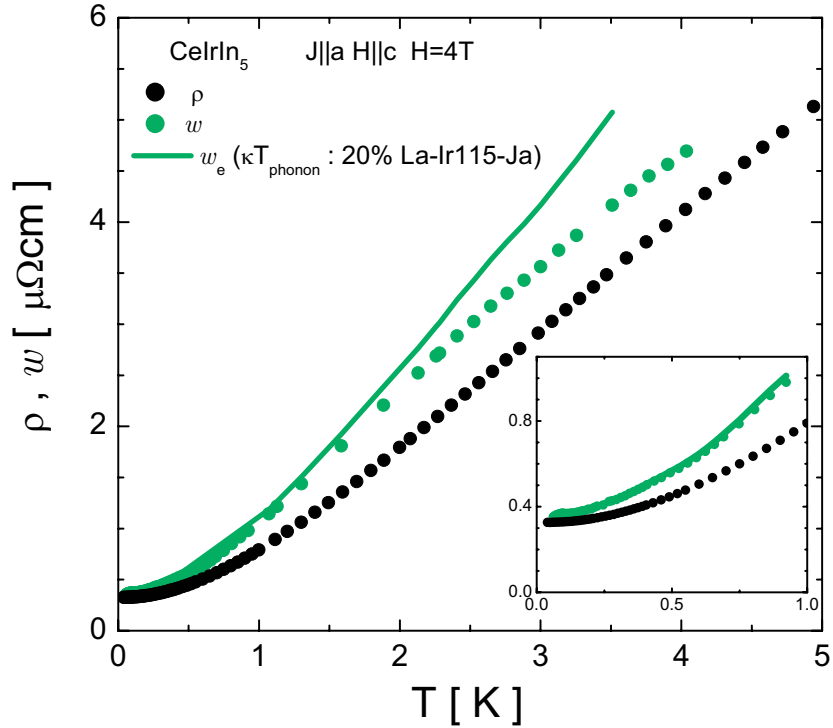
FIGURE 5.1: The electrical resistivity, ρ, compared with the thermal resistivity, $w \equiv \rho_{thermal} = L_0 T/\kappa$, for pure CeIrIn$_5$ sample. At zero temperature the Wiedemann-Franz law is satisfied to a precision better than 1 %. w_e is the electronic thermal resistivity that obtained from the subtracted phonon thermal conductivity (see text and Appendix C). It is obvious that the phonon thermal conductivity is nearly zero below 1 K.

5.3 Thermal conductivity in the normal state

We start by looking at the normal state behaviour, obtained by applying a magnetic field of 0.5 T. The thermal conductivity of CeIrIn$_5$ is plotted in Fig. 5.2 as κ/T vs T, for a heat current parallel ($J \parallel c$) and perpendicular ($J \parallel a$) to the c axis. Actually because the bulk $H_{c2} = 0.5$ T is not reachable form the electrical resistivity measurement, to check the WF law we take resistivity value at the resistive $H_{c2} \approx 4$ T.

At 4 T (above the *resistive* $H_{c2}(0) \simeq 3$ T), a measurement of the electrical resistivity $\rho(T)$ using the same contacts for thermal conductivity shows the Wiedemann-Franz law to be satisfied to a precision better than 1 %, giving $\kappa_N/T = L_0/\rho_0$, where $L_0 = \frac{\pi^2}{3}(\frac{k_B}{e})^2$), in the $T \to 0$ limit. This demonstrates that our thermal conductivity measurement does not suffer from electron-phonon decoupling effects (see Fig. 5.1) (see theory in this regard in [217]). Applying this formula to the 0.4 T data of Fig. 5.2 yields $\rho_0 = L_0 T/\kappa_N =$

0.2 $\mu\Omega$ cm (for $J \parallel a$).

κ_N (at $H_{c2} \sim 0.5$ T) exhibits the standard temperature dependence of a Fermi liquid, namely $\kappa_N(T)/T = 1/(a + bT^2)$, with $a = 8.5$ (19.6) K^2 cm / W and $b = 36$ (90) cm / W for $J \parallel a$ ($J \parallel c$). This data confirms that the two samples have the same level of impurity scattering, in that their (thermal) residual resistivity ratio (RRR) is the same: $RRR(0.6$ K$) \equiv \kappa/T(T \to 0)/\kappa/T(0.6$ K$) = 2.5$ (2.4) or, equivalently, $b/a = 4.6(4.3)$ K^{-2}, for $J \parallel c$ ($J \parallel a$). (At $H = 4$ T the resistivity shows a FL behaviour, $\rho(T) = \rho_0 + AT^2$ for both samples. However at $H = 0$ T and above $T_{c\ onset}$, the electrical resistivity shows a nearly linear behaviour for both current directions, $\rho(T) \propto T^{1.2-1.3}$. It is believed that this material is near a quantum critical instability; see Chapter 8.)

5.4 Thermal conductivity in the superconducting state

Now we discuss the superconducting state, starting with $J \parallel a$ (Fig. 5.2(a)). κ/T increases with decreasing of temperature, reaches a maximum at $T_c \simeq 0.4$ K, because of decreasing of huge inelastic e-e scattering in this heavy fermion system, and then begins to fall below T_c, because of decreasing of number of quasiparticles when the gap opens below T_c. This behaviour is also seen for c-axis heat current direction (Fig. 5.2(b)).

In the Fig. 5.2(a), κ_a/T is seen to extrapolate to a large residual linear term as $T \to 0$, of magnitude $\kappa_{0a}/T = 20 \pm 3$ mW / K^2 cm. The following arguments show that such residual heat transport is due to nodal quasiparticles, as expected for a superconductor with nodes in the gap. There are only two other possibilities: unpaired electrons and gapless superconductivity. Unpaired electrons may come either from pronounced sample (real-space) inhomogeneity, whereby some regions are simply not superconducting, or from pronounced multi-band effects (k-space inhomogeneity). The former is ruled out by the extremely low value of ρ_0 and the latter, shown to occur in CeCoIn$_5$ [217], is ruled out by the lack of any residual linear term in κ_c (in Fig. 5.2(b)). Indeed, if part of the Fermi surface (or indeed part of the sample) were normal (ungapped), the associated metallic conductivity would show up along both current directions. The same arguments rule out gapless superconductivity. Moreover, the actual magnitude of κ_{0a}/T is in excellent agreement with theoretical estimates for a line node, as we now show.

The quasiparticle thermal conductivity of a superconductor with line nodes in the
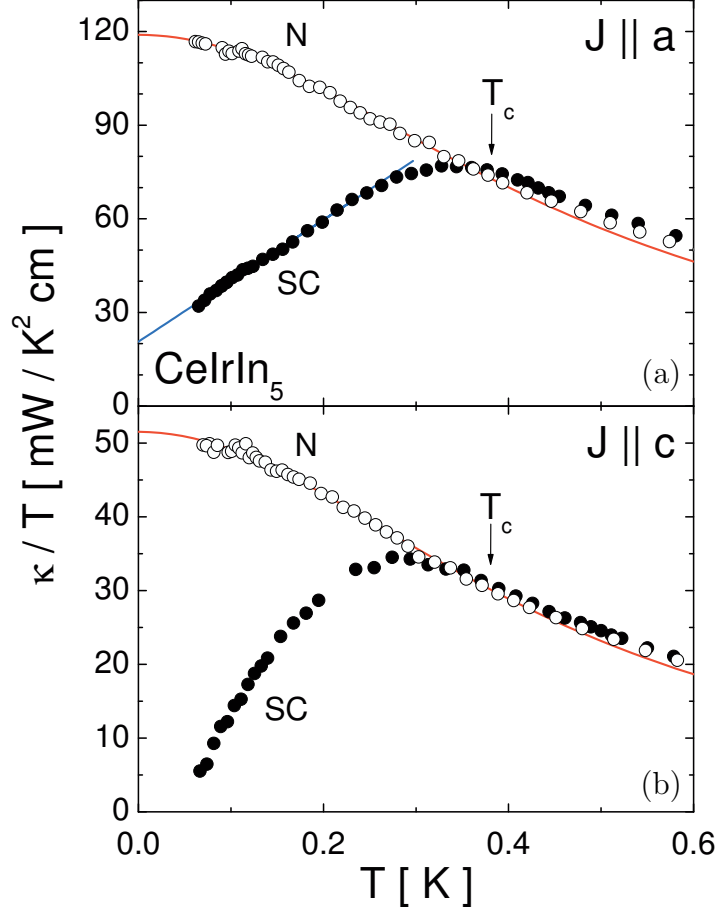
FIGURE 5.2: Thermal conductivity κ of CeIrIn$_5$, plotted as κ/T vs T, for a heat current perpendicular (a) and parallel (b) to the c-axis, in the superconducting state (SC; $H = 0$) and the normal state (N; $H = 0.5$ T). The normal state data are fitted to the Fermi-liquid dependence $\kappa_N/T = 1/(a + bT^2)$ (red lines). A linear fit to the superconducting state data for $J \parallel a$ (below $T_c/2$) is also shown (blue line).

gap is given by [74]:

$$\frac{\kappa_e(T)}{T} = \frac{\kappa_0}{T}[1 + O(\frac{T}{\gamma})^2]$$

$$\frac{\kappa_0}{T} = \frac{1}{3} \, \gamma_N \, v_F^2 \, \frac{a\hbar}{2\mu\Delta_0} \tag{5.1}$$

where κ_0/T is the universal value of the conductivity in the clean limit when $\gamma << \Delta_0$, γ is the impurity bandwidth, γ_N the residual linear term in the specific heat, v_F the Fermi velocity, Δ_0 the maximum value of the gap, μ the slope of the gap at the node, and a is a constant of order unity whose value depends on the particular gap symmetry. The

coefficient of the T^2 term is a finite temperature correction, strongly dependent on the scattering phase shift. κ_0/T is called "universal" because it does not depend on impurity concentration and can therefore be used to measure the magnitude of the gap (at the nodes).

We can apply Eq. (5.1) to CeIrIn$_5$ and estimate the magnitude of κ_{0a}/T expected theoretically from a state with a line node in the gap. The allowed order parameter representations in tetragonal D_{4h} symmetry are listed in Table 5.1 (for singlet pairing). Two line node topologies are possible: *vertical* line nodes (where the Fermi surface cuts the $x = 0$ plane or the $y = 0$ plane, or both), such as in the two d-wave states ($d_{x^2-y^2}$ in B_{1g} or d_{xy} in B_{2g}), and a *horizontal* line node (where the Fermi surface cuts the $z = 0$ plane), such as in the hybrid gap of the $(1, i)$ state of the E_g representation. For hybrid gap, the simplest gap function is $\Delta = 2\Delta_0 cos\theta sin\theta e^{i\phi}$, where $a = 3/2$ and $\mu \equiv \mu_{\text{line}} = 2$ [72]. Using the measured values of γ_N (7300 J K^{-2} m^{-3} [150]), v_F (2 $\times 10^4$ m/s [78]), and Δ_0 (2.5 $k_B T_c$ [243]), yields $\kappa_{0a}/T = 28$ mW / K^2 cm for hybrid gap symmetry, in remarkable agreement with the measured value; the experimental value is $\kappa_{0a}/T \simeq 20$ mW/K^2 cm (Fig. 5.2).

It should be stressed that Eq. (5.1) is only strictly valid in the clean limit, when $\gamma << \Delta_0$. This γ is a measure of the pair-breaking effect of impurity scattering, so it may be estimated by looking at the suppression of T_c with impurity doping. The effect of introducing 0.1 % La into CeIrIn$_5$ doubles ρ_{0a}, from 0.2 to 0.4 $\mu\Omega$ cm, and it lowers T_c by at most 10 % (complete discussion comes in the next chapter). Using the standard Abrikosov-Gorkov formula for T_c/T_{c0} vs Γ/Γ_c [178], where Γ is the normal state impurity scattering rate (proportional to ρ_0) and Γ_c is the critical value of Γ that suppresses T_c to zero, we obtain $\Gamma/\Gamma_c = 0.13$. In the unitary limit of strong impurity scattering, which yields the largest value of γ for a given Γ, we have: $\gamma/\Delta_0 \simeq 0.4\sqrt{\Gamma/\Gamma_c} = 0.14$. This confirms that both samples are safely in the clean limit.

The temperature dependence is also in qualitative agreement with theoretical calculations [74]. The general dependence is close to linear, as one would expect roughly for a density of states that depends linearly on energy, as also observed in Sr$_2$RuO$_4$ [216,93] and CePt$_3$Si [91]. At a finer level, although, the initial T^2 term in Eq. (5.1) is not quite resolved maybe because of too low γ.

Representation	Gap	Basis function	Nodes
A_{1g}	s-wave	1, $(x^2 + y^2)$, z^2	none
A_{2g}	g-wave	$xy(x^2 - y^2)$	V
B_{1g}	$d_{x^2-y^2}$	$x^2 - y^2$	V
B_{2g}	d_{xy}	xy	V
$E_g\,(1,0)$	-	xz	V+H
$E_g\,(1,1)$	-	$(x+y)z$	V+H
$E_g\,(1,i)$	hybrid	$(x+iy)z$	H+points

TABLEAU 5.1: Even-parity (spin-singlet) pair states in a tetragonal crystal with point group D_{4h} [219]. (V = vertical line node, H = horizontal line node.)

5.4.1 Anisotropy

Fig. 5.3 shows the anisotropy of thermal conductivity in CeIrIn$_5$, κ_c/κ_a, as a function of temperature in both superconducting and normal states. In the normal state, κ_c/κ_a is virtually independent of temperature, changing by less than 5 % below 0.5 K, going from $\kappa_a/\kappa_c = 2.3$ at 0.1 K to 2.5 at 0.6 K. The anisotropy in $\rho(T)$ is similarly constant, with $\rho_c/\rho_a \simeq 2.7$ between 1.2 K and 8 K (we will see it in the last chapter). This simply reflects the anisotropy of the Fermi velocity averaged over the Fermi surface.

The superconducting state anisotropy shows different behaviour, a difference that can only come from gap anisotropy. Two distinct features are manifest: 1) an initial increase starting immediately below T_c and 2) a drop below $T \simeq T_c/3$. These two features combine to produce a broad peak centered around $T \simeq T_c/2$. We attribute the first feature to an anisotropic suppression of inelastic scattering, brought about as electrons pair up and cease to participate in the electron-electron scattering responsible for the bT^2 term in κ_N/T. The fact that κ_c/κ_a *exceeds* its normal state value suggests that the gap opens more rapidly or fully in the c direction. It is interesting that only by taking the ratio can a peak be resolved, as it is not apparent directly in either $\kappa_c(T)$ or $\kappa_a(T)$ separately. By contrast, CeCoIn$_5$ exhibits a huge peak in both $\kappa_a(T)$ [150, 217] and $\kappa_c(T)$, thanks to a ratio of inelastic to elastic scattering rates at T_c which is some 30 times larger (T_c^2 is 36 times larger).

The second feature is more directly diagnostic of the nodal structure, as it comes from low-energy quasiparticles. The factor of ~ 3 drop in κ_c/κ_a between $T_c/3$ and $\sim T_c/8$
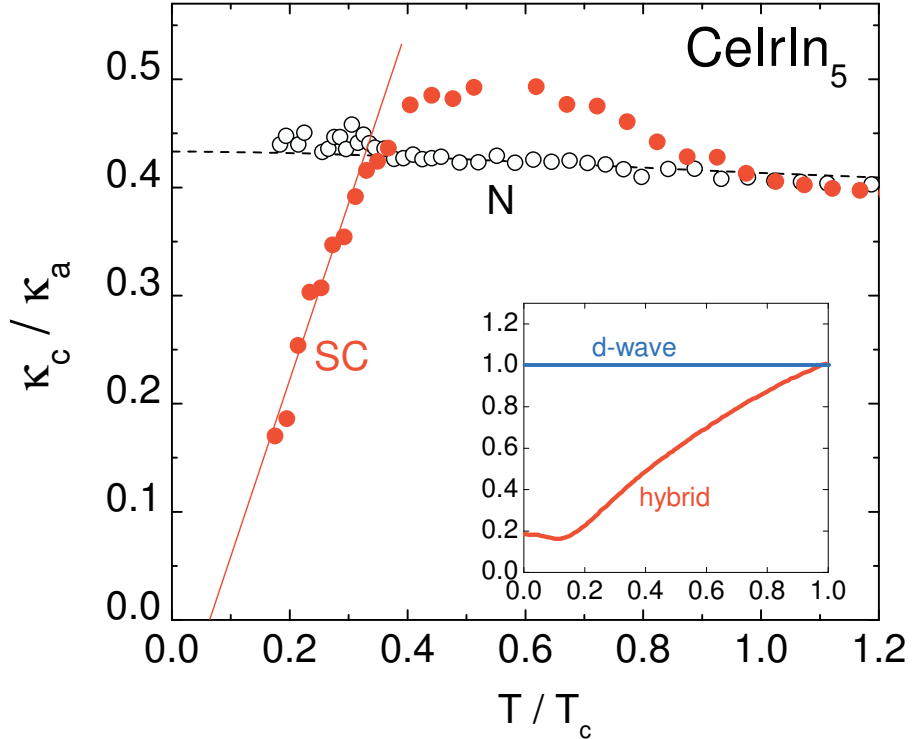
FIGURE 5.3: Temperature dependence of the anisotropy ratio κ_c/κ_a of CeIrIn$_5$, in the normal state (N) and in the superconducting state (SC). The dotted line is the ratio of the two fit lines (to the normal state data) displayed in Fig. 1 and the solid line is a linear fit to the superconducting state data below $T_c/3$. The precipitous drop at low temperature reflects a strongly anisotropic gap whose nodal structure is inconsistent with vertical line nodes (running along the c-axis). The small peak below T_c is due to inelastic scattering (see text). Inset: calculated anisotropy (normalized at T_c) for the gaps d-wave [225] and hybrid [60].

extrapolates to zero as $T \rightarrow 0$. This reveals a *qualitative a-c* anisotropy in the velocity of thermally excited nodal quasiparticles. In other words, those k-states responsible for c-axis conduction in the normal state appear to be much more strongly gapped. This excludes any nodal structure where the line nodes are along the c-axis, irrespective of the shape of the Fermi surface. Indeed, such vertical line nodes would simply reproduce the underlying mass tensor anisotropy (in v_F), and κ_c/κ_a would basically mimic the normal state anisotropy. This expectation, confirmed by Vekhter et al. calculations [225], is illustrated in the inset of Fig. 5.3. By arbitrarily introducing a modulation of the gap maximum along the c-axis, whereby $\Delta_0 = \Delta_0(\theta)$, one can generate some degree of additional anisotropy in the superconducting state, but it is typically modest and weakly

T dependent [225]. More importantly, it would never bring to zero for $J \parallel c(\theta = 0)$ the residual linear term present when $J \parallel a$. The absence of any evidence for a residual linear term in the $\kappa_c(T)$ data of Fig. 5.2 down to $T \simeq T_c/8$ is therefore most conclusive in this respect. It is difficult to imagine that by smoothly extrapolating κ_c/T to $T \to 0$ a value greater than 2-3 mW / K^2 cm could be generated, an order of magnitude smaller than for $J \parallel a$.

By excluding vertical line nodes in the gap of CeIrIn$_5$, all of the allowed spin-singlet representations for the order parameter listed in Table 5.1 [219] are eliminated, except one: the two-component E_g representation. In particular, both d-wave states are ruled out: $d_{x^2-y^2}$ in B_{1g} and d_{xy} in B_{2g} symmetry. Of the three states allowed in the E_g representation, only the $(1, i)$ state is generically free of vertical line nodes. Its typical $(x + iy)z$ dependence produces a hybrid gap, which, in addition to the line node in the $z = 0$ basal plane as already mentioned, possesses point nodes along the $z \equiv c$ direction at the poles (see Fig. 1.2). Note that this state breaks time-reversal symmetry, and could therefore in principle spontaneously generate an internal magnetic moment around impurities. However, in high-quality samples, this effect could well be vanishingly small. (For example, such a spontaneous moment was initially observed by zero-field μSR in UPt$_3$ below T_c [124], but not later on in the best crystals [49].) In CeIrIn$_5$, similar μSR studies have so far produced a null result [84].

This raises the question of whether our data is compatible with the c-axis point nodes of a hybrid gap. The fact that these are *linear* point nodes, *i.e.* that $\Delta(k) \propto k$ at the node and so $N(E) \propto E^2$ at low E, implies that κ_0/T in that direction is *not* universal. Furthurmore, κ_{0c}/T is smaller than the universal value for $J \parallel a$ by a fact or γ/Δ_0 [74] (beyond the normal state anisotropy). The prediction for our crystals is $\kappa_{0c}/T = (\kappa_{0a}/T) \times (\kappa_{Nc}/\kappa_{Na}) \times (\gamma/\Delta_0) = 28 \times 1/2.3 \times 0.14 = 1.7$ mW / K^2 cm. This is very small, smaller than our lowest data point (at 50 mK) by a factor 6, but certainly is still consistent with the current data. Our doping dependence of the residual linear term studied in the next chapter, confirms the presence of point nodes.

5.4.2 Relation to prior work

Heat transport was previously measured in CeIrIn$_5$ by Movshovich et al. [150]. This study was restricted to transport in the plane ($J \parallel a$). This result offered good early evidence for the presence of a line node in the superconducting gap, and our report confirms this. But
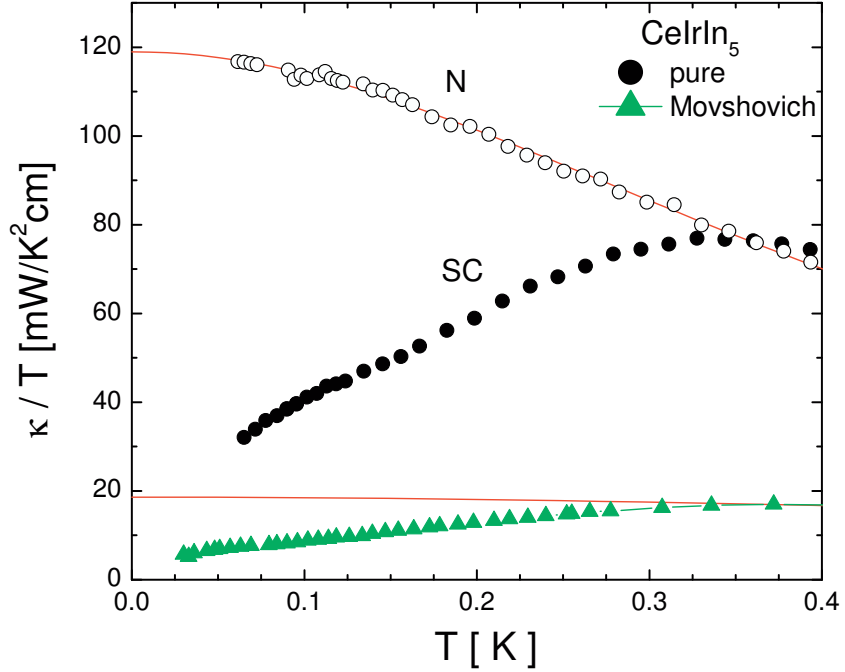
FIGURE 5.4: Thermal conductivity of CeIrIn$_5$, plotted as κ/T vs T, for a pure sample and 0.1% La doped sample, in both the normal and superconducting states. Also shown is the data of Movshovich et al. [150]. Solid lines are the Fermi-liquid dependence $\kappa_N/T = 1/(a + bT^2)$.

this information only eliminates one out of the seven possible states allowed by symmetry (see Table 5.1). The novelty of our study is that we have also measured heat transport along the other high-symmetry direction ($J\|c$), thereby allowing us to say where the line node is located. This directional information eliminates all but one of the possible states. Here, we provide a comparison with their data (see Fig. 5.4).

The two in-plane measurements agree qualitatively, in the sense that both find a residual linear term (RLT), but not quantitatively, with the RLT being five times smaller in Movshovich et al. (4.6 mW / K^2 cm versus our 20 mW / K^2 cm). The data sets are compared directly in Fig. 5.4. We can think of three reasons for the large discrepancy. The first is that their geometric factor is off by a factor 5. Given the lack of details about either the room-temperature resistivity [150] or the uncertainty on their geometric factor, we cannot assess whether this is indeed a possible explanation. The second scenario is that their measurement on CeIrIn$_5$ is plagued with the same problems encountered in their measurement on CeCoIn$_5$, reported in the same paper [150], namely an apparent loss of electronic conductivity below 0.3 K due to poor contacts and electron-phonon
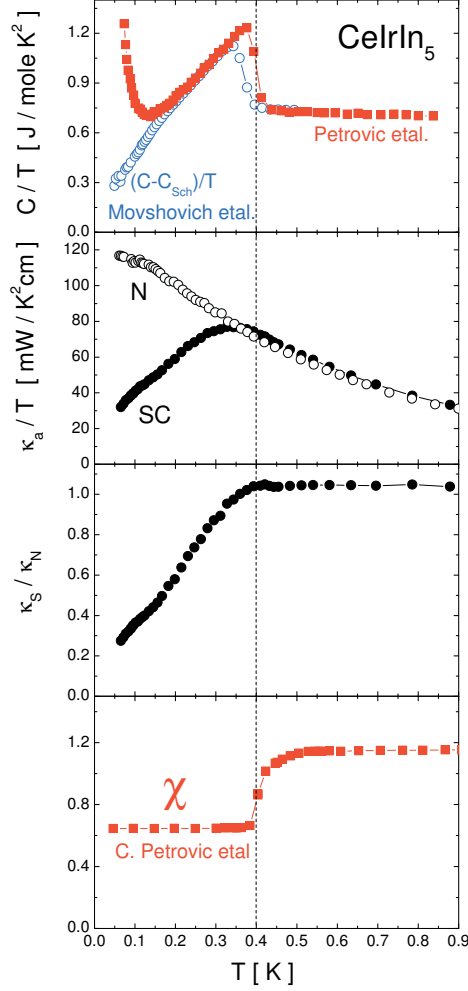
FIGURE 5.5: Comparison of the temperature dependence of the specific heat (data from Movshovich et al [150], and Petrovic et al [173]), thermal conductivity (our data) and magnetization data, showing same bulk T_c determination.

decoupling. Electron-phonon decoupling can cause an arbitrarily large suppression of the RLT (see discussion in [217]). The third possibility is that their measurement is fine, but their sample has much lower quality. This shows up as a lower field-induced normal-state residual conductivity, by a factor 6 or so (see Fig. 5.4). The correspondingly smaller zero-field superconducting-state conductivity (by a factor 5) is not expected from standard theory for a superconductor with a line node, where the RLT should be constant ("universal") or larger when the scattering becomes too large. In order to test this third hypothesis, we performed additional measurements on ultra-high quality samples with a deliberate addition of very small amount of La impurities and we found a
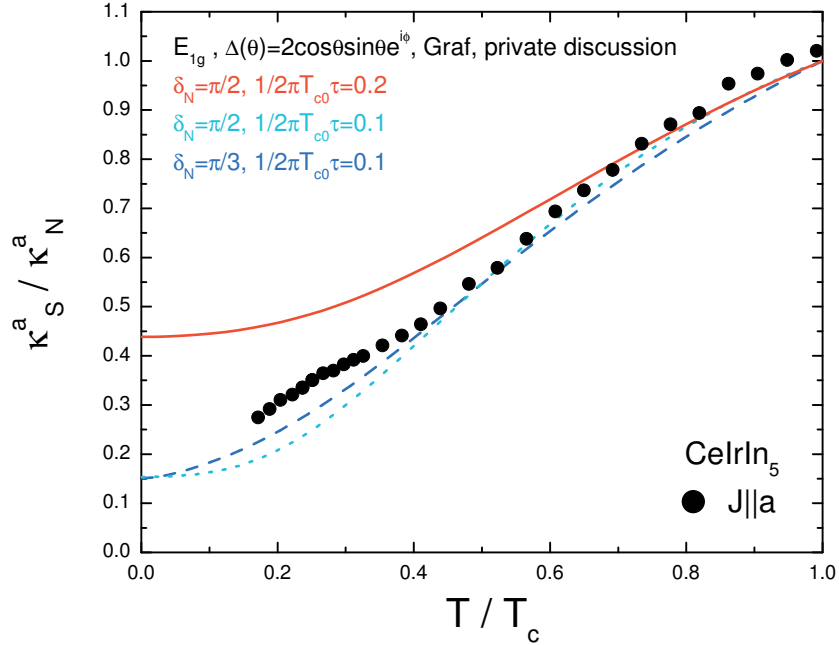
FIGURE 5.6: Comparison of the temperature dependence of the theoretical calculation of κ (considering a negligible inelastic scattering by phonons and quasiparticles and assuming isotropic scattering off impurities in a spherical Fermi surface; private communication by M.J. Graf) with our experimental in-plane thermal conductivity data.

universal behaviour, as expected for a line node in the basal plane (see next chapter). The Movshovich sample must therefore have had a different kind of disorder or defects, possibly pronounced inhomogeneity.

We conclude that Movshovich et al. had problems either with their sample, their geometric factor or their contacts, perhaps a combination of these.

Furthermore, in Fig. 5.5 we compare our data with electronic specific heat and susceptibility data from [150, 173]. The bulk nature of thermal conductivity measurement comes from the fact that contrary to resistivity and point-contact spectroscopy measurements, it is insensitive to filamentary superconducting inclusions. In this sense it is completely analogous to specific heat measurement, as can be seen from the Fig. 5.5. Both measurements give the same value of T_c. Simultaneously, both measurements do not reveal any trace of resistive transition with onset at 1.3 K and zero resistance state at 1.2 K. Thus we conclude that SC phase with $T_c \simeq 1$ K exists in the filamentary form and does not affect our bulk measurements.
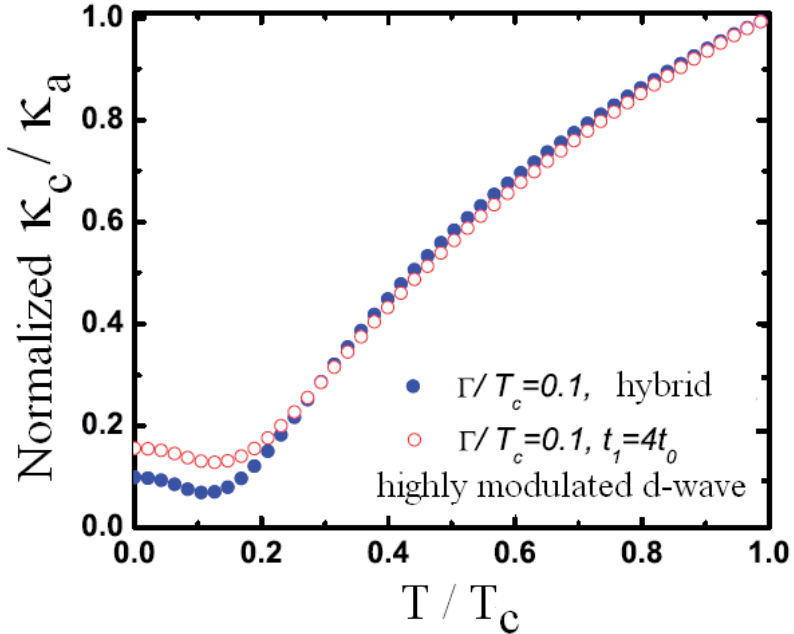
FIGURE 5.7: Comparison of temperature dependence of the anisotropy of the thermal conductivity calculated for hybrid E_g and d-wave gap symmetries (in d-wave calculation a highly modulated cylindrical Fermi surface was considered). In their one electronic band model, the impurity scattering in the unitarity limit was considered (figure from [225]).

5.4.3   Comparison with theory

Here we make a comparison between our data and theories.

Recalling Chapter 2, Arfi et al. [16] calculated the two components of κ, while they considered a spherical Fermi surface, neglected inelastic electron-electron scattering and assumed isotropic scattering off impurities, in the Born and unitarity scattering limits. It seems the data does not fit the theoretical prediction for the hybrid gap symmetry in this theory.

Fledderjohann and Hirschfeld [60] considered the self-consistent treatment of impurity scattering for states with line nodes and found a gapless behaviour for hybrid gap, what was absent in the theory of Arfi [16]. The calculation for this state (inset in Fig. 5.3) on a spherical Fermi surface yields a residual anisotropy κ_c/κ_a that is 20 % of the normal state anisotropy at $T \to 0$. This is roughly compatible with the data.

As we mentioned in Chapter 2, Graf et al. [74] and Barash and Svidzinsky [23, 22] suggested that at sufficiently low temperatures only a knowledge of the topology of the gap at the nodes is needed to calculate the thermal conductivity and probe gap symmetry,

and the low energy spectrum can be determined accurately. In their calculation [74] a negligible inelastic scattering by phonons and quasiparticles compared to scattering from impurities was considered. Despite this theory gives a comparable residual linear term and a power law temperature dependence of thermal conductivity with experiment, but the model still needs to be improved (see Fig. 5.6; the theory is still not consistent very well with data).

Recently Vekhter and Vorontsov [225] calculated thermal conductivity for a- and c-axis crystal lattice directions. They considered a few models in their calculations. Two following models show a large thermal conductivity anisotropy in the superconducting state, comparable with experiments: (i) a d-wave gap model on a *highly modulated* cylindrical Fermi surface; they considered an additional θ dependence into the energy dispersion relation so that this additional term does not affect the in-plane thermal conductivity, but does modify the out of plane κ_c. (ii) a hybrid gap model on an open Fermi surface. Both models give similar behaviour of the thermal conductivity as a function of temperature, with a low residual value of the anisotropy κ_c/κ_a, and therefore authors have suggested both models may be relevant to CeIrIn$_5$ (see Fig. 5.7). However, the considered highly modulated Fermi surface in the first model implies highly anisotropic band structure that the published band structure data do not allow to reliably extract [225].

5.5   Conclusion

In conclusion, the in-plane thermal conductivity κ_a of CeIrIn$_5$ measured down to $T_c/8$ reveals a sizable residual linear term κ_0/T, consistent with the theoretical prediction, which establishes the presence of line nodes in the superconducting gap. The c-axis thermal conductivity κ_c reveals a profound anisotropy in the limit $T \rightarrow 0$, which rules out the possibility that this line is vertical (running along the c-axis). This eliminates all but one of the allowed spin-singlet pairing states in the tetragonal structure D$_{4h}$ point group symmetry, including the d-wave states proposed for the closely related compound CeCoIn$_5$, leaving as sole candidate the E_g symmetry.

Chapter 6

Universal Heat Transport in CeIrIn$_5$

Study of the response to doping is one of the efficient ways to elucidate the superconducting pairing mechanism. Fundamental differences between unconventional and conventional superconductors are illustrated by the unique effects that impurities have on the low temperature transport properties of unconventional superconductors. Doping with non-magnetic impurities suppresses superconducting condensate in unconventional superconductors similar to magnetic impurities in conventional ones [2,85]. A remarkable theoretical prediction about constancy of the electronic residual thermal conductivity in special class of nodal superconductors with variation of impurity density [74], so called *universal* behavior of thermal conductivity, was indeed confirmed experimentally in two-dimensional cuprates [210] and in triplet superconductor Sr$_2$RuO$_4$ [209], and is considered now a hallmark of unconventional superconductivity.

The existence of a universal limit, i.e. independent of the impurity concentration and scattering phase shift, depends on the symmetry of the order parameter and is achieved at low temperature, $k_B T << \gamma << \Delta_0$, where γ is the bandwidth of the impurity induced Andreev bound states. To recall, this universality can be understood as the cancellation of an increase in $N_s(0) \propto \gamma \propto \Gamma$ induced by adding disorder and a decrease in the scattering time, $\tau \propto 1/\Gamma$, by the same disorder, so that $\frac{\kappa_0}{T} \sim \frac{N_s(0)}{\Gamma} \sim constant$ (see Chapter 2, page 29). Despite the general belief of unconventional character of superconductivity in heavy fermion materials, universal conductivity was *never* observed in any of them [204,217].

Various thermodynamic and transport measurements indicate the existence of line nodes in the superconducting gap of CeMIn$_5$ compounds [150,243,112,94,13]. Nevertheless, the debates over the precise location of the nodes and possible multicomponent structure of the order parameter still continue [94,13]. Based on the anisotropy of ther-

mal conductivity we showed in the previous chapter [193] that the superconducting state of CeIrIn$_5$ has equatorial line node [193], which in the tetragonal symmetry implies the hybrid structure of the superconducting gap [219]. This state is characterized by the presence of point nodes at the poles, which in turn suggest different response of in-plane and inter-plane transport to doping. To recall, the linear energy dependence of density of states in the superconducting state is obtained for line node, $N_s(E) \propto E$, while for linear point nodes it is $N_s(E) \propto E^2$ (see Table 2.3 in Chapter 2). These different energy dependences lead different behaviour of transport properties.

In this chapter, we study the effects of impurity scattering on the in-plane and inter-plane thermal conductivity of heavy-fermion superconductor CeIrIn$_5$. The experiments were performed on both highly pure and intentionally La-doped single crystals. We found (i) impurity-insensitive residual linear term κ_0/T in the ab-plane (universal thermal conductivity) and (ii) an increasing residual linear term (non-universal thermal conductivity) with impurity density in the c-axis heat current direction. This difference in response provides key support for a hybrid state as the gap symmetry of CeIrIn$_5$. Furthermore, a comparison of c-axis transport in CeIrIn$_5$ with b- and c-axis heat transport of heavy fermion superconductor UPt$_3$ [204] sheds new light on the pairing state in the latter compound.

6.1 Experimental details

Substitution of 0.1% Ce with La doubles ρ_{0a}, from 0.2 to 0.48 $\mu\Omega$ cm, increases four times ρ_{0c} from 0.5 to 2 $\mu\Omega$ cm and lowers bulk T_c by 10%. To recall the bulk transition temperature for pure samples is $T_c = 0.38 \pm 0.02$ K and the upper critical field $H_{c2} = 0.49$ T for $H \parallel c$. We can prove, in the same way as we showed in the previous chapter, that the contribution of phonons to the thermal conductivity is entirely negligible below 1 K for all samples. Fig. 6.1 shows the electrical resistivity of pure CeIrIn$_5$ and doped samples (Ce$_{1-x}$La$_x$IrIn$_5$) with $x =$0.001 and 0.002.

6.2 Universality of heat transport of CeIrIn$_5$

The thermal conductivity plotted as κ/T vs T, for the pure and 0.1%La-doped CeIrIn$_5$ (Ce$_{0.999}$La$_{0.001}$IrIn$_5$) samples is shown in Fig. 6.2, for a heat current perpendicular ($J \parallel a$, top panel) and parallel ($J \parallel c$, bottom panel) to the c axis. The results for the pure
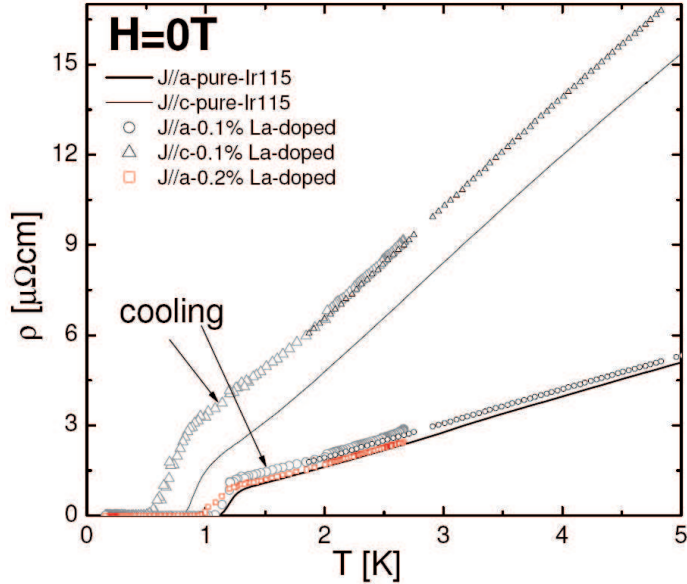
FIGURE 6.1: The in-plane and inter-plane resistivity of pure CeIrIn$_5$ and doped Ce$_{1-x}$La$_x$IrIn$_5$ with x=0.001 and 0.002. Resistivity data of three doped samples at the lowest temperatures obtained during cooling of temperature (gray signs).

samples were discussed extensively in the previous chapter. As $T \to 0$ the electrical and thermal conductivity in the normal state converge to satisfy the Wiedemann-Franz law: $\kappa_N/T = L_0\rho_0$, where $L_0 = \frac{\pi^2}{3}(\frac{k_B}{e})^2$, for both in-plane and inter-plane directions and in pure and all La doped samples. This shows that our measurements do not suffer from electron-phonon decoupling (see [217]). In all samples κ_N exhibits the temperature dependence characteristic of a Fermi liquid, $\kappa_N(T)/T = 1/(a + bT^2)$, with $a = 0.18$ (0.78) K^2 m/W and $b = 0.32$ (0.95) m/W for 0.1%La-doped samples for $J \parallel a$ ($J \parallel c$), see Fig. 6.2 (for pure samples $a = 0.085$ (0.196) and $b = 0.36$ (0.90)). Note that the inelastic scattering coefficients, b, are independent of the residual resistivity (within 10% error bar), indicating that doping does not alter the normal phase properties significantly.

0.1%La-doped samples show the same thermal residual resistivity ratio (RRR), namely $\kappa/T(T \to 0)/\kappa/T(0.4 \text{ K}) = 1.3$ (1.2) or, equivalently, $b/a = 1.8(1.22)$K^{-2} for $J \parallel a$ ($J \parallel c$), which suggests the same level of impurity scattering for both samples.

6.2.1 Temperature dependence

In the superconducting state, κ_a/T shows a power law temperature dependence as $T \to 0$. For the pure sample, Fig. 6.2 (top), starting from close to T_c and down to the base
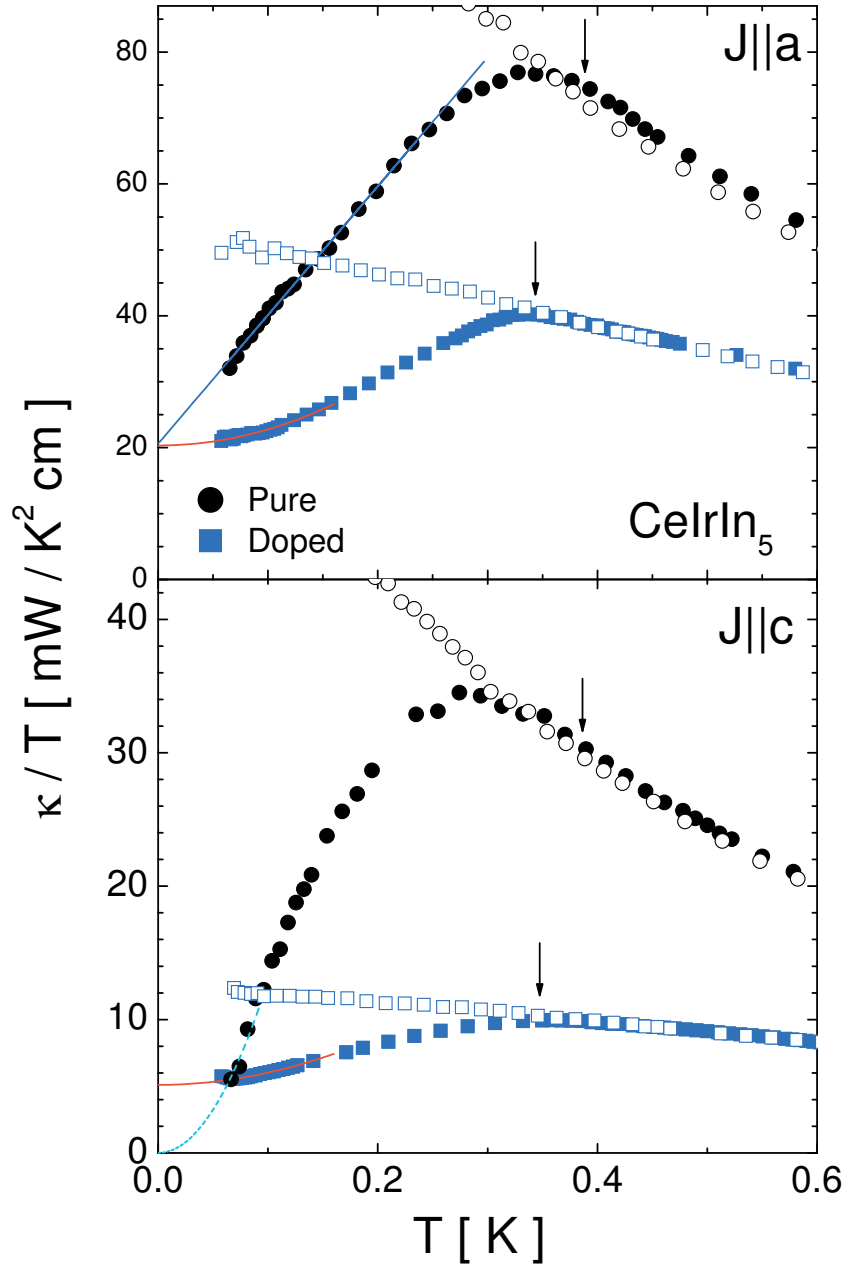
FIGURE 6.2:   The in-plane (top panel) and inter-plane (bottom panel) thermal conductivity κ/T in the superconducting (zero field) and normal (magnetic field of 0.5 T , higher than H_{c2}=0.49 T) states of pure CeIrIn$_5$ and Ce$_{0.999}$La$_{0.001}$IrIn$_5$. Arrows show T_c. Lines show extrapolation of residual term, assuming linear (pure sample) and T^2 (doped sample; red line) variation of κ/T. In c-axis pure sample (bottom) linear extrapolation towards $T = 0$ gives negative value, which implies higher than linear power law below our experimentally accessible temperature range. Thus dashed line shows a T^2 dependence of κ_c/T which points to a negligible residual linear term consistent with linear point node.
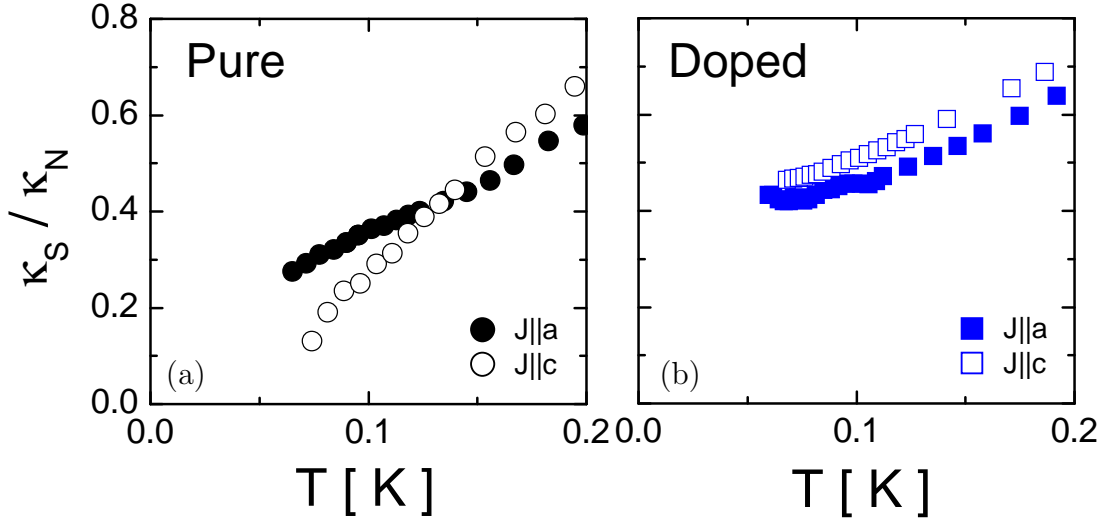
FIGURE 6.3: Normalized in-plane and inter-plane thermal conductivity of pure and 0.1% La-doped CeIrIn₅ samples in the superconducting state. The large anisotropy of the thermal conductivity in pure samples at low temperature that is due to the gap anisotropy (b), decreases by adding impurity to the system (a).

temperature of our experiment, κ_a/T is close to linear. La doping does not alter this dependence at high temperatures, however leads to a saturation of κ_a/T as $T \to 0$ with T^2 behaviour in the crossover regime. This brings the two curves together in $T \to 0$ limit, revealing universal limit of thermal conductivity.

The temperature dependence of the c-axis conductivity is notably different, Fig. 6.2 (bottom). On entering the superconducting state, κ_c/T dives down steeply below 0.2 K. In the pure samples linear extrapolation towards $T = 0$ gives negative value, which immediately implies higher than linear power law below our experimentally accessible temperature range. Doping results in the appearance of finite extrapolation towards $T \to 0$, and actually reveals a T^2 power law in the low temperature range. This shows that c-axis thermal conductivity is not universal.

The difference between the two directions becomes even more obvious when normalizing thermal conductivity by the value in the normal state, κ_S/κ_N, as shown in Fig. 6.3. While in pure samples low temperature behaviour is notably anisotropic, with κ_S/κ_N extrapolation to a zero (finite) for $J\|c$ $(J\|a)$, doping makes the two directions equivalent and reveals characteristic saturation of κ/T vs T as $T \to 0$ followed by a T^2 upward curvature at low temperatures.

Two groups of theories suggested existence of the T^2 contribution to thermal con-

ductivity, κ/T . In Zhitomirsky and Walker [245] and Graf-Balatsky [69] models this dependence is predicted to exist for $T > \gamma$, where γ is the impurity bandwidth, while in Graf theory [74] the T^2 term appears as a finite temperature correction of the universal limit. This difference would imply a low temperature cut-off of the T^2 contribution in the first group of models and while it should start from $T = 0$ in Graf model and its range should extend to higher T with doping. Since the latter is observed in our experiment, where in 0.1% La doped sample, possessing higher γ, the range of the T^2 behavior extends to higher temperatures, we stick in the following to Graf model. The data for doped samples in Fig. 6.2 and Fig. 6.3, for both heat current directions show the same T^2 temperature dependence at low temperature, which is consistent with Graf *et al.* calculation. This would imply that for pure samples γ is below temperature range of our experiment and we are not able to reach a T^2 regime.

6.2.2   Zero temperature limit

As can be seen from the top panel of Fig. 6.2, the extrapolations of in-plane thermal conductivity for pure and 0.1%La-doped samples in zero field reach the same value at zero temperature, despite the two-fold difference in the normal state conductivity. This provides the first instance of universal heat transport in heavy fermion compounds.

Doping with 0.1% of La also suppresses T_c to about 0.35 K. Using the standard Abrikosov-Gorkov formula for suppression of T_c by impurity scattering at a rate Γ (proportional to ρ_0),

$$ln(\frac{T_{c0}}{T_c}) = \Psi(\frac{1}{2} + \frac{\hbar\Gamma}{k_B T_{c0}}) - \Psi(\frac{1}{2}) \tag{6.1}$$

where $\Psi(x)$ is the digamma function, T_{c0} is the maximum T_c for the disorder free material, and Γ is the nonmagnetic impurity scattering rate in the normal state , we obtain for the doped sample $\frac{\hbar\Gamma}{k_B T_{c0}} \sim 0.2$. In the unitarity limit of impurity scattering, which gives the largest value of γ for a given Γ, we have: $\gamma = 0.63\sqrt{\hbar\Delta_0\Gamma} \sim 0.17\Delta_0$, were $\Delta_0 = 2.5 k_B T_{c0}$ was assumed [243, 105]. This compares favourably with the experimentally deduced criterion for the observation of universal conductivity in Sr$_2$RuO$_4$ [1] [209], and is consistent

---

[1]Suzuki et al., [209] derived the experimental condition of the low temperature and small γ "universality limit" which is theoretically described as $k_B T \leq \gamma << \Delta_0$. They observed that above $\hbar\Gamma/k_B T_{c0} = 0.2$ the universality starts to break and this crossover point corresponds to $\gamma/k_B \simeq 0.3K \simeq 0.1\Delta_0/k_B$. Thus they considered $k_B T \leq \gamma \leq 0.1\Delta_0$ as an experimentally deduced criterion for the observation of universal conductivity.

with the observation of unchanged residual linear term in Fig. 6.2 (top).

Experimentally, the impurity bandwidth can be estimated from the parameters of the fitting formula close to the universal limit, $\kappa/T = a + bT^2$. In the unitarity limit, the deviation of κ/T from the universal value at finite temperature is described as [74]:

$$\frac{\kappa}{T} = \frac{\kappa_0}{T}[1 + \frac{7\pi^2}{60}(\frac{k_B T}{\gamma})^2] \quad , \qquad\qquad (6.2)$$

and we find γ=0.3 K for the a-axis doped sample. This large impurity band width means that the scattering is strong. We note that the value determined in this way is approximately two times larger than the value extracted from T_c suppression through $\gamma = 0.63\sqrt{\hbar\Delta_0\Gamma}$. It is possible that there is a deviation of the scattering phase shift from the unitarity limit in the doped samples; in the Born limit the impurity band width becomes exponentially small with increase of impurity scattering, $\gamma = 4\Delta_0 \exp(-\pi\Delta_0/2\Gamma)$ [86].

6.3   Non-universality of c-axis heat transport of CeIrIn$_5$

For c-axis transport the effect of doping is notably different. The residual extrapolation of thermal conductivity rapidly increases with residual resistivity in the normal state. We now explore this behavior in a more systematic way.

In Fig. 6.4 we show the evolution of the inter-plane thermal conductivity with variation of impurity scattering rate of the samples. Decrease of the conductivity in the normal state is accompanied by a systematic increase of the residual linear term. Since in the doped samples a T^2 contribution is dominating, we estimated residual linear term in pure samples assuming the validity of this functional form and using two lowest-in-T data points. This gives values very close to zero and definitely not higher than 2 mW/cmK^2 (as we showed it in the previous chapter) in the two purest samples, which we take as an estimated error bar.

In the inset in Fig. 6.4 we plot a value of the residual linear term as a function of residual resistivity ratios, RRR=ρ_0/ρ_{room}. In the unitarity scattering limit, a square root behaviour for the residual linear term vs impurity scattering rate is expected theoretically [74] for a spherical Fermi surface, $\frac{\kappa_c}{T} \propto \frac{\gamma}{\mu_1^2\Delta_0^2}$ and $\gamma \propto \sqrt{\Gamma}$, while for open Fermi surface it is close to linear, $\frac{\kappa_c}{T} \propto \frac{\gamma^2}{\Delta_0^2} \ln \frac{\Delta_0}{\gamma} \propto \Gamma$ [225]. Uncertainty of residual linear term in the pure samples prevents quantitative comparison with these theoretical expectations. But the strong point is that the residual linear term, $\frac{\kappa_{0c}}{T}$, is increasing with impurity, which
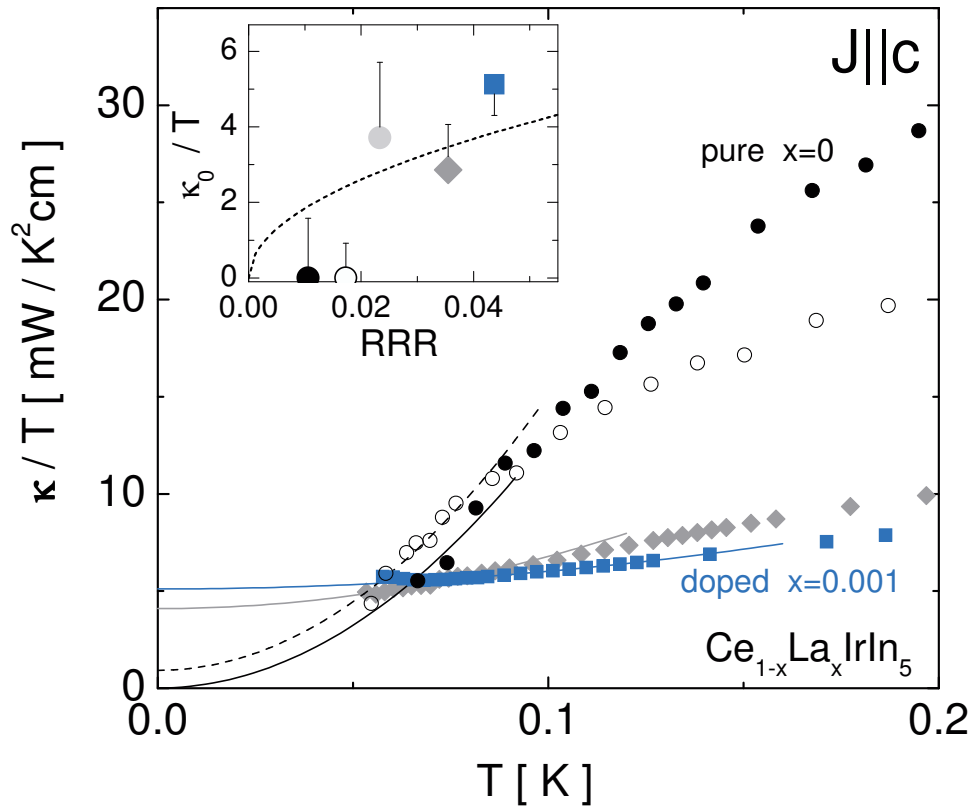
FIGURE 6.4: Evolution of the temperature dependence of κ_c/T in the superconducting state ($H = 0$ T) of CeIrIn$_5$ with sample residual resistivity. ρ_0 is 0.56, 0.91, 1.33, 1.87 and 2.3 $\mu\Omega$cm in order for purest (CeIrIn$_5$, solid-black circle) to dirtiest samples (Ce$_{0.999}$La$_{0.001}$IrIn$_5$, blue square). The low temperature region for each sample is fitted with a T^2 dependence (shown in lines) according to the theory [72, 74]. Inset: the dependence of residual linear term on Normalized sample impurity scattering rate, RRR$\equiv \rho_0/\rho_{room}$, $\Gamma_0 \equiv \rho_{room}$ and $\Gamma \equiv \rho_0$, revealing non-universal character of c-axis heat transport, $\frac{\kappa_{0c}}{T} \propto \gamma \propto \sqrt{\Gamma}$; dashed line is guide to the eye.
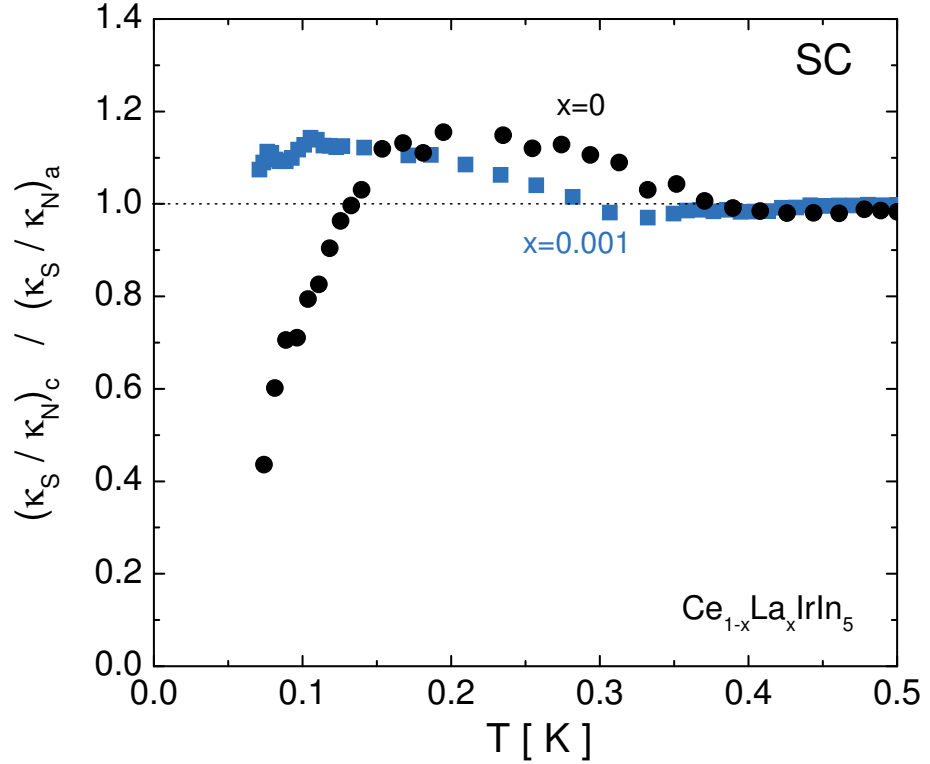
FIGURE 6.5: The anisotropy ratio κ_c/κ_a of pure and doped CeIrIn$_5$ in the supercon-
ducting state. The precipitous drop at low temperature for pure samples reflects strong
anisotropy of the superconducting gap, inconsistent with vertical line nodes. Doping
broadens point nodes at the poles, resulting in smearing of the anisotropy ratio decrease.
The small peak below T_c is due to the inelastic scattering.

shows nonuniversality of the *c*-axis heat transport.

6.4 Anisotropy

The increase of the *c*-axis residual linear term with impurity density can be easily observed
in the anisotropy ratio. In Fig. 6.5 we can see that by adding 0.1% of La impurity to the
system eliminates the sharp drop in the anisotropy ratio at low temperatures. This is
consistent with broadening of the point nodes at the poles and increasing of the density
of the quasiparticles there, while the residual linear term in the *a*-axis with linear line
node remains universal.
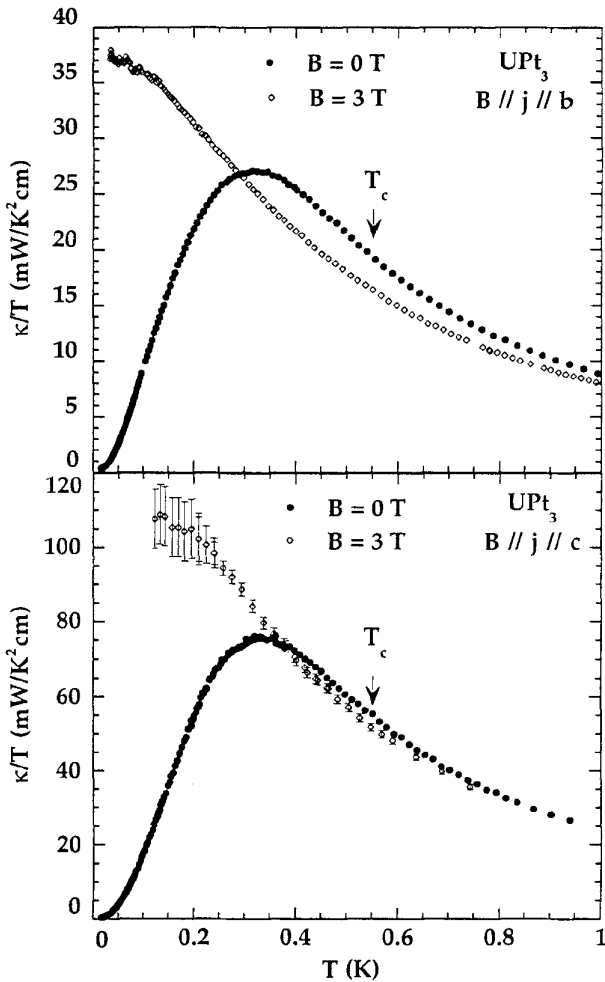
FIGURE 6.6:   The in-plane and inter-plane thermal conductivity of UPt$_3$, in the normal and superconducting states [203]. Note to the similarity of this Figure to Fig. 5.2 in the previous chapter.

6.5   Comparison with HF superconductor UPt$_3$

Superconductivity in UPt$_3$ was first found by Stewart [201] in 1984 with a transition temperature of 0.5 K. Considerable attention has been received since a complex phase diagram was observed in UPt$_3$, which is reminiscent of the superfluid phases of ^{3}He. Because of similarity that we found between the heat transport properties of UPt$_3$ and our data on CeIrIn$_5$, which we are showing as follows, it is instructive to have a short review on the physical properties of UPt$_3$. For a comprehensive review on UPt$_3$ reader is referred to [97].

6.5.1 A review on UPt$_3$

UPt$_3$ has a hexagonal crystal structure with the lattice parameters $a = 5.764$ $\mathring{A}$ and $c = 4.899$ $\mathring{A}$ so that $c/a = 0.845$, not too far from the hard sphere limit of 0.816. The b axis is normally defined as being perpendicular to a.

The low temperature normal state of UPt$_3$ is a strongly renormalized Fermi liquid, as evidenced by the large electronic specific heat coefficient, γ=430 mJ/molK^2 [59]. It orders antiferromagnetically at $T_N \sim 6$ K [5], but the ordered moment $m = 0.02\mu_B$/U is unusually small. The magnetic order is collinear and commensurate with the lattice, with a moment aligned with the b axis in the basal plane. While the coupling is antiferromagnetic in the plane, it is ferromagnetic between planes. Although, the exact nature of the magnetic order is still under debate. The interplay of magnetism with superconductivity has been studied by doping with Pd on the Pt site. A long-range antiferromagnetic phase exists in U(Pt$_{1-x}$Pd$_x$)$_3$ for $x > 0.006$ and it becomes instable for smaller Pd concentrations [50]. In this material superconductivity appears together with a small-moment antiferromagnetic phase. This has been interpreted in terms of a competition between large-moment antiferromagnetism and superconductivity and has lead to the suggestion that superconductivity is not mediated by antiferromagnetic interactions, but rather by ferromagnetic spin fluctuations, which cannot coexist with long-range antiferromagnetic order [50]. Inelastic neutron scattering experiments carried out on pure UPt$_3$ [67] show that the magnetic fluctuation spectrum is complex and consists of both antiferro- and ferromagnetic components.

As the temperature is reduced, the resistivity goes to zero without showing any Kondo-like peak, in contrast to other heavy fermion systems. Above the superconducting transition temperature, the electrical resistivity shows a Fermi-liquid behaviour up to 2 K. The low-temperature specific heat $C(T)$ shows to include a $T^3 \ln T$ term which is absent in other heavy fermion systems. This term in $C(T)$ has been attributed to long-range ferromagnetic spin fluctuations. Moreover, later specific-heat measurements did not define a definite statement on the low temperature dependence due to the existence of an anomaly at very low temperature. Therefore, the reported T^2 dependence which was deduced for $T > 0.1$K [205, 79, 59, 97] has to be considered with caution.

Nodal structure

Thermal conductivity measurement has reported a two-dimensional order parameter in this material. A number of groups have measured the thermal conductivity of UPt$_3$
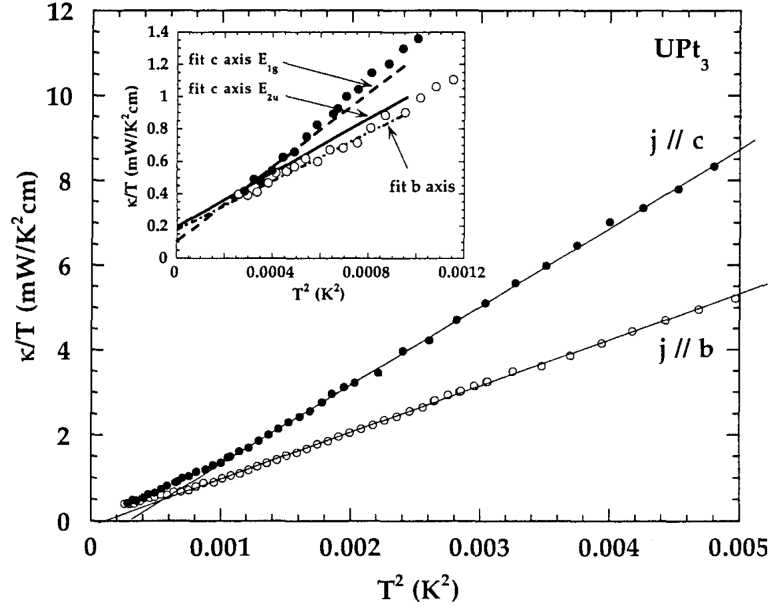
FIGURE 6.7: Thermal conductivity of UPt$_3$ in the low-temperature regime (between 16 mK and 70 mK) as a function of T^2 with fit curves based on the theoretical predictions of Graf *et al.* [72] (from [203]).

[30, 126, 203]. Lussier et al. [126] found an anisotropy between the heat flow parallel and perpendicular to the *ab* plane with a large finite value for the anisotropy ratio κ_c/κ_b as $T \to 0$, which leaded to conclude an E_{2u} order parameter for system (see Fig. 6.8). In E_{2u} gap symmetry because of quadratic point nodes at the poles, there are a large number of zero temperature quasiparticles to carry heat in the *c*-direction. Thus the thermal conductivity anisotropy at low temperature, κ_c/κ_b, shows a large finite value compared to E_{1g} model (see Table 2.4 in this regard). Further measurements at very low temperature were performed by Suderow et al. [203] down to 16mK. They found the temperature dependence of κ below 30mK, fits very well with E_{1g} model. Thus they concluded that very low temperature data are slightly better explained within E_{1g}, compared to the E_{2u} (see inset of Fig. 6.7).

As we reviewed in the theoretical Chapter 2, a universal residual linear term of thermal conductivity, κ_0/T, for certain order-parameter symmetries is predicted [72]. Universal conductivity is naturally expected for E_{2u} gap structure, for both κ_b/T and κ_c/T. The universality could not be observed in UPt$_3$ so far (see Fig. 6.9). In this chapter, by comparing CeIrIn$_5$ and UPt$_3$ heat transport data, we suggest that the lack of universality in UPt$_3$ might be a sign for the absence of any line node in the gap symmetry of this
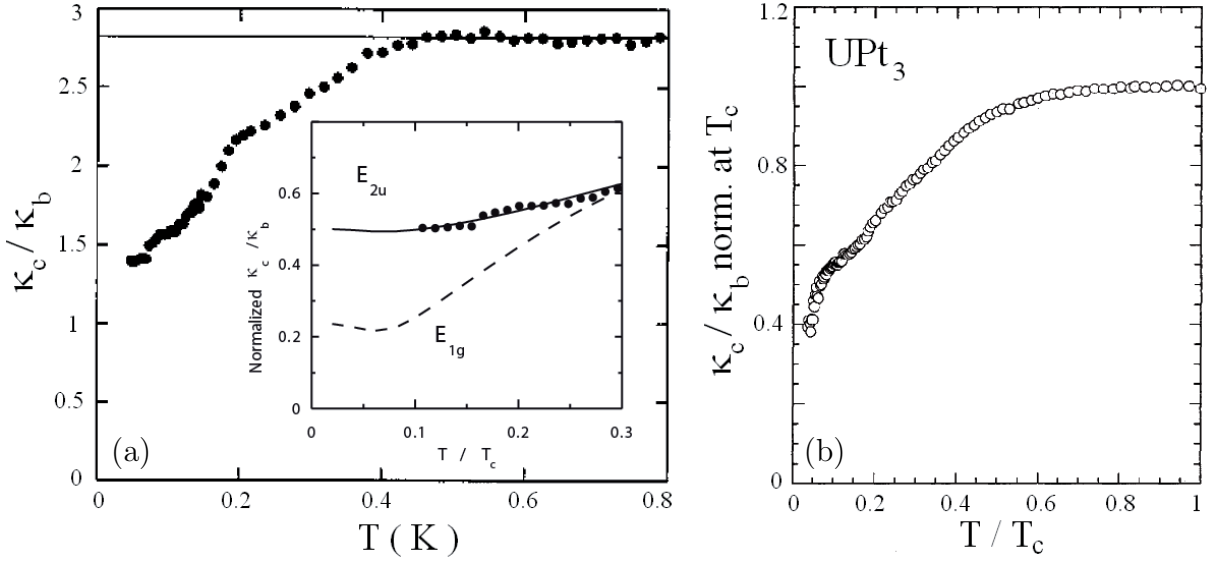
FIGURE 6.8: Anisotropy ratio vs temperature in UPt$_3$. Figures from (a) B. Lussier et al. [126] and (b) H. Suderow et al. [203].

material.

Theoretical calculations including the real Fermi surface of UPt$_3$ were reported by Norman and Hirschfeld [155]. Their results show that both E_{1g} (hybrid-I) and E_{2u} (hybrid-II) gaps can account for $\kappa(T)$. Although, a large value of the anisotropy ratio (around half of the normal state value) as $T \rightarrow 0$ was reported to favor the E_{2u} gap (at least in the limit of low scattering rates; lower than $0.1T_c$).

The field dependence of the thermal conductivity of UPt$_3$ at very low temperatures showed scaling as a function of $x = (T/T_c)(H_{c2}/H)^{1/2}$, confirming the theoretical prediction for a superconductor with lines of nodes [226, 198].

Penetration depth measurements extracted the magnetic penetration depth $\lambda_c(T)$ and $\lambda_a(T)$, which appear to be consistent with a superconducting gap with a line of nodes in the basal plane. However, no definitive distinction between E_{1g} and E_{2u} gap symmetry can be drawn [238].

The ultrasound attenuation measurements [55, 196] report a linear T dependence of the attenuation for transverse sound waves propagating in the basal plane with polarization also in the basal plane, but a T^3 power law for polarization parallel to c. This anisotropy was interpreted in favour of the existence of horizontal line nodes, but says nothing about nodes along $c-$axis.
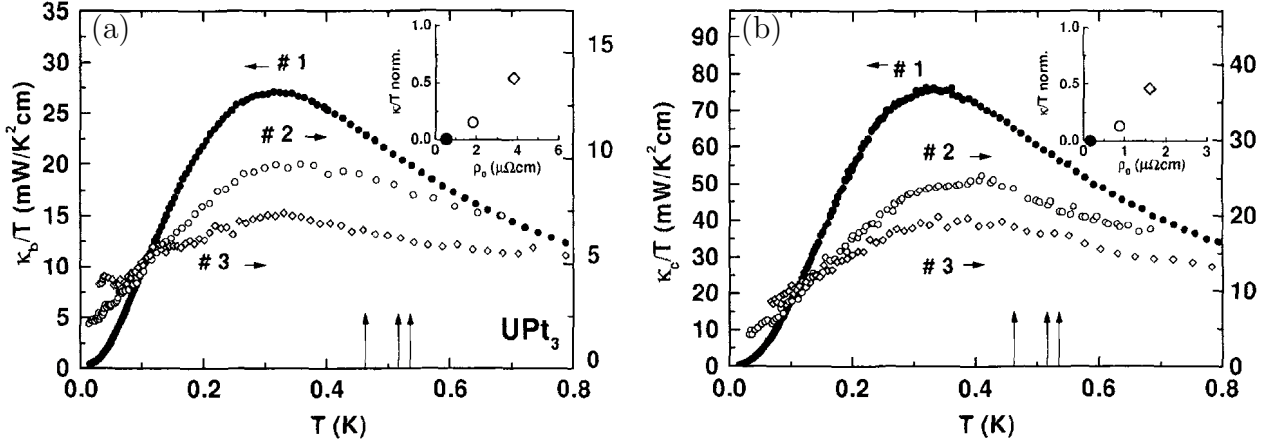
FIGURE 6.9: The thermal conductivity of the irradiated samples UPt$_3$, along the b-(a) and c-axis (b). The data (# 1) is for the non irradiated samples. The insets show the dependence of the zero temperature extrapolation of κ/T in the superconducting phase, normalized by the normal state data as estimated by the Wiedemann-Franz law ($\kappa/T = L_0/\rho_0$) as a function of the residual resistivity ρ_0 (from [204]).

The nuclear magnetic relaxation measurements indicates the presence of a line node as well. Below T_c no Hebel-Slichter peak is seen and a T^3 dependence is observed at low temperature between 0.1 and 0.3 K, which is compatible with a density of states that grows linearly with energy. Here also because there is no information below $T \sim 0.1$ K, one should be careful to get any conclusion.

In brief, at present, the most promising model is based on the E_{2u} representation which seems to be consistent with most of the experimental results. Theoretical work by Yang and Maki [236] also proposed the E_{2u} gap symmetry. For a recent review of the normal state and superconducting properties of UPt$_3$ see [97].

6.5.2   A comparison between CeIrIn$_5$ and UPt$_3$

It is instructive to compare our results with those obtained on the hexagonal heavy-fermion superconductor UPt$_3$ [203] (see Fig. 6.6). Not only is the value of the critical temperature the same ($T_c = 0.44$ K), but the normal state heat transport is essentially identical, with the same residual resistivity in the best crystals ($\rho_0 = 0.2\ \mu\Omega$ cm), the same strength of inelastic scattering ($b/a = 4.0$ K^{-2}), and the same temperature-independent anisotropy, albeit in reverse order ($\kappa_{Nc}/\kappa_{Nb} = 2.7$). The electronic specific heat of UPt$_3$ is a factor 1.4 larger ($\gamma_N = 1.04 \times 10^4\ J\ /\ K^2\ mole$). However, the in-plane v_F is very different: $v_{Fa} = 20$ km/s in CeIrIn$_5$ and $v_{Fb} \sim 4$ km/s in UPt$_3$. This means from
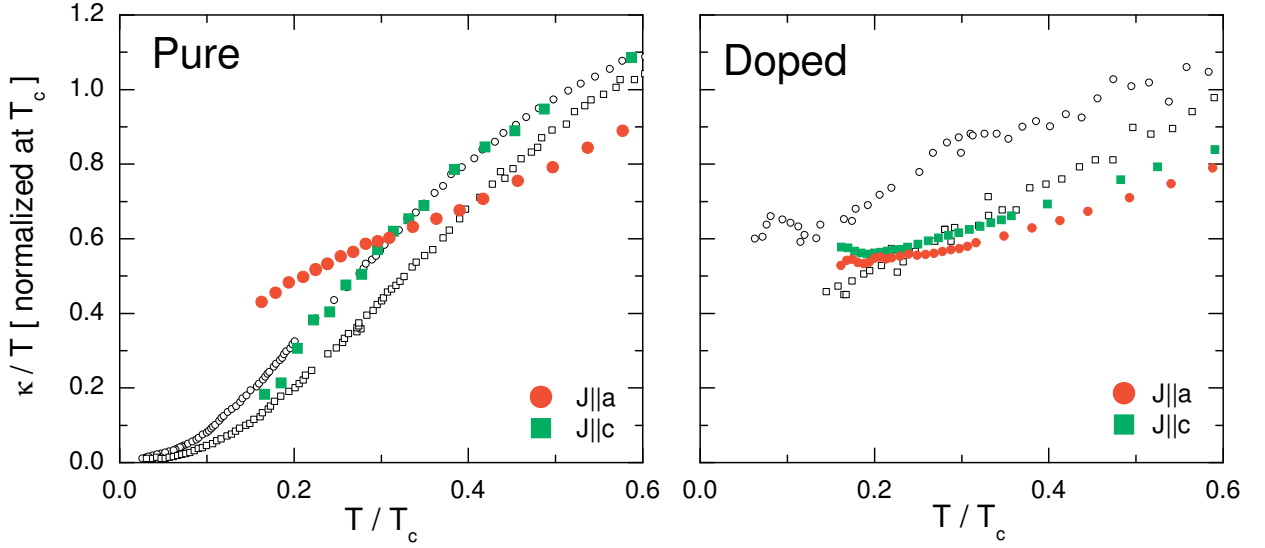
FIGURE 6.10: The in-plane and inter-plane thermal conductivity normalized at T_c, $\kappa/T \,/\, \kappa(T_c)/T_c$, of pure CeIrIn$_5$ and doped Ce$_{0.999}$La$_{0.001}$IrIn$_5$ (solid signs) comapred to pure and irradiated samples UPt$_3$ (open signs) (data taken from [204]) in the superconducting state. The c-axis transport in CeIrIn$_5$ samples perfectly follow data of both b- and c-axis heat transport UPt$_3$, for pure and doped cases.

$\frac{\kappa_0}{T} = \frac{1}{3}\,\gamma_N\,v_F^2\,\frac{a\hbar}{2\mu\Delta_0}$ that all other things being equal (ı.e. Δ_0 and μ), the predicted κ_{0b}/T in UPt$_3$ should be 20 times smaller (compare to $\kappa_{0a}/T = 28$ estimated for CeIrIn$_5$ in the previous chapter) or so, namely 1.5 mW / K^2 cm. Suderow *et al.* [203] went down as low as 16 mK, and their data for κ_b/T extrapolates to 0.2 mW / K^2 cm. This is one order of magnitude too small. This raises the question of a line node in basal plane.

In Fig. 6.11 we plot κ/T for CeIrIn$_5$ and UPt$_3$, normalized to the normal state values. As can be seen, the c-axis transport in CeIrIn$_5$ perfectly follows the temperature dependence observed for b-axis in UPt$_3$. This suggests that in both cases the superconducting gap affects the transport in the same way, producing no residual linear term in κ_0/T and notable upward curvature with T, both expectations in line with theoretical predictions for point nodes.

Comparison of the in-plane transport in CeIrIn$_5$ with b- and c-axis transport in UPt$_3$, however, reveals a clear difference. While in CeIrIn$_5$ κ/T extrapolates to a finite value and remains unchanged with doping (universal), neither is the case in UPt$_3$ (see Fig. 6.9 and Fig. 6.10); the extrapolated κ/T at $T \to 0$ K of UPt$_3$ rapidly increases with the density of defects, in both heat current directions a- and c-axis, showing no universal behaviour. Moreover, heat transport in pure UPt$_3$ shows a temperature dependence
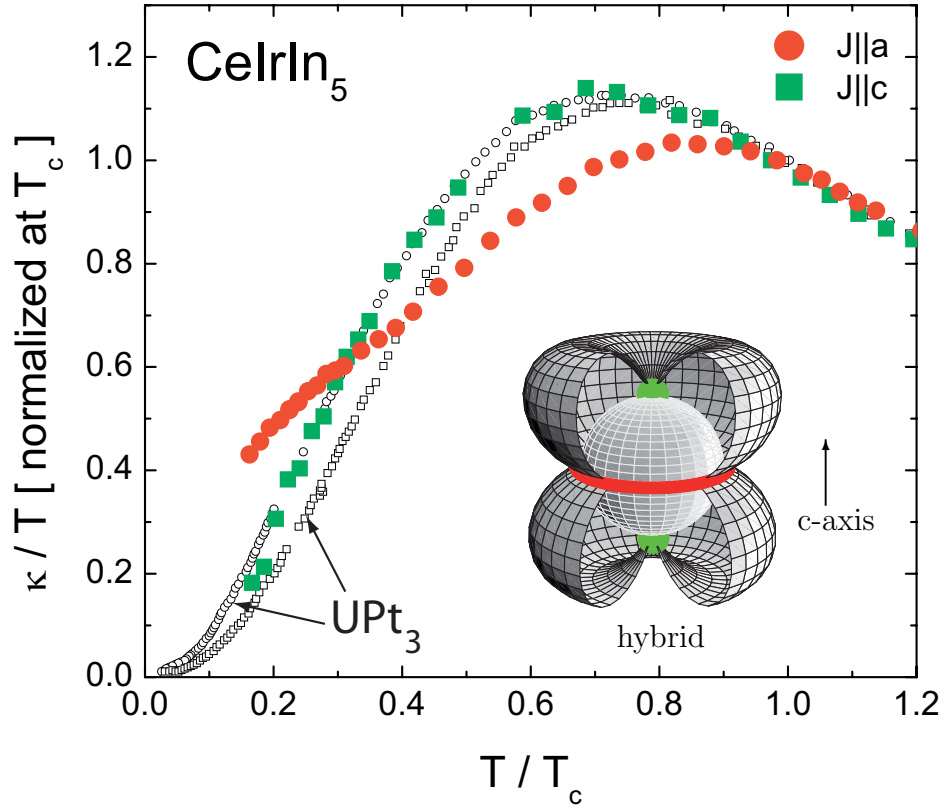
FIGURE 6.11: The in-plane and inter-plane thermal conductivity normalized at T_c, κ/T / $\kappa(T_c)/T_c$, of pure CeIrIn$_5$ (solid signs) and UPt$_3$ (open signs) (data taken from [204]) in the superconducting state. The data for c-axis transport in CeIrIn$_5$ perfectly follow data of both b- and c-axis heat transport UPt$_3$, while the a-axis data in CeIrIn$_5$ is qualitatively different.

notably different from a-axis transport in CeIrIn$_5$ over the whole temperature range, however, qualitatively similar to c-axis transport in CeIrIn$_5$ (Fig. 6.11).

Universal in-plane conductivity $(J \perp c)$ is naturally expected for a hybrid gap structure, and therefore increase of κ_0/T with irradiation in UPt$_3$ represented the biggest challenge for understanding this material. It was suggested that the increase may be due to preferential concentration of the irradiation defects at the surface with density exceeding locally the range of the universal behaviour [179]. Comparison with CeIrIn$_5$ suggests that not only the lack of the universality, but a qualitative difference in the temperature dependence of κ/T distinguish the two cases.

This inconsistency seems to have escaped previous authors [126, 127], and it suggests that a line node may not be present in the gap of UPt$_3$. This is further compounded by the fact that $\kappa_b(T)$ and $\kappa_c(T)$ are basically identical over the entire temperature range,

from $T_c/20$ to T_c; see Fig. 6.11. There is some modest degree of additional anisotropy that leads to a gradual decrease in κ_c/κ_b reaching a factor 2 or so by $T_c/10$. In particular, at the lowest temperature, namely 16 mK, $\kappa_b = \kappa_c$. This is in total contradiction with the presence of a line node. In the clean limit, at $T = T_c/25$, the anisotropy should be enormous. One very special way out was to invoke a hybrid-II gap, associated with the $(1, i)$ state of the E_{2u} representation in D_{6h} symmetry. It has *quadratic* point nodes along the c-axis, which also give rise to universal transport, with an expected anisotropy ratio as $T \to 0$ which is close to unity, as observed. We conclude that gap structure and order parameter symmetry in UPt$_3$ is totally open question.

6.6 Conclusion

In conclusion, nonmagnetic impurities strongly affect the superconducting state of CeIrIn$_5$ compound. In particular, they wipe out the anisotropy seen in pure samples. We observed the universal thermal conductivity along the conducting plane as expected for superconductors with line of nodes in the superconducting gap. This is the *first* observation of this sort in heavy fermion superconductors. In stark contrast inter-plane heat transport rapidly increases with doping in the $T \to 0$ limit, consistent with linear point node character. Both these observations are compatible with the hybrid gap E_g symmetry.

A comparison between CeIrIn$_5$ and well known heavy fermion superconductor UPt$_3$ reveals an amazing similarity between the c-axis CeIrIn$_5$ and UPt$_3$ transport in both directions ($J\|c$, $J\perp c$). This, together with absence of universality in UPt$_3$ lead to doubt on the presence of line node in the gap structure of UPt$_3$.

Chapter 7

Multi-Component Order Parameter in CeIrIn$_5$

7.1 Introduction

As was shown in the previous chapters, anisotropy of thermal conductivity and response to doping both suggest superconducting gap with equatorial line node and polar point nodes in CeIrIn$_5$. The hybrid gap structure, the only possible representation in the crystal lattice of the tetragonal symmetry consistent with these observations, is multi-component and should reveal *qualitatively* different response to magnetic field of different orientation. To get further insight into superconductivity of CeIrIn$_5$ we study thermal conductivity of pure crystals as a function of magnetic field. In this chapter, we present the *first* study of magnetic field effect on the heat transport of CeIrIn$_5$. In this road a multi-phase diagram was found for this compound.

We begin with brief review of the previous studies on systems with multi-component order parameter. Then in the remainder, the results of measurements are presented in two main parts. In the first part (7.3) we present $H\|c$ data and then in the second part (7.4) $H\|a$ results.

7.1.1 Superconductivity with multi-component order parameter

Theoretical investigation of unconventional pairing began with the publication by Anderson and Morel [10] of the generalization of BCS theory, aiming at the explanation
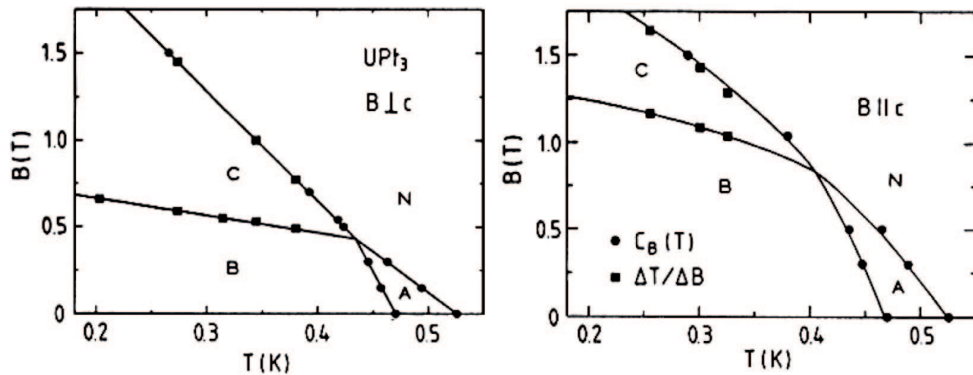
FIGURE 7.1: Superconducting phase diagram of UPt$_3$ for magnetic fields along ($H\|c$) and perpendicular to ($H\perp c$) the hexagonal axis as determined by the specific heat and the magnetocaloric effect (From [228]). N labels the normal phase and A, B and C label different superconducting phases.

of the low temperature phase of ^{3}He. They studied the physical consequences of BCS pairing with non-zero angular momentum. Following the discovery of the superfluidity in ^{3}He, it soon became clear that conventional s-wave BCS superfluid model fails to explain existence of several superfluid phases.

Soon after, study of unconventional superconductors lead to discovery of multiple superconducting phases in UPt$_3$, followed by Sr$_2$RuO$_4$ [138, 137] and quite recently in PrOs$_4$Sb$_{12}$ [92]. Three phases are observed in the $H - T$ phase diagram of UPt$_3$ (see Fig. 7.1). Much effort was devoted to determine the superconducting order parameter of each phase. For a complete discussion see [97].

There are three features in the phase diagram of UPt$_3$, Fig. 7.1. (1) The existence of two superconducting phases in zero field, (2) the existence of three superconducting phases in magnetic field, (3) three phases meet each other at a tetracritical point (T^*,H^*) on the upper critical field line. In order to explain the zero-field splitting and the topology of the phase diagram, a number of different Ginzburg-Landau models was proposed, most of which require an unconventional superconducting order parameter. Two most plausible models, are based on: (i) a single multi-component order parameter coupled to a symmetry breaking field [187, 71, 72]. Here the degeneracy of a two-dimensional even or odd parity order parameters is lifted by a symmetry breaking field, and (ii) theories based on two symmetry un-related order parameters which are accidentally nearly degenerate [40, 244, 73].

In the former model, so called 2D E-representation model, the theory has only one

(a) $\Delta = (x + iy)z$ (b) $\Delta = (x + i0.2y)z$ (c) $\Delta = xz$
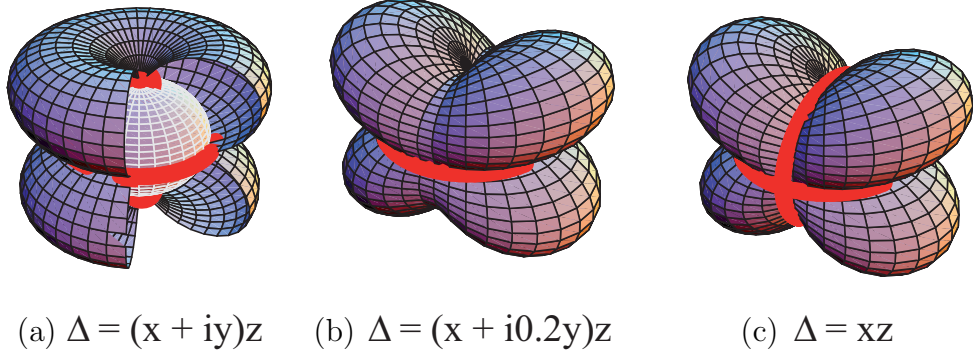
FIGURE 7.2: (a) $E_g(1, i)$ with basis function $(x + iy)z$ (hybrid gap), (b) $(x + i0.2y)z$, (c) and $E_g(1, 0)$ with basis function xz gap symmetries.

phase transition in zero field and by itself cannot explain the double transition [187]. The splitting ΔT_c is caused by lifting of the degeneracy of a two-component superconducting order parameter by a symmetry-breaking field. The evidence for that in UPt$_3$, for example, is that the small-moment antiferromagnetic phase below a Neel temperature of $T_N \sim 6$ K, detected by neutron scattering experiments, acts as a symmetry-breaking field [80, 106]. In this model, the possible 2D representations of symmetry are E_{1g}, E_{2g}, E_{1u} or E_{2u}. A superconducting order parameter belonging to one of these representations can be represented by a complex vector $\vec{\eta} = (\eta_1, \eta_2)$, whose components are the coefficients multiplying the basis functions ψ of the two dimensional representation:

$$\Delta(\mathbf{k}) = \eta_1 \psi_1(\mathbf{k}) + \eta_2 \psi_2(\mathbf{k}). \tag{7.1}$$

As we mentioned before, the most possible 2D representations for UPt$_3$ are E_{1g} or E_{2u}. The orbital order parameter differs for the two models, particularly for the high temperature A phase [71]. For E_{1g} pairing the A phase has the structure, $\Delta_A \sim zx$, which has an equatorial line node in the basal plane, as well as a longitudinal line node on Fermi surface (see Fig. 7.2). For the E_{2u} representation, $\Delta_A \sim (x^2 - y^2)z$ also has an equatorial line node, but has two longitudinal line nodes oriented 90 degrees to one another. The low-temperature B phase of both models breaks time-reversal symmetry. As a result the longitudinal line nodes are closed by the growth of the second component of the order parameter; for $T \to 0$, $\Delta_B \sim (x + iy)z$ for E_{1g} symmetry (see Fig. 7.2), while $\Delta_B \sim (x + iy)^2 z$ for the E_{2u} representation [71].

Although, despite all E representation models are based on two-component orbital

order parameters it was reported that they yield different predictions for the thermodynamic, magnetic and transport properties, including the $H - T$ phase diagram [71]. For example, in E_{2u} representation model there is an apparent tetracritical point for all field orientations, while the spin-singlet E_{1g} model appears to be incompatible with the tetracritical point for $H \| c$ [71].

In the accidentally degenerate models the phase diagram is accounted for by two primary order parameters belonging to different irreducible representations, which are selected in order to enforce a tetracritical point in the GL theory for the $H - T$ phase diagram of UPt$_3$, for example [73] [1]. The splitting of the phase transition is due to accidental degeneracy, not to coupling to the magnetism. Once two representations are involved, the possibilities for the form of the order parameter become numerous. [2].

7.1.2 Thermal conductivity of unconventional superconductors in magnetic field

To recall, a strong test for the order-parameter symmetry of superconductors is provided by the magnetic-field dependence of thermal conductivity. As pointed out by Volovik, in contrast to fully gapped superconductors, where at low fields thermal conductivity is determined by quasi-particle hopping between vortex cores, in nodal superconductors the quasi-particles are spread from the cores into the bulk and thus can participate in heat transport at fields just above H_{c1} [115, 226, 113] (see section 2.4.2). This leads to immediate increase of κ at low fields, which is proportional to the density of states $N(E_F) \propto \sqrt{H}$ for $H_{c1} < H << H_{c2}$ and thus $\kappa(H) \propto \sqrt{H}$, as observed in several unconventional superconductors [42, 91].

Moreover, the thermodynamic and transport characteristics of superconductors with nodes exhibit scaling behaviour at low fields and low temperatures. Kubert and Hirschfeld [116] derived a scaling relation, proposed by Simon and Lee [198], for the quasiparticle transport properties in the variables $T/\sqrt{H}$, mixing field and temperature dependence,

---

[1]In the accidentally degenerate models the two representations can have the same or different parity [40].

[2]The AB model, for instance, is one of the proposals that explains the $H - T$ phase diagram for UPt$_3$ [40]. In this theory, the two transitions are due to the separate T_c equations for A and B: the closeness of the two transitions is accidental. In the AB model, "AB" refers to a mixture of an A$_1$ or A$_2$ representation with a B$_1$ or B$_2$ representation. The combined order parameter can still have nodes that may be detectable by power-law behaviour of thermodynamic and transport quantities [40]. To write the GL free energy in this mixed presentation model shows two transition temperatures in zero field and can explain all features of the phase diagram of UPt$_3$ [40].

which can be used as a probe for nodal structure. Barash and Svidzinsky [23] have argued that precisely this kind of scaling is expected for E_{2u} gap (having quadratic point nodes at poles), while noticeable deviations from scaling are expected for the hybrid gap (having linear point nodes at poles) [3].

7.1.3 Response to magnetic field in multi-component supercon-ductors in tetragonal crystal structure

In a tetragonal crystal structure with point group symmetry D_{4h} for spin-singlet even-parity pairing, there are four one-dimensional (A_{1g}, A_{2g}, B_{1g} and B_{2g}) and three possible two-dimensional representations (E_g) (see Table 5.1). Each of the four one-dimensional representations corresponds to a single, scalar gap function, so these pair states should exhibit only one superconducting transition. In the E_g-representation, the three allowed states characterized by different symmetries, $E_g(1,0)$, $E_g(1,1)$ and $E_g(1,i)$. Of the three states, only $E_g(1,i)$ has broken time reversal symmetry. A general consequence of the time reversal symmetry broken state is that a finite magnetic field oriented along a high symmetry direction in the basal plane lowers the symmetry of the normal state and leads to a second superconducting transition in the mixed phase as the temperature is reduced [6, 7]. The $E_g(1,i)$ representation described by $\vec{\eta} = (1,i)$, while the two other phases are described by $\vec{\eta}=(1,0)$ and $\vec{\eta}=(1,1)$, respectively. The nodal structure is characterized by linear point nodes in the c direction and a line node in the basal plane for the $E_g(1,i)$ phase, and at least an additional longitudinal line node in the c direction for two other phases.

Looking at the Ginzburg-Landau model, the free energy for the E_g representation of D$_{4h}$ with a basis $\vec{\eta} = (\eta_1, \eta_2)$ is given by [197] [4]

$$F_{GL} = - |\vec{\eta}|^2 + |\vec{\eta}|^4 /2 + \beta_2(\eta_1\eta_2^* - \eta_2\eta_1^*)^2/2 + \beta_3 |\eta_1|^2 |\eta_2|^2 , \qquad (7.2)$$

where the coefficients β_i are material-dependent constants. There are three stable ho-mogenous phases: (a) $\vec{\eta} = (1,i)/\sqrt{2}$ ($\beta_2 > 0$ and $\beta_2 > \beta_3/2$), (b) $\vec{\eta} = (1,0)$ ($\beta_3 > 0$ and $\beta_2 < \beta_3/2$), and (c) $\vec{\eta} = (1,1)/2$ ($\beta_3 < 0$ and $\beta_2 < 0$) [197, 6, 7, 103]. The applica-tion of a magnetic field in the basal plane breaks the degeneracy of the two components

---

[3]Their calculation was done for $J\|aH\|a$ and $J\|cH\|c$ configurations [23].

[4]Here in the GL free energy only fourth-order invariant terms are considered and gradient terms are neglected; see details in [197].

η_1 and η_2. Symmetry arguments for this imply that the vortex lattice phase diagram contains at least two vortex lattice phases for magnetic fields applied along any of the symmetry axes in the *ab* plane: (1,0,0), (0,1,0),(1,1,0),(1,-1,0). To illustrate the origin of these phase transitions, consider a zero field ground state $\vec{\eta} = (1, i)$ and a magnetic field applied along the (1,0,0) direction. Due to the broken tetragonal symmetry, the degeneracy of the $\vec{\eta} = (1, 0)$ and the $\vec{\eta} = (0, 1)$ solutions is removed by the magnetic field. Consequently only one of these two possibilities will order at the upper critical field [103]. When field is applied along *c*-axis, calculation predicts that $\vec{\eta} = (1, i)$ is stable (since this phase minimize the number of nodes in the order parameter) and no change in the symmetry [6,7].

In brief, for multi-component order parameter superconductors external magnetic field acts similar to the small internal magnetic field. If the direction of magnetic field is different from the highest symmetry axis, the response of the superconductor is determined by lifting the degeneracy of the two order parameters, and a phase transition with nodal topology change is expected. Lifting the degeneracy creates vertical line nodes, so this topology change should be the most obvious for the heat current along *c*-axis. On the contrary, for magnetic field parallel to the high symmetry direction (*c*-axis), the response is the same as for single component order parameter superconductors, i.e. it should reveal nodal behaviour for in-plane transport and activated behaviour for inter-plane transport.

7.2 Samples

The experiments were performed on the same pure samples in Chapter 5. The bulk upper critical fields are $H_{c2} = 0.49$ T and 1 T for $H\|c$ and $H\perp c$, respectively.

7.3 Magnetic field along tetragonal *c*-axis, $H\|c$

7.3.1 In-plane and inter-plane heat transport

In Fig. 7.3 we show the evolution of κ/T vs T for in-plane and inter-plane currents with application of magnetic field. The isotherms are plotted in the right panels, with κ normalized to the normal state value κ_N. In Fig. 7.4 we compare the low-temperature behaviour of κ_a and κ_c with classical cases: that of s-wave superconductor Nb [122] and *d*-wave superconductor Tl-2201 [177]. The H dependence of κ_a/T in CeIrIn$_5$ is
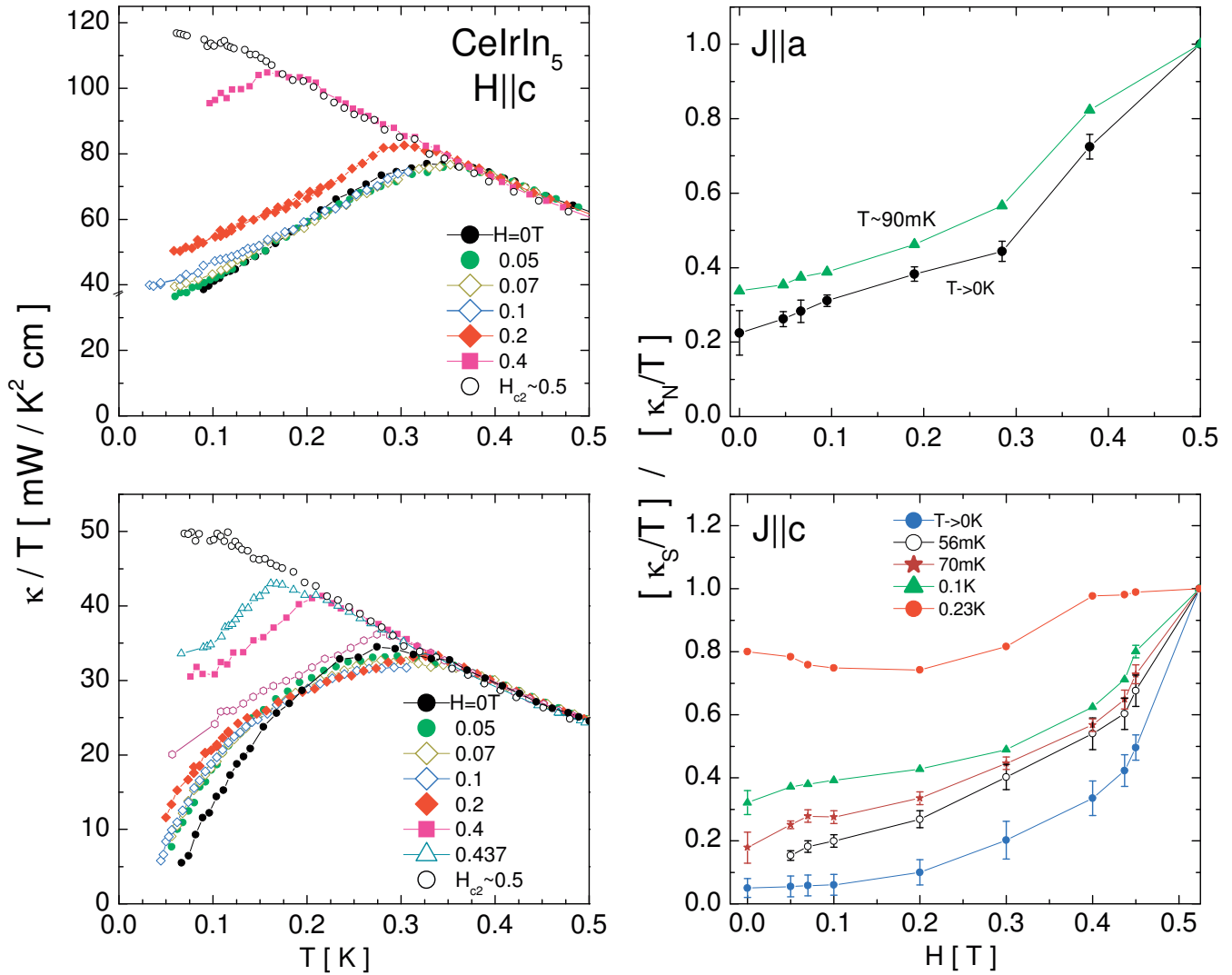
FIGURE 7.3: Temperature and field dependence of thermal conductivity in CeIrIn₅ for two current directions $J\|a$ (upper panels) and $J\|c$ (lower panels).
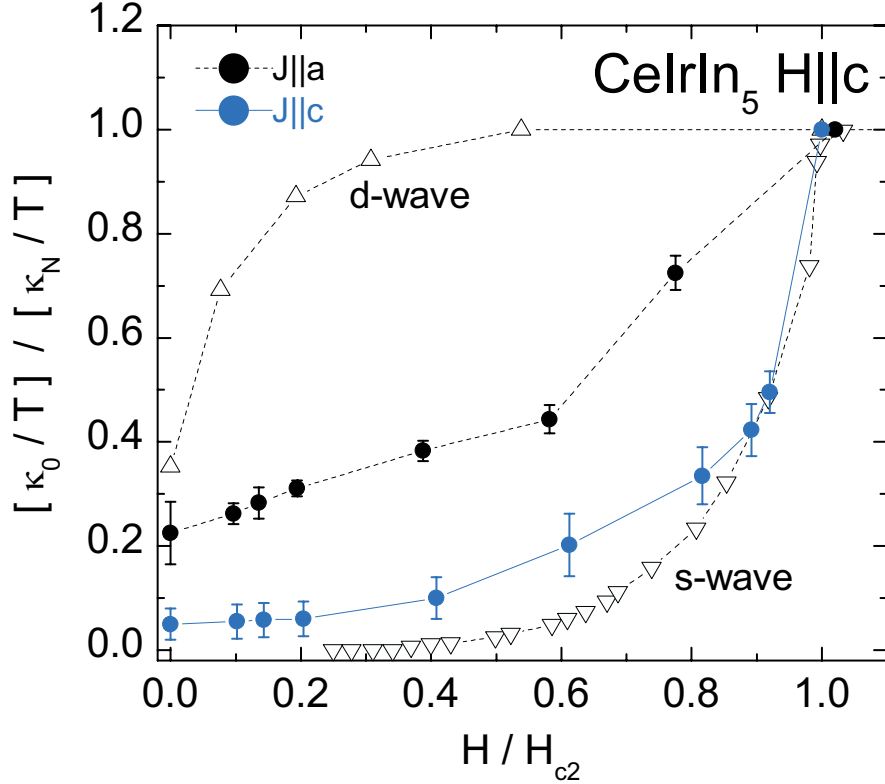
FIGURE 7.4: Low temperature field dependence of thermal conductivity in CeIrIn$_5$ for two current directions along the plane, $J\|a$, and perpendicular to the plane, $J\|c$. A comparison with typical behaviour of conventional s-wave (Nb [122]) and d-wave (Tl2201 [177]) superconductors has been made. Qualitatively different field dependence between $J\|a$ and $J\|c$ directions in $T \to 0$ limit is consistent with the hybrid E_g gap symmetry with equatorial line node and polar point node. This anisotropy becomes evident below some characteristic temperature T^* (see text).

between classic s-wave or d-wave behaviours: κ_a increases linearly with H at low magnetic fields, and then speeds up towards H_{c2}. The linear increase, as opposed to the variation proportional to density of states, $N(E_F) \propto \sqrt{H}$, may indicate notable variation of the mean free path with field. A similar almost linear H-dependence of κ is observed in Sr$_2$RuO$_4$ [216, 93] and UPt$_3$ [203], for both of which a horizontal line nodes in their gap symmetries were suggested, which may bear some similarity to our case. It has been shown that in the superconductors with line nodes, κ increases linearly with H in the superclean regime, where the condition $\frac{\Gamma}{\Delta} << \frac{H}{H_{c2}}$ is satisfied [93].

Inter-plane thermal conductivity, on the contrary, closely follows expectations for the superconductors without nodes, Fig. 7.3(lower panel). As shown in the Fig. 7.4 variation
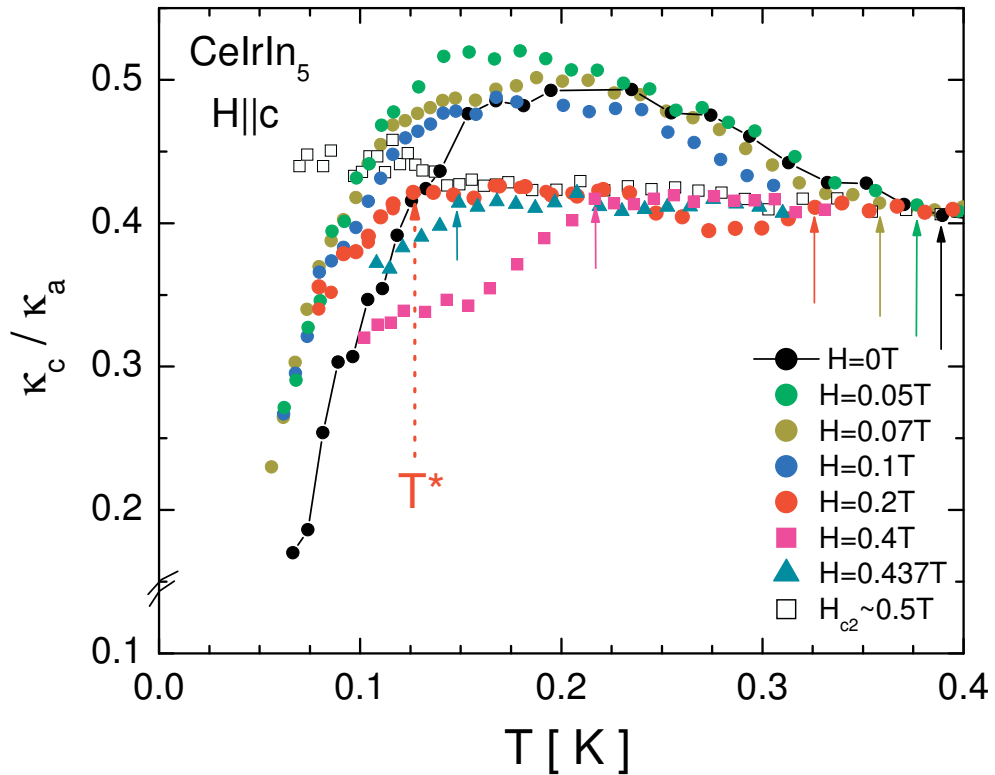
FIGURE 7.5: Temperature dependence of the anisotropy ratio κ_c/κ_a of highly pure crystals CeIrIn$_5$, in various applied magnetic fields ($H\|c$). Solid arrows show T_c at any related applied field; with increasing field T_c is decreasing. Note to H=0.2 T that does not show a clear transition at $T_c \sim 0.32$ K and instead we observe a transition at much lower temperature nearly 0.136 K, called T^* that is shown with dashed arrow.

of κ_c with field is dramatically different. Since these two configurations are different *only* in the direction of the current flow, we must take that the quasi-particles, although generated by the magnetic field, cannot move along c-axis in the superconducting state in pure samples. The only possible explanation to this fact is that nodal quasi-particles are localized near the regions where their movement is hindered by the whole superconducting gap for all possible directions. This is again consistent with the horizontal line node, as suggested from anisotropy of thermal conductivity in zero field.

7.3.2 Anisotropy of thermal conductivity

Fig. 7.5 shows the anisotropy of thermal conductivity, κ_c/κ_a, as a function of temperature in various applied magnetic fields (as determined from the κ_a and κ_c data shown in Fig. 7.3). (Zero field and normal state anisotropy was discussed in Chapter 5).

For a hybrid E_g gap structure, the anisotropy of thermal conductivity was calculated by Fledderjohann [60], Norman [155] and recently by Vekhter and Vorontsov [225]. All calculations predict an immediate decrease of anisotropy below T_c. This is indeed seen for fields H=0.4 and 0.437 T in Fig. 7.5. However, at low magnetic fields, 50, 70 and 100 mT, an increase is observed below T_c. This increase can be due to inelastic scattering (as discussed in Chapter 5), and/or notable difference in the gap structure as compared to low temperatures.

In Fig. 7.5 the superconducting transition temperature, T_c, and a new characteristic temperature T^*, below which anisotropy starts to decrease, are labeled with solid and dashed arrows respectively. In intermediate field of 0.2 T crossing $T_c = 0.32K$ does not reveal any change in the anisotropy before reaching $T^*(0.136K)$. Thus we conclude that the anisotropy characteristic of hybrid gap structure is found only below T^*.

7.3.3 Summary

In-plane and inter-plane thermal conductivity in $H \parallel c$ configuration reveal qualitatively different field dependence in $T \to 0$ limit. These are consistent with the hybrid E_g gap structure with equatorial line node and polar point node. This anisotropy becomes evident below some characteristic temperature T^*.

7.4 Magnetic field parallel to the conducting plane, $H\|ab$

In Fig. 7.6(left) we present inter-plane thermal conductivity of CeIrIn$_5$ in magnetic field parallel to conducting plane. The same high purity sample was studied in $H \parallel c$ configuration, as presented in Fig. 7.3. There are three features in this figure:

High temperature (near T_c)

i) In both configurations, application of magnetic field reveals a clear kink in κ/T at T_c, which was not visible in zero field (The kink is steeper in $H\|c$ direction). This is a usual behaviour in conventional superconductors and has been also seen in the heavy fermion UPt$_3$ [203].

ii) At temperatures near T_c, κ first decreases at low fields as a function of magnetic field, and then increases up to its value in the normal phase. This behaviour is more
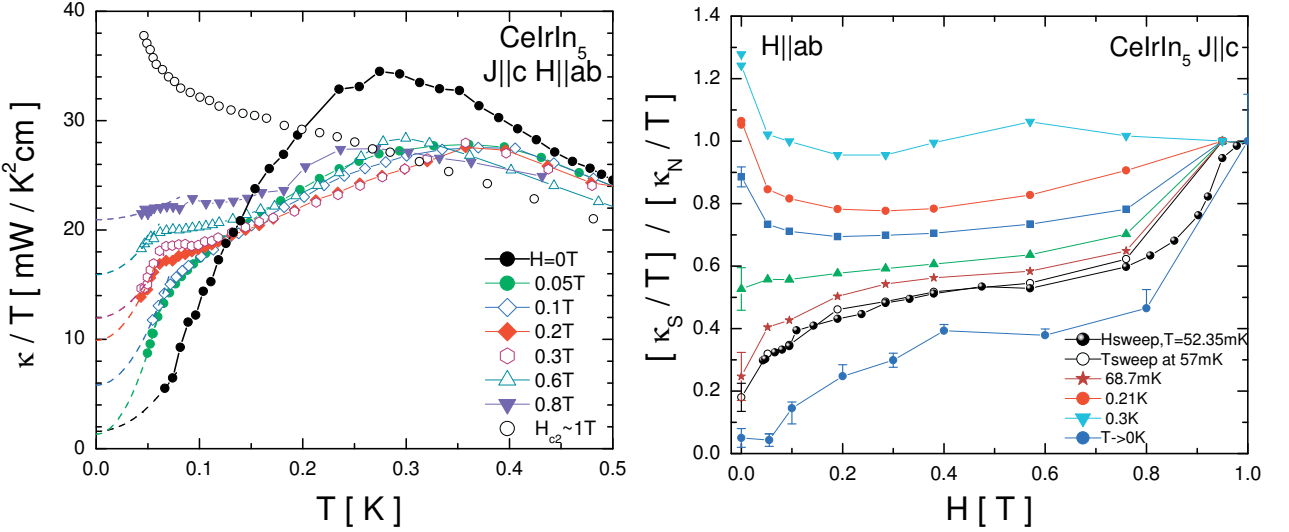
FIGURE 7.6: *Left*: The inter-plane thermal conductivity κ_c/T of pure CeIrIn$_5$ in zero and various magnetic field up to H_{c2} ($H \perp c$). With applying magnetic field two kinks are appeared; the first steep one is at the superconducting transition temperature, T_c, and the second one, placed at very low temperature, nearly at 80 mK, that might be because of multi-component of order parameter. This anomaly can be seen in highly pure samples and when the field is in the *ab* plane. *Right*: The inter-plane thermal conductivity as a function of magnetic field in field orientation $H \perp c$.

obvious in high purity single crystal, and in the magnetic field in the *ab* plane; see Fig. 7.6(left). We reproduced measurements on two more *c*-axis samples with lower purity; $\rho_{0c} \approx 1$ and $2\mu\Omega$cm ($\rho_{0c} \approx 0.5\mu\Omega$cm is for the purest sample shown in the figure.). We observed that the drop in κ_c near T_c at low fields become progressively weaker with increase of residual resistivity. This observation supports the view that the origin of suppression of κ with field may be similar to the case of conventional superconductors where it has been attributed to the extra scattering of quasiparticles from the vortex cores [122]. This effect would be compensated at higher fields by an increase in the number of carriers. Also this mechanism would be more obvious in the very pure samples so that the mean free paths is greater than the distance separating vortices at low field where vortices can be treated as independent scattering centers [30].

In a simple model for low fields [122], the decrease in the thermal conductivity due to this process is expressed as:

$$1/\kappa = 1/\kappa_0 (1 + \frac{Bld(1 + \sin^2\theta)}{2\Phi_0}) \tag{7.3}$$

where κ_0 is the zero field conductivity, Φ_0 is the flux quantum, l is the mean free path in the superconducting state, d is the vortex effective diameter, and θ is the angle between heat current and magnetic field directions. According to this simple model, the scattering of quasiparticles is more effective when the electrons move perpendicular to the vortices ($\theta = 90^o$, $J\|cH\|a$) as compared to when they move along the vortices ($\theta = 0^o$, $J\|H\|c$)[5].

The decreasing of κ at low fields can be seen well in the Fig. 7.6(right). Fig. 7.6(right) shows the H dependence of κ_c of a sample measured in the ab plane ($H\|ab$) field directions. At intermediated temperatures, $\kappa_c(H)$ shows a minimum at low fields. This type of scattering was reported in the simple type-II superconductors, such Nb [122], in HF UPt$_3$ [30, 88] and Sr$_2$RuO$_4$ [93].

Low temperatures ($0 << T << T_c \sim$ 80 mK)

iii) In Fig. 7.7 (a) we zoom the low temperature part of κ_c vs T data of Fig. 7.6(left). The κ_c/T reveals a clear second feature/kink at low temperature ($\sim$ 80 mK), when the field is in the ab plane. The position of this anomaly is shown by arrow in Fig. 7.7 (a-d). This sharp feature can signal phase change in the superconductor with multi-component order parameter. As summarized in the $H - T$ phase diagram, Fig. 7.13, the position of this kink at various applied fields constructs a new phase inside of the superconducting dome.

The low temperature phase in the phase diagram in Fig. 7.13 shows the physical properties (anisotropy, response to doping and magnetic field along c-axis) consistent with $E_g(1, i)$ state, as discussed previously. The high temperature phase does not reveal characteristic anisotropy of the horizontal line node and thus may have $E_g(1,0)$ symmetry, if the theoretical discussions on 2D representation models in 7.1.3 is considered, or $d_{x^2-y^2}$ symmetry, if the accidental degenerate models discussed in 7.1.1 in page 93 is considered. Here more discussion is given as follows.

Comparison with other group data

Quite recently Matsuda group [100] have measured the in-plane thermal conductivity in magnetic fields H rotated relative to the crystal axes. They found a fourfold oscillation when H is rotated within the ab-plane, while no oscillation was observed within the bc-plane, at the lowest measured temperature T=0.2 K (see Fig. 7.8). They suggested a

---

[5]However, in our in-plane thermal conductivity study on single crystals, $J\|aH\|a$ and $J\|aH\|c$ (not shown here), we did not see this effect well.
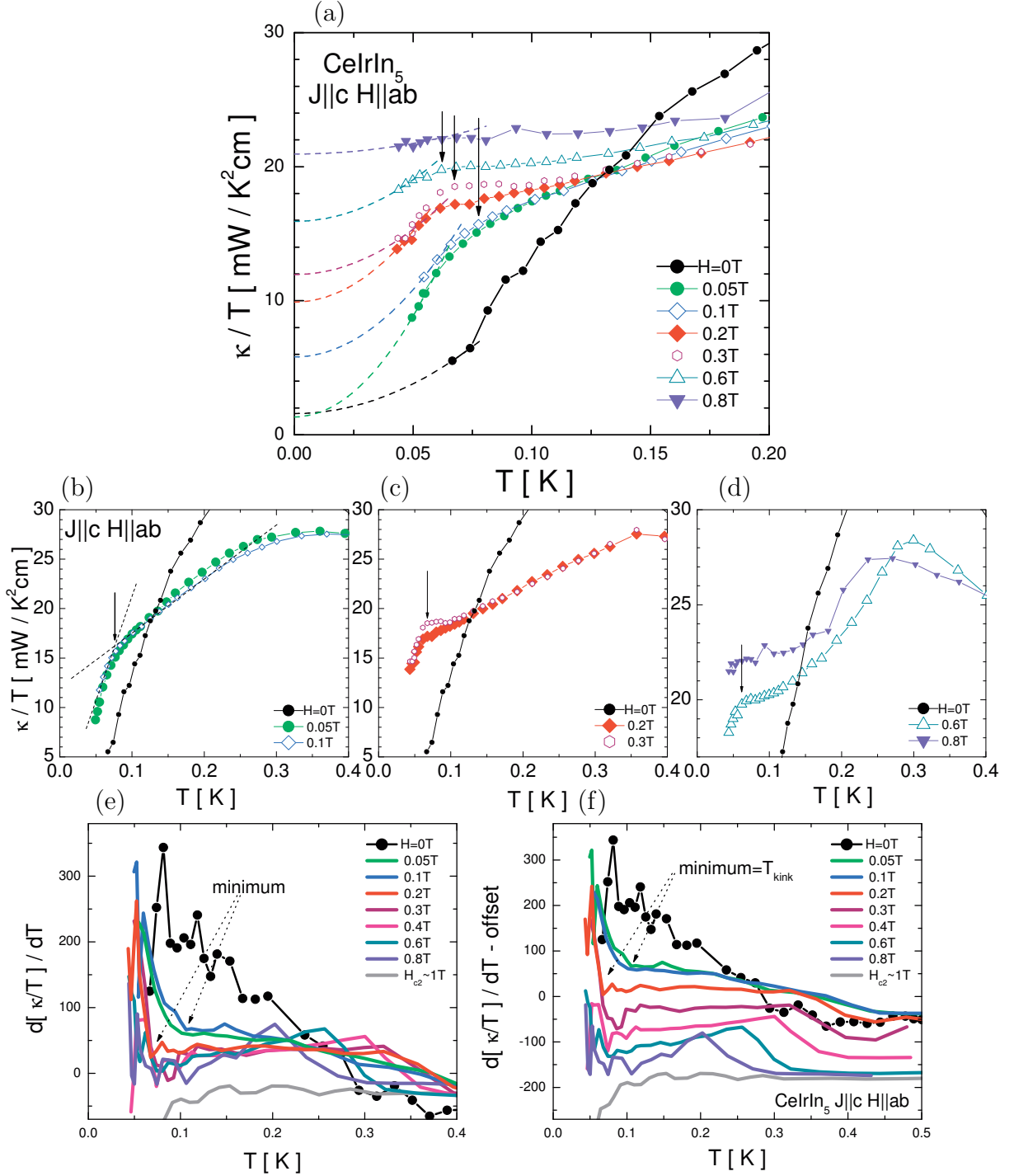
FIGURE 7.7: (a-d) κ_c/T of pure CeIrIn$_5$ in zero and various magnetic field in $H\|a$. Under applying magnetic field a kink appears at low temperature, is shown in arrow. (e-f) The derivative of κ_c/T vs T. There is a plateau behaviour below transition temperature in any applied magnetic field; *no plateau* in zero field. This plateau ends to a big jump at low temperature, nearly 70-80 mK. The temperature at this jump, called "minimum", at various applied fields leads to a new phase line in the phase diagram dome, called T_{kink} (see Fig. 7.13).
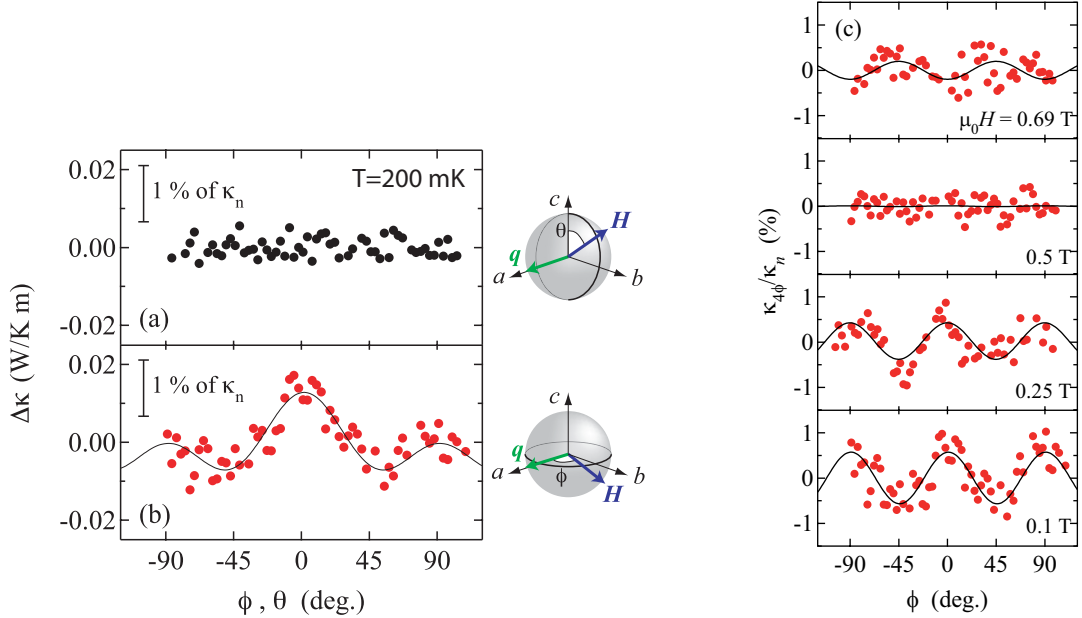
FIGURE 7.8: Angular variation of the in-plane thermal conductivity of CeIrIn$_5$ measured by Matsuda group [100] at T=200 mK with rotating H (a) within the bc-plane as a function of polar angle θ ($H = 0.05$ T) and (b) within the 2D ab-plane as a function of azimuthal angle ϕ ($H = 0.10$ T). The solid line shows the fourfold symmetry. (c) The fourfold component, $\kappa_{4\phi}$, normalized by κ_n at $T = 200$ mK at $H = 0.69, 0.5, 0.25,$ and 0.1 T. The upper critical field is $H_{c2} > 0.7$T at this temperature (figure from [100]).

$d_{x^2-y^2}$ gap symmetry (B$_{1g}$ symmetry) for CeIrIn$_5$ and thus the same gap symmetry for two reported superconducting domes in the phase diagram of CeRh$_{1-x}$In$_x$In$_5$ [100]. This observation is consistent with our predicted multi component order parameter, where we are suggesting a hybrid gap symmetry for low temperatures *below* 0.1 K. In other words, to interpret the whole phase diagram in Fig. 7.13 it looks the accidentally degenerate models may be applied; the system shows a d-wave symmetry (B$_{1g}$) at high temperatures and hybrid gap symmetry (E$_g$) at low temperatures.

Moreover, recent theoretical work on gap symmetry of CeIrIn$_5$ by Maki et al., [135] based on a weak-coupling BCS theory, at low temperatures, below $T << 0.3T_c \sim 0.12$K, shows a good consistency with our observation and in contrast to d-wave symmetry (see Fig. 7.9) [135].

A similar low temperature anomaly has been observed in heavy fermion superconductors UPt$_3$ in the $\kappa(H)$ curves but *no* sign in the κ/T vs T plots was detected [30]. Line of anomalies in the thermal conductivity data of UPt$_3$ tracks closely the anomalies
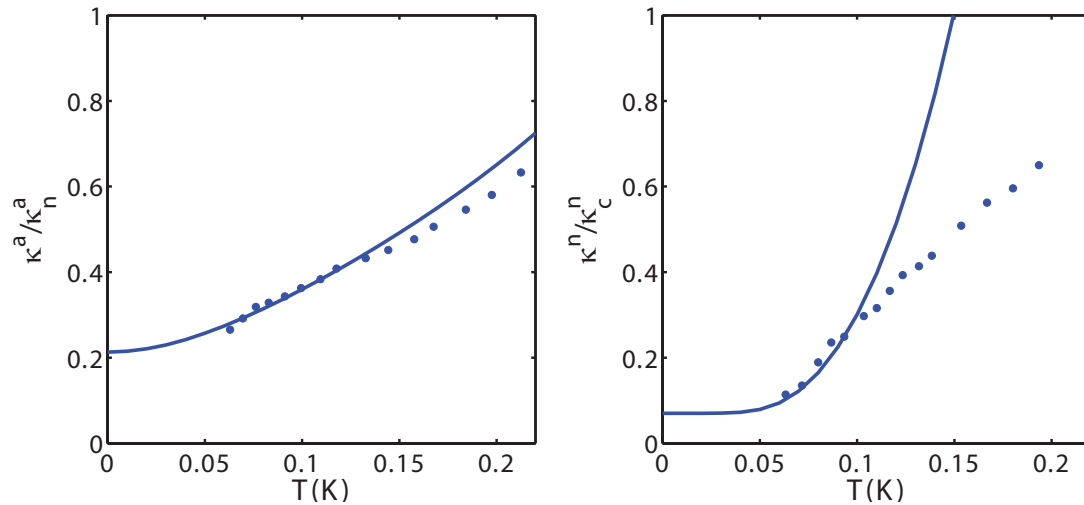
FIGURE 7.9: Low temeprature thermal conductivity calculated for CeIrIn$_5$ compound by Maki et al. [135], based on weak-coupling BCS theory, compared with the experimental data.

in the field dependence of ultrasonic attenuation [189] and sound velocity [4].

Similar anomaly was also observed in PrOs$_4$Sb$_{12}$ [92] (see Fig. 7.10). Here a clear anomaly has been seen in κ_c/T vs T plot in zero field and when field was applied in the ab plane. The existence of two distinct superconducting phases with different symmetries was suggested according to an accidentally nearly degenerate model [151]. [6]

7.4.1 κ_c vs H in $T \to 0$ limit

Fig. 7.11 shows the H dependence of κ_c at constant temperatures of $T = 45.41$ and $T = 52.35$ mK ($H\|ab$), and in $T \to 0$ extrapolations. Because of very steep decrease of thermal conductivity at the lowest temperatures, the latter were made assuming a

---

[6]Superconductivity with $T_c = 1.8$ K in HF PrOs$_4$Sb$_{12}$ with tetrahedral (T$_h$) symmetry was discovered by Bauer [27] in 2002. PrOs$_4$Sb$_{12}$ crystallizes in BCC structure. This is the first HF compound that shows HF behaviour in light of the interaction of the electric quadrupole moments of Pr^{3+}, rather than local magnetic moments as in the other HF superconductors, with the conduction electrons [27,92]. Therefore the relation between the superconductivity and the orbital fluctuation of f-electron state (*i.e.*, quadrupole fluctuation) has attracted great interest on this compound [27,92]. Thermal conductivity measurements in angle dependent magnetic field has revealed a multi-phase structure, characterized by a gap function with point nodes [92]; the gap function at high field phase has six point nodes (phase A), while that at low field phase has two point nodes (phase B). The theoretical calculation of the thermal conductivity by Maki et al., has proposed a triplet $p + h$-wave superconductivity to interpret the data of this compound [133,134]. Although, multi-band superconductivity also has been suggested [192]. More information on this compound can be found in [151,14,46].
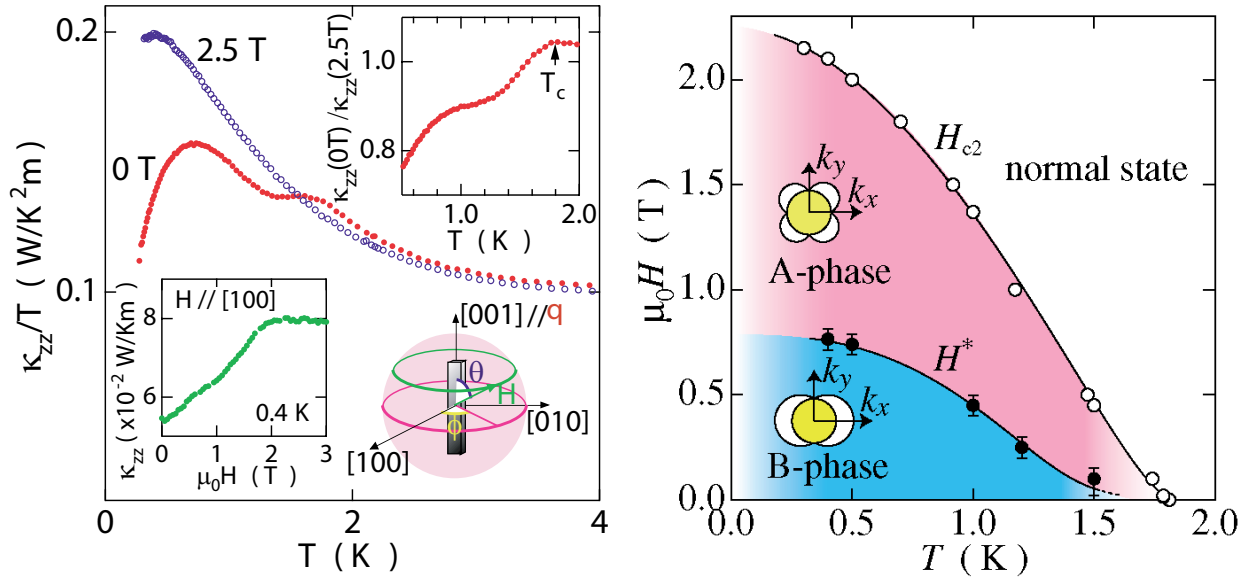
FIGURE 7.10: (Left) κ_c/T vs T in zero field and above H_{c2} in PrOs$_4$Sb$_{12}$ ($H\|a$). Upper inset: T dependence of normalized thermal conductivity. Lower inset: H dependence of κ_c at 0.4 K. Note to two anomalies in zero field. (Right) The phase diagram of the superconducting gap symmetry of PrOs$_4$Sb$_{12}$ determined by angular variation of the inter-plane thermal conductivity experiments. The filled circles represent the magnetic field H^* at which the transition from fourfold to twofold symmetry takes place (from [92]).

T^2 dependence of κ_c/T, as discussed in detail in Chapters 5 and 6 [7]. It is clear that in $T \to 0$ extrapolation κ_c/T remains close to zero at the lowest fields, while with further field increase shows unusual double-hump structure. This is in marked contrast to the behaviour in $H\|c$ and in any known conventional superconductor. This is apparently consistent with the transformation of the superconducting gap structure with magnetic field, as depicted in Fig 7.12. In Fig 7.12 we compare the response of the inter-plane heat transport of CeIrIn$_5$ for two directions of magnetic field with the behaviour of PrOs$_4$Sb$_{12}$, for magnetic field leading to phase transformation of the superconducting state. PrOs$_4$Sb$_{12}$ shows two different superconducting phases in its phase diagram. Two phases have point nodes in the gap structure. Interestingly enough, the two curves show some similarity, however, low-field increase is much steeper in PrOs$_4$Sb$_{12}$. [8]

---

[7]For extrapolation of κ_c/T to zero temperature, we used the theory of Graf [74] that predicts $\kappa_c/T \propto T^2$ in the clean limit for hybrid gap symmetry. I fitted a few low T points data (2 to 5 points) with this function, as shown by dashed lines in Fig 7.7. The error bars in Fig 7.11 come from the minimum and maximum values of extrapolated residual linear terms.

[8]One point more that would be good to think on is, it looks κ_c near H_{c2}, has the same behaviour for both directions of field; κ_c increases rapidly to reach to its normal state (see Fig. 7.12). We found
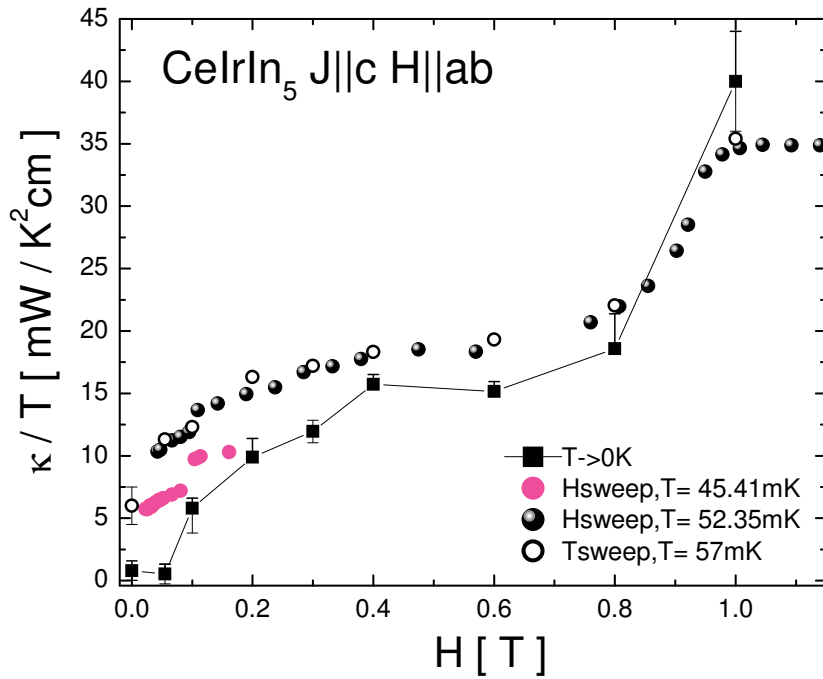
FIGURE 7.11: κ_c/T as a function of H in fixed temperatures T=45.41 and 52.35 mK ($H\|a$). The big difference in the residual linear term, nearly 5 mW/K²cm, at to nearly close held temperatures confirms the steep increasing of κ_c vs T at low temperatures. Note to the non smooth behaviour of κ_c in the whole range of applied field.

Quite recently, the thermal transport and field-angle-dependence specific heat measurements of the heavy fermion compound URu_2Si_2, with body centered tetragonal structure, shows hybrid E_g gap symmetry in the entire Brillouin zone [101, 237]. This compound has two low temperature phase transitions, one at a "hidden order" phase T_N=17.5 K and second a superconducting transition at T_c=1.5 K. The field dependence of the in-plane thermal conductivity of URu_2Si_2 shows a nearly similar unusual behaviour as we observed in CeIrIn₅ (in Fig. 7.11), which was related to the behaviour of line and point nodes (hybrid symmetry) under applied magnetic field [101].

nearly the same similarity for $J\|a$ in $H\|a$ and $H\|c$ study; $\kappa_a \propto H$ near H_{c2} for both field directions (not shown here). The triplet SC Sr_2RuO_4 shows a linear and steep increasing of thermal conductivity near its H_{c2} for $H\|c$ and $H\|a$ field directions, respectively. The observation of different behaviour was related to the difference of the vortex core structure [93].
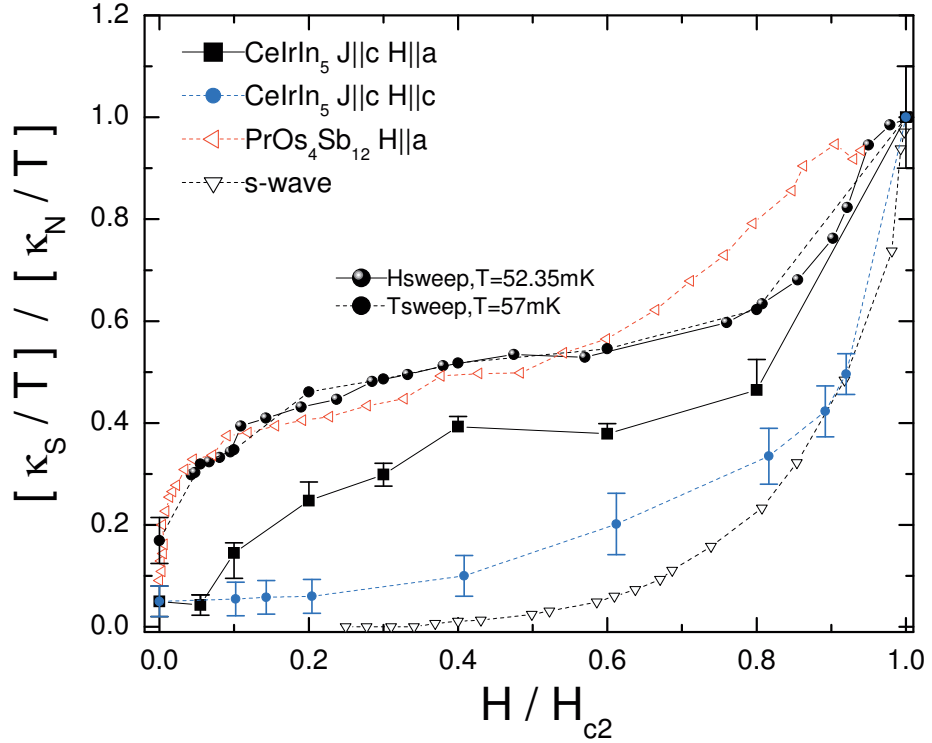
FIGURE 7.12: Low temperature behaviour of $\kappa_c(H)$ in $H\|a$, compared with $\kappa_c(H)$ in $H\|c$, conventional s-wave superconductor Nb [122] and HF PrOs$_4$Sb$_{12}$ [192]. The comparison between PrOs$_4$Sb$_{12}$ and CeIrIn$_5$ is striking, and supports multi-phases superconductivity in our system.

7.4.2 Phase diagram

The $H - T$ phase diagram obtained from inter-plane thermal conductivity measurements in $H\perp c$ is shown in Fig. 7.13. T_c, the superconducting transition temperature, was determined either from the steep kink at the superconducting transition temperature in κ_c/T (Fig. 7.6(left)) or from κ_s/κ_n. T_{kink} have been determined by the second anomaly in the κ_c/T (Fig. 7.7 (a-d)) (triangle-green signs) or a minimum in the $d(\kappa/T)/dT$ vs T curves (square-blue signs) (see Fig. 7.7 (e-f)). Both ways for determining T_{kink} at various magnetic fields lead to a phase transition into the superconducting state, as shown in Fig. 7.13. The low temperature phase with a strong gap anisotropy has a hybrid E_g symmetry [193]. The high temperature phase which shows four fold symmetry by thermal conductivity measurements might have d-wave symmetry [100]. This phase diagram would be consistent with the theoretical accidental degeneracy models. Although, according to the theoretical 2D representation models the $E_g(1, 1)$ or $E_g(1, 0)$ symmetries
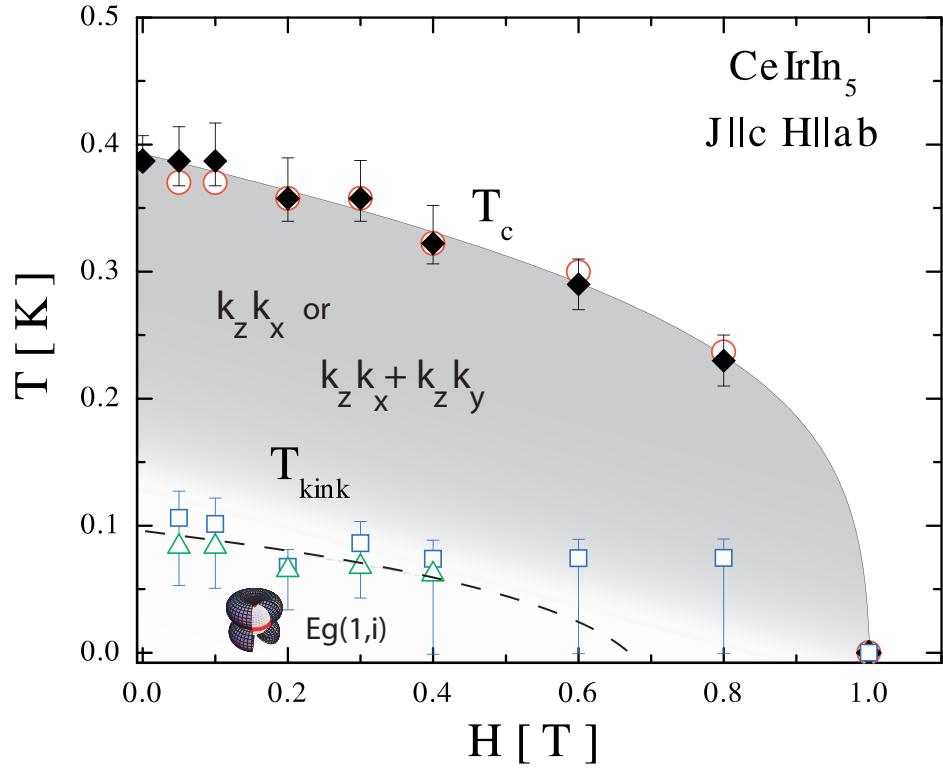
FIGURE 7.13: $H - T$ phase diagram of c-axis CeIrIn$_5$, determined by the thermal conductivity measurements. T_c points have been determined in the different ways: from the steep kink at the transition temperature in κ/T (Fig. 7.6 left) and κ_s/κ_n. T_{kink} have been determined by the second anomaly in κ/T (Fig. 7.7 (a-d)) or a minimum in the $d(\kappa/T)/dT$ vs T curves (Fig. 7.7 (e-f)).

also can be possible.

There are few examples of superconductors with multiple phases. High-field phases were observed in CeCoIn$_5$ [33] and Sr$_2$RuO$_4$ [138, 137], while several low-field phases were observed only in UPt$_3$ [97, 128] and PrOs$_4$Sb$_{12}$ [92]. The interesting point is that UPt$_3$ and PrOs$_4$Sb$_{12}$ superconductors have point nodes in their gap symmetries, similar to CeIrIn$_5$.

7.5 $T/\sqrt{H}$ scaling

As it was mentioned above, the scaling relation for thermodynamic and transport properties can be used as an additional test of the nodal structure. The scaling relation arises in the assumption that all thermal excitations are confined to nodal regions in the gap and
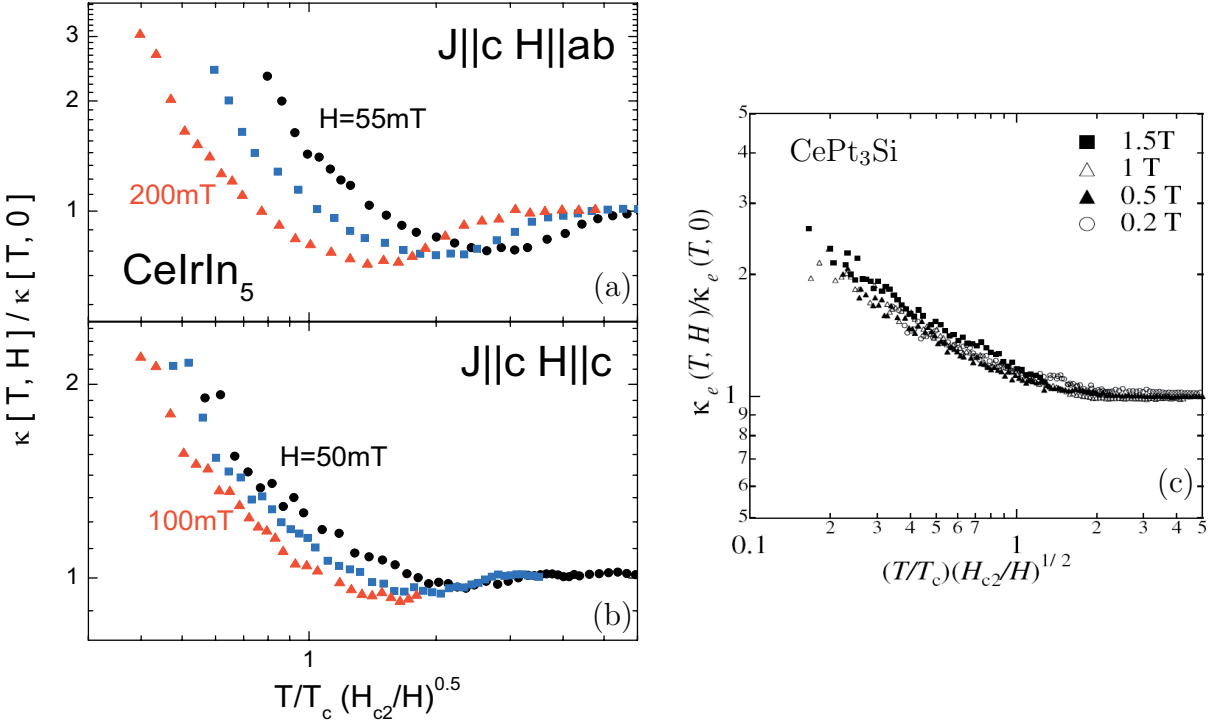
FIGURE 7.14: (a-b): Scaling relation plotted as $\kappa(T,H)/\kappa(T,0) \equiv F(x)$ for low magnetic fields for $J\|cH\|ab$ and $J\|cH\|c$ as a function of $x = (T/T_c)\sqrt{H_{c2}/H}$. Note, even for two nearly the same low fields 50 mT and 70 mT (black and blue) in $H\|c$ (b), data do not follow each other; no scaling. (c): The same scaling plot for a HF nodal superconductor CePt$_3$Si with $T_c = 0.75K$ and $H_{c2} = 4T$ in $J\|a$ $H\|b$ configuration. Note that the data in different magnetic fields collapse into the same curve (from [91]).

are not localized in the vortex cores. These relate the zero field temperature dependence of thermodynamic and transport properties to their in-field behaviour. A scaling relation of the single parameter $x = (\frac{T}{T_c})\sqrt{\frac{H_{c2}}{H}}$ is expressed as $\kappa(T,H)/\kappa(T,0) \equiv F(x)$, where $F(x)$ is a scaling function. The scaling is expected to be valid for T/T_c and $H/H_{c2} << 1$. As seen in Fig. 7.14(b), the data even for two very close low fields of 50 mT (circle-black) and 70 mT (square-blue) do not follow each other. This finding that is consistent with theoretical work, as *no scaling* for *linear point node*, supports the presence of point node in the gap symmetry in conflict with the *d*-wave gap scenario.

Experimentally, scaling laws have been verified in the thermal conductivity of heavy-fermion superconductors UPt$_3$ [202] (for both κ_b and κ_c heat current direction) and CePt$_3$Si (κ_a in $H\|b$) [91]; see Fig. 7.14(c) as a example. These measurements are consistent with theoretical calculations for line and quadratic point nodes. Hence, scaling

relations can be regarded as one of the hallmarks of nodal superconductivity.

7.6   Conclusion

In conclusion, the measurements of the overall temperature and magnetic field dependence of the inter-plane thermal conductivity, κ_c, in the mixed state of heavy fermion superconductor CeIrIn$_5$ shows a clear anomaly at low temperature. This anomaly is most pronounced in the highest purity samples and in the magnetic field parallel to the ab plane. The constructed $H - T$ phase diagram of this feature suggests an existence of a new phase inside the superconducting domain, as might be related to the two-component order parameter in this material.

Supporting this interpretation, the field dependence of κ_c at low temperatures in $H \| c$ direction shows activated increase, while that for $H \| ab$ direction is inconsistent with one component theories. We also found break-up of scaling relation for c-axis conductivity in $T/\sqrt{H}$ variable, confirming the presence of a linear point node in the gap symmetry.

Chapter 8

CeIrIn$_5$: Quantum Criticality, A Comparison with CeCoIn$_5$

8.1 Introduction

It is believed that quantum fluctuations provide a glue for exotic superconductivity [139] and drive materials to many different exotic phases. That is why the compounds, in which quantum fluctuations play important role, attract great interest recently. A convenient way to enhance quantum fluctuations is to drive a transition temperature of the continuous (second-order) phase transition to zero by some tuning parameter. A point where this happens is called quantum critical point (QCP). When happening in metals, quantum fluctuations lead to notable deviations from usual electronic behaviour, described in a Fermi-liquid theory. The key results of this standard theory of metals are the electronic specific heat which is linear in temperature, $C(T) = \gamma T$, and the electrical resistivity showing a T square behaviour, $\rho \propto AT^2$. The deviations occurring near QCP, frequently termed as "non-Fermi-liquid" (NFL) behaviour, lead to a diverging specific heat coefficient $\gamma(T) = C/T$, as either $\log(1/\text{T})$ or T^α with $\alpha < 0$, and a power law temperature dependent resistivity $\rho = \rho_0 + AT^n$, with n different from 2. Heavy fermion materials offer a unique opportunity to study quantum criticality in metals because of the coexistence and competition of different ground states in their phase diagrams and small, experimentally accessible energy scales involved.

Heavy fermion compound CeMIn$_5$ shows various ground states and thus rich possibilities for driving materials to QCP and magnetically mediated superconductivity. In

CeCoIn$_5$ a magnetic field can be used as a tuning parameter to drive material to a QCP [164]. Interestingly enough, the critical field for this QCP coincides with the superconducting upper critical field H_{c2}. A field-induced FL state is established below some cross-over temperature, T_{FL}, which grows linearly with the field $H > H_{c2}$. A sublinear temperature dependence of in-plane resistivity is seen at the critical field, while the low-temperature behavior is described by $T^{3/2}$ exponent [163]. The coefficient of the electron-electron scattering rate, obtained from resistivity and thermal conductivity measurements, is found to diverge at $H^*=H_{c2}$ [163] in line with the divergent behaviour of the electronic specific heat coefficient and effective mass in dHvA measurement at this value of magnetic field [32, 191]. The field-induced QCP at H_{c2} has been seen for both directions of the magnetic field applied parallel and perpendicular to the tetragonal c-axis [180]. This suggests that the presence of a quantum critical point, tied with the upper critical field of superconductivity, H_{c2}, is not a coincidence and its study can be insightful into the nature of critical fluctuations in the class of heavy fermion systems.

Since the two compounds CeIrIn$_5$ and CeCoIn$_5$ have similar electronic structures, both calculated and experimentally determined by dHvA studies [78, 54, 129], it is interesting to make a comparative study of the NFL behaviour in both compounds. Initial characterization of CeIrIn$_5$ found electrical resistivity in the normal state which is close to T-linear [173], while the specific heat C/T weakly increases as the temperature approaches T_c, which might be consistent with Fermi-liquid behaviour [173]. A strong $T^{1/2}$ temperature dependence of the nuclear spin lattice relaxation rate, $1/T_1$, in the normal state was explained by proximity to an AF instability [112]. These raise question about possible field-tuning of critical fluctuations in CeIrIn$_5$, similar to CeCoIn$_5$. This chapter is devoted to study of field-tuned effects in the normal state of CeIrIn$_5$ in magnetic fields scale of H_{c2}.

In this chapter, first we compare zero field in- and inter-plane electrical resistivities of CeIrIn$_5$ with each other and with CeCoIn$_5$ and then study the normal state of the in-plane resistivity and thermal conductivity of CeIrIn$_5$, $J\|a\ H\|c$. A $\rho_a \propto T^{1.2}$ behaviour was found in zero field above T_c till 3K. It seems application of magnetic field does not change the power law. A FL state was observed at low temperatures at H_{c2} (bulk) and above. A comparison with CeCoIn$_5$ shows dramatic difference: in CeIrIn$_5$ the inelastic electron-electron scattering coefficient remains essentially unchanged through all the range of applied magnetic fields, showing no divergence or QCP towards H_{c2}.
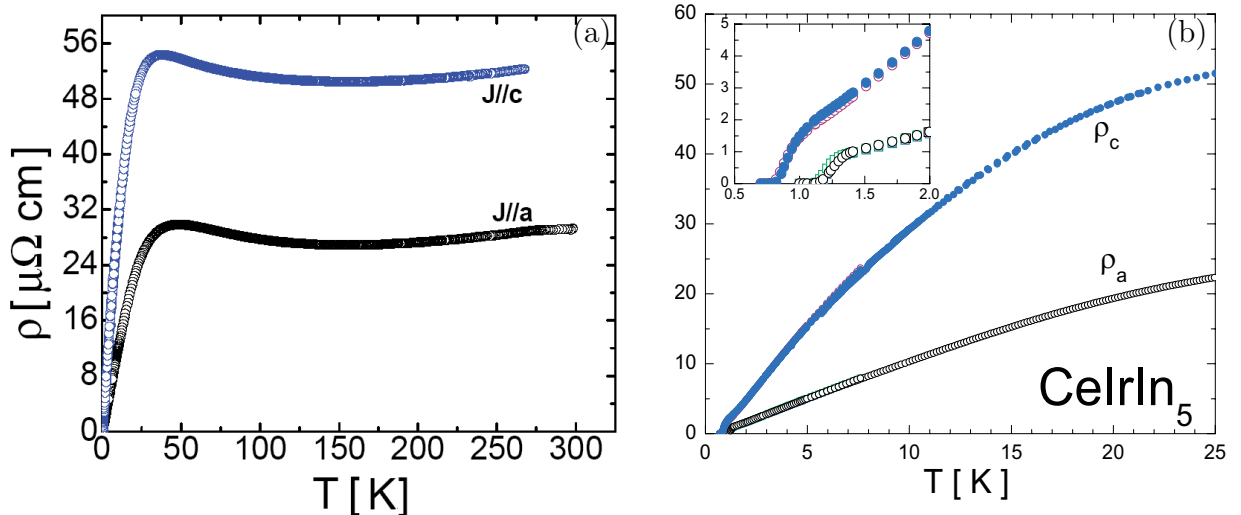
FIGURE 8.1: (a) The in-plane and inter-plane electrical resistivity, ρ_a and ρ_c of CeIrIn$_5$. (b) Low temperature of the resistivity of three a-axis and two c-axis samples. Inset shows zoom of the main plot at lowest temperatures.

8.2 General characterization

8.2.1 Experimental details

We measured the electrical resistivity of three a-axis and two c-axis samples from two different batches in this study (The thermal conductivity measurements in previous chapters have been done on the same samples here), down to 40 mK and under applied magnetic fields up to 11 T along the c-axis direction ($H\|c$). The zero field results fall exactly on top of each other for a-axis samples and c-axis samples separately; see Fig. 8.1(b). The dimension of samples are $\sim 4.5 \times 0.14 \times 0.045$ mm^3 and $\sim 2 \times 0.1 \times 0.01$ mm^3 for a-axis samples and $\sim 1 \times 0.15 \times 0.086$ mm^3 and $\sim 0.6 \times 0.15 \times 0.086$ mm^3 for c-axis samples. The electrical resistivity was measured with an ac resistance bridge, operating at a frequency of 16Hz, by applying 0.1 mA excitation currents. For a- and c-axis current directions we found $H_{c2} \approx 3.7$ T and ≈ 2.16 T, respectively. The residual electrical resistivity, ρ_0, of samples was about $\sim 0.3(0.5)$ $\mu\Omega$ cm at 40mK at magnetic field 4 T for a-axis (c-axis) samples.

8.2.2 General characterization

High temperature
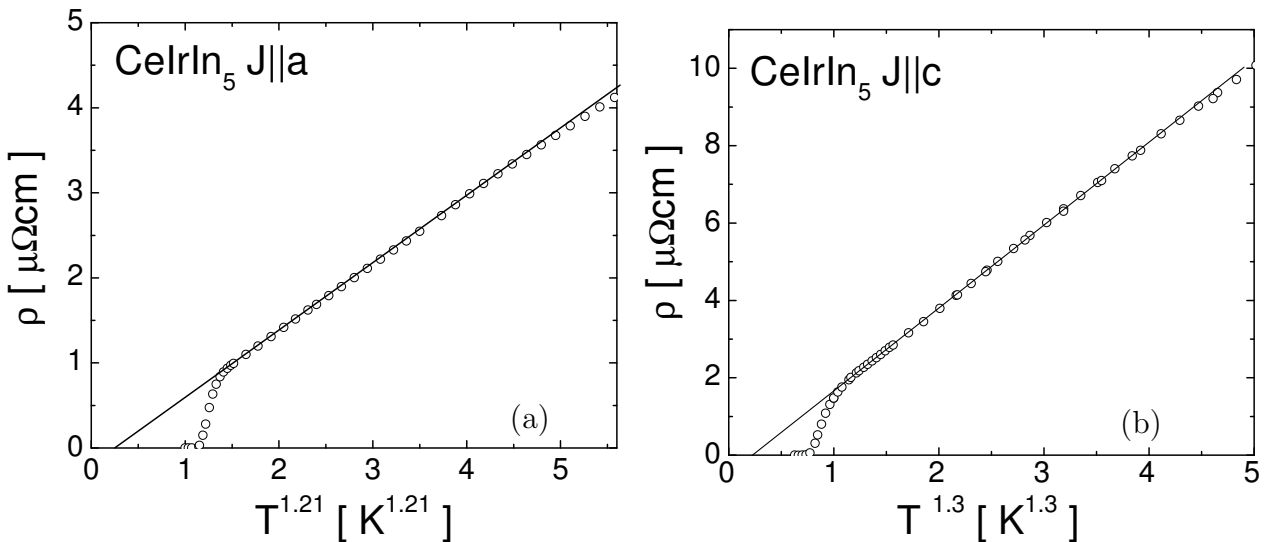
FIGURE 8.2: Low temperature power law behaviour of the electrical resistivity of (a) ρ_a and (b) ρ_c of CeIrIn$_5$.

The temperature dependence of the electrical resistivity ρ of CeIrIn$_5$ for two directions of the electrical current, along a-axis in the tetragonal plane, ρ_a, and along tetragonal c-axis, ρ_c, is shown in Fig. 8.1(a). On cooling from room temperature resistivity passes through a maximum around 50 K that is typically attributed to the cross-over from incoherent scattering of conduction electrons at high T to the development of the correlated bands at low T.

The resistivity at room temperature is $\rho(room) \approx 50$ and $28\mu\Omega$cm for c-axis and a-axis current directions (Fig. 8.1(a)). The only previous resistivity measurement on both c- and a-axis current directions at high temperature [195] show $\rho(room) \approx 67$ and $44\mu\Omega$cm, respectively. Although, the resistivity ratio is nearly the same in our data and the previous reported measurement.

Low temperature

The low-temperature part of ρ is zoomed in Fig. 8.1(b) and in Fig. 8.2. We can see from Fig. 8.1(b) that there is modest anisotropy in the electrical resistivity, $\rho_c/\rho_a \sim 3$. This anisotropy is temperature independent below 8 K down to $T_{c\ onset}$. This temperature-independent anisotropy of electrical resistivity is consistent with the temperature-independent anisotropy of thermal conductivity in the normal state, $\kappa_a/\kappa_c \sim 2.5$ at $H_{c2} \sim 0.5$ T, shown in the previous chapters.
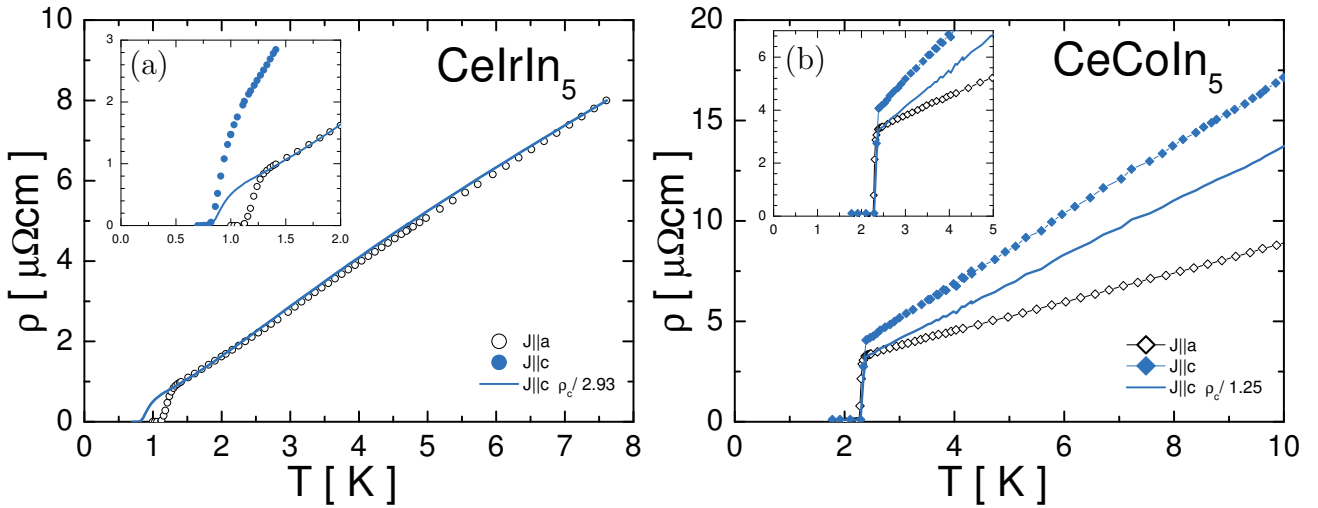
FIGURE 8.3: (a) ρ_a vs scaled of ρ_c of CeIrIn$_5$. (b) The same plot for CeCoIn$_5$(data taken from [162]).

At zero field, the electrical resistivity $\rho(T)$ above T_c is well described by the power law behaviour $\rho(T) \propto \rho_0 + AT^n$, with $n \sim 1.2$ and $n \sim 1.3$ for a-axis and c-axis resistivities, respectively (Fig. 8.2). This exponent can be tracked at low temperature up to 3.5 K, while on further temperature increase the exponent decreases to 1 (*only* in a-axis transport), for a short temperature range, and then becomes lower than 1. Nearly T-linear resistivity, rather than quadratic temperature dependence as expected of a Landau Fermi Liquid, has been suggested in consistency with the two dimensional AFM spin fluctuations theory [82, 181]. The theoretical calculation on nearly antiferromagnetic metals in the framework of a spin density wave scenario shows a power law resistivity with temperature as $\rho(T) \propto T^{3/2}$ and $\rho(T) \propto T$ for 3D and 2D spin fluctuations, respectively [181]. Such NFL power law resistivity has been observed in some heavy fermion systems which show quantum critical behaviour: quasi-2D system CePd$_2$Si$_2$ ($n \sim 1.2$), 3D CeIn$_3$ ($n \sim 1.5$) [139] ,YbRh$_2$Si$_2$ and CeCu$_{5.2}$Ag$_{0.8}$ ($n \sim 1$) [48, 83], and CeCoIn$_5$ ($n \sim 1$ at low field and 2/3 at high field) [163]. More discussion on the power law resistivity behaviour will be presented in the inter-plane transport Chapter 9.

Different T_c between $a-$ and c-axis transports

The electrical resistivity shows a different T_c for a- and c-axis current directions; resistivity goes to zero at about 1.21 K and 0.8 K for ρ_a and ρ_c, respectively (Fig. 8.1(b-inset)). This leads to different critical magnetic fields for these two current directions. The unam-

biguous reproducibility of this behaviour, for three *a*-axis and two *c*-axis samples, makes a doubt that this comes from any inhomogeneity or filamentary superconductivity as a reason. It is interesting to note that the 0.1%La-doped *a*- and *c*-axis samples show the same behaviour as the pure ones; different T_c for *a*- and *c*-axis current directions (see Fig. 6.1).

The previous in-plane electrical resistivity measurements by Petrovic [173] reports the same T_c and power law behaviour as ours in this study.

Scaling, transport anisotropy

In Fig. 8.3(a) we are comparing *a*- and *c*-axis resistivities while the *c*-axis is scaled. The scaled *c*-axis data, blue line, completely fall on the *a*-axis ones in a large range of temperatures, at least until 8 K. This shows a nearly isotropic electrical resistivity in this compound (doing the same scaling for CeCoIn₅ shows anisotropic behaviour (see Fig. 8.3(b))).

8.3 In-plane transport in magnetic field, $J\|a$

Charge transport

In Fig. 8.4 and Fig. 8.5, the in-plane resistivity for different values of the magnetic field is shown. A T^2 regime at low T is clearly observed for fields above H_{c2}, below a crossover temperature T_{FL}, corresponding to an onset of the Fermi-Liquid behaviour, that grows with field. T_{FL} goes roughly linearly from T_{FL}=0.65 K to $\sim 1\ K$ at fields $\sim$ 4 T and 11 T, respectively while the T^2 coefficient A, the slope of the FL regime, decreases weakly; $A \sim 0.55\ \mu\Omega$ cm K^{-2} to 0.33 $\mu\Omega$ cm K^{-2}. This nearly field independent of A is consistent with the specific heat and the dHvA experiments, where there is a weak field dependence of the finite electronic specific heat γ_0 (for fields up to 10 T) and the cyclotron effective mass, m^*, (for field between 6 to 17 T) at low temperature [38, 78]. Comparing with the closely related superconductor CeCoIn₅, this behaviour is different, in which magnetic field strongly affects on the properties of this material and strongly suppresses A coefficient (from A=7.5 to 0.5 $\mu\Omega$ cm K^{-2} for fields $\sim$ 6 to 16 T) [164], and the effective mass [191].

Power law in magnetic field
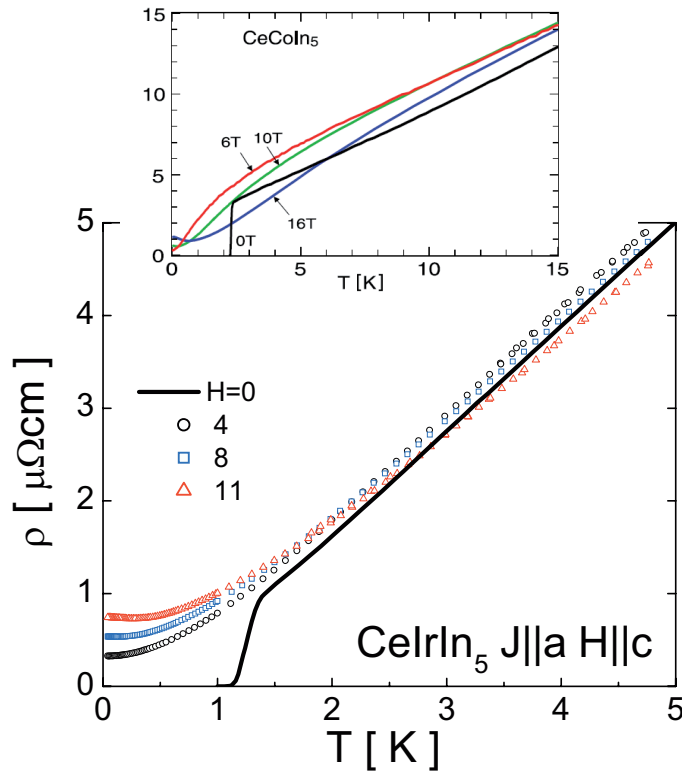
FIGURE 8.4: Temperature dependence of the in-plane electrical resistivity of CeIrIn$_5$ at different magnetic fields 0, 4, 8, 11 T oriented along *c*-axis. Inset: compared with the same plot of Co-115 [164].

With the application of the magnetic field up to 11 T (Fig. 8.4), nearly the same power law behaviour for resistivity extents up to 5 K. In other words, there is no evolution of the power law *in the range* of applied magnetic field in CeIrIn$_5$, in contrast to CeCoIn$_5$ that its in-plane electrical resistivity shows different power law resistivity for low and high magnetic field in the normal state [163].

Thermal transport in the FL regime

To reach to near bulk H_{c2} in CeIrIn$_5$ and investigate of field-tuned quantum criticality at H_{c2}, we did thermal conductivity measurements. The inset of Fig. 8.6(left) shows the thermal resistivity of CeIrIn$_5$ vs. T^2, obtained from thermal conductivity data, for fields $H \sim H_{c2}$=0.5 T and higher field 4 T. As we see, at H=0.5 T there is Fermi liquid behaviour at low temperature and this regime is expanding slowly with increasing of the magnetic field, which is consistent with our resistivity data. The field dependence of the T^2 Fermi liquid coefficients of charge (A) and heat (B) transport is shown in
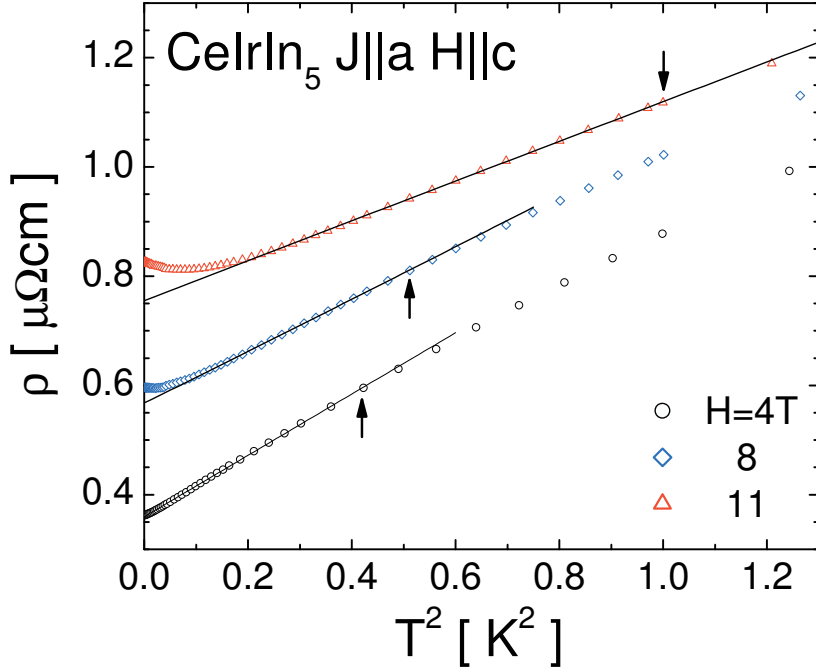
FIGURE 8.5: Resistivity of CeIrIn₅ vs T^2 at low temperature for magnetic fields near H_{c2} ($H_{c2} \sim 3.6$ T), 8 and 11 T ($H \parallel c$). The solid lines represent the T^2 fits to data in a range below T_{FL} indicated by arrows. The slope of these lines is the inelastic electron-electron scattering coefficient, A.

Fig. 8.6(right). In this plot is seen both A and B coefficients are consistent with each other and decrease smoothly with increasing of the field. This weak field dependence is in contrast to the case of closing to a QCP that is expected to see divergent behaviour for A and B coefficients [163]. Observation of the same critical behaviour for these coefficients in CeCoIn₅ is interpreted that the critical fluctuations are of magnetic nature in this compound [163].

Kadowaki Woods Ratio

To have better feeling about the value of scattering rate in CeIrIn₅ compare to other HF systems, we calculate a known FL ratio. In heavy fermion systems, the A coefficient is found to be roughly proportional to γ_0^2 and the empirical ratio of $r_{KW} \equiv A/\gamma_0^2$, known as the Kadowaki-Wood ratio, has been shown to have a nearly universal value of about $a_0 = 10$ $\mu\Omega$ cm mol² K²/ J² $= 1.0 \times 10^{-5}$ $\mu\Omega$ cm mol² K²/ (mJ)² in these systems [99,144]. We obtain the value of this ratio, $\sim 0.1a_0$ at near H_{c2} for Ir-115, considering $A \sim 0.5$ $\mu\Omega$ cm and $\gamma_0 = 720$ mJ/molK^2. This value is nearly small compare to the universal value for
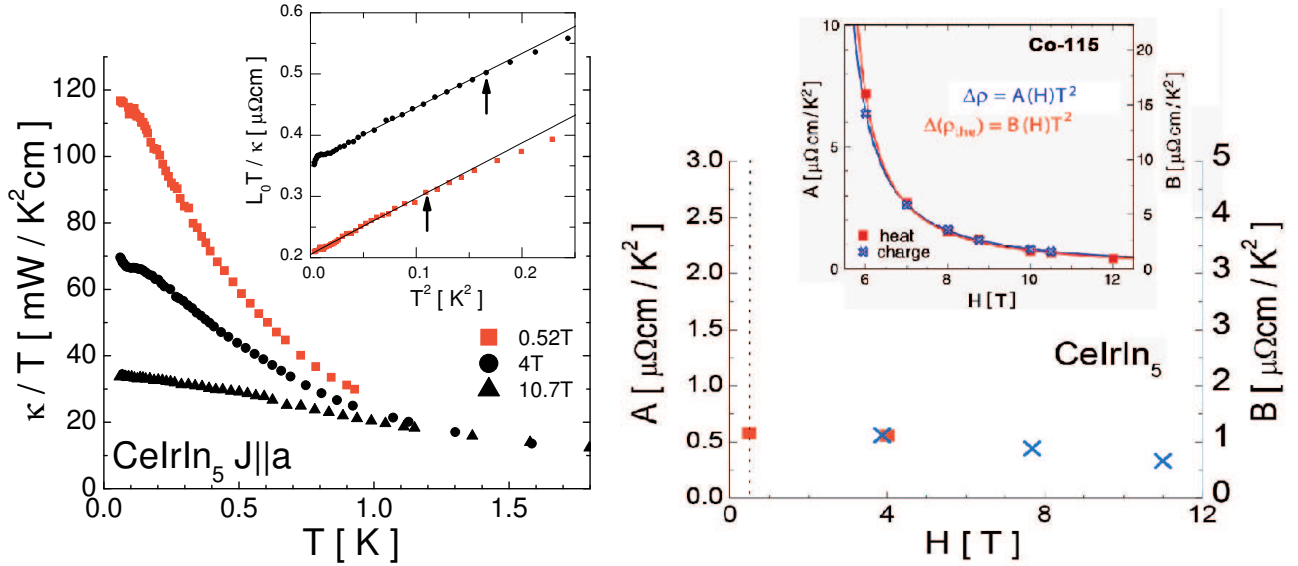
FIGURE 8.6:   (*Left*) The thermal conductivity of CeIrIn$_5$ vs T in normal state. Inset shows the thermal resistivity $L_0 T/\kappa$ vs T^2, for fields 0.5 and 4 T. The solid lines represent the T^2 fits to the data in a range below T_{FL} indicated by arrows. The slope of these lines is the inelastic electron-electron scattering coefficient B. (*Right*) Field dependence of the T^2 Fermi-liquid coefficients of charge (A) and heat (B) transport. The cross is e-e scattering coefficient (A) from resistivity and the red-bold square is e-e scattering coefficient (B) taken form thermal conductivity measurements. Inset: compared with the same plot of Co-115 [164].

heavy fermion systems [99, 144]. In CeCoIn$_5$, for instance, this ratio is about 0.52 a_0 at $H_{c2} \sim 6T$ that falls on the universal line for other heavy fermions [164].

Magnetoresistance

As the Fig. 8.7 and Fig. 8.4 show the magnetoresistance is small above 1 K and there is a different magnetoresistance behaviour at very low temperature; with increasing the field, the sample shows a positive magnetoresistance, nearly 70% for applied magnetic field 8 T compared to 4 T at the lowest temperature. As was shown in CeCoIn$_5$ this resistance increase at the lowest temperatures can be orbital in origin, which should be large in the samples as pure as CeIrIn$_5$.

Look at the high temperature in Fig. 8.7(or Fig. 8.4), MR is very weak above 1 K up to applied fields nearly 12 T; there is a positive magnetoresistance from zero till to 5 T and then it becomes negative for field above 5 T. On the other hand, CeCoIn$_5$ shows a pronounced crossover from positive to negative magnetoresistance at high temperature
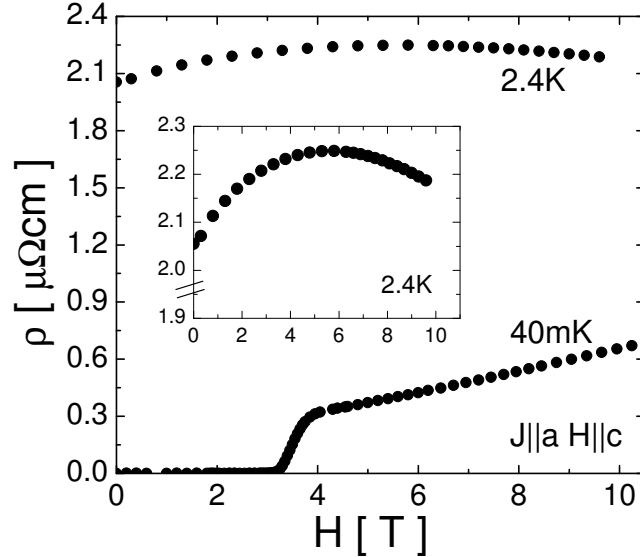
FIGURE 8.7: Field dependence of the in-plane resistivity of CeIrIn$_5$. $\rho(H)$ increases by magnetic field as $\rho(H) \propto aH = 0.06H$ at low temperature.

(It is interesting to note the peak in $\rho - H$ curve in CeCoIn$_5$ is around of H=4-5T at T=2.5 K, too.). This magnetoresistance crossover was interpreted as an indication of a change in the character of spin fluctuations with increasing field strength and its possible link to field-tuned QCP was pointed out [164]. The initial increase of ρ with field might be related to an increase of spin disorder. The presence of a large external field is expected to have a strong influence on AFM spin fluctuations [148] (However there is no evidence for long-range AFM order in CeCoIn$_5$ or CeIrIn$_5$ [84]). Therefore, a crossover to negative MR might occur at progressively increasing fields at higher temperatures, as observed in CeCoIn$_5$ [162]. [1]

8.3.1 Comparing heat and charge transport, $\delta(T)$ and Lorenz ratio, L/L_0

Here to better investigate of effect of magnetic scattering on conduction electrons in CeIrIn$_5$ and to compare it with CeCoIn$_5$, we compare the thermal and electrical resistivities with each other. In Fig. 8.8 we are comparing the electrical resistivity, ρ, with the thermal resistivity, $w \equiv \rho_{the} \equiv L_0 T/\kappa$ (the electronic thermal resistivity, $w_e \equiv L_0 T/\kappa_e$,

---

[1]It is interesting to note that in the spin fluctuations theory of weakly AFM metals in the calculation of magnetoresistance, a peak is predicted in the $\rho - H$ curve at the critical field of transition between antiferromagnetism and ferromagnetism [148].
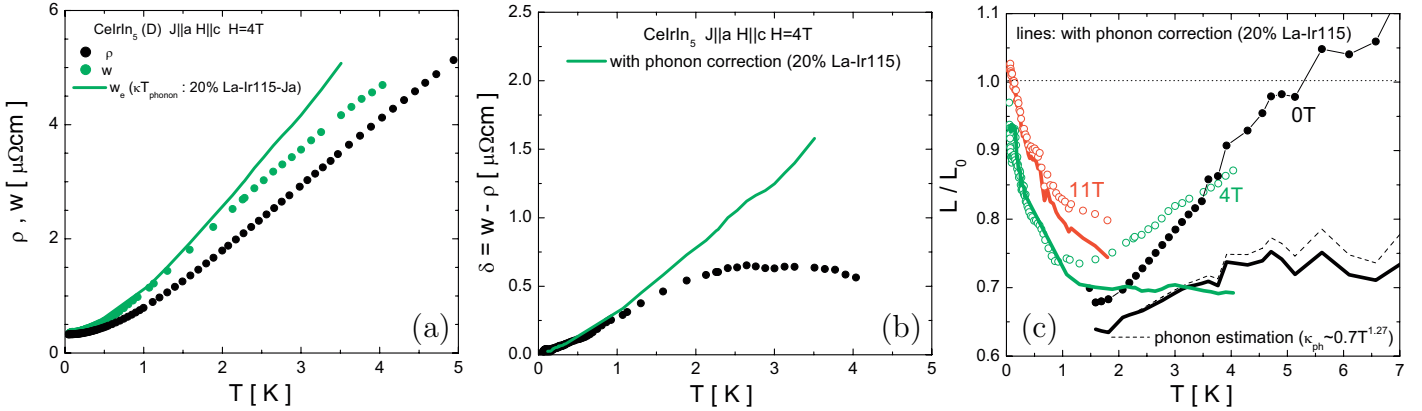
FIGURE 8.8: (a) In-plane electrical and thermal resistivity of CeIrIn$_5$ at magnetic field 4 T oriented along c-axis. (b) Difference between thermal ($w \equiv L_0 T/\kappa$) and electrical (ρ) resistivities, $\delta(T) \equiv w(T) - \rho(T)$ with and without phonon corrections. (c) Temperature dependence of normalized Lorenz ratio, L/L_0.

is obtained by subtracting the phonon contribution via measuring 20%La-doped CeIrIn$_5$ sample, that was explained in the Appendix C).

From (a) and (c) parts in Fig. 8.8 we observe that the Wiedemann-Franz law $L(T) = L_0$ is satisfied in the elastic regime, $T \to 0$, at applied $H = H_{c2} \sim 4\,T$; $w \to \rho$ in the limit $T \to 0$. However in the inelastic regime, nearly above 1 K, we can see $L/L_0 \sim$ constant vs T up to 4 K. In closely related compound CeCoIn$_5$ Lorenz ratio goes back to zero at $T \equiv T_{sf} \sim 5\,K$. In CeRhIn$_5$, an AFM compound in the same family, this quantity also goes to zero at $T_{sf} = 8\,K$.

Furthermore, in Fig. 8.8(b) we are comparing theses two resistivities with looking at their difference, $\delta(T) \equiv w_e(T) - \rho(T)$. We observe a linear temperature dependence of $\delta(T)$ vs T up to highest measured temperature 4 K, which is a fundamentally new result in 115 family. Recent work on a 3D weak FM compound ZrZn$_2$ shows the same linearity of $\delta(T)$ vs T [208]. Moreover, c-axis transport of CeCoIn$_5$ [215] and antiferromagnet YbRh$_2$Si$_2$ (measured by J.-P. Reid et al., in our group), two heavy fermion with AFM quantum critical point, show also a linear temperature dependence for $\delta(T)$ at low temperature. It is interesting to note that both compound show colinear behaviour in their magnetic structure. Recent NMR and NQR measurements on YbRh$_2$Si$_2$ strongly suggest the presence and competition of FM spin fluctuation with AFM spin fluctuations in the vicinity of the QCP near H =0.5 KOe [90]. In AFM metals the $\delta(T)$ is proportional to
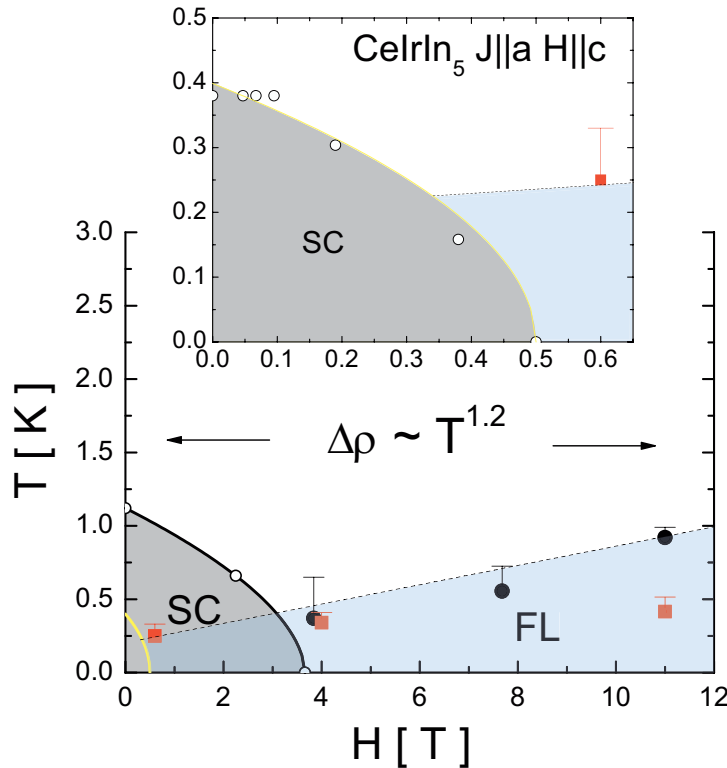
FIGURE 8.9: The phase diagram of $CeIrIn_5$ for $J\|a\ H\|c$ current and field configuration, obtained by electrical resistivity and thermal conductivity measurements. Inset show zoom at very low temperature and low magnetic field. Solid circles and squares obtained by charge and heat transport measurements, respectively.

T^2 at low temperature, because of $\rho(T) = \rho_0 + AT^2$ and $w_e(T) = w_0 + BT^2$ (so-called Fermi-Liquid regime). In AFM metal $CeRhIn_5$ Paglione et al., [165] found that $\delta(T)$ shows a $aT^2 + bT^5$ behaviour below the Neel temperature and then goes to zero at high temperature at $T \equiv T_{sf}$. The T^5 contribution was interpreted as strongly scattering of conduction electrons by fluctuation of local magnetic moments [165].

In $CeCoIn_5$, $\delta(T)$ goes to zero at $T \equiv T_{sf} \sim 5$ K at applied field H_{c2}. Going to zero of the difference of the electrical and thermal resistivities signals the presence of AFM spin fluctuations in the system [165].

Thus with observation of a linear temperature dependence of the difference of electrical and thermal resistivities in $CeIrIn_5$, it looks the type of spin fluctuations or magnetic scattering are nearly different in $CeIrIn_5$, compared to the suggested AFM spin fluctuation in this family. More discussion will come in the inter-plane transport Chapter 9.

8.4 $H - T$ phase diagram ($J\|a$)

Fig. 8.9 shows $T - H$ phase diagram of pure CeIrIn$_5$ compound for $J\|a$ and $H\|c$ current and magnetic field configuration. The diagram has been obtained from the whole electrical and thermal conductivity measurements in this study. Inset shows the phase diagram from the thermal conductivity measurements (bulk measurements).

There is nearly unchanged power law temperature dependent of electrical resistivity in the normal state, $\rho_a \propto T^{1.2}$. Co115 shows different power law behaviour in the normal state. While a-axis transport shows two different power law temperature dependence, $\rho_a \propto T$ and $\rho_a \propto T^{2/3}$ at low and high magnetic fields, respectively, the c-axis transport shows a linear temperature dependence in the whole range of applied fields, $\rho_c \propto T$. It means the $H - T$ phase diagram of CeCoIn$_5$ shows anisotropic behaviour in contrast with isotropic behaviour in CeIrIn$_5$ (see inter-plane transport of CeIrIn$_5$ in next chapter). This raises a question to think on; is there any relation between quantum criticality and transport anisotropy?

Moreover, the observation of an strongly anisotropic violation of WF law in Co115, while WF law is obeyed for a-axis transport at H_{c2}, $J\|aH\|c$, it is violated for c-axis transport, $J\|cH\|c$, in contrast to verification of WF law for both a- and c-axis current directions at H_{c2} in Ir115, is another issue that seems is consistent with other our findings in these two compound; more isotropic transport behaviour in Ir115 vs anisotropic transport behaviour on Co115.

8.5 Conclusion

In conclusion, in-plane charge and heat transport measurements of CeIrIn$_5$ in magnetic field around H_{c2} revealed FL behaviour at low temperature for the field out of the plane ($H \| c$) orientation. The electron-electron scattering rate is nearly field independent; there is no divergent electron-electron scattering behaviour and QCP at H_{c2} in CeIrIn$_5$ in spite of the presence of NFL behaviours in the normal state and similarity to the electronic band structure to CeCoIn$_5$; CeCoIn$_5$ shows a large enhancement of effective mass and a huge inelastic e-e scattering at H_{c2}.

Moreover, we find a linear temperature behaviour for the difference of the electrical and thermal resistivities, $\delta(T)$. It seems this linearity is not consistent with the AFM spin fluctuations theory.

Chapter 9

CeIrIn$_5$: Quantum Criticality at High Magnetic Field

In the previous chapter we found no quantum criticality at H_{c2} of CeIrIn$_5$, in contrast to CeCoIn$_5$ which shows a field-tuned QCP at H_{c2}. Non Fermi liquid behaviours of physical properties in the normal state of CeIrIn$_5$ raises questions about the source of these behaviours.

In this chapter we study the normal state of the inter-plane charge and heat transport of CeIrIn$_5$ down to 40 mK and under applied magnetic fields up to 17 T along the c-axis direction ($H\|c$). We find an anomalous $T^{4/3}$ power law resistivity, $\rho_c(T) = \rho_0 + AT^{4/3}$, in the high field non-Fermi liquid regime in a large temperature range, which suggests the presence of ferromagnetic spin fluctuations that lead to quantum phase transition in this compound. We suggest that this is one of the main factors that causes different behaviour among the materials in 115 family.

9.1 Inter-plane transport in magnetic field, $J\|c$

Magnetoresistance

Fig. 9.1 shows the c-axis electrical resistivity in zero and various magnetic fields. At low temperature below 1 K magnetoresistance is nearly weak consistent with the thermal conductivity measurements.

At high temperatures, magnetoresistance is very weak until $H = 4$ T while above this
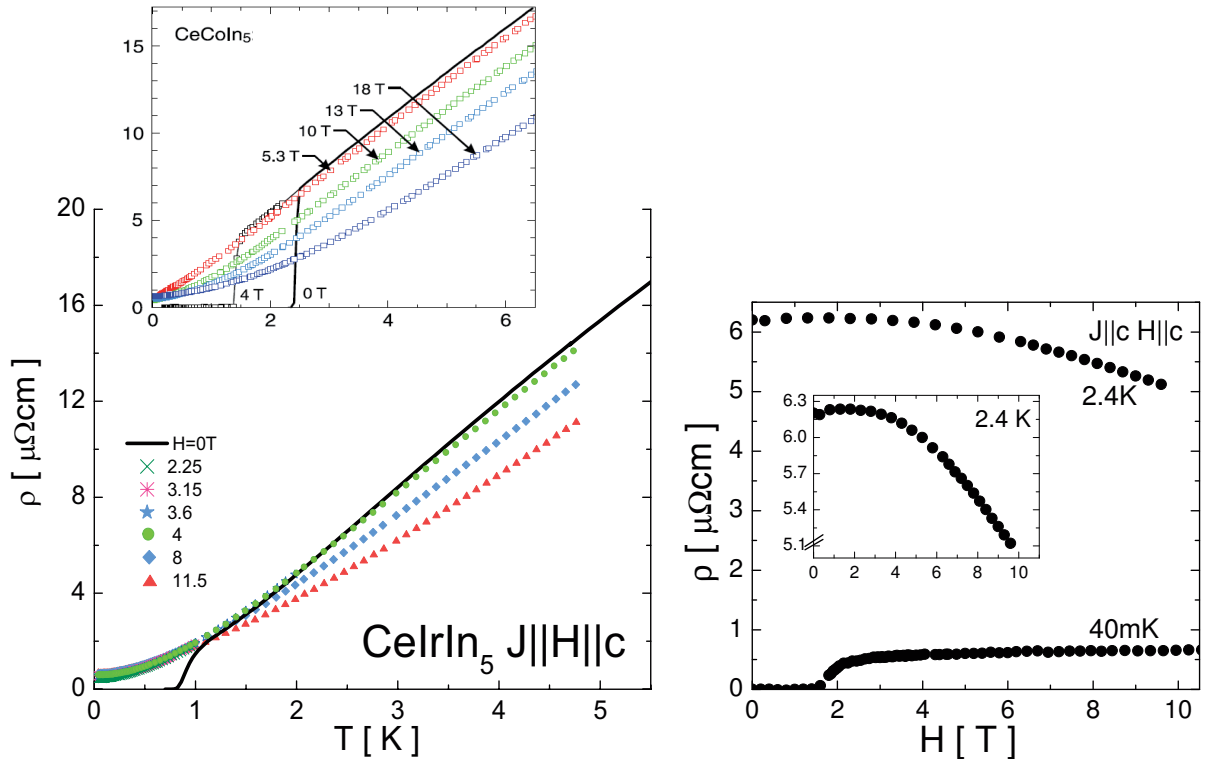
FIGURE 9.1: Main panels: Temperature and field dependence of the inter-plane electrical resistivity of CeIrIn₅ in magnetic fields oriented along c-axis. Inset-left: the same plot for CeCoIn₅ [162].

field there is a large negative magnetoresistance, which is in contrast to a-axis transport that shows *weak* negative magnetoresistance in the temperature and magnetic field range (Magnetoresistance is nearly 6% and 20% between $H = 4$ T and 10T at $T = 2.4$ K for a- and c-axis electrical transport, respectively.). This large negative c-axis magnetoresistance at high temperature behaves very similar to the c-axis transport of Co115 under applied field (see inset Fig. 9.1). In Co115, there is no magnetoresistance in the c-axis electrical resistivity up to applied fields $H_{c2} \sim 5.5$ T and above this field there is large negative magnetoresistance. Negative magnetoresistance is related to the ordering spins in applied magnetic field [162].

Magnetization measurement for [001] direction of magnetic field and at T=4.2 K in CeCoIn₅ shows a continual increase of magnetisation up to 50 T, showing no obvious sign of field-induced ferromagnetism order [195]. The absence of any saturation in M(H) until at least 50 T suggests that the strength of AFM correlations is strong in this compounds, even in the absence of long-range AFM order [162]. However, a weak metamagnetic
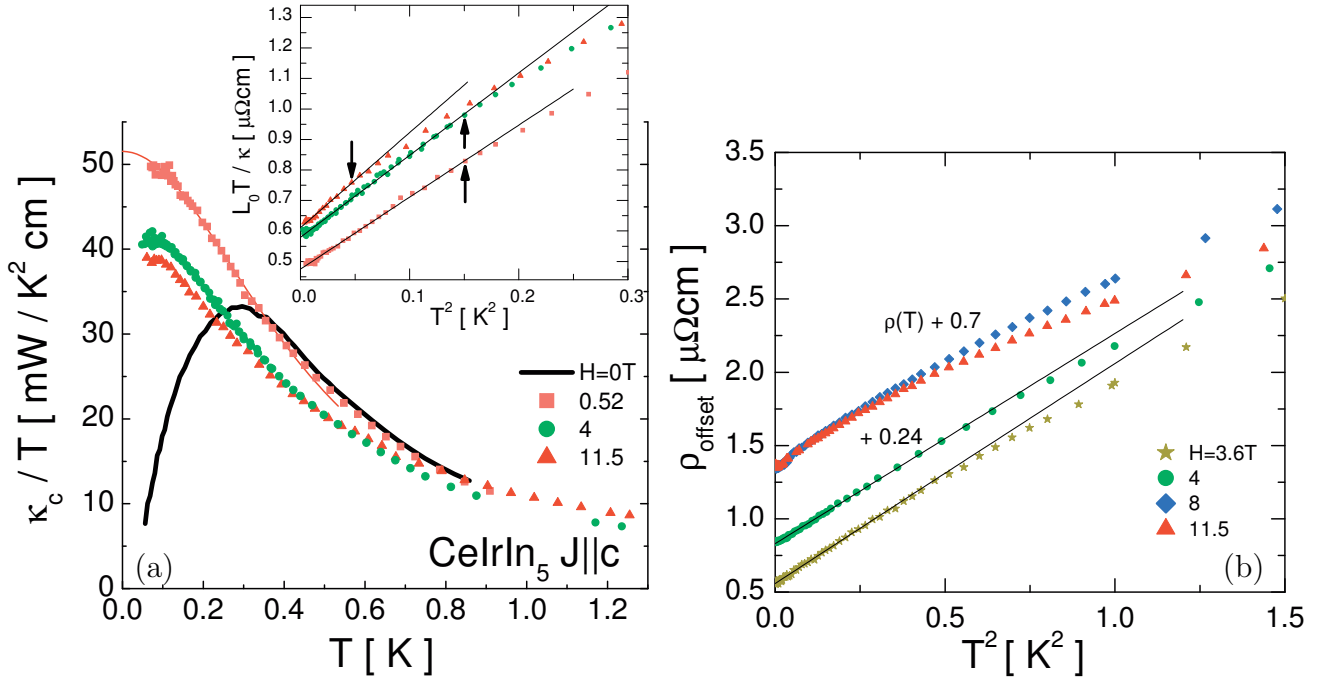
FIGURE 9.2: (a) The inter-plane thermal conductivity vs T. Inset shows the thermal resistivity vs T^2. Arrows show the end of T^2 regime, T_{FL}. (b) The inter-plane electrical resistivity vs T^2 at magnetic fields oriented along c-axis. Note to the FL region at low fields. At high field 11.5 T, the FL region is narrowed or disappeared in both heat and charge channels.

transition is found in CeIrIn$_5$ around 29.5 T at measured temperature 45 mK [168,108]. This metamagnetic-like increase shifts to higher fields and becomes broad with increasing the temperature [211]. Moreover, for this direction of the field a clear hysteretic behaviour at fields above 37 T has been observed. The origin of this ferromagnetic-like behaviour in CeIrIn$_5$ is not known so far [168].

FL regime at low T

In Fig. 9.2, the inter-plane thermal conductivity and electrical resistivity in the normal state for different values of the magnetic field is shown. Like a-axis transport shown in Chapter 8, a T^2 regime, in both the electrical and thermal resistivities, is observed for fields above bulk, $H_{c2} = 0.5$ T (inset of Fig. 9.2(a)), and above resistive critical fields, $H_{c2} = 2.16$ T (Fig. 9.2(b)), below a crossover temperature T_{FL}.

It looks T_{FL} grows with field up to $H = 4$ T (Fig. 9.2(b)); $T_{FL} \sim 0.335$ K, 0.575 K

and 0.7 K at fields $\sim$ 3.15, 3.6 and 4 T, respectively, while the T^2 coefficient A, the slope of the FL regime, decreases weakly; $A \sim$ 1.82, 1.63, 1.50 and 1.45 $\mu\Omega$ cm K^{-2}, for fields $H = 2.25$, 3.15, 3.6 and 4 T, respectively. From thermal conductivity measurement, we find $T_{FL} \sim 0.39K$ for fields $H \sim H_{c2} = 0.52$ T and 4 T (the T^2 coefficient, B, is nearly $\sim$2.36 and 2.75 $\mu\Omega$ cm K^{-2} for $H = 0.52$ and 4 T, respectively.). Nearly twice bigger thermal coefficient B compare to electrical coefficient A is usual in metals; for any type of electron-electron scattering process it is reported $L(T) \equiv \frac{\rho(T) - \rho_0}{w_e(T) - w_0} = \frac{A}{B} \approx 0.5$. See more information in this regard in [162].

Power law $\rho_c \propto T^{4/3}$

The interesting point here, it is difficult to detect any T^2 regime at higher fields above 4 T, both in charge and heat transport measurements. It seems with applying higher magnetic fields on c-axis samples, the T^2 regime holds only in a very narrow low temperature range, or at all, and the electrical resistivity shows a pure power law $T^{4/3}$ in a large temperature range, up to 7 K at 12T (Fig. 9.3). Note the resistivity increases nearly 40-fold in the temperature range between zero and 5 K (from nearly 0.25 $\mu\Omega$cm at 0 K to 10 $\mu\Omega$cm at 5 K). The inter-plane electrical resistivity of CeCoIn$_5$ at the QCP ($H_{c2} = 5.3$ T) shows a purely linear T dependence, from 0.4 $\mu\Omega$cm at 25 mK all the way to 40 $\mu\Omega$cm at 16 K, nearly 100-fold increase in resistivity (nealry 60-fold increase between 0 K and 5 K). This huge increase in resistivity in this temperature range was suggested as a strong prove that the power law is an intrinsic property of electrons scattered by critical fluctuations [215]; see Fig. 9.5. In UPt$_3$, showing NFL behaviour in physical properties at the metamagnetic transition $\sim$ 20 T, the resistivity increases nearly 10-fold at the critical regime between 0.5 K and 3 K, where the resistivity shows a $\sim T^{1.2}$ power law [109]. In the itinerant ferromagnet ZrZn$_2$, a metal close to a 3D ferromagnetic critical point, resistivity only increases nearly 3-fold between nearly $T = 0$ K and 12 K, where the resistivity shows a $T^{5/3}$ power law consistent with 3D FM spin fluctuation models [208]; see Fig. 9.5.

To understand the meaning of the 4/3 power law found in CeIrIn$_5$, lets have a look at the theoretical models:

Theoretical investigation of the spin fluctuations effect on the electrical and thermal resistivities of nearly antiferromagnet and weakly ferromagnet metals have been started in early 70's [221, 148, 220]. The self-consistent renormalization (SCR) theory of spin fluctuations, has been succeeded in extensive explanations of physical properties. The
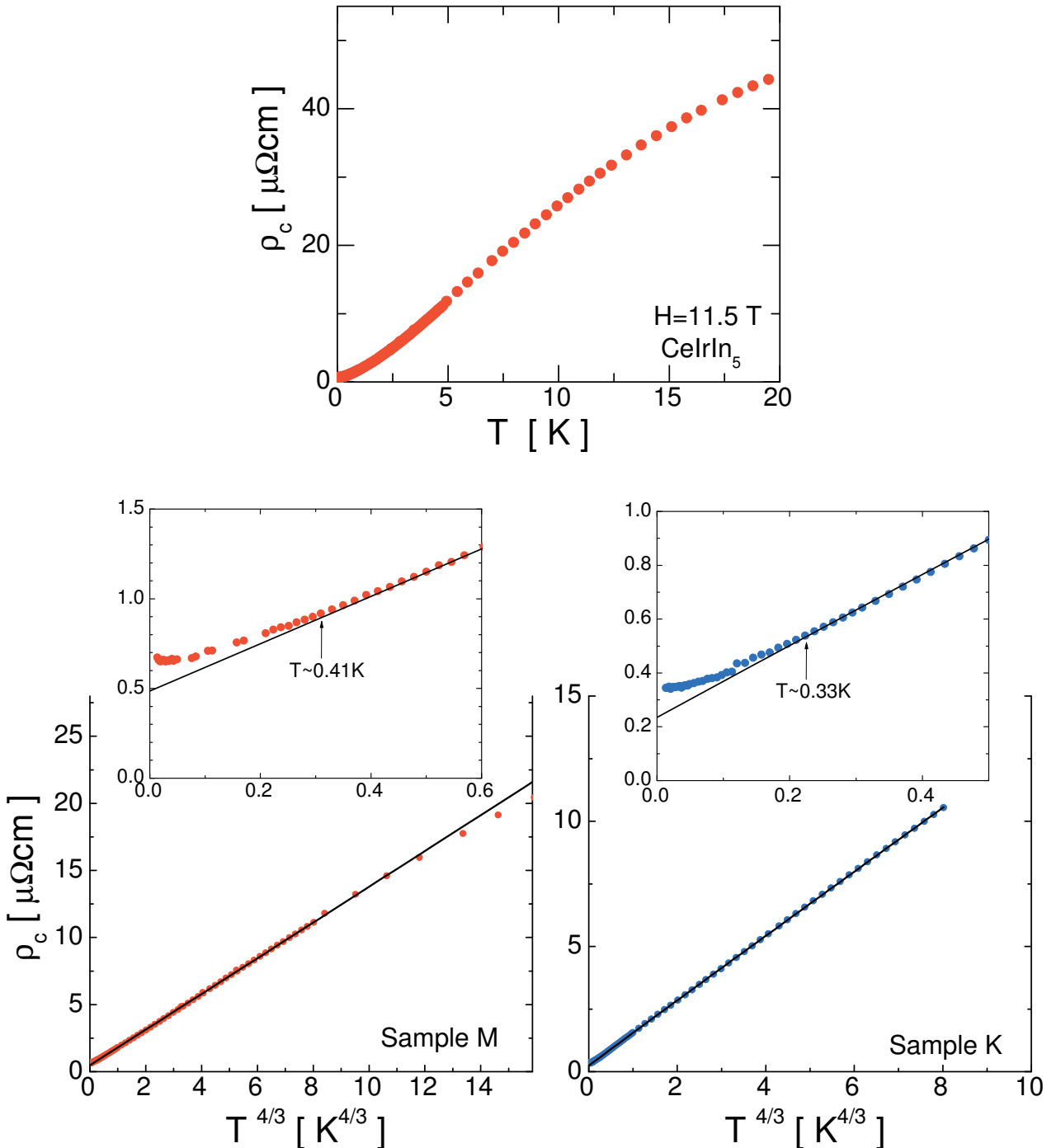
FIGURE 9.3: Inter-plane electrical resistivity vs T (top) and $T^{4/3}$ of two CeIrIn₅ samples (bottom) at magnetic field 11.5 T oriented along c-axis. Insets: show zoom of the main panels.
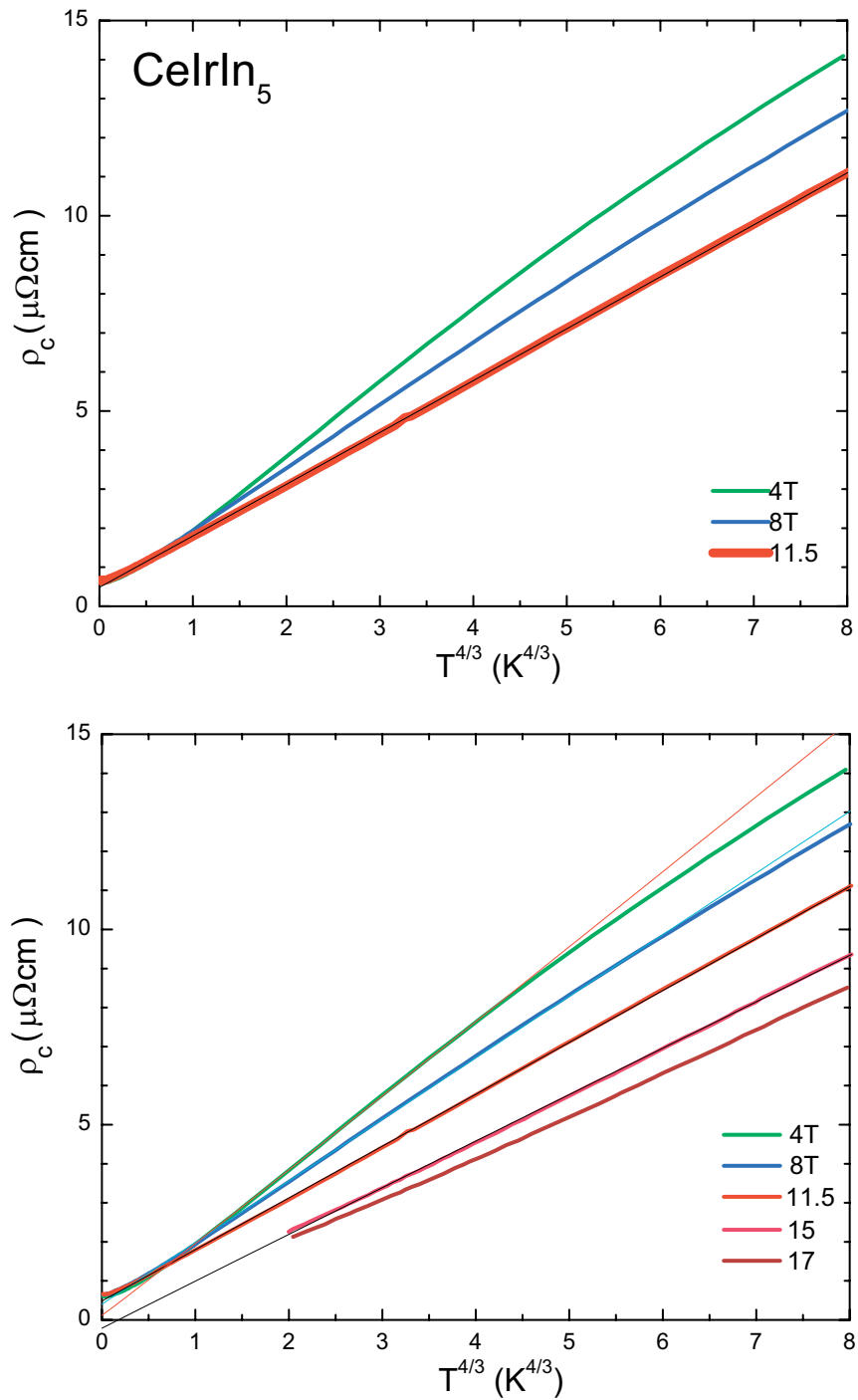
FIGURE 9.4: Inter-plane electrical resistivity vs $T^{4/3}$ of CeIrIn$_5$ sample at magnetic fields 4, 8, 11.5, 15, 17 T oriented along c-axis.
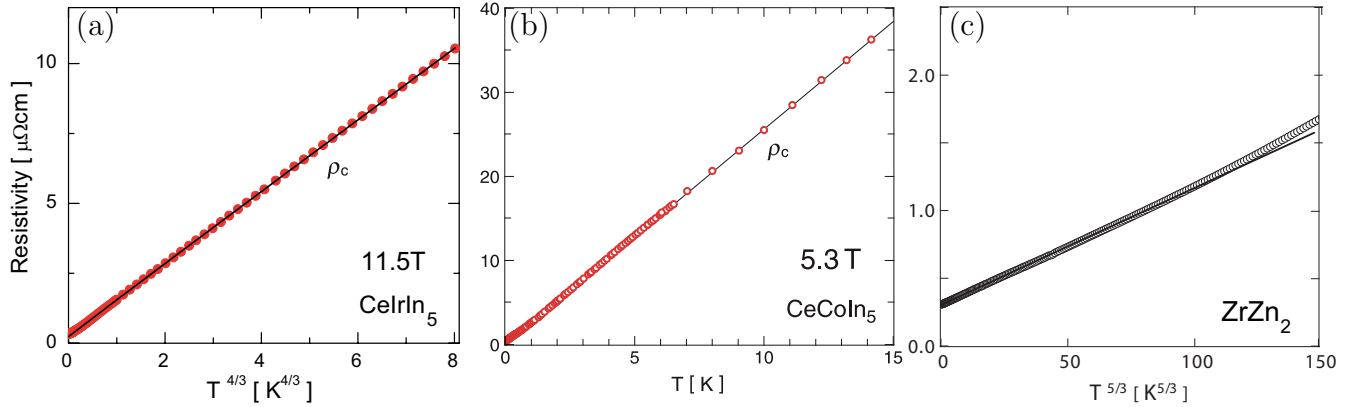
FIGURE 9.5: A comparison between the power law electrical resistivity of CeIrIn$_5$ at a high magnetic field, $H\|c$ (a), CeCoIn$_5$ at its QCP (b) and the itinerant ferromagnet ZrZn$_2$, a metal close to a 3D ferromagnetic critical point (c). The inter-plane electrical resistivity of CeCoIn$_5$ at the QCP ($H_{c2} = 5.3$ T, $H\|c$) shows a purely linear T dependence, from 25 mK to 16 K, and nearly 100-fold increase in resistivity [215]. In ZrZn$_2$ the resistivity shows a $T^{5/3}$ power law consistent with 3D FM spin fluctuation models [208].

idea in the model is based on considering two isotropic bands, s- and d-band electrons. In this model, only the s-electrons contribute to the conductivity and the d-electrons play a role of scattering the s- electrons, i.e., the conduction electrons are scattered by the spin fluctuations of the d-band electrons via an s-d exchange interaction [221].

The electrical and thermal resistivities of 3D nearly ferromagnetic metals have been calculated by Ueda and Moriya for the whole temperature range of interest including a ferromagnetic phase [221]. In the limit of zero temperature they obtained a T^2 temperature dependence for the electrical and thermal resistivities. The temperature range of these T^2 power laws becomes narrow and the coefficients of them are large when the system approach the ferromagnetic instability (critical boundary). As the temperature increases these quantities show $\rho \propto T^{5/3}$ and $w \propto T^{5/3} + T$. Thus one can find a linear temperature dependence for difference of the electrical and thermal resistivities, $\delta(T) \propto T$ for nearly ferromagnetic metals. In brief, it has been pointed out that the $\Delta\rho(T) \propto T^n$ with $n = (d + 2)/z$, where d is the effective dimension of spin fluctuation spectrum and z is the dynamical exponent. Thus with $z = 3$ for ferromagnetic spin fluctuations it can be found $n = 5/3$ in three dimension and $n = 4/3$ in two dimension. [1]

---

[1]In the calculation by Ueda and Moriya [221, 148] they pointed out that the resistivity at the critical boundary, $\Delta\rho \propto T^{5/3}$ or $\propto T^{4/3}$ show no discontinuity at the Curie temperature, while the derivative
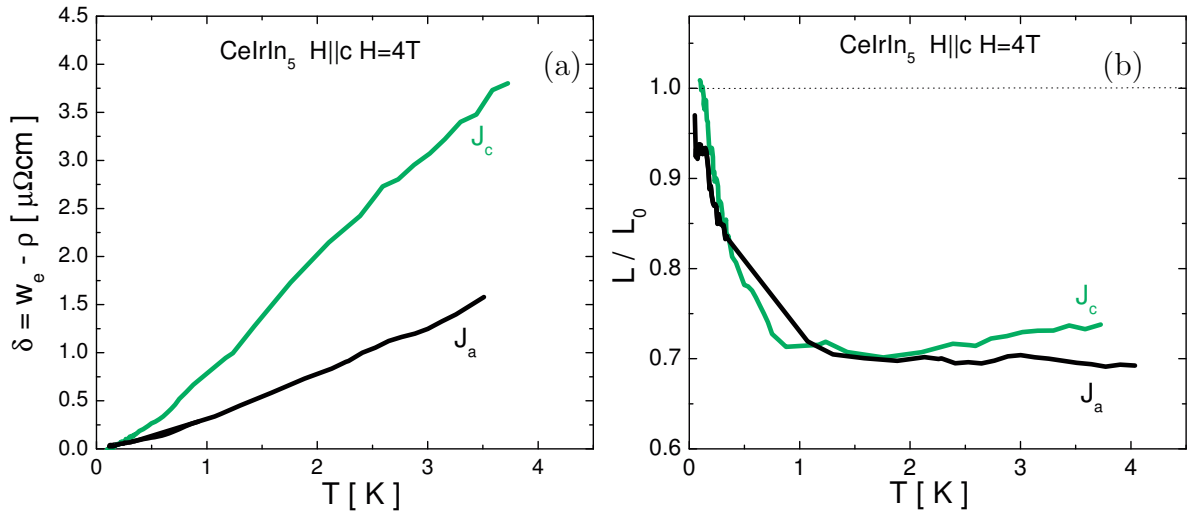
FIGURE 9.6: A comparison between in-plane and inter-plane (a) $\delta(T) \equiv w_e(T) - \rho(T)$ and (b) normalized Lorenz ratio, L/L_0, in CeIrIn$_5$.

The excellent fit to a pure $T^{4/3}$ power law of c-axis electrical resistivity in a large temperature range at high field, indicates the system is closing to a QCP existing at higher fields. More evidence that the T^2 coefficient in the electrical resistivity, after decreasing in field and obtaining the lowest value at $H = 4$ T, obtains a larger value at $H = 11.5$ T (see inset Fig. 9.2(a), for example). Thus, it seems our results suggest the importance of the effect of FM spin fluctuations in CeIrIn$_5$ which lead to quantum phase transition, mostly in the c-axis transport.

$\delta(T) \propto T$ **and** $\frac{L(T)}{L_0} \propto constant$

Furthermore, like the a-axis transport (see 8.3.1 in previous chapter), looking at the difference between the effect of scattering on the electrical and thermal current also can help us to understand the nature of scatterings on this material. Observing a linear temperature behaviour of $\delta(T)$ (Fig. 9.6(a)) can guide us to expect the presence of FM type of spin fluctuations in this compound (see 8.3.1 in Chapter 8).

The Lorenz ratio, L/L_0, for both current directions shows an independent temperature behaviour up to 4 K (Fig. 9.6). In AFM metal CeRhIn$_5$ this quantity goes back to 1 at the characteristic spin fluctuation temperature, T_{sf} (see 8.3.1 in Chapter 8).

Kadowaki Woods Ratio, $J\|c$

shows, which is very small in weakly ferromagnetic metals.
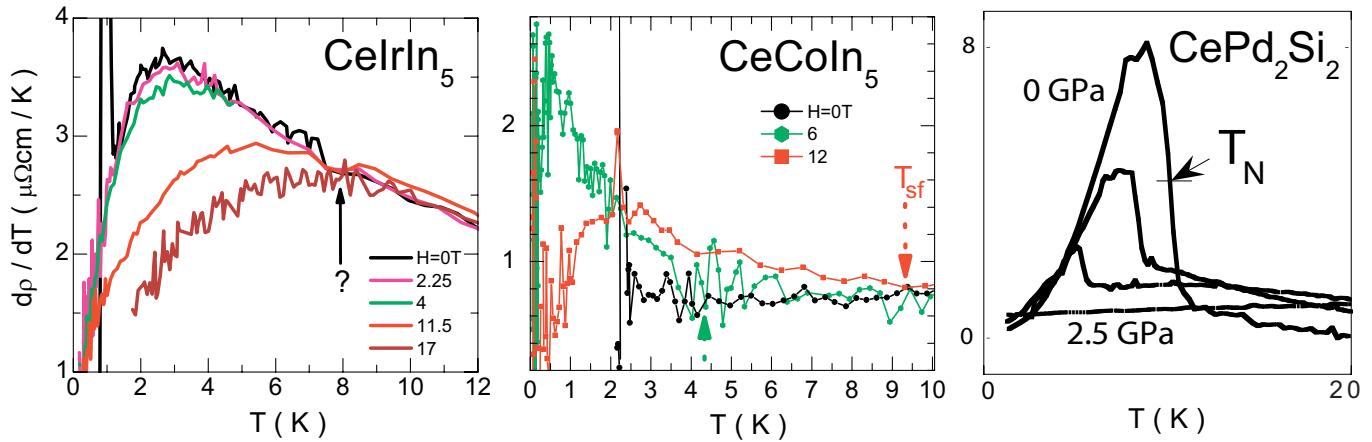
FIGURE 9.7:   Derivative of inter-plane resistivity of CeIrIn$_5$ vs T for various magnetic fields ($H\|c$, $H_{c2} \sim 2.16\ T$), compared with CeCoIn$_5$ ($J\|aH\|c$) (data taken from [162]) and CePd$_2$Si$_2$ [77]. Electrical resistivity of CeCoIn$_5$ shows a clear curvature at $T \equiv T_{sf}$ for magnetic fields H_{c2} and above it. The T_{sf} (shown as dotted arrows), the characteristic temperature of antiferromagnetic spin fluctuations, is increasing with field in this compound. There is a curvature below 8 K in CeIrIn$_5$, too (Left). By applying high fields the anomaly is disappeared. *Note to the similarity* of the derivative behaviour of the resistivity in CeIrIn$_5$ to of AFM metal CePd$_2$Si$_2$ (Right).

We obtain the value of the Kadowaki-Wood ratio for c-axis current direction nearly $0.35 a_0$ ($a_0 = 10\ \mu\Omega$ cm mol^2 K^2/ J^2) at near $H_{c2} \sim 2.5\ T$. It is interesting to note this value for c-axis transport, is comparable to the universal value for other heavy fermion systems [99, 144].

Low temperature anomaly in the electrical resistivity

Fig. 9.7 shows derivative of the electrical resistivity vs temperature in various magnetic fields. It seems there is an anomaly below $T \cong 8$ K at low fields. By applying high field 17 T the anomaly is disappeared. To have a better meaning of this anomaly, we made a comparison with CeCoIn$_5$. The electrical resistivity of CeCoIn$_5$ shows a clear curvature at $T \equiv T_{sf} \sim 5$ K at $H_{c2} \sim 5.5\ T$ [162]. The related derivative of resistivity for CeCoIn$_5$ compound is shown in Fig. 9.7; the derivative start to increase around $T_{sf} \sim 5$ K at $H = 6$ T. T_{sf} is a characteristic temperature of the AFM spin fluctuations, a temperature that above it the fluctuations have insufficient energy to scatter electrons [166]. It seems this characteristic temperature increases with increasing magnetic field in CeCoIn$_5$ [166].

Coming back to CeIrIn$_5$, the observed anomaly around 8 K may related to this kind

of magnetic characteristic temperature, or may related to different type of magnetic scattering, say FM spin fluctuation scattering, compared to AFM scattering found in CeCoIn$_5$ [164]. Although, the evolution of the anomaly by field in CeIrIn$_5$ looks differently in comparison with CeCoIn$_5$'s. Thus, the latter reason looks more reasonable.

$H - T$ phase diagram ($J \| c$)

Fig. 9.8 shows $T - H$ phase diagram of pure CeIrIn$_5$ compound for $J \| c$ and $H \| c$ current and magnetic field configuration. We see a Fermi liquid regime at H_{c2} at low temperatures. However, the FL temperature shows a different behaviour in applied field compared to other heavy fermion compound; with increasing field above $H \sim 4$ T we see the FL region is decreasing. At high magnetic field the power law electrical resistivity shows a pure $T^{4/3}$ till to nearly 8 K at $H = 17$ T. In the theoretical treatment this power law indicates the presence of 2D FM spin fluctuations that scatter conduction electrons.

For the first time this unusual behaviour (decreasing of T_{FL} with field) has been reported in the *a*-axis electrical resistivity and specific heat measurements by Capan et al. [38]. Actually they observed this unusual behaviour at applied magnetic fields *above* 12 T in the electrical resistivity measurements and *no information* below this value of magnetic field in this measurement. They als observed a logarithmic divergence behaviuor of C/T at low temperatures in magnetic fields above 12 T much larger than $H_{c2}(0)$ [38], suggesting that there might be a field induced quantum-critical point near $H = 25$ T, which is where a metamagnetic transition [108] in CeIrIn$_5$ also extrapolates to $T = 0$ [38]; see Fig. 9.9.

9.2 $\rho \propto T^{4/3}$ in systems with co-linear magnetic structure

By a comparison between CeIrIn$_5$ compound and other heavy fermions, we found that the electrical resistivity of a few systems shows the strange power law temperature dependence $\rho \propto T^{1.3} \sim T^{4/3}$ in the proximity of their quantum critical point. There is no real interpretation for this power law behaviour so far. The more interesting point is that all these compounds seem to have a co-linear magnetic structure.
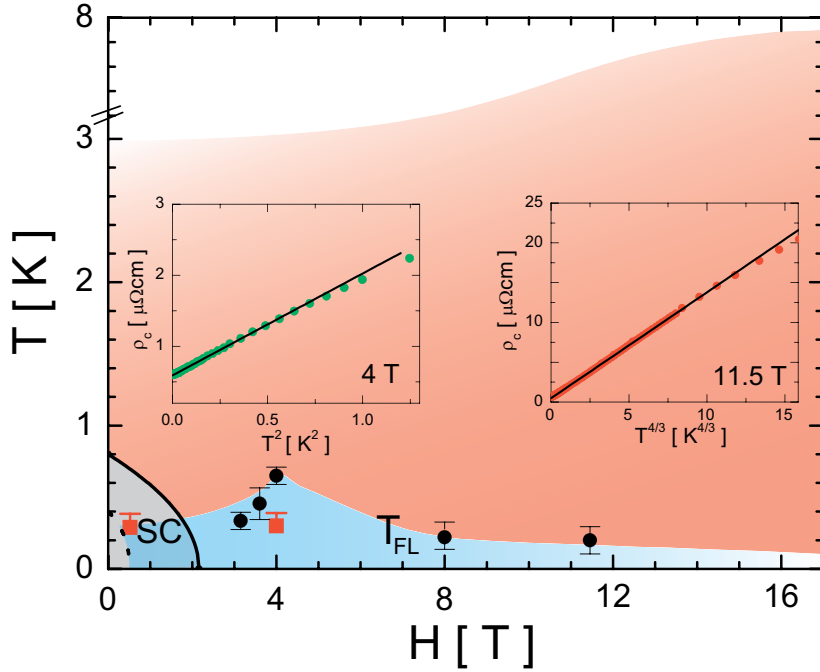
FIGURE 9.8: The phase diagram of $CeIrIn_5$ for $J\|c\ H\|c$ current and field configuration, obtained by electrical resistivity and thermal conductivity measurements. Insets show the electrical resistivities at a low magnetic field ($H = 4$ T), where there is a FL regime at low temperature and at a high field ($H = 11.5$ T), where there is approximately a pure power law resistivity $\rho_c \propto T^{4/3}$ in a large temperature range, till to nearly 7 K. This power law may define the presence of ferromagnetic spin fluctuations in $CeIrIn_5$ which leads to non-Fermi liquid behaviour in the normal state of this compound. Solid circles and squares obtained by charge and heat transport measurements, respectively.

9.2.1 $CePd_2Si_2$ and $CeNi_2Ge_2$

Two heavy fermions $CePd_2Si_2$ and $CeNi_2Ge_2$ are electronically and structurally equivalent compound. At ambient pressure, $CePd_2Si_2$ is an antiferromagnet with a $T_N \sim 10$ K. The magnetic structure can be pictured as ferromagnetic (110) planes with spins normal to the planes and alternating in directions along the spin axis [75, 139]. $CePd_2Si_2$ shows superconductivity below 430 mK in a limited pressure region on either side of p_c=2.8 GPa [75, 139]. The electrical resistivity is characterized by a power-law with exponent n nearly $1.2 \sim 1.3$ at the critical pressure (see Fig. 9.10) [52, 75, 77].

  $CeNi_2Ge_2$, the isoelectronic relative to $CePd_2Si_2$, with no magnetic order at low pressures, has a slightly smaller lattice constant and its zero pressure behaviour is expected to be similar to that of $CePd_2Si_2$ just behind critical pressure [75]. $CeNi_2Ge_2$ is a SC
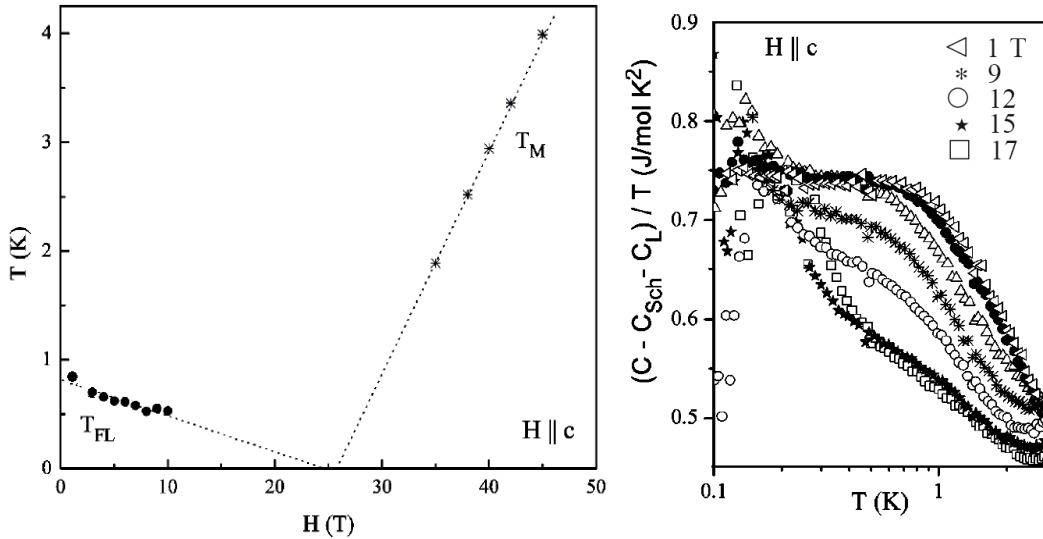
FIGURE 9.9: (*Left*) The $H - T$ phase diagram of CeIrIn₅ obtained from specific heat measurement. Fermi-liquid temperatures T_{FL} derived from the electronic specific heat. T_M is the metamagnetic transition temperature taken from [108]. (*Right*) Electronic specific heat, obtained by subtracting the Schottky and lattice contributions from the total specific heat, as a function of temperature at various magnetic fields up to 17 T. Fig adapted from [38].

at ambient pressure with T_c nearly 0.2 K. The resistivity shows the same temperature dependence as for CePd₂Si₂ [75, 111, 62]. The observed exponent in both CePd₂Si₂ and CeNi₂Ge₂ is nearly constant over almost two orders of magnitude in temperature. For the origin of this exponent a frustrated spin coupling along the *c*-axis and hence a strongly anisotropic spin fluctuation spectrum that may be more nearly 2D than 3D was suggested [75]. However, recent dHvA measurements on CePd₂Si₂ have shown that the Fermi surface does not present a low-dimensional character and then the magnetic correlations have mainly a 3D character [194].

It should be noted that two SC domes have been reported in CeNi₂Ge₂ from resistivity measurements under pressure [75, 37]. A maximum T_c in the second SC dome at high pressures is nearly 0.4 K, the same T_c as in Ir115 compound. Moreover, recent neutron scattering measurements on this compound show the presence of two low energy spin fluctuations with an energy scale of 0.6 meV around the antiferromagnetic wave vectors (1/2,1/2,0) and (0,0,3/4) that coexist with high-energy spin fluctuations with an energy scale 4 meV and a vector (0.23,0.23,1/2) [98]. It is interesting to note it seems there are two superconducting domes in CePd₂Si₂, too [75].
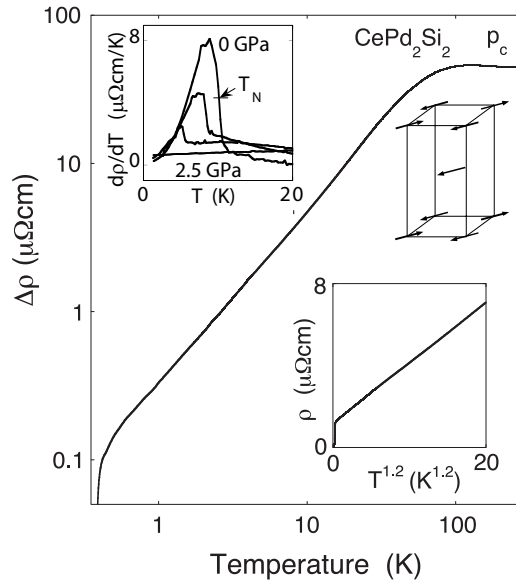
FIGURE 9.10: Temperature dependence of resistivity in CePd$_2$Si$_2$ near the critical pressure $p_c \cong 2.8$GPa, where $T_N \rightarrow 0$K. Inset-bottom: resistivity plotted against $T^{1.2}$. Inset-top: derivative of electrical resistivity in various pressures [77].

9.2.2 UPt$_3$

The electrical resistivity of heavy fermion UPt$_3$ with a $T_N \sim 6$ K and superconducting transition $T_c \sim 0.5$ K, shows also a $\rho \propto T^{1.2}$ in high magnetic field. This compound shows FL behaviour in the normal state, below 3 K. In high magnetic fields ($H\|a$), the specific heat, electrical resistivity and susceptibility all show NFL behaviour nearly at metamagnetic transition $B_{metamag} \sim 20$ T; $C/T \propto -logT$ over more than a decade in temperature, $\rho = \rho_0 + AT^{1.2}$ (0.5K $\leq T \leq 3$ K) and $\chi = \chi_0 - aT$ (0.5K $\leq T \leq 20$K) [109]. The resistivity increases nearly 10-fold at the critical regime between 0.5 and 3 K. The data in all theses measurements at magnetic fields below and above metamagnetic field indicate the presence of FL behaviour at low temperatures for $B \neq B_{metamag}$. Note the power law in the resistivity decrease from 2 to 1.2 by increasing field till to $B_{metamag}$ and then grows at higher fields [109]. The T_{FL} also decreases by increasing field to $B_{metamag}$, as the same behaviour we observed in the c-axis Ir115, and then increases.

9.3 Evolution of magnetism and its interplay with superconductivity

CeIr(In$_{1-x}$Cd$_x$)$_5$ compound show a *competition* between superconducting state and long range AFM state, while in CeCoIn$_5$ both these states *coexist* with each other [175] (see Fig. 3.12 in Chapter 3). It seems in CeIr(In$_{1-x}$Cd$_x$)$_5$ compound superconductivity suppressed to zero at the *same* Cd content where the antiferromagnetism emerges ($x_{c,AF} = x_{c,SC} \approx 0.05$).

Exactly the same competition between superconductivity and antiferromagnetism states has been reported in UPt$_3$ doped with small amount of Pd. Neutron diffraction and transverse-field muon spin relaxation measurements carried out U(Pt$_{1-x}$Pd$_x$)$_3$ show that the critical Pd concentration for the emergence of the large-moment antiferromagnetic phase is $x \approx 0.006$. At the same Pd content, superconductivity also is completely suppressed ($x_{c,AF} = x_{c,SC} \approx 0.006$) (see Fig. 9.11). It was suggested the existence of a magnetic quantum critical point, which coincides with the critical point for superconductivity, provides evidence for ferromagnetic spin-fluctuation mediated superconductivity, which competes with antiferromagnetic order [51,50] [2]. Interestingly enough that the existence of QCP at $x_{c,AF} \approx 0.006$ is supported by a decrease of the Fermi-liquid exponent of the resistivity (n=2) to a value n=1.55 [70], *i.e.* close to the value n=1.5 predicted for 3D antiferromagnetic critical fluctuations. [3]

All of these evidences, together with a hybrid gap symmetry at low temperature for CeIrIn$_5$, support the presence of ferromagnetic spin fluctuations in CeIrIn$_5$. It seems two sorts of spin fluctuations, AFM and FM types are in competition with each other in pure CeIrIn$_5$ compound, so that at high magnetic fields the FM ones may dominate and leads to a quantum phase transition, which appeared via the electrical resistivity power law

---

[2]In neutron diffraction measurements on U(Pt$_{1-x}$Pd$_x$)$_3$, two antiferromagnetic order were found [50]. One is the small moment antiferromagnetic order (SMAF) with $T_N \sim 6$ K reported for pure UPt$_3$ and in doped compound till at least x=0.005. The small related ordered moment grows from 0.018 μ_B/U-atom for x=0 to 0.048μ_B/U-atom for x=0.005. T_N of the SMAF phase does not vary with alloying. Note no signal of the SMAF phase was detected in zero-field μSR (and NMR measurements) so far [50, 107]. A second large-moment antiferromagnetic phase (LMAF) sets in at x=0.006 with a maximum $T_{N,LMAF} \sim 6$K for optimal doping (x=0.05) with moment 0.62μ_B/U-atom. LMAF emerges between x=0.005 and 0.01 [50].

[3]It has been suggested that no finding of the antiferromagnetic quantum critical point in pure UPt$_3$ but upon doping, may help to understand of how an odd parity superconducting state can arise, while the dominant fluctuations seem to be of antiferromagnetic nature. Thus, it was proposed that Pd doping leads to a shift of the spectral weight from "ferromagnetic" to "antiferromagnetic" fluctuations [50].
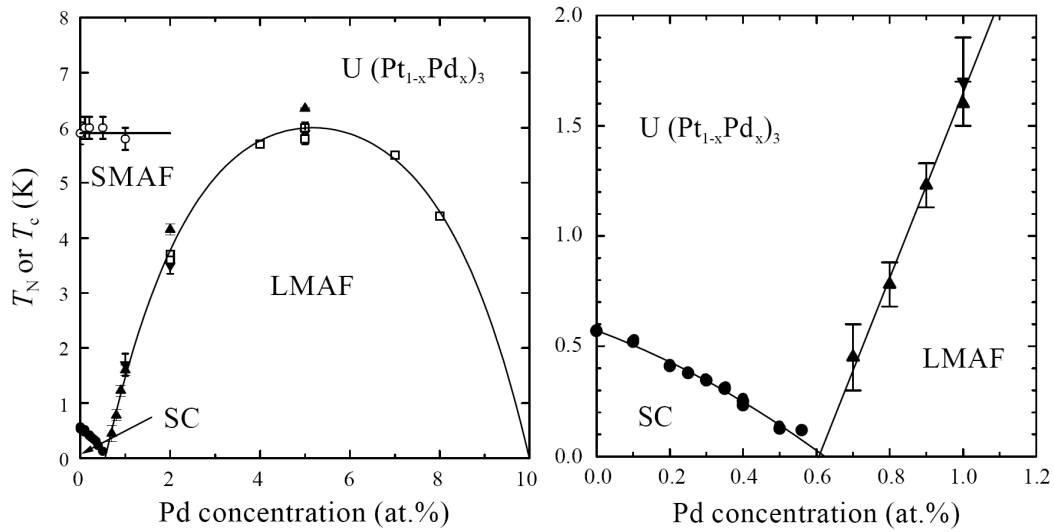
FIGURE 9.11: Magnetic and superconducting phase diagram for U(Pt$_{1-x}$Pd$_x$)$_3$ alloys. SMAF=small-moment antiferromagnetic phase, LMAF=large-moment antiferromagnetic phase, SC=superconducting phase. (*Right*) The same phase diagram with $x <0.012$ (from [50]). Note to the similarity of this figure to Fig. 3.12 for CeIr(In$_{1-x}$Cd$_x$)$_5$.

4/3, decreasing of T_{FL} by increasing field and diverging of C/T at low temepratures.

9.4   Conclusion

From the inter-plane charge and heat transport measurements in the normal state on CeIrIn$_5$ we have found:

- A pure $T^{1.33} \equiv T^{4/3}$ power law in a wide temperature range at high magnetic fields in c-axis transport. The power law $\rho_c \propto T^{4/3}$ can be interpreted in 2D FM spin fluctuations model.

- A linear temperature dependence for the difference between thermal and electrical resistivities, $\delta(T) \equiv L_0 T/\kappa_e - \rho$, up to $T = 4$ K. This linear behaviour seems to be consistent with the FM spin fluctuations models.

- Lorenz ratio, L/L_0, shows a temperature independent behaviour up to $T = 4$ K at applied field $H_{c2} \sim 4\,T$, in contrast to AFM metal CeRhIn$_5$ that this quantity goes back to 1 at $T = T_{sf}$.

- An interesting similarity between the results of Cd doped CeIrIn$_5$ and Pd doped UPt$_3$ compounds; in both compounds superconductivity is in competition with long range antiferromagnetism [50,175]. This beautiful competition lead to suggest a ferromagnetic spin-fluctuation mediated superconductivity, which competes with antiferromagnetic order, in UPt$_3$ compound [50]. Ferromagnetic spin fluctuations have not, to our knowledge, been predicted or observed in any compound in 115 family.

These evidences suggest the presence of *different type of spin fluctuation* in CeIrIn$_5$ compound, in addition to the well-known AFM spin fluctuations in the 115 family. We believe these evidences together with a diverging electronic specific heat at low temperatures at high field provides compelling evidence for the existence of QCP. It seems the type of spin fluctuations and their dimensionality have strong effects on physical behaviour of CeIrIn$_5$ and CeCoIn$_5$, so that lead to different transport behaviours in these two closely related compounds.

Chapter 10

Conclusions

In this thesis we have studied the normal and superconducting state of unconventional superconductor CeIrIn$_5$ by heat and charge transport measurements. The main goal was to identify the order parameter in this heavy fermion compound, which will be the first step to explore the microscopic mechanism of superconductivity in this system and closely related systems. This is the *first* systematic study of thermal conductivity and electrical resistivity of highly pure and doped single crystals of CeIrIn$_5$ in two axial crystal directions, $J\|a$ and $J\|c$ (heat current in the ab plane and along c-axis) in zero and applied magnetic field.

While most experimental and theoretical research has reported d-wave gap symmetry for CeMIn$_5$ family, based on our thermal conductivity data we suggest a hybrid gap symmetry, E_g, for CeIrIn$_5$. This model describes very well the residual linear term of thermal conductivity in both heat current directions, the thermal conductivity anisotropy, and the behaviour of impurity and magnetic field effects on heat transport. The results can be summarized as follows.

First, the in-plane thermal conductivity κ_a of CeIrIn$_5$, measured down to $T_c/8$, reveals a sizeable residual linear term κ_0/T, which establishes the presence of nodes in the superconducting gap. For $J \parallel c$, on the other hand, $\kappa/T \to 0$ as $T \to 0$. This profound anisotropy in the limit $T \to 0$, shows that the low-energy nodal quasiparticles carry heat very well in the basal plane but very poorly, if at all, along the c-axis. This rules out the possibility that this line-node is vertical (running along the c-axis). This eliminates all but one of the allowed spin-singlet pairing states in the tetragonal structure with D$_{4h}$ point group symmetry, including the d-wave states proposed for the closely related compound CeCoIn$_5$. The sole candidate left is the $z(x + iy)$ state of E_g symmetry. This

result points to a fundamentally different type of superconductivity in CeIrIn$_5$ at low temperatures.

However μSR measurements on pure and 0.3%La-doped crystals showed no enhancement of the spin relaxation rate in the spectra below T_c. This meant the absence of a spontaneous magnetic field or the time-reversal symmetry-breaking expected for this hybrid gap symmetry in the superconducting state. A comparison with Pd doped UPt$_3$ (U(Pt$_{1-x}$Pd$_x$)$_3$), where small moment antiferromagnetism coexisting with superconductivity at low x has been detected by neutron scattering measurements, but never observed in μSR and NMR measurements, suggests one possible explanation for this negative result in Ir-115.

Second, nonmagnetic impurities strongly affect the superconducting state of CeIrIn$_5$. The first observation of universal thermal conductivity in a heavy fermion compound have been performed via a doping study. Thermal conductivity along the conducting plane shows universal response to doping, as expected for superconductors with line-nodes in the superconducting gap. In stark contrast, the inter-plane heat transport rapidly increases with doping in the $T \rightarrow 0$ limit. These observations are compatible with hybrid E_g gap symmetry.

Furthermore, we made a comparison between CeIrIn$_5$ and the well known heavy fermion superconductor UPt$_3$. An amazing similarity between c-axis CeIrIn$_5$ and b-axis UPt$_3$ data (allowing for the absence of universality in UPt$_3$) all leave no doubt about the absence of line nodes in the gap structure of UPt$_3$ compound.

Third, measurements of the temperature and magnetic field phase diagram of the inter-plane thermal conductivity in the mixed state in CeIrIn$_5$ show multi-phase superconductivity. We observed a strange anomaly at low temperature in the thermal conductivity. This anomaly is obvious in highly pure samples and for fields applied in the ab plane. This anomaly delineates a new region in the $H - T$ phase diagram. This might be a sign of a two-component order parameter in this material, consistent with the two previous observations.

We also found that the inter-plane thermal conductivity data does not scale as $T/\sqrt{H}$. This confirms the presence of a linearly-dispersing point node in the gap, consistent with hybrid E_g gap symmetry.

Fourth, the inter-plane electrical resistivity shows a power law temperature dependence $\rho(T) \propto T^{4/3}$ in a large temperature range at high fields. In addition to the exponent 4/3, which is consistent with 2D FM spin-fluctuation theory, a comparison be-

tween electrical and thermal resistivities has revealed a linear temperature dependence of $\delta(T) \equiv w_e(T) - \rho(T)$. The linear behaviour of this physical quantity, predicted and observed in ferromagnetic systems, confirms the presence of a ferromagnetic spin fluctuations in CeIrIn$_5$. The *competition* between superconductivity and long range antiferromagnetism observed in the Cd-doped CeIrIn$_5$ compound confirms this suggestion and supports the proposal of *superconductivity mediated by ferromagnetic spin fluctuations in Ir115*. We believe the $T^{4/3}$ power law resistivity together with a diverging electronic specific heat C/T at low temperatures at high field provide compelling evidence for the existence of a ferromagnetic quantum phase transition in CeIrIn$_5$.

In summary, having extremely clean and stoichiometric single crystals in this study has enabled the observation of new physics in the 115 materials. This work has stimulated theoretical and experimental interest which have confirmed our conclusions. We hope this low temperature work will help us to understand one of the main questions in the wide world of superconductivity: what causes room temperature superconductivity?

A few future views:

- It has been predicted theoretically that for the two component superconductivity in the tetragonal structure, the phase transition into the superconducting state must be split into two phase transitions by an application of uniaxial stress in $a-$ or $b-$ direction [141], while uniaxial stress in $c-$ direction does not change the tetragonal symmetry [141].

  Moreover, it has been quite recently predicted that a multiband-multicomponent tetragonal superconductor can show in-plane upper critical field anisotropy [141]. To explore experimentally those predictions would be interesting.

- There are no measurements on Ce$_{1-x}$La$_x$IrIn$_5$ alloys. What is the role of La impurity in this compound? What effect do La ions have on FM and AFM spin fluctuations? What is the ground state of the compound at high-La doped percentage, compare with AFM ground state in CeIr(Cd$_x$In$_{1-x}$)$_5$ alloys? What is the critical amount of La to kill superconductivity? Is the critical amount of doping for killing superconductivity the same in resistivity and bulk measurements?

- The hybrid gap symmetry breaks time reversal symmetry. In other words, there should be an internal magnetic moment. μSR could not detect it. Inelastic neutron

scattering may help in this regard.

- Heavy fermion UPt$_3$ shows a metamagnetic transition and NFL behaviour at high fields, around 20T; resistivity shows a power law $\sim T^{1.2}$ at this magnetic field. It has been suggested that the superconductivity is mediated by FM spin fluctuation in this compound. Comparing charge and heat transport of this material in field, to explore the temperature behaviour of $\delta(T)$, may help to understand the meaning of the $n = 1.2$ power law that has been seen in a few quantum critical systems.

- CeRhIn$_5$ shows superconductivity under pressure, with the same power law resistivity behaviour and T_c (at the critical pressure, 21 Kbar) as of Co-115. Moreover, the dHvA measurements under pressure show a divergence of the effective mass and change of the Fermi surface at nearly the same critical pressure. It would be interesting to explore the $T - H$ phase diagram and any quantum criticality in this compound at the critical pressure, to compare it with of Co-115 at ambient pressure.

Appendix A

Investigation of Broken Time Reversal Symmetry in CeIrIn$_5$ by μSR

Besides of the thermal conductivity measurement which was the main measurement in this study, this Appendix presents our Zero Field muon spin relaxation (ZF-μSR) study on pure and La-doped CeIrIn$_5$ materials. The aim is to search for spontaneous currents in the superconducting state in this compound according to the predicted hybrid E_g gap symmetry, as a gap symmetry in this material.

A.1 Introduction

Hybrid E_g structure, with the basic function $(x + iy)z$ breaks time-reversal symmetry and therefore spontaneously generates an internal magnetic moment around impurities. Zero field μSR is one of the most sensitive techniques for detecting any weak static and dynamic local magnetism. Time reversal-broken superconducting states are quite rare, since unambiguous observation of such fields has been reported only in spin-triplet superconductor Sr$_2$RuO$_4$ [123] (see Fig. A.1) and recently in PrOs$_4$Sb$_{12}$ [15]. Previous zero field μSR measurements on CeIrIn$_5$ have failed to detect such moments [84]. One possible explanation is that the associated fields are too small in these high purity samples, as also found in high quality crystals of UPt$_3$ [49]. Another possibility for the absence of a signal of moment in ZF-μSR in pure and Pd-doped (at low doping) UPt$_3$ compound was
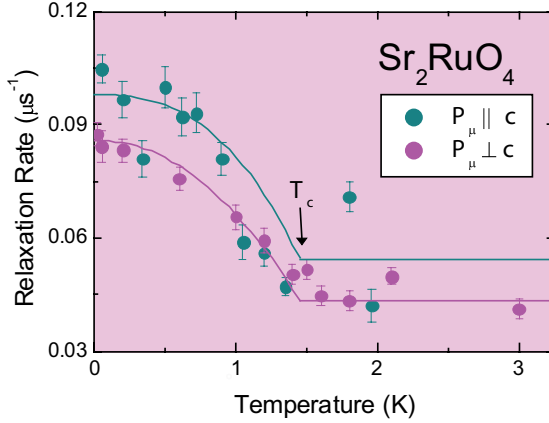
FIGURE A.1: Zero-field relaxation rate in Sr$_2$RuO$_4$ with the initial muon spin polarization perpendicular and parallel to the *c*-axis of the crystal [123].

attributed to a moment fluctuating at a rate > 10MHz [50, 107].

Introducing non magnetic impurity to the system locally perturb the superconducting order parameter, and thus create local currents due to a gradient in the phase, thus allows the chance to detect the local magnetism. We tested the former hypothesis by studying ZF-μSR of two orientations of CeIrIn$_5$ (*ab*-plane and *ac*-plane) with 0.3% non-magnetic La substituted for Ce. We also measured a pure sample as a reference.

A.2   A brief introduction to μSR

μSR spectroscopy uses implanted muons[1] to probe the structure and dynamics of matter at the microscopic level. Their spin (magnetic moment) is used as a magnetic probe. The experiments must be performed at accelerator laboratories where suitable muon beams are available. The beam is stopped in the material of interest.

Muons, like electrons, are elementary particles which do not feel the strong interaction. Both charge states exist (particle and antiparticle). So negative muons are like heavy electrons, positive muons like heavy positrons. Muons are produced when a target of graphite or other light element is exposed to a sufficiently high-energy proton beam; proton-nucleon interactions generate pions in the first step and these particles then decay quickly to muons; see Fig. A.2. Muons are injected into materials one at a time. After quickly coming to rest (at a typical depth of ~ 0.1 mm), the muon spins evolve in the

---

[1]The muons properties: spin 1/2, mass $m_\mu \cong 0.113 m_p \cong 207 m_e$, magnetic moment $\mu_\mu \cong 3.18 \mu_p$.
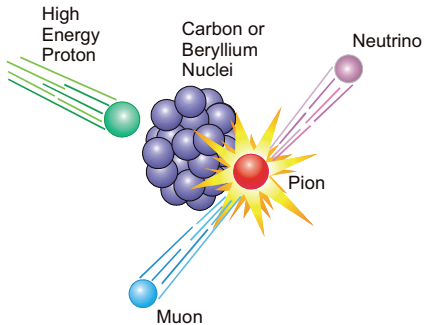
FIGURE A.2: A schematic of producing muon beams, using high-energy protons to produce short-lived muons.

local magnetic environment. The muon subsequently decays (lifetime of about $2.2\mu s$), emitting a positron preferentially in the direction of the muon spin at the time of decay. By monitoring the polarization of the muon as a function of time, the information of the local spin environment at each muon site can be provided [123].

In a μSR experiment, positive muons start off 100% spin polarized and are implanted in the sample one at a time. In the absence of magnetic order, the spin polarization is relaxed by randomly-orientated static nuclear dipole moments and is well-described by the Gaussian Kubo-Toyabe function:

$$P_\mu(t) = \frac{1}{3} + \frac{2}{3}(1 - t^2\Delta^2)e^{-\frac{1}{2}\Delta^2 t^2} \quad , \tag{A.1}$$

where Δ/γ_μ is the width of the local field distribution and γ_μ is the muon gyromagnetic ratio. In the magnetically ordered state, the μSR spectrum will exhibit precession (where the frequency is proportional to the ordered moment) if the internal field is sufficiently uniform. If the spontaneous field is weak, or there is a broad distribution of local fields then one observes an increase in the relaxation of $P_\mu(t)$, where the increase in relaxation corresponds to an order parameter [123].

A.3 Experiments

A.3.1 Samples

Three different batches of the same 0.3%La-doped level and one pure CeIrIn$_5$ batch were cut by Makariy Tanatar and I. Single crystals were cut into two types of slabs, *ab* and *ac*
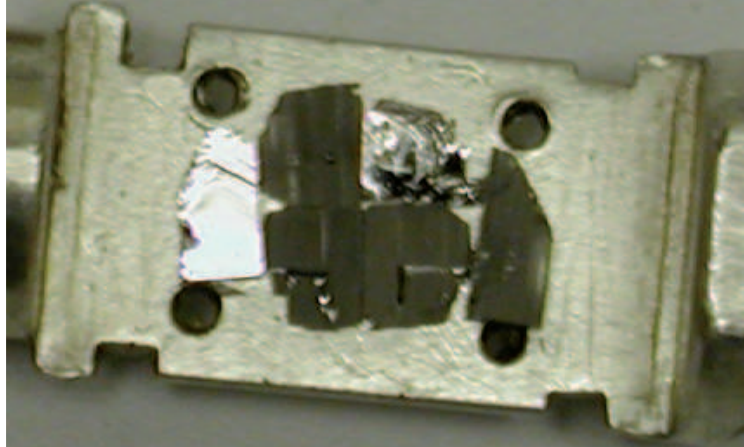
FIGURE A.3: Sample mount for zero field μSR measurements. The probe inserted such that the initial muon spin polarization is $\perp$ to the face of the crystals.

plane, with an average thickness of 0.5 mm and a mosaic surface nearly 1 cm^2.

A.3.2 μSR: experimental details

Measurements were performed in the Meson Laboratory on the M15 beamline of TRI-UMF, located in Vancouver, Canada. The spin-polarized positive muons with a momentum of 29.8 MeV/c were implanted one at a time into the single crystals. The initial muon spin polarization was parallel and perpendicular to the c-axis for ab and ac plane samples, respectively. Samples were aligned and glued onto a silver holder (silver gives a temperature-independent and essentially non-relaxing μSR signal in zero field measurements). A dilution refrigerator was used to cool the samples down to 11 mK.

A.3.3   Results

Fig. A.4 shows the time evolution of the muon spin polarization in doped and pure CeIrIn$_5$ crystals at different temperatures, T=35, 100, 150, 200, 300, 500, 750, 900mK and 1K. We have observed nearly no change in the time spectra with decreasing temperature down to 35 mK, which is also indicated by Fig. A.5 where the relaxation rate is nearly independent of temperature for either orientation of the La-doped and pure CeIrIn$_5$. So it looks there is no evidence of time-reversal symmetry breaking or any spontaneous magnetic field in the superconducting phase, or at least can not be detected by μSR. Using previous experiences on UPt$_3$ [50, 107], which the small moments have been detected in neutron
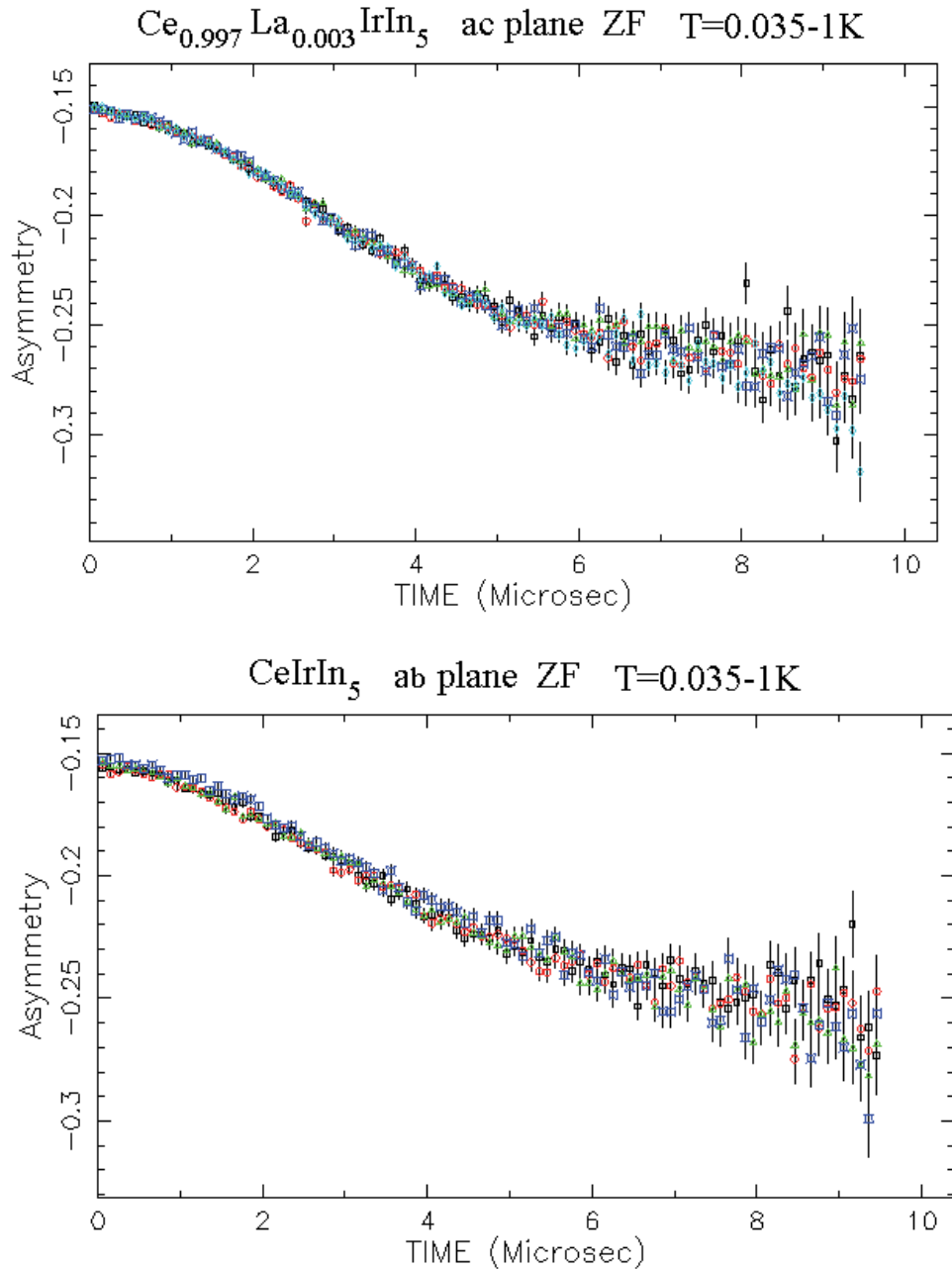
FIGURE A.4: Asymmetry in Ce$_{0.997}$La$_{0.003}$IrIn$_5$ *ac*-plane and pure CeIrIn$_5$ *ab*-plane samples at $T = 35$mK, 100mK, 150mK, 200mK, 300mK,... to 1K (below and above T_c). Preliminary analysis of ZF μSR spectra. All curves have fall on top of each other. The same result was observed for *ab*-plane doped crystals.

scattering measurements and not at all in the μSR, neutron scattering measurements on Ir115 crystals is suggested.
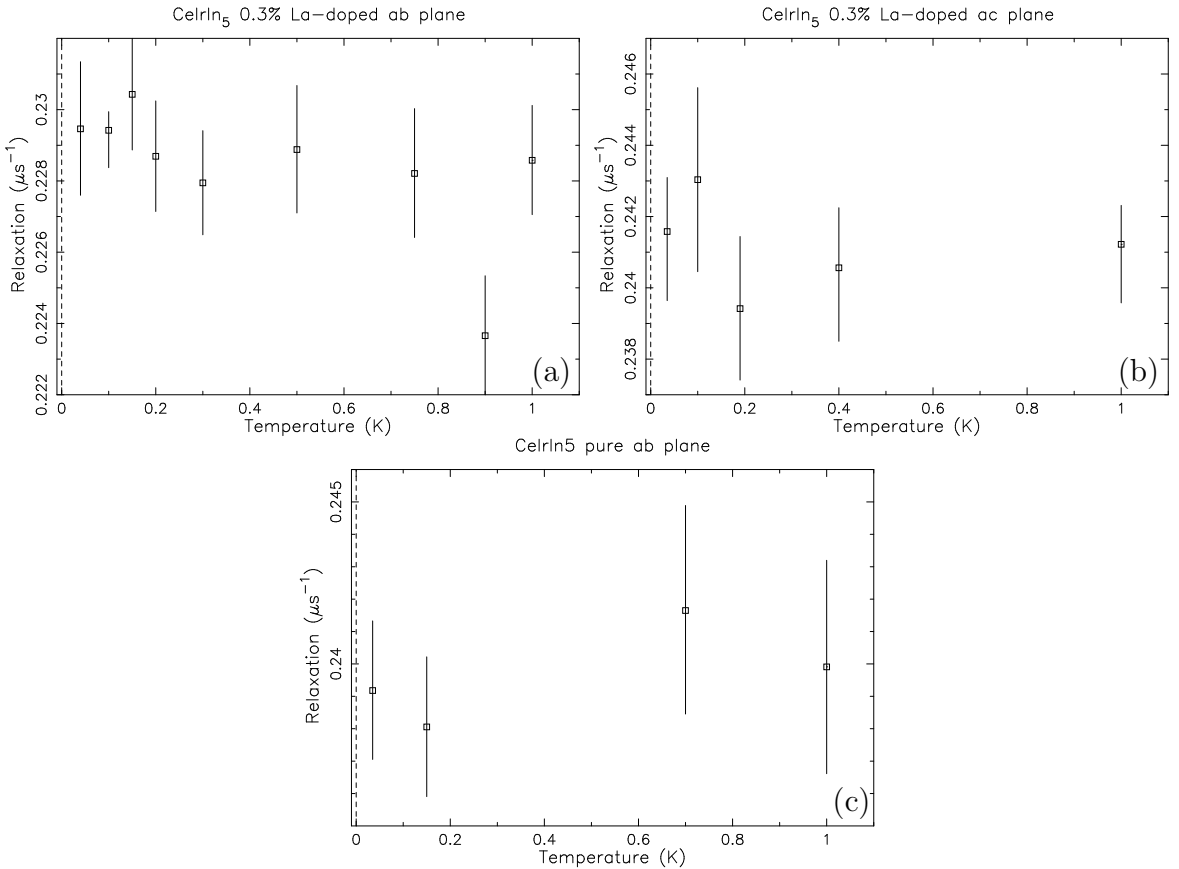
FIGURE A.5: Preliminary analysis of zero field muon spin relaxation rate vs temperature measured in (a) *ab*-plane doped, (b) *ac*-plane doped and in (c) *ab*-plane pure CeIrIn$_5$. It seems there is no enhancement of relaxation rate in the SC state (below $T_c \approx 0.4$ K).

Appendix B

CeRhIn$_5$: Inter-plane Thermal and Electrical Transport

This Appendix presents a summary of results provided by charge and heat transport measurements on $c-$axis CeRhIn$_5$. This is the first systematic study of the inter-plane thermal conductivity and resistivity of this compound.

B.1 Introduction

CeRhIn$_5$ is a well-characterized material in which spin fluctuations dominate the scattering of electrons [162, 165]. In a detailed and systematic study of heat and charge transport on $a-$axis CeRhIn$_5$, J. Paglione *et al.* have obtained the **q** and ω dependence of antiferromagnetic spin fluctuations and their effect on scattering of electrons in this AFM compound. They found that the spin fluctuations are as effective in scattering of electrons as they are in disordering moments, via observing the prefect similar behaviour of the thermal resistivity and the magnetic entropy [165]. Furthurmore, they suggested that the difference between the electronic thermal ($w_e = \frac{L_0 T}{\kappa_e}$) and electrical ($\rho$) resistivities, called $\delta(T)$, can be used as a direct probe of the characteristic energy of the spin fluctuation spectrum (called T_{sf}).

Going through CeCoIn$_5$ compound and comparing the normal state charge and heat data shows an anisotropic behaviour for spin fluctuations; while T_{sf} is nearly 5K in the in-plane transport, it goes to zero in the $c-$axis transport [166]. This looks consistent with more recently observation of an strong anisotropy violation of WF law at QCP in this compound [215].

TABLEAU B.1: Sample characteristics

sample	$\alpha \times 10^{-3}$(cm)	R(mΩ)	$\rho(\mu\Omega$cm) (room T)	T$_N$(K) (room T)
Rh115-$J\|c$ F472S-"sample B"	1.596	20.32	32.43	3.8
Rh115-$J\|c$ F708-"sample small"	1.036	31.3	32.43	3.8

Therefore to search for the dimensionality of spin fluctuations and its role on the properties of 115 family was one of the motivations for measuring $c-$axis CeRhIn$_5$. We found *the same value of T_{sf}* and *the same temperature dependence of resistivity below Neel temperature* for either orientation of CeRhIn$_5$ crystals, suggesting a *3D characteristic behaviour of the spin fluctuations* in CeRhIn$_5$.

In the following, the results are just presented as figures. First we show the inter-plane resistivity at low and high temperatures compared with the previous reported data. Then we go through the heat transport results and make a comparison with the charge transport.

Final point, the behaviour of spin fluctuations in the magnetic field is another interesting story to look in. The $H - T$ phase diagram CeRhIn$_5$ displays at least three separate phases as a function of applied field. Moreover, neutron scattering on Rh115 has shown insensitivity of the incommensurate magnetic structure and ordered moment to pressure up to the applied pressure that superconductivity appears and coexist with magnetism [121]. This insensitivity suggests the pressure does not change the nature of magnetic order gradually. Moreover, in CeCoIn$_5$ it was suggested that magnetic field has effect on the nature of magnetic order [162], by observing a field-induced change in the sign of magnetoresistance. Thus to probe effect of magnetic field on spin fluctuations may help for further understanding of this family.

B.2   Results
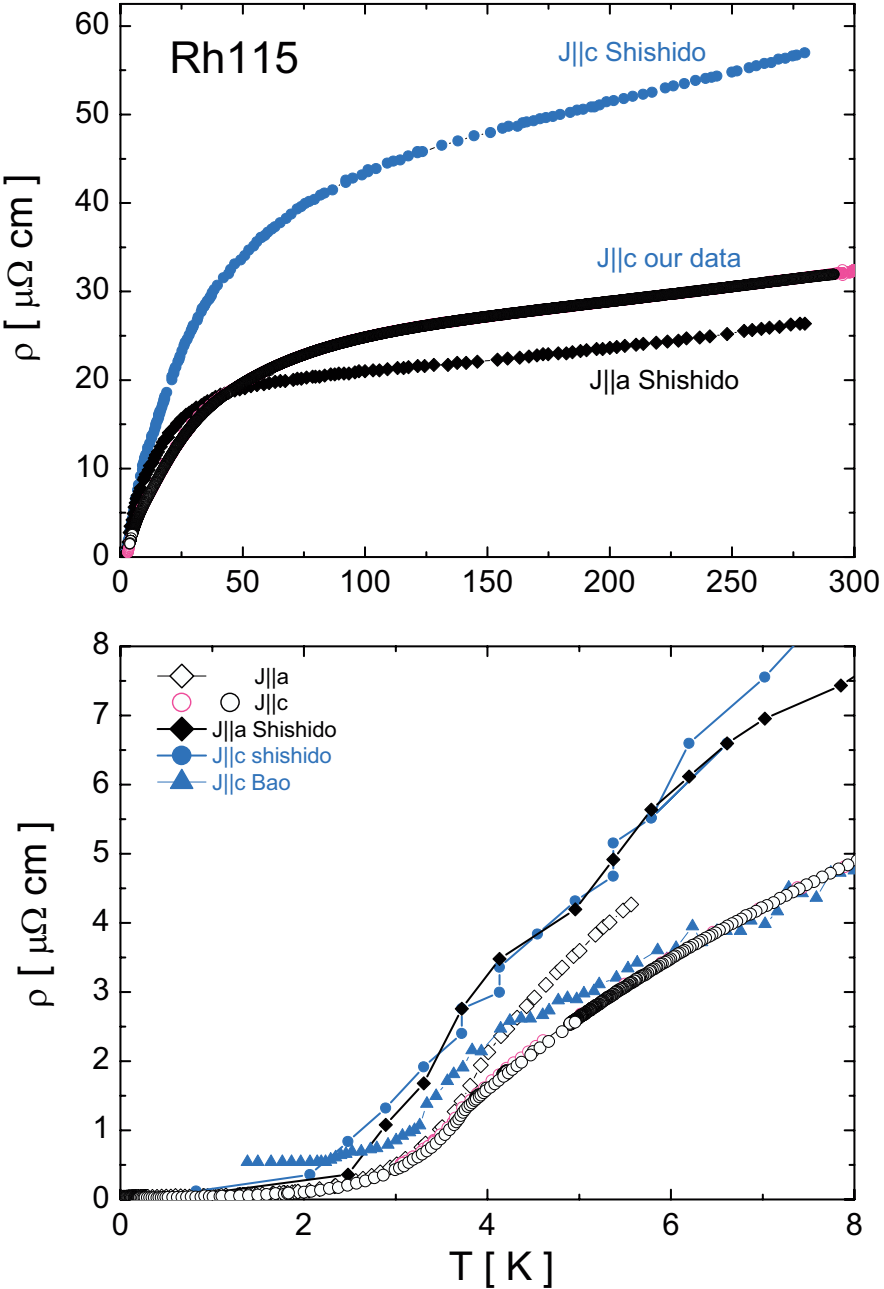
FIGURE B.1: Inter-plane resistivity of Rh115 compared with other group data at high (top) and low temperatures (bottom). Bao data [20] at low temperature seems to behave similar to ours. Note to the same Neel temperature for both current orientations in our measurements (bottom). The electron conductivity is better in the $c-$axis than $a-$axis direction, consistent with the thermal conductivity results shown later (see Fig. B.3.) (data of other group are taken from [195, 20, 44]).

$$\rho = \rho_0 + AT^2 + cT^f$$

$\rho_0 = 0.02181 \pm 0.0008$
$A = 0.01811 \pm 0.0013$
$c = 0.00038 \pm 0.00006$
$f = 5.9977 \pm 0.098$

comparison with Rh115, J||a
$\rho_0 = 0.038$
$A = 0.021$
$c = 0.00042$
$f = 6.0 \pm 0.1$
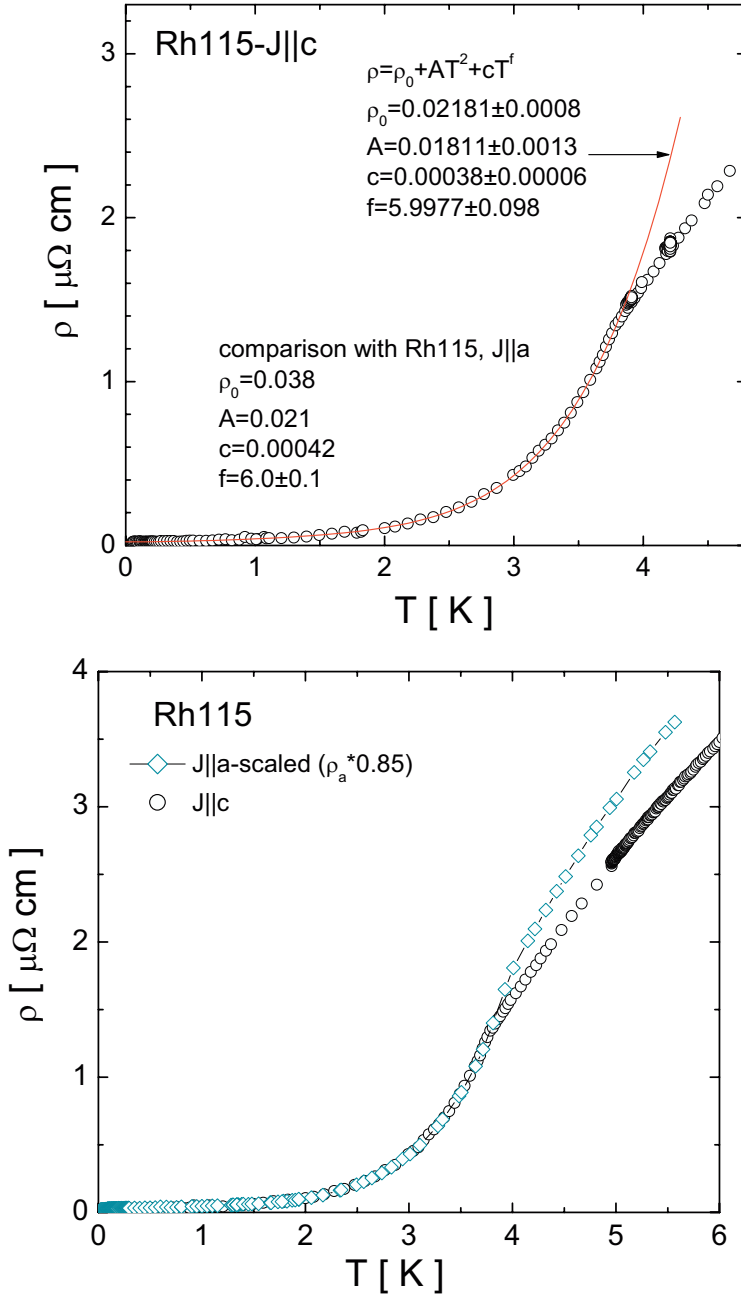
FIGURE B.2: (*Top*) Power law-fit of $c-$axis electrical resistivity of Rh115. The parameters of fitting have been compared with the ones of the $a-$axis sample. A few points we observe: 1. $\rho_0 \approx 0.02\mu\Omega$cm for $c-$axis shows the higher purity of the $c-$axis sample ($a-$axis sample shows $\rho_0 \approx 0.04\mu\Omega$cm). 2. Other obtained fitting parameters, inelastic scattering parts, look nearly the same as $a-$axis transport ones. 3. The power law behaviours, T^2 and T^6, are exactly the same as of the $a-$axis electrical resistivity. (*Bottom*) A comparison between $c-$ and scaled $a-$axis resistivities. It seems the electrical resistivity behaves nearly isotropic at least below T_N. All these suggest a more *3D magnetic correlation* in Rh115.
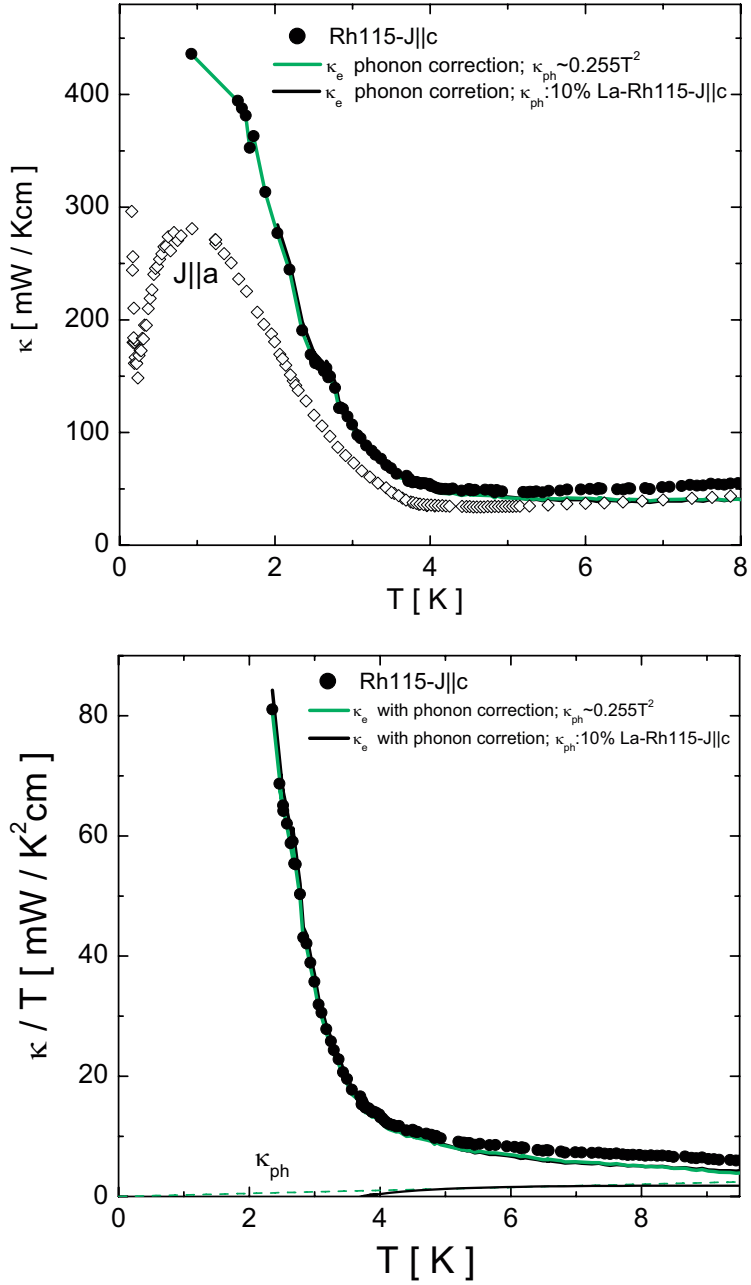
FIGURE B.3: Inter-plane thermal conductivity, κ, of Rh115 compared with the in-plane data from [165]. Solid lines show the electronic thermal conductivity, κ_e, that has been obtained in two ways: 1. assuming a phonon thermal conductivity for the $c-$axis sample, $\kappa_{ph} \sim 0.255T^2$, nearly the same as what obtained experimentally for $a-$axis sample (green line) (for a discussion on how to obtain the phonon thermal conductivity for CeCoIn$_5$ and $a-$axis CeRhIn$_5$ see [162]). 2. by measuring 10%La-doped $c-$axis Rh115 (black line). *Heat transport is higher in the c-axis* crystal direction. This is *invert* of what have been observed in two cousin compound CeCoIn$_5$ and CeIrIn$_5$.
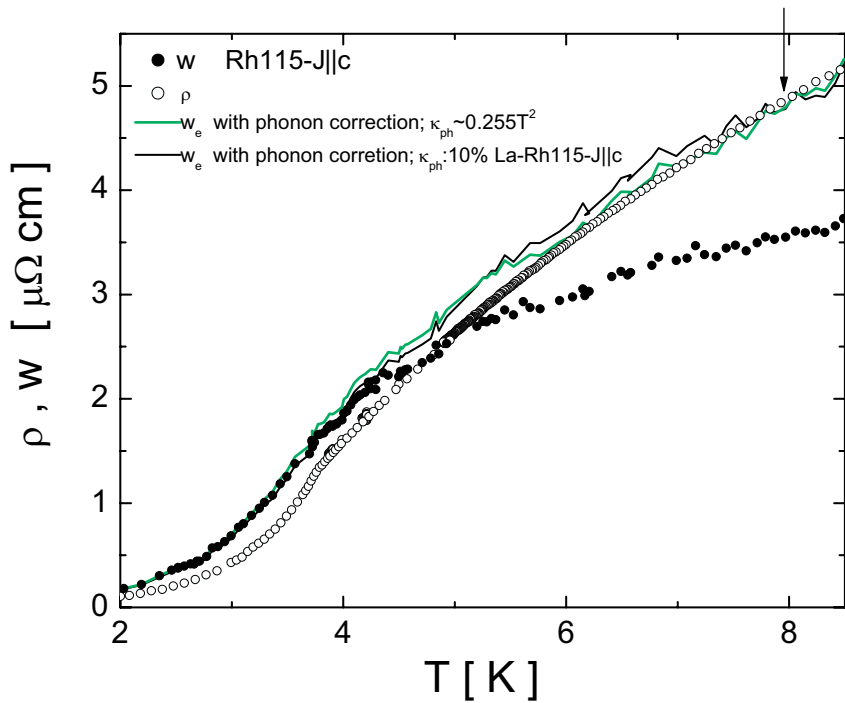
FIGURE B.4: Electrical resistivity (ρ) compared to thermal resistivity (w) in Rh115 ($J\|c$). Solid lines show the electronic thermal resistivity (w_e); see notation in Fig. B.3. The electrical resistivity and the electronic thermal resistivity meet each other around $T =$8K.
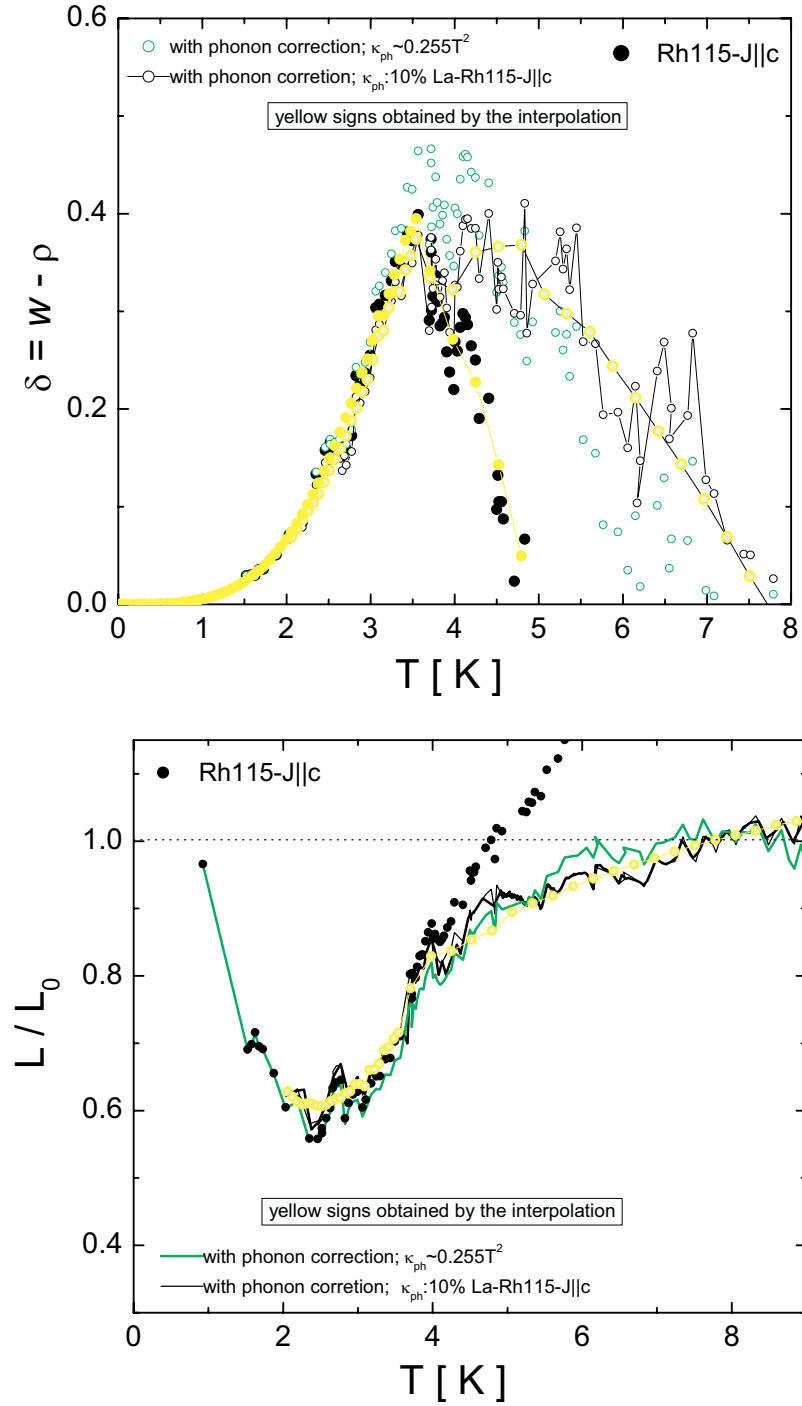
FIGURE B.5: (*Top*) The $\delta(T) \equiv w_e(T) - \rho(T)$ in the $c-$axis CeRhIn$_5$ vanishes around $T \cong 8$ K. This is exactly the temperature where the δ for $a-$axis transport vanishes; see [165]. This can be seen also in the bottom plot, where the $c-$axis normalized Lorenz ratio reaches 1 at higher temperature ($\cong 8$ K). Same notation as Fig. B.3.

Appendix C

Phonon Conductivity

In this Appendix a review on how to extract phonon conductivity, especially in high conductive 115 compound is given. For more details the reader is referred to the thesis of J. Paglione [162].

C.1 Phonon conductivity in CeIrIn$_5$

In a typical metal, heat is mainly transported by electrons and phonons. Thus the total thermal conductivity is the sum of the conductivities of these heat carriers, $\kappa = \kappa_e + \kappa_{ph}$ (see Chapter 2 in this regard). In order to estimate the phonon contribution in pure CeIrIn$_5$ sample, we measured the thermal conductivity κ of a CeIrIn$_5$ sample doped with La impurities (with x=0.2), Ce$_{1-x}$La$_x$IrIn$_5$, which is structurally-equivalent material with low electronic conductivity. This level of doping increases strongly the elastic impurity scattering so that the inelastic scattering can be ignored at low temperatures. Therefore one expects the electronic conductivity to satisfy the WF law at low temperatures. Thus, considering $\frac{\kappa_e}{T} = \frac{L_0}{\rho}$, one can estimate a phonon conductivity by $\kappa_{ph}/T = \kappa/T - L_0/\rho$.

For such a study, we measured two x=0.2 doped samples (a-axis and c-axis). The residual resistivities increased to $\rho_{0a} = 16.2$ and $\rho_{0c} = 53$ $\mu\Omega$cm. This means the elastic scattering increased by a factor of nearly 80 for either current directions (for pure CeIrIn$_5$ samples: $\rho_{0a} = 0.2$ and $\rho_{0c} = 0.6$ $\mu\Omega$cm at $H_{c2} = 0.5$ T), thus it is reasonable to assume that inelastic scattering is negligible at low temperatures.

Fig. C.1(a) shows an example of the results on c-axis Ce$_{0.8}$La$_{0.2}$IrIn$_5$, plotted as $\kappa_{ph}/T = \kappa/T - L_0/T$ vs T. The result is shown in zero and a high field. The negligible field dependence of the results supports the truly phononic approach, which magnetic
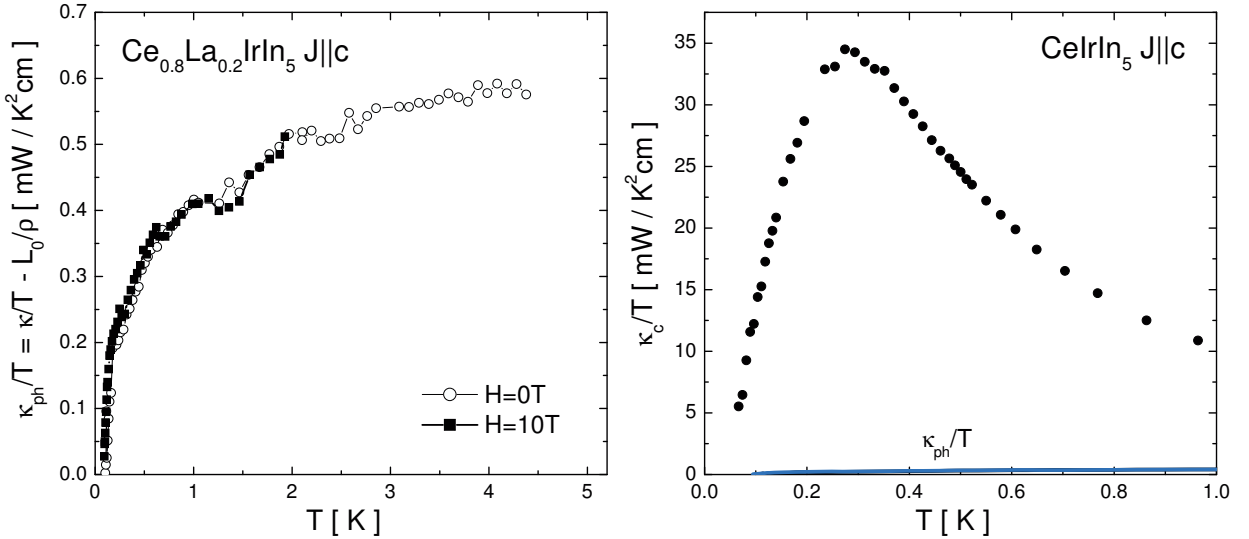
FIGURE C.1: (a) Estimate of inter-plane phonon contribution to the thermal conductivity of CeIrIn$_5$. In an impurity-doped sample, where elastic scattering dominates entirely at low temperature, the difference between thermal and electrical conductivities gives the phonon conductivity κ_{ph}. The phonon conductivity is field independent. (b) A comparison between the same phonon contribution and the thermal conductivity of pure CeIrIn$_5$.

field does not affect the phonon conductivity. κ_{ph}/T varies approximately linear with temperature at very low temperatures, below 0.5 K, followed by a maximum and saturation behaviour at higher temperatures. $\kappa_{ph} \propto T^2$ at low temperatures is expected for the phonon conductivity of pure metals, where phonon-electron scattering is the dominant scattering process.

A comparison between the phonon conductivity and the total thermal conductivity in the *c*-axis of pure sample is shown in Fig. C.1(b). It shows that κ_{ph} is on the order of 3% of the measured inter-plane conductivity at $T = 1K$ (approximately the same percentage is observed for in-plane current direction at $T = 1K$). Thus we can say the phonon contribution to the measured thermal conductivity in pure CeIrIn$_5$ samples is negligible below 1 K.

C.2   Phonon conductivity in 115 family, a comparison

Here it is instructive to have a comparison among all the extracted phonon conductivities for $CeCoIn_5$ [162, 215], $CeIrIn_5$ in this study and $CeRhIn_5$ (measured by J.-P.Reid et al., in our group), which is shown in Fig. C.2. In this figure, we have also shown temperature dependence of the phonon conductivity in each compound for temperature ranges up to nearly 5K. We have found:

- In $CeIrIn_5$ the phonon term κ_{ph} is smaller for inter-plane transport, by a factor 2 at $T = 1K$ (or at higher temperatures). Also, the temperature dependence of phonon conductivity is approximately the same for either current orientation, $\kappa_{ph} \sim T^{1.3}$.

- The in-plane phonon conductivity is larger in $CeCoIn_5$ than $CeIrIn_5$, by a factor 2 at $T = 4K$ (Although, it seems the magnitude of phonon conductivity is the same in $CeCoIn_5$ and $CeIrIn_5$ and negligible compared to κ_e below 1K). This also seems true in a comparison between the inter-plane transport of these two compounds.

- The power law temperature dependence of the phonon conductivity in $CeCoIn_5$ at high temperature range depends stronger on temperature compared to that of $CeIrIn_5$; $\kappa_{ph} \sim T^{1.65}$ and $\kappa_{ph} \sim T^{1.3}$, respectively.

- Phonon conductivity is nearly negligible below T_N for inter-plane $CeRhIn_5$. It is approximately 2.7% of the measured thermal conductivity of pure sample at $T_N = 4K$ (see the thermal conductivity of pure c-axis $CeRhIn_5$ in Appendix B).
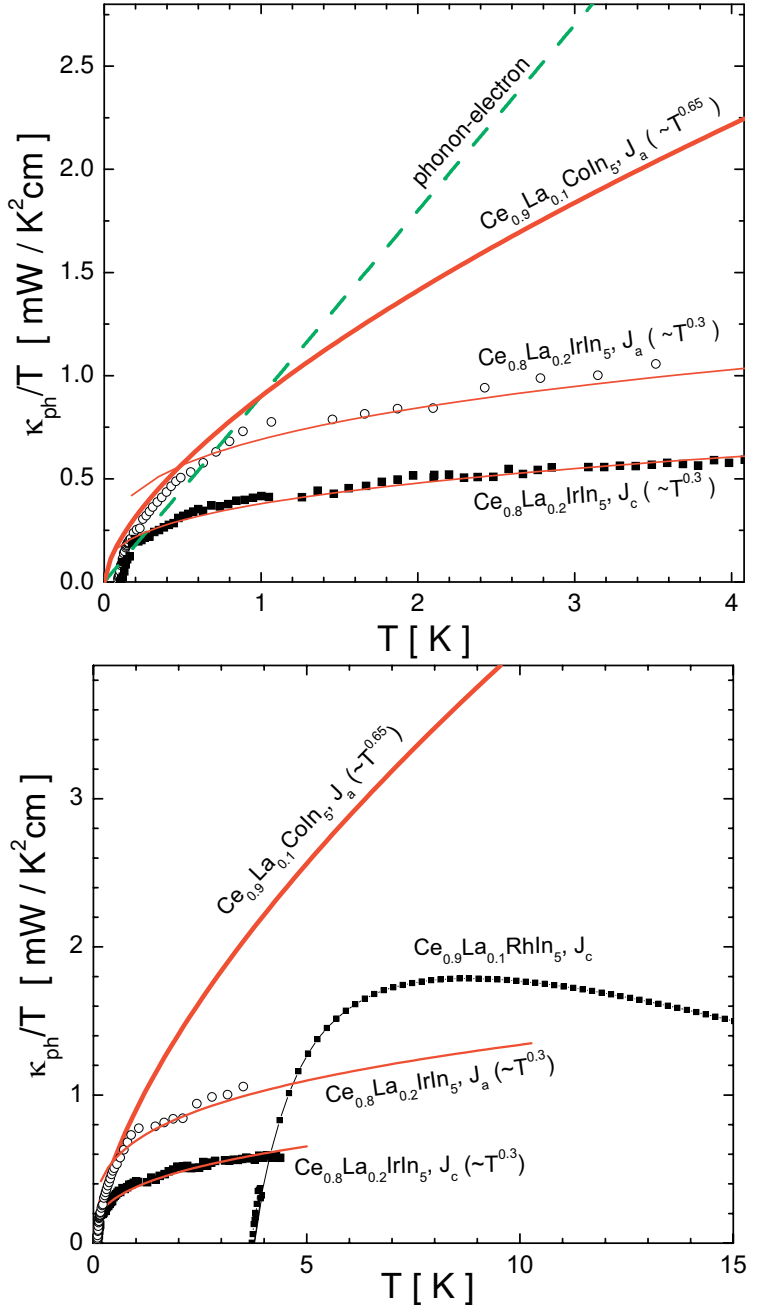
FIGURE C.2: (a) A comparison between estimations of phonon thermal conductivity for CeCoIn$_5$ [162] and CeIrIn$_5$. Red lines have been obtained by fitting data above 0.5 K (1 K) in doped CeIrIn$_5$ (doped CeCoIn$_5$ [162]). The green-dashed line was obtained by fitting data of doped CeCoIn$_5$ below 1 K [162]; at low temperatures, $\kappa_{ph} \propto T^2$, consistent with the expected phonon-electron scattering in pure metals, where the electron scattering is dominant scattering. (b) The same as (a), here inter-plane phonon conductivity of CeRhIn$_5$ has been compared.

Appendix D

Ce$_{0.999}$La$_{0.001}$IrIn$_5$: Thermal Conductivity in Magnetic Field

This Appendix presents the field dependence of thermal conductivity of doped CeIrIn$_5$ samples which is not shown in the main text.

The thermal conductivity of a- and c-axis doped samples in the magnetic field have been measured (the results of application of field on pure samples came in Chapter 7). Fig. D.1 shows the in-plane and inter-plane thermal conductivity of 0.1%La-doped samples as a function of magnetic field parallel to $c-$axis with temperature held constant at 90 mK. As we mentioned previously, in this range of temperature the thermal conductivity is completely electronic in the system. We observe two features.

First, both curves show nearly the same field dependence up to H$_{c2}$; $J\|c$ and $J\|a$ show nearly *isotrpic* behaviour at low fields and near H_{c2}. This is consistent with broadening point nodes with impurity and acting like line nodes. Although, impurity scattering effects can mask the real gap structure of the system. Note in the pure crystals (in Chapter 7) we observed an *anisotropic* behaviour at low temperature under applied field between a- and c-axis heat transport data, suggesting that the density of states associated with the linear point nodes and that associated with the line node has different energy and field dependence, as this is the case for the hybrid gap symmtery.

Second, in impure samples the transition to the normal state is broadened (κ is more linear vs H) compared to the pure ones that shows (at least for the c-axis samples) a steep transition to the normal state near H$_{c2}$. In the pure limit, Maki [131] has calculated the thermal conductivity by making use of an analogy with the case of a thin film carrying
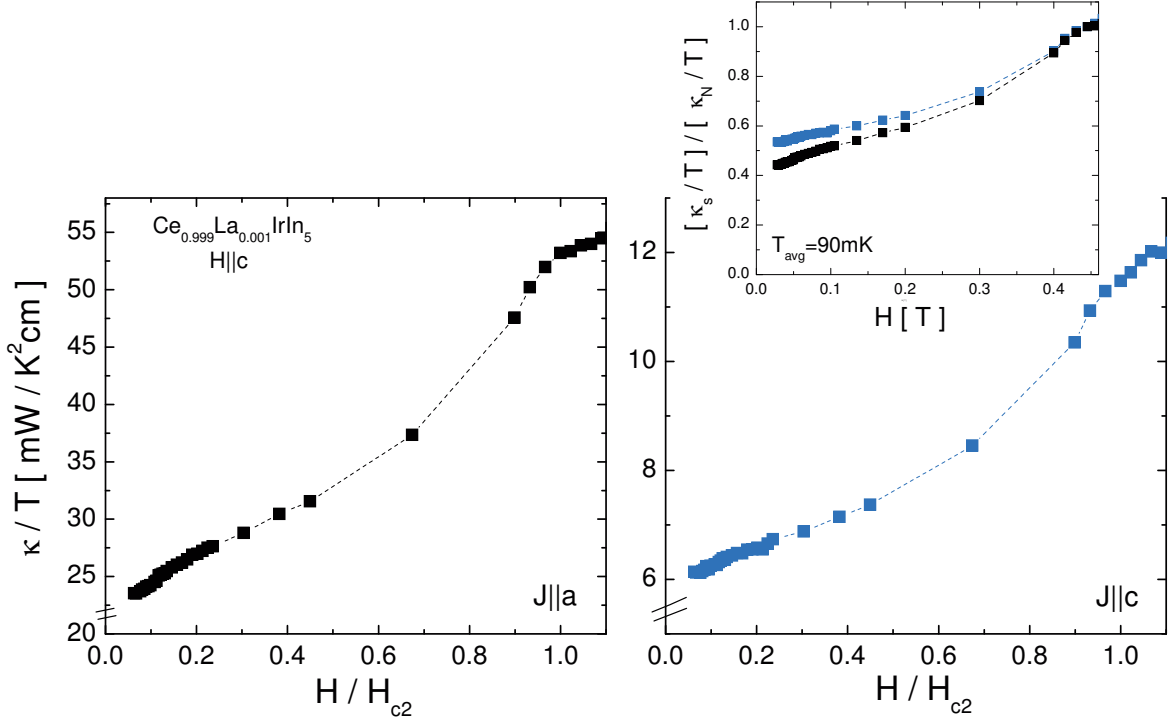
FIGURE D.1: The in-plane and inter-plane thermal conductivity, κ/T, of 0.1% La-doped CeIrIn$_5$ at $T = 90$ mK as a function of applied field. Note to the similar behaviour of two heat current directions. We argue impurities broaden the linear point nodes at the poles so that they behave as a line node.

an electronic current, and concludes that the thermal conductivity should vary as $(H_{c2} - H)^{1/2}$ near H_{c2}, so that the slope of the conductivity vs field at H_{c2} should be infinite. For the impure samples and at high fields, Lowell [122] observed a linear increase of thermal conductivity with field. Although, the linear behaviour extends well below H_{c2}.

In brief, it is clear that $\kappa(H)$ at low temperatures in CeIrIn$_5$ compound is not like as well-known behaviour for s-wave or d-wave superconductors and has a peculiar behaviour that not explained by the existing models. The isotropic field dependence of thermal conductivity of La-doped sampels seems to consist with the suggested hybrid gap symmetry.

Bibliography

[1] ABRIKOSOV, A. On the magnetic properties of superconductors of the second group. *Soviet Phys. JETP 5*, 6 (1957), 1174.

[2] ABRIKOSOV, A., AND GOR'KOV, L. On the theory of superconducting alloys.I. the electrodynamics of alloys at absolute zero. *Soviet Phys. JETP 8*, 6 (1959), 1090–1098.

[3] ABRIKOSOV, A., AND GOR'KOV, L. Contribution of the theory of superconducting alloys with paramagnetic impurities. *Soviet Phys. JETP 12*, 6 (1961), 1243–1253.

[4] ADENWALLA, S., LIN, S. W., RAN, Q., ZHAO, Z., KETTERSON, J., SAULS, J., TAILLEFER, L., HINKS, D., LEVY, M., AND SARMA, B. K. Phase diagram of UPt_3 from ultrasonic velocity measurements. *Phys. Rev. Lett. 65*, 18 (Oct 1990), 2298–2301.

[5] AEPPLI, G., BUCHER, E., BROHOLM, C., KJEMS, J. K., BAUMANN, J., AND HUFNAGL, J. Magnetic order and fluctuations in superconducting UPt_3. *Phys. Rev. Lett. 60*, 7 (1988), 615–618.

[6] AGTERBERG, D. Vortex lattice structures of Sr_2RuO_4. *Phys. Rev. Lett. 80*, 23 (Jun 1998), 5184–5187.

[7] AGTERBERG, D. Probing the pairing symmetry of Sr_2RuO_4 with magnetic field. *Physica C 364-365* (2001), 383–385.

[8] ALVER, U., GOODRICH, R., HARRISON, N., HALL, D., PALM, E., MURPHY, T., TOZER, S., PAGLIUSO, P., MORENO, N., SARRAO, J., AND FISK, Z. Localized f electrons in $Ce_xLa_{1-x}RhIn_5$:dHvA measurements. *Phys. Rev. B 64*, 18 (Oct 2001), 180402.

[9] ANDERSON, P. Theory of dirty superconductors. *J. Phys. Chem. Solids 11* (1959), 26–30.

[10] ANDERSON, P., AND MOREL, P. *Phys. Rev. 123* (1961), 1911.

[11] ANNETT, J. *Superconductivity, Superfluids and Condensates.* Oxford university press, 2005.

[12] AOKI, D., HUXLEY, A., RESSOUCHE, E., BRAITHWAITE, D., FLOUQUET, J., BRISON, J.-P., LHOTEL, E., AND PAULSEN, C. Coexistence of superconductivity and ferromagnetism in URhGe. *Nature 413* (2001), 613–16.

[13] AOKI, H., SAKAKIBARA, T., SHISHIDO, H., SETTAI, R., ONUKI, Y., MIRANOVIC, P., AND MACHIDA, K. Field-angle dependence of the zero-energy density of states in the unconventional heavy-fermion superconductor $CeCoIn_5$. *J. Phys.: Condens. Matter 16* (2004), L13–L19.

[14] AOKI, Y., SUGAWARA, H., AND SATO, H. Heavy fermion behaviors in the Pr-based filled skutterudites. *Journal of Alloys and Compounds 408–412* (2006), 21–26.

[15] AOKI, Y., TSUCHIYA, A., KANAYAMA, T., SAHA, S., SUGAWARA, H., SATO, H., HIGEMOTO, W., KODA, A., OHISHI, K., NISHIYAMA, K., AND KADONO, R. Time-reversal symmetry-breaking superconductivity in heavy-fermion $PrOs_4Sb_{12}$ detected by muon-spin relaxation. *Phys. Rev. Lett. 91*, 6 (Aug 2003), 067003.

[16] ARFI, B., BAHLOULI, H., AND PETHICK, C. Transport properties of anisotropic superconductors: Influence of arbitrary electron-impurity phase shifts. *Phys. Rev. B 39*, 13 (1989), 8959–8983.

[17] ARFI, B., AND PETHICK, C. Thermal conductivity and ultrasonic attenuation in heavy-fermion superconductors. *Phys. Rev. B 38*, 4 (1988), 2312–2325.

[18] ASHCROFT, N., AND MERMIN, N. *Solid State Physics*. W. B. Saunders Company, 1976.

[19] AUBIN, H., BEHNIA, K., RIBAULT, M., GAGNON, R., AND TAILLEFER, L. Angular position of nodes in the superconducting gap of YBCO. *Phys. Rev. Lett. 78*, 13 (1997), 2624–2627.

[20] BAO, W., AEPPLI, G., CHRISTIANSON, A., FISK, Z., HUNDLEY, M., LARCERDA, A., LYNN, J., PAGLIUSO, P., SARRAO, J., AND THOMPSON, J. Magnetic properties of heavy fermion superconductors $CeRhIn_5$ and Ce_2RhIn_8. *J. Modern Phys. B 16* (2002), 3244–3249.

[21] BAO, W., PAGLIUSO, P., SARRAO, J., THOMPSON, J., FISK, Z., LYNN, J., AND ERWIN, R. Incommensurate magnetic structure of $CeRhIn_5$. *Phys. Rev. B 62*, 22 (2000), R14621–R14624.

[22] BARASH, Y., AND SVIDZINSKY, A. Low-temperature properties and specific anisotropy of pure anisotropically paired superconductors. *Phys. Rev. B 53*, 22 (1996), 15254–15264.

[23] BARASH, Y., AND SVIDZINSKY, A. Nonmonotonic magnetic-field dependence and scaling of the thermal conductivity for superconductors with nodes of the order parameter. *Phys. Rev. B 58*, 10 (1998), 6476–6492.

[24] BARDEEN, J., COOPER, L., AND SCHRIEFFER, J. Theory of superconductivity. *Phys. Rev. 108* (1957), 1175–1204.

[25] BARDEEN, J., RICKAYZEN, G., AND TEWORDT, L. Theory of the thermal conductivity of superconductors. *Phys. Rev. 113*, 4 (1959), 982–994.

[26] BARZYKIN, V., AND GOR'KOV, L. Gapless fermi surfaces in superconducting CeCoIn$_5$? *Phys. Rev. B 76* (2007), 014509.

[27] BAUER, E., FREDERICK, N., HO, P.-C., ZAPF, V., AND MAPLE, M. Superconductivity and heavy fermion behavior in PrOs$_4$Sb$_{12}$. *Phys. Rev. B 65*, 10 (2002), 100506.

[28] BAUER, E., THOMPSON, J., SARRAO, J., MORALES, L., WASTIN, F., REBIZANT, J., GRIVEAU, J., JAVORSKY, P., BOULET, P., COLINEAU, E., LANDER, G., AND STEWART, G. Structural tuning of unconventional superconductivity in PuMGa$_5$ (M = Co,Rh). *Phys. Rev. Lett. 93*, 14 (2004), 147005.

[29] BEDNORZ, J., AND MULLER, K. Possible high T_c superconductivity in the Ba-La-Cu-O system. *Zeitschrift fur Physik B 64* (1986), 189–193.

[30] BEHNIA, K., TAILLEFER, L., FLOUQUET, J., JACCARD, D., MAKI, F., AND FISK, Z. Thermal conductivity of superconducting UPt$_3$. *J. Low Temp. Phys. 84* (1991), 261–278.

[31] BERMAN, R. *Thermal conduction in solids*. Clarendon Press, Oxford, 1976.

[32] BIANCHI, A. Avoided antiferromagnetic order and quantum critical point in CeCoIn$_5$. *Phys. Rev. Lett. 91* (2003), 257001.

[33] BIANCHI, A., MOVSHOVICH, R., CAPAN, C., LACERDA, A., PAGLIUSO, P., AND SARRAO, J. Fulde-ferrell-larkin-ovchinnikov superconducting state in CeCoIn$_5$. *Phys. Rev. Lett. cond-mat-0304420*.

[34] BIANCHI, A., MOVSHOVICH, R., JAIME, M., THOMPSON, J., PAGLIUSO, P., AND SARRAO, J. Origin of the zero-resistance anomaly in heavy fermion superconducting CeIrIn$_5$: a clue from magnetic-field and Rh-doping studies. *Phys. Rev. B 64*, 22 (2001), 220504.

[35] BIANCHI, A., MOVSHOVICH, R., OESCHLER, N., GEGENWART, P., STEGLICH, F., THOMPSON, J., PAGLIUSO, P., AND SARRAO, J. First-order superconducting phase transition in CeCoIn$_5$. *Phys. Rev. Lett. 89*, 13 (2002), 137002.

[36] BOAKNIN, E. *Thermal Conduction in the Vortex State of Unconventional Superconductors.* PhD thesis, University of Toronto, 2003.

[37] BRAITHWAITE, D., FUKUHARA, T., DEMUER, A., SHEIKIN, I., KAMBE, S., BRISON, J.-P., MAEZAWA, K., NAKAK, T., AND FLOUQUET, J. Superconductivity, upper critical field and normal state resistivity in $CeNi_2Ge_2$ under pressure. *J. Phys.: Condens. Matter 12* (2000), 1339–1349.

[38] CAPAN, C., BIANCHI, A., RONNING, F., LACERDA, A., THOMPSON, J., HUNDLEY, M., PAGLIUSO, P., SARRAO, J., AND MOVSHOVICH, R. Non-fermi-liquid behavior in $CeIrIn_5$ near a metamagnetic transition. *Phys. Rev. B 70*, 18 (2004), 180502.

[39] CASIMIR, H. *Physica (Amsterdam) 5* (1938), 495.

[40] CHEN, D.-C., AND GARG, A. Accidental near degenercy of the order parameter for superconducting UP_3. *Phys. Rev. Lett. 70* (1993), 1689.

[41] CHIA, E., VAN HARLINGEN, D., SALAMON, M., YANOFF, B., BONALDE, I., AND SARRAO, J. Nonlocality and strong coupling in the heavy fermion superconductor $CeCoIn_5$: a penetration depth study. *Phys. Rev. B 67*, 1 (2003), 014527.

[42] CHIAO, M., HILL, R., LUPIEN, C., POPIC, B., GAGNON, R., AND TAILLEFER, L. Quasiparticle transport in the vortex state of $YBa_2Cu_3O_{6.9}$. *Phys. Rev. Lett. 82*, 14 (1999), 2943–2946.

[43] CHOI, C., AND SAULS, J. Anisotropy of the upper critical field in a heavy-fermion superconductor. *Phys. Rev. B 48*, 18 (1993), 13684–13690.

[44] CHRISTIANSON, A. D., LACERDA, A. H., HUNDLEY, M. F., PAGLIUSO, P. G., AND SARRAO, J. L. Magnetotransport of $CeRhIn_5$. *Phys. Rev. B 66*, 5 (Aug 2002), 054410.

[45] CHUBUKOV, A., PINES, D., AND SCHMALIAN, J. *A Spin Fluctuation Model for d-wave Superconductivity, Vol. 1: Conventional and High-T_c Superconductors.* Springer, Berlin, 2003.

[46] CURNOE, S., ABU ALRUB, T., SERGIENKO, I., AND VEKHTER, I. Superconducting gap nodes in $PrOs_4Sb_{12}$. *Journal of Magnetism and Magnetic Materials cond-mat-0608122* (2006).

[47] CURRO, N., SIMOVIC, B., HAMMEL, P., PAGLIUSO, P., SARRAO, J., THOMPSON, J., AND MARTINS, G. Anomalous nmr magnetic shifts in $CeCoIn_5$. *Phys. Rev. B 64*, 18 (2001), 180514.

[48] Custers, J., Genewart, P., Wilhelm, H., Neumaier, K., Tokiwa, Y., Trovarelli, O., Geibel, C., Steglich, F., Pepin, C., and Coleman, P. The break-up of heavy electrons at a quantum critical point. *Nature 424* (2003), 524–7.

[49] Dalmas de Reotier, P., Huxley, A., Yaouanc, A., Flouquet, J., Bonville, P., Imbert, P., Pari, P., Gubbens, P., and Mulders, A. Absence of zero field muon spin relaxation induced by superconductivity in the B phase of UPt$_3$. *Phys. Lett. A 205* (1995), 239–243.

[50] de Visser, A. Evolution of magnetism and its interplay with superconductivity in heavy-fermion UPt$_3$ doped with Pd. *Physica B 319* (2002), 233–245.

[51] de Visser, A., Graf, M., Estrela, P., Amato, A., Baines, C., Andreica, D., Gygax, F., and Schenck, A. Magnetic quantum critical point and superconductivity in UPt_3 doped with Pd. *Phys. Rev. Lett. 85*, 14 (2000), 3005–3008.

[52] Demuer, A., Jaccard, D., Sheikin, I., Raymond, S., Salce, B., Thomasson, J., Braithwaite, D., and Flouquet, J. Further pressure studies around the magnetic instability of CePd$_2$Si$_2$. *J. Phys.: Condens. Matter 13* (2000), 9335–9347.

[53] Durst, A., and Lee, P. Impurity-induced quasiparticle transport and universal-limit wiedemann-franz violation in d-wave superconductors. *Phys. Rev. B 62*, 2 (2000), 1270–1290.

[54] Elgazzar, S., Opahle, I., Hayn, R., and Oppeneer, P. Calculated de haas van Alphen quantities of CeMIn$_5$ ($M =$Co, Rh, and Ir) compounds. *Phys. Rev. B 69*, 21 (2004), 214510–1–8.

[55] Ellman, B., Taillefer, L., and Poirier, M. Transverse ultrasound revisited: A directional probe of the A phase of UPt$_3$. *Phys. Rev. B 54*, 13 (1996), 9043–9046.

[56] Enss, C., and Hunklinger, S. *Low Temperature Physics*. Springer-Verlag Berlin Heidelberg, 2005.

[57] Eskildsen, M., Dewhurst, C., Hoogenboom, B., Petrovic, C., and Canfield, P. Hexagonal and square flux line lattices in CeCoIn$_5$. *Phys. Rev. Lett. 90*, 18 (2003), 187001.

[58] Fisher, R., Gordon, J., Reklis, S., Wright, D., Emerson, J., Woodfield, B., McCarron, E., and Phillips, N. Magnetic-field dependence of the low temperature specific heat of some high-T$_c$ copper-oxide superconductors evidence for an $H^{1/2}T$ contribution in the mixed state. *Physica C 252* (1995), 237.

[59] FISHER, R., KIM, S., WOODFIELD, B., PHILLIPS, N., TAILLEFER, L., HASSEL-BACH, K., FLOUQUET, J., GIORGI, A., AND SMITH, J. Specific heat of UPt$_3$: Evidence for unconventional superconductivity. *Phys. Rev. Lett. 62*, 12 (1989), 1411–1414.

[60] FLEDDERJOHANN, A., H. P. Thermal conductivity anisotropy in superconducting UPt$_3$. *Solid State Communications 94* (1995), 163–7.

[61] FRANZ, M. Mixed-state quasiparticle transport in high-T_c cuprates. *Phys. Rev. Lett. 82*, 8 (1999), 1760–1763.

[62] GEGENWART, P., KROMER, F., LANG, M., SPARN, G., GEIBEL, C., AND STEGLICH, F. Non-fermi-liquid effects at ambient pressure in a stoichiometric heavy-fermion compound with very low disorder: CeNi$_2$Ge$_2$. *Phys. Rev. Lett. 82* (1999), 1293.

[63] GEIBEL, C., SCHANK, C., THIES, S., KITAZAWA, H., BREDL, C., BOHM, A., RAU, M., GRAUEL, A., CASPARY, R., HELFRICH, R., AHLHEIM, U., WEBER, G., AND STEGLICH, F. Heavy-fermion superconductivity at T_c =2 K in the antiferromagnet UPd$_2$Al$_3$. *Zeitschrift fur Physik B 84* (1991), 1–2.

[64] GEIBEL, C., THIES, S., KACZOROWSKI, D., MEHNER, A., A. GRAUEL, A. B. S., AHLHEIM, U., HELFRICH, R., PETERSEN, K., BREDL, C., AND STEGLICH, F. A new heavy-fermion superconductor:UNi$_2$Al$_3$. *Zeitschrift fur Physik B 83* (1991), 305–306.

[65] GILARDI, R., MESOT, J., DREW, A., DIVAKAR, U., LEE, S., FORGAN, E., ZAHARKO, O., CONDER, K., ASWAL, V., DEWHURST, C., CUBITT, R., N., M., AND ODA, M. Direct evidence for an intrinsic square vortex lattice in the overdoped high-T_c superconductor La$_{1.83}$Sr$_{0.17}$CuO$_{4+\delta}$. *Phys. Rev. Lett. 88*, 21 (2002), 217003.

[66] GINZBURG, V., AND LANDAU, L. *Zh. Eksp. Teor. Fiz. 20* (1950), 1064.

[67] GOLDMAN, A., SHIRANE, G., AEPPLI, G., BATLOGG, B., AND BUCHER, E. Antiferromagnetic order in U$_{1-x}$Th$_x$Pt$_3$. *Phys. Rev. B 34*, 9 (1986), 6564–6566.

[68] GOLL, G. *Unconventional Superconductors: Experimental Investigation of the Order-Parameter Symmetry*. Springer-Verlag Berlin Heidelberg, 2006.

[69] GRAF, M., AND BALATSKY, A. Identifying the pairing symmetry in the Sr$_2$RuO$_4$ superconductor. *Phys. Rev. B 62*, 14 (2000), 9697–9702.

[70] GRAF, M., KEIZER, R., DE VISSER, A., AND HANNAHS, S. Search for a quantum phase transition in U(Pt$_{1-x}$Pd$_x$)$_3$. *Physica B 284-288* (2000), 1281–1282.

[71] GRAF, M., YIP, S.-K., AND SAULS, J. Identification of the orbital pairing symmetry in UPt$_3$. the same as "Graf-Ultrasound".

[72] GRAF, M., YIP, S.-K., AND SAULS, J. Thermal conductivity of superconducting UPt$_3$ at low temperatures. *J. Low Temp. Phys. 102* (1996), 367–379.

[73] GRAF, M., YIP, S.-K., AND SAULS, J. Thermal conductivity of the accidental degeneracy and enlarged symmetry group models forsuperconducting UPt$_3$. *J. Low Temp. Phys. 114* (1999), 257.

[74] GRAF, M., YIP, S.-K., SAULS, J., AND RAINER, D. Electronic thermal conductivity and the Wiedemann-Franz law for unconventional superconductors. *Phys. Rev. B 53*, 22 (1996), 15147–15161.

[75] GROSCHE, F., AGARWAL, P., JULIAN, S., WILSON, N., HASELWIMMER, R., LISTER, S., MATHUR, N., CARTER, F., SAXENA, S., AND LONZARICH, G. Anomalous low temperature states in CeNi$_2$Ge$_2$ and CePd$_2$Si$_2$. *J. Phys.: Condens. Matter 12* (2000), L533–L540.

[76] GROSCHE, F., JULIAN, S., MATHUR, N., AND LONZARICH, G. Magnetic and superconducting phases of CePd$_2$Si$_2$. *Physica B 223-224* (1996), 50–52.

[77] GROSCHE, F., WALKER, I., JULIAN, S., MATHUR, N., FREYE, D., STEINER, M., AND LONZARICH, G. Superconductivity on the threshold of magnetism in CePd$_2$Si$_2$ and CeIn$_3$. *J. Phys.: Condens. Matter 13* (2001), 2845–2860.

[78] HAGA, Y., INADA, Y., HARIMA, H., OIKAWA, K., MURAKAWA, M., NAKAWAKI, H., TOKIWA, Y., AOKI, D., SHISHIDO, H., IKEDA, S., WATANABE, N., AND ONUKI, Y. Quasi-two-dimensional fermi surfaces of the heavy fermion superconductor CeIrIn$_5$. *Phys. Rev. B 63*, 6 (2001), 060503.

[79] HASSELBACH, K., TAILLEFER, L., AND FLOUQUET, J. Critical point in the superconducting phase diagram of UPt$_3$. *Phys. Rev. Lett. 63*, 1 (1989), 93–96.

[80] HAYDEN, S., TAILLEFER, L., VETTIER, C., AND FLOUQUET, J. Antiferromagnetic order in UPt$_3$ under pressure: Evidence for a direct coupling to superconductivity. *Phys. Rev. B 46*, 13 (1992), 8675–8678.

[81] HEGGER, H., PETROVIC, C., MOSHOPOULOU, E., HUNDLEY, M., SARRAO, J., FISK, Z., AND THOMPSON, J. Pressure-induced superconductivity in Quasi-2D CeRhIn$_5$. *Phys. Rev. Lett. 84*, 21 (2000), 4986–4989.

[82] HERTZ, J. Quantum critical phenomena. *Phys. Rev. B 14*, 3 (1976), 1165–1184.

[83] HEUSER, K., KIM, J., SCHEIDT, E., SCHREINER, T., AND STEWART, G. Inducement of non-fermi-liquid behavior with magnetic field in heavy-fermion antiferromagnets. *Physica B: Condensed Matter 261* (1999), 392.

[84] HIGEMOTO, W., KODA, A., KADONO, R., KAWASAKI, Y., HAGA, Y., AOKI, D., SETTAI, R., SHISHIDO, H., AND ONUKI, Y. μSR studies on heavy fermion superconductors CeIrIn$_5$ and CeCoIn$_5$. *J. Phys. Soc. Japan 71* (2002), 1023.

[85] HIRSCHFELD, J., VOLLHARDT, D., AND WOFFL, P. Resonant impurity scattering in heavy fermion superconductors. *Solid State Communications 59* (1986), 111–15.

[86] HIRSCHFELD, P., AND GOLDENFELD, N. Effect of strong scattering on the low-temperature penetration depth of a *d*-wave superconductor. *Phys. Rev. B 48*, 6 (1993), 4219–4222.

[87] HIRSCHFELD, P., AND PUTIKKA, W. Theory of thermal conductivity in YBa$_2$Cu$_3$O$_{7-\delta}$. *Phys. Rev. Lett. 77*, 18 (1996), 3909–3912.

[88] HUXLEY, A., SUDEROW, H., BRISON, J., AND FLOUQUET, J. Thermal conductivity and symmetry of the superconductivity in UPt$_3$. *Phys. Lett. A 209* (1995), 365.

[89] IKEDA, S., SHISHIDO, H., NAKASHIMA, M., SETTAI, R., AOKI, D., HAGA, Y., HARIMA, H., AOKI, Y., NAMIKI, T., SATO, H., AND ONUKI, Y. Unconventional superconductivity in CeCoIn$_5$ studied by the specific heat and magnetization measurements. *J. Phys. Soc. Japan 70* (2001), 2248–51.

[90] ISHIDA, K., OKAMOTO, K., KAWASAKI, Y., KITAOKA, Y., TROVARELLI, O., GEIBEL, C., AND STEGLICH, F. YbRh$_2$Si$_2$: spin fluctuations in the vicinity of a quantum critical point at low magnetic field. *Phys. Rev. Lett. 89*, 10 (Aug 2002), 107202.

[91] IZAWA, K., KASAHARA, Y., MATSUDA, Y., BEHNIA, K., YASUDA, T., SETTAI, R., AND ONUKI, Y. Line nodes in the superconducting gap function of noncentrosymmetric CePt$_3$Si. *Phys. Rev. Lett. 94*, 19 (2005), 197002.

[92] IZAWA, K., NAKAJIMA, Y., GORYO, J., MATSUDA, Y., OSAKI, S., SUGAWARA, H., SATO, H., THALMEIER, P., AND MAKI, K. Multiple superconducting phases in new heavy fermion superconductor PrOs$_4$Sb$_{12}$. *Phys. Rev. Lett. 90*, 11 (2003), 117001.

[93] IZAWA, K., TAKAHASHI, H., YAMAGUCHI, H., MATSUDA, Y., SUZUKI, M., SASAKI, T., FUKASE, T., YOSHIDA, Y., SETTAI, R., AND ONUKI, Y. Superconducting gap structure of spin-triplet superconductor Sr$_2$RuO$_4$ studied by thermal conductivity. *Phys. Rev. Lett. 86*, 12 (2001), 2653–2656.

[94] IZAWA, K., YAMAGUCHI, H., MATSUDA, Y., SHISHIDO, H., SETTAI, R., AND ONUKI, Y. Angular position of nodes in the superconducting gap of Quasi-2D heavy-fermion superconductor CeCoIn$_5$. *Phys. Rev. Lett. 87*, 5 (2001), 057002.

[95] JACCARD, D. K. B., AND SIERRO, J. Pressure induced heavy fermion superconductivity of CeCu$_2$Ge$_2$. *Phys. Lett. A 163* (1992), 475–80.

[96] JOSEPHSON, B. Possible new effects in superconductive tunnelling. *Phys. Lett. 1,* 7 (1962), 251–253.

[97] JOYNT, R., AND TAILLEFER, L. The superconducting phases of UPt$_3$. *Rev. Mod. Phys. 74*, 1 (2002), 235–294.

[98] KADOWAKI, H., FAK, B., FUKUHARA, T., MAEZAWA, K., NAKAJIMA, K., ADAMS, M. A., RAYMOND, S., AND FLOUQUET, J. Spin fluctuations and non-fermi-liquid behavior of CeNi$_2$Ge$_2$. *Phys. Rev. B 68*, 14 (Oct 2003), 140402.

[99] KADOWAKI, K., AND S.B.WOODS. Universal relationship of the resistivity and specific heat in heavy-fermion compounds. *Solid State Communications 58* (1986), 507–9.

[100] KASAHARA, K., IWASAWA, T., SHIMIZU, Y., SHISHIDO, H., SHIBAUCHI, T., VEKHTER, I., AND MATSUDA, Y. Thermal conductivity evidence for d$_{x^2-y^2}$ pairing symmetry in the heavy-fermion CeIrIn$_5$ superconductor, 07122604.

[101] KASAHARA, Y., IWASAWA, T., SHISHIDO, H., SHIBAUCHI, T., BEHNIA, K., HAGA, Y., MATSUDA, T. D., ONUKI, Y., SIGRIST, M., AND MATSUDA, Y. Exotic superconducting properties in the electron-hole-compensated heavy-fermion "semimetal" URu$_2$Si$_2$. *Phys. Rev. Lett. 99*, 11 (2007), 116402.

[102] KASAHARA, Y., SHIMONO, Y., SHIBAUCHI, T., MATSUDA, Y., YONEZAWA, S., MURAOKA, Y., AND HIROI, Z. Thermal conductivity of the pyrochlore superconductor KOs$_2$O$_6$: Strong electron correlations and fully gapped superconductivity. *Phys. Rev. Lett. 96*, 24 (2006), 247004.

[103] KAUR, R., AGTERBERG, D., AND KUSUNOSE, H. Quasiclassical determination of the in-plane magnetic field phase diagram of superconducting Sr$_2$RuO$_4$. *Phys. Rev. B 72*, 14 (2005), 144528.

[104] KAWASAKI, S., MITO, T., ZHENG, G.-Q., THESSIEU, C., KAWASAKI, Y., ISHIDA, K., KITAOKA, Y., MURAMATSU, T., KOBAYASHI, T. C., AOKI, D., ARAKI, S., HAGA, Y., SETTAI, R., AND ONUKI, Y. Pressure-temperature phase diagram of antiferromagnetism and superconductivity in CeRhIn$_5$ and CeIn$_3$: $^{115}In - NQR$ study under pressure. *Phys. Rev. B 65*, 2 (2001), 020504.

[105] KAWASAKI, S., Q. ZHENG, G., KAN, H., KITAOKA, Y., SHISHIDO, H., AND ONUKI, Y. Enhancing the superconducting transition temperature of the heavy fermion compound CeIrIn$_5$ in the absence of spin correlations. *Phys. Rev. Lett. 94*, 3 (2005), 037007.

[106] KEIZER, R., DE VISSER, A., GRAF, M., MENOVSKY, A., AND FRANSE, J. Superconductivity in heavy-fermion U(Pt, Pd)$_3$ and its interplay with magnetism. *Phys. Rev. B 60*, 14 (1999), 10527–10538.

[107] KEIZER, R., DE VISSER, A., MENOVSKY, A., FRANSE, J., AMATO, A., GYGA, F., PINKPANK, M., AND SCHENCK, A. Magnetism in heavy-fermion U(Pt,Pd)$_3$ studied by muSR. *J. Phys.: Condens. Matter 11* (1999), 8591–8606.

[108] KIM, J., ALWOOD, J., KUMAR, P., AND STEWART, G. Field-induced transition in the specific heat of CeIrIn$_5$ for $B > 30T$. *Phys. Rev. B 65*, 17 (2002), 174520.

[109] KIM, J., HALL, D., HEUSER, K., AND STEWART, G. Indications of non-fermi liquid behavior at the metamagnetic transition of UPt$_3$. *Solid State Communications 114* (2000), 413–418.

[110] KNEBEL, G., AOKI, D., BRAITHWAITE, D., SALCE, B., AND FLOUQUET, J. Coexistence of antiferromagnetism and superconductivity in CeRhIn$_5$ under high pressure and magnetic field. *Phys. Rev. B 74*, 2 (2006), 020501.

[111] KOERNER, S., SCHEIDT, E.-W., SCHREINER, T., HEUSER, K., AND STEWART, G. Crossover to fermi-liquid behavior at lowest temperatures in pure CeNi$_2$Ge$_2$. *Journal of Low Temperature Physics 119* (2000), 147–153.

[112] KOHORI, Y., YAMATO, Y., IWAMOTO, Y., KOHARA, T., BAUER, E., MAPLE, M., AND SARRAO, J. NMR and NQR studies of the heavy fermion superconductors CeTIn$_5$ ($T =$Co and Ir). *Phys. Rev. B 64*, 13 (2001), 134526.

[113] KOPNIN, N., AND VOLOVIK, G. Singularity of the vortex density of states in d-wave superconductors. *JETP Lett. 64* (1996), 690–4.

[114] KRISHANA, K., ONG, N., LI, Q., GU, G., AND KOSHIZUKA, N. Plateaus observed in the field profile of thermal conductivity in the superconductor Bi$_2$Sr$_2$CaCu$_2$O$_8$. *Science 277* (1997), 83–5.

[115] KUBERT, C., AND HIRSCHFELD, P. Quasiparticle transport properties of d-wave superconductors in the vortex state. *Phys. Rev. Lett. 80*, 22 (1998), 4963–4966.

[116] KUBERT, C., AND HIRSCHFELD, P. Vortex contribution to specific heat of dirty d-wave superconductors: breakdown of scaling. *Solid State Communications 105* (1998), 459–63.

[117] KYCIA, J., HONG, J., GRAF, M., SAULS, J., SEIDMAN, D., AND HALPERIN, W. Suppression of superconductivity in UPt$_3$ single crystals. *Phys. Rev. B 58*, 2 (1998), R603–R606.

[118] LEE, P. Localized states in a d-wave superconductor. *Phys. Rev. Lett. 71*, 12 (1993), 1887–1890.

[119] LISTER, S., GROSCHE, F., CARTER, F., HASELWIMMER, R., SAXENA, S., MATHUR, N., JULIAN, S., AND LONZARICH, G. Quantum critical behaviour in the CePd$_2$Si$_2$/CeNi$_2$Ge$_2$ system. *Zeitschrift fur Physik B 103* (1997), 263–5.

[120] LLOBET, A., CHRISTIANSON, A. D., BAO, W., GARDNER, J. S., SWAINSON, I. P., LYNN, J. W., MIGNOT, J.-M., PROKES, K., PAGLIUSO, P. G., MORENO, N. O., SARRAO, J. L., THOMPSON, J. D., AND LACERDA, A. H. Novel coexistence of superconductivity with two distinct magnetic orders. *Phys. Rev. Lett. 95*, 21 (2005), 217002.

[121] LLOBET, A., GARDNER, J., MOSHOPOULOU, E., MIGNOT, J.-M., NICKLAS, M., BAO, W., MORENO, N., PAGLIUSO, P., GONCHARENKO, I., SARRAO, J., AND THOMPSON, J. Magnetic structure of CeRhIn$_5$ as a function of pressure and temperature. *Phys. Rev. B 69*, 2 (2004), 024403.

[122] LOWELL, J., AND SOUSA, J. Mixed-state thermal conductivity of type II superconductors. *J. Low Temp. Phys. 3* (1970), 65–87.

[123] LUKE, G., FUDAMOTO, Y., KOJLMA, K., LARKIN, M., MERRIN, J., NACHUMI, B., UEMURA, Y., MAENO, Y., MAO, Z., MORI, Y., NAKAMURA, H., AND SIGRIST, M. Time-reversal symmetry-breaking superconductivity in Sr$_2$RuO$_4$. *Nature 394* (1998), 558.

[124] LUKE, G., KEREN, A., LE, L., WU, W., UEMURA, Y., BONN, D., TAILLEFER, L., AND GARRETT, J. Muon spin relaxation in UPt$_3$. *Phys. Rev. Lett. 71*, 9 (1993), 1466–1469.

[125] LUSSIER, B. *Heat conduction in unconventional superconductors.* PhD thesis, Université de McGill, 1996.

[126] LUSSIER, B., ELLMAN, B., AND TAILLEFER, L. Anisotropy of heat conduction in the heavy fermion superconductor UPt$_3$. *Phys. Rev. Lett. 73*, 24 (1994), 3294–3297.

[127] LUSSIER, B., ELLMAN, B., AND TAILLEFER, L. Determination of the gap structure in UPt$_3$ by thermal conductivity. *Phys. Rev. B 53*, 9 (1996), 5145–5148.

[128] MACHIDA, K. Orbital symmetry of a triplet pairing in a heavy fermion superconductor UPt$_3$. *J. Phys. Soc. Japan 68* (1999), 3364.

[129] MAEHIRA, T., HOTTA, T., UEDA, K., AND HASEGAWA, A. Relativistic band structure calculations for CeTIn$_5$ (T = Ir and Co) and analysis of the energy bands by using tight-binding method. *J. Phys. Soc. Japan 72* (2003), 854–864.

[130] MAENO, Y. Superconductivity in a layered perovskite without copper. *Nature 372* (1994), 532–4.

[131] MAKI, K. Thermal conductivity of pure type-II superconductors in high magnetic fields. *Phys. Rev. 158*, 2 (1967), 397–399.

[132] MAKI, K. gapless superconductivity. 1035.

[133] MAKI, K., HAAS, S., D. PARKER, a. H. W., IZAWA, K., AND MATSUDA, Y. Triplet superconductivity in the skutterudite $PrOs_4Sb_{12}$. *Europhys. Lett. 68* (2004), 720.

[134] MAKI, K., HAAS, S., PARKER, D., AND WON, H. Perspectives on nodal superconductors. *Chinese Journal of Physics 43* (2005), 532.

[135] MAKI, K., RAGHAVAN, A., AND HAAS, S. Chiral d-wave superconductivity in the heavy-fermion compound $CeIrIn_5$, 07123058.

[136] MAKI, K., AND WON, H. Why d-wave superconductivity? *J. Phys. I France 6* (1996), 2317–26.

[137] MAO, Z., AKIMA, T., ANDO, T., AND MAENO, Y. Experimental search for the second superconducting transition in Sr_2RuO_4. *Physica B 284* (2000), 541–542.

[138] MAO, Z., MAENO, Y., NISHIZAKI, S., AKIMA, T., AND ISHIGURO, T. In-plane anisotropy of upper critical field in Sr_2RuO_4. *Phys. Rev. Lett. 84* (2000), 991.

[139] MATHUR, N., GROSCHE, F., JULIAN, S., WALKER, I., FREYE, D., HASELWIMMER, R., AND LONZARICH, G. Magnetically mediated superconductivity in heavy fermion compounds. *Nature 394* (1998), 39.

[140] MATSUDA, Y., IZAWA, K., AND VEKHTER, I. Nodal structure of unconventional superconductors probed by angle resolved thermal transport measurements. *J. Phys.: Condens. Matter 18* (2006), R705–R752.

[141] MINEEV, V. In-plane magnetic field phase diagram of superconducting Sr_2RuO_4. arXiv:0712.0286.

[142] MINEEV, V., AND SAMOKHIN, K. *Introduction to unconventional superconductivity.* Gordon and Breach Science, 1999.

[143] MIYAKE, K., AND MAEBASHI, H. Huge enhancement of impurity scattering due to critical valence fluctuations in a Ce-based heavy electron system. *J. Phys. Soc. Japan 71* (2002), 1007–10.

[144] MIYAKE, K., MATSUURA, T., AND VARMA, C. Relation between resistivity and effective mass in heavy-fermion and A15 compounds. *Solid State Communications 71* (1989), 1149–1153.

[145] MOLER, K., BAAR, D., URBACH, J., LIANG, R., HARDY, W., AND KAPITULNIK, A. Magnetic field dependence of the density of states of $YBa_2Cu_3O_{6.95}$ as determined from the specific heat. *Phys. Rev. Lett. 73*, 20 (1994), 2744–2747.

[146] MOLER, K. A., SISSON, D. L., URBACH, J. S., BEASLEY, M. R., KAPITULNIK, A., BAAR, D. J., LIANG, R., AND HARDY, W. N. Specific heat of $yba_2cu_3o_{7-\delta}$. *Phys. Rev. B 55*, 6 (1997), 3954–3965.

[147] MONTHOUX, P., AND LONZARICH, G. Magnetically mediated superconductivity in quasi-two and three dimensions. *Phys. Rev. B 63*, 5 (2001), 054529.

[148] MORIYA, T. *Spin Fluctuations in itinerant Electron Magnetism.* Springer-Verlag Berlin Heidelberg, 1985.

[149] MOVSHOVICH, R., GRAF, T., MANDRUS, D., THOMPSON, J. D., SMITH, J. L., AND FISK, Z. Superconductivity in heavy-fermion $CeRh_2Si_2$. *Phys. Rev. B 53*, 13 (1996), 8241–8244.

[150] MOVSHOVICH, R., JAIME, M., THOMPSON, J., PETROVIC, C., FISK, Z., PAGLIUSO, P., AND SARRAO, J. Unconventional superconductivity in $CeIrIn_5$ and $CeCoIn_5$: specific heat and thermal conductivity studies. *Phys. Rev. Lett. 86*, 22 (2001), 5152–5155.

[151] MUKHERJEE, S., AND AGTERBERG, D. Microscopic theories for cubic and tetrahedral superconductors: Application to $PrOs_4Sb_{12}$. *Phys. Rev. B. 74* (2006), 174505.

[152] NAKAMURA, S., AND MORIYA, T., U. K. Spin fluctuation-induced superconductivity in two and three dimensional systems. *J. Phys. Soc. Japan 65* (1996), 4026–4033.

[153] NICKLAS, M., SIDOROV, V., BORGES, H., PAGLIUSO, P., SARRAO, J., AND THOMPSON, J. Two superconducting phases in $CeRh_{1-x}Ir_xIn_5$. *Phys. Rev. B 70*, 2 (2004), 020505.

[154] NISIKAWA, Y., IKEDA, H., AND YAMADA, K. Perturbation theory on the superconductivity of heavy fermion superconductors $CeIr_xCo_{1-x}In_5$. *J. Phys. Soc. Japan 71* (2002), 1140–1147.

[155] NORMAN, M., AND HIRSCHFELD, P. Heat transport and the nature of the order parameter in superconducting UPt_3. *Phys. Rev. B 53*, 9 (1996), 5706–5715.

[156] OHIRA-KAWAMURA, S., SHISHIDO, H., YOSHIDA, A., OKAZAKI, R., KAWANO-FURUKAWA, H., SHIBAUCHI, T., HARIMA, H., AND MATSUDA, Y. Competition between unconventional superconductivity and incommensurate antiferromagnetic order in $CeRh_{1-x}Co_xIn_5$. *Phys. Rev. B 76*, 13 (2007), 132507.

[157] ONISHI, Y., AND MIYAKE, K. Enhanced valence fluctuations caused by f-c coulomb interaction in Ce-based heavy electrons: Possible origin of pressure-induced enhancement of superconducting transition temperature in $CeCu_2Ge_2$ and related compounds. *J. Phys. Soc. Japan 69* (2000), 3955–3964.

[158] ORMENO, R. J., SIBLEY, A., GOUGH, C. E., SEBASTIAN, S., AND FISHER, I. Microwave conductivity and penetration depth in the heavy fermion superconductor $CeCoIn_5$. *Phys. Rev. Lett. 88*, 4 (2002), 047005.

[159] OTT, H., RUDIGIER, H., FELDER, E., FISK, Z., AND SMITH, J. Influence of impurities and magnetic fields on the normal and superconducting states of UBe_{13}. *Phys. Rev. B 33*, 1 (1986), 126–131.

[160] OZAKI, M., MACHIDA, K., AND OHMI, T. On p-wave pairing superconductivity under hexagonal and tetragonal symmetries. *Prog. Theor. Phys. 75* (1986), 442.

[161] OZCAN, S., BROUN, D., MORGAN, B., HASELWIMMER, R., WALDRAM, J., SARRAO, J., KAMAL, S., BIDINOSTI, C., AND TURNER, P. $CeCoIn_5$ - a quantum critical superfluid. *Europhys. Lett. 62* (2002), 412.

[162] PAGLIONE, J. *Quantum Criticality in the Heavy-Fermion Superconductor $CeCoIn_5$.* PhD thesis, University of Toronto, 2004.

[163] PAGLIONE, J. $T^{2/3}$ resistivity and the field-tuned quantum critical point in $CeCoIn_5$, 2004.

[164] PAGLIONE, J., TANATAR, M., HAWTHORN, D., BOAKNIN, E., HILL, R., RONNING, F., SUTHERLAND, M., TAILLEFER, L., PETROVIC, C., AND CANFIELD, P. Field-induced quantum critical point in $CeCoIn_5$. *Phys. Rev. Lett. 91*, 24 (Dec 2003), 246405.

[165] PAGLIONE, J., TANATAR, M. A., HAWTHORN, D. G., HILL, R. W., RONNING, F., SUTHERLAND, M., TAILLEFER, L., PETROVIC, C., AND CANFIELD, P. C. Heat transport as a probe of electron scattering by spin fluctuations: The case of antiferromagnetic $CeRhIn_5$. *Phys. Rev. Lett. 94*, 21 (2005), 216602.

[166] PAGLIONE, J., TANATAR, M. A., HAWTHORN, D. G., RONNING, F., HILL, R. W., SUTHERLAND, M., TAILLEFER, L., AND PETROVIC, C. Nonvanishing energy scales at the quantum critical point of $CeCoIn_5$, 2006.

[167] PAGLIUSO, P., PETROVIC, C., MOVSHOVICH, R., HALL, D., HUNDLEY, M., SARRAO, J., THOMPSON, J., AND FISK, Z. Coexistence of magnetism and superconductivity in $CeRh_{1-x}Ir_xIn_5$. *Phys. Rev. B 64*, 10 (2001), 100503.

[168] PALMA, E., MURPHY, T., HALL, D., TOZER, S., GOODRICH, R., AND SARRAO, J. Magnetic transitions in $CeIrIn_5$. *Physica B 329-333* (2003), 587–588.

[169] PANAGOPOULOS, C., COOPER, J., ATHANASSOPOULOU, N., AND CHROSCH, J. Effects of Zn doping on the anisotropic penetration depth of $YBa_2Cu_3O_7$. *Phys. Rev. B 54*, 18 (1996), R12721–R12724.

[170] PARK, W., GREENE, L., SARRAO, J., AND THOMPSON, J. Andreev reflection spectroscopy of the heavy-fermion superconductor $CeCoIn_5$ along three different crystallographic orientations, 2006.

[171] PARKER, D. S. *Unconventional Superconductivity in $PrOs_4sb_{12}$*. PhD thesis, University of Southern California, 2006.

[172] PETHICK, C., AND PINES, D. Transport processes in heavy-fermion superconductors. *Phys. Rev. Lett. 57*, 1 (1986), 118–121.

[173] PETROVIC, C., MOVSHOVICH, R., JAIME, M., PAGLIUSO, P., HUNDLEY, M., SARRAO, J., FISK, Z., AND THOMPSON, J. A new heavy-fermion superconductor $CeIrIn_5$: a relative of the cuprates? *Europhys. Lett. 53* (2001), 354–359.

[174] PETROVIC, C., PAGLIUSO, P., HUNDLEY, M., MOVSHOVICH, R., SARRAO, J., THOMPSON, J. D., FISK, Z., AND MONTHOUX, P. Heavy-fermion superconductivity in $CeCoIn_5$ at 2.3 K. *J. Phys.: Condens. Matter 13* (2001), L337–L342.

[175] PHAM, L., PARK, T., MAQUILON, S., THOMPSON, J., AND FISK, Z. Reversible tuning of the heavy-fermion ground state in $CeCoIn_5$. *Phys. Rev. Lett. 97* (2006), 05640497, 056404 (2006).

[176] POBELL, F. *Matter and Methods at Low Temperatures*. Springer-Verlag, Berlin, second edition, 1996.

[177] PROUST, C., BOAKNIN, E., HILL, R., TAILLEFER, L., AND MACKENZIE, A. Heat transport in a strongly overdoped cuprate: Fermi liquid and a pure d-wave BCS superconductor. *Phys. Rev. Lett. 89*, 14 (2002), 147003.

[178] PUCHKARYOV, E., AND MAKI, K. Impurity scattering in d-wave superconductivity. unitarity limit versus born limit. *Eur. Phys. J. B 4* (1998), 191–4.

[179] RODIERE, P., BRISON, J., HUXLEY, A., RULLIER ALBENQUE, F., AND FLOUQUET, J. Characterization of high energy electron irradiation damage in UPt_3 samples. *J. Low Temp. Phys. 132* (2003), 119–134.

[180] RONNING, F., CAPAN, C., BIANCHI, A., MOVSHOVICH, R., LACERDA, A., HUNDLEY, M., THOMPSON, J., PAGLIUSO, P., AND SARRAO, J. Field-tuned quantum critical point in $CeCoIn_5$ near the superconducting upper critical field. *Phys. Rev. B 71*, 10 (2005), 104528.

[181] ROSCH, A. Magnetotransport in nearly antiferromagnetic metals. *Phys. Rev. B 62*, 8 (2000), 4945–4962.

[182] ROURKE, P., TANATAR, M., TUREL, C., BERDEKLIS, J., PETROVIC, C., AND WEI, J. Spectroscopic evidence for multiple order parameter components in the heavy fermion superconductor $CeCoIn_5$. *Phys. Rev. Lett. 94*, 10 (2005), 107005.

[183] SARRAO, J., MORALES, L., THOMPSON, J., SCOTT, B., STEWART, G., WASTIN, F., REBIZANT, J., BOULET, P., COLINEAU, E., AND LANDER, G. Plutonium-based superconductivity with a transition temperature above 18 K. *Nature(London) 420* (2002), 297–9.

[184] SARRAO, J., AND THOMPSON, J. Superconductivity in Cerium- and Plutonium-based '115' materials. *J. Phys. Soc. Japan 76* (2007), 051013.

[185] SARRAO, J., THOMPSON, J., MORENO, N., MORALES, L., WASTIN, F., REBIZANT, J., BOULET, P., COLINEAU, E., AND LANDER, G. Discovery of Plutonium-based superconductivity. *J. Phys.: Condens. Matter 15* (2003), S2275–S2278.

[186] SATTERTHWAITE, C. Thermal conductivity of normal and superconducting Aluminum. *Phys. Rev. 125*, 3 (1962), 873–876.

[187] SAULS, J. The order parameter for the superconducting phases of UPt_3. *Advances in Physics 43* (1994), 113–141.

[188] SAXENA, S., AGARWAL, P., AHILAN, K., GROSCHE, F., HASELWIMMER, R., STEINER, M., PUGH, E., WALKER, I., JULIAN, S., MONTHOUX, P., LONZARICH, G., HUXLEY, A., SHEIKIN, I., BRAITHWAITE, D., AND FLOUQUET, J. Superconductivity on the border of itinerant-electron ferromagnetism in UGe_2. *Nature 406* (2000), 587–92.

[189] SCHENSTROM, A., XU, M. F., HONG, Y., BEIN, D., LEVY, M., SARMA, B. K., ADENWALLA, S., ZHAO, Z., TOKUYASU, T., HESS, D. W., KETTERSON, J., SAULS, J., AND HINKS, D. Anisotropy of the magnetic-field-induced phase transition in superconducting UPt_3. *Phys. Rev. Lett. 62*, 3 (1989), 332–335.

[190] SCHMITT-RINK, S., MIYAKE, K., AND VARMA, C. Transport and thermal properties of heavy-fermion superconductors: A unified picture. *Phys. Rev. Lett. 57*, 20 (1986), 2575–2578.

[191] SETTAI, R., SHISHIDO, H., IKEDA, S., MURAKAWA, Y., NAKASHIMA, M., AOKI, D., HAGA, Y., HARIMA, H., AND ONUK, Y. Quasi-two-dimensional fermi surfaces and the de haasvan alphen oscillation in both the normal and superconducting mixed states of $CeCoIn_5$. *Journal of Physics: Condensed Matter 13* (2001), L627–L634.

[192] SEYFARTH, G., BRISON, J., MÉASSON, M.-A., FLOUQUET, J., IZAWA, K., MATSUDA, Y., SUGAWARA, H., AND SATO, H. Multiband superconductivity in the heavy fermion compound $PrOs_4Sb_{12}$. *Phys. Rev. Lett. 95*, 10 (2005), 107004.

[193] SHAKERIPOUR, H., TANATAR, M., LI, S., PETROVIC, C., AND TAILLEFER, L. Hybrid gap structure of the heavy-fermion superconductor $CeIrIn_5$. *Phys. Rev. Lett. 99*, 18 (2007), 187004.

[194] SHEIKIN, I., GROGER, A., RAYMOND, S., D. JACCARD, D. AOKI, H. H., AND FLOUQUET, J. High magnetic field study of $CePd_2Si_2$. *Phys. Rev. B. 67* (2003), 094420.

[195] SHISHIDO, H., SETTAI, R., AOKI, D., IKEDA, S., NAKAWAKI, H., NAKAMURA, N., IIZUKA, T., INADA, Y., SUGIYAMA, K., TAKEUCHI, T., KINDO, K., KOBAYAHSI, T., HAGA, Y., HARIMA, H., AOKI, Y., NAMIKI, T., SATO, H., AND ONUK, Y. Fermi surface, magnetic and superconducting properties of $LaRhIn_5$ and $CeTIn_5$ (T: Co, Rh and Ir). *J. Phys. Soc. Japan 71* (2002), 162–173.

[196] SHIVARAM, B., JEONG, Y., ROSENBAUM, T., AND HINKS, D. Anisotropy of transverse sound in the heavy-fermion superconductor UPt_3. *Phys. Rev. Lett. 56*, 10 (1986), 1078–1081.

[197] SIGRIST, M., AND UEDA, K. Phenomenological theory of unconventional superconductivity. *Rev. Mod. Phys. 63*, 2 (Apr 1991), 239–311.

[198] SIMON, S. H., AND LEE, P. Scaling of the quasiparticle spectrum for d-wave superconductors. *Phys. Rev. Lett. 78*, 8 (1997), 1548–1551.

[199] STEGLICH, F., AARTS, J., BREDL, C. D., LIEKE, W., MESCHEDE, D., FRANZ, W., AND SCHÄFER, H. Superconductivity in the presence of strong pauli paramagnetism: $CeCu_2Si_2$. *Phys. Rev. Lett. 43*, 25 (1979), 1892–1896.

[200] STEWART, G. Heavy-fermion systems. *Rev. Mod. Phys. 56*, 4 (1984), 755–787.

[201] STEWART, G., FISK, Z., WILLIS, J., AND SMITH, J. Possibility of coexistence of bulk superconductivity and spin fluctuations in UPt_3. *Phys. Rev. Lett. 52*, 8 (1984), 679–682.

[202] SUDEROW, H., BRISON, J., HUXLEY, A., AND FLOUQUET, J. Scaling and thermal conductivity in unconventional superconductors: The case of UPt_3. *Phys. Rev. Lett. 80*, 1 (1998), 165–168.

[203] SUDEROW, H., AND J.P. BRISON, A. HUXLEY, J. F. Thermal conductivity and gap structure of the superconducting phases of UPt_3. *J. Low Temp. Phys. 108* (1997), 11.

[204] SUDEROW, H., KAMBE, S., BRISON, J., HUXLEY, A., FLOUQUET, J., , AND RULLIER, A. Controlled creation of structural defects in the heavy fermion superconductor UPt$_3$ and its influence on the superconducting properties. *J. Low Temp. Phys. 116* (1999), 393.

[205] SULPICE, A., GANDIT, P., CHAUSSY, J., FLOUQUET, J., JACCARD, D., LEJAY, P., AND THOLENCE, J. Thermodynamic and transport properties of UPt$_3$. *J. Low Temp. Phys. 62* (1986), 39.

[206] SUMIYAMA, A., KATAYAMA, D., ODA, Y., INADA, Y., AOKI, D., TOKIWA, Y., HAGA, Y., AND ONUKI, Y. Observation of the Josephson effect in the heavy-fermion superconductor CeIrIn$_5$ above T_c. *J. Phys.: Condens. Matter 13* (2001), L879–L884.

[207] SUN, Y., AND MAKI, K. Transport properties of d-wave superconductors with impurities. *Europhys. Lett. 32* (1995), 355–359.

[208] SUTHERLAND, M. Thermal and electrical transport in ZrZn$_2$: probing the logarithmic fermi liquid state. to be published in Phys. Rev. B.

[209] SUZUKI, M., TANATAR, M., KIKUGAWA, N., MAO, Z., MAENO, Y., AND ISHIGURO, T. Universal heat transport in Sr_2RuO_4. *Phys. Rev. Lett. 88*, 22 (2002), 227004.

[210] TAILLEFER, L., LUSSIER, B., GAGNON, R., BEHNIA, K., AND AUBIN, H. Universal heat conduction in $YBa_2Cu_3O_{6.9}$. *Phys. Rev. Lett. 79*, 3 (1997), 483–486.

[211] TAKEUCHI, T., INOUE, T., SUGIYAMA, K., AOKI, D., TOKIWA, Y., HAGA, Y., KINDO, K., AND ONUKI., Y. Magnetic and thermal properties of CeIrIn$_5$ and CeCoIn$_5$. *J. Phys. Soc. Japan 70* (2001), 877.

[212] TAKIMOTO, T., HOTTA, T., AND UEDA, K. Strong-coupling theory of superconductivity in a degenerate hubbard model. *Phys. Rev. B 69*, 10 (2004), 104504.

[213] TAKIMOTO, T., AND MORIYA, T. Superconductivity and antiferromagnetism in the three-dimensional hubbard model. *Phys. Rev. B 66*, 13 (2002), 134516.

[214] TANAKA, K., IKEDA, H., NISIKAWA, Y., AND YAMADA, K. Theory of superconductivity in CeMIn$_5$ (M=Co, Rh, Ir) on the basis of the three dimensional periodic anderson model. *J. Phys. Soc. Japan 75* (2006), 024713.

[215] TANATAR, M., PAGLIONE, J., PETROVIC, C., AND TAILLEFER, L. Anisotropic violation of the wiedemann-franz law at a quantum critical point. *Science 316* (2007), 1320–1322.

[216] Tanatar, M. A., Nagai, S., Mao, Z. Q., Maeno, Y., and Ishiguro, T. Thermal conductivity of superconducting Sr_2RuO_4 in oriented magnetic fields. *Phys. Rev. B 63*, 6 (2001), 064505.

[217] Tanatar, M. A., Paglione, J., Nakatsuji, S., Hawthorn, D. G., Boaknin, E., Hill, R. W., Ronning, F., Sutherland, M., Taillefer, L., Petrovic, C., Canfield, P. C., and Fisk, Z. Unpaired electrons in the heavy-fermion superconductor $CeCoIn_5$. *Phys. Rev. Lett. 95*, 6 (2005), 067002.

[218] Tayama, T., Harita, A., Sakakibara, T., Haga, Y., Shishido, H., Settai, R., and Onuki, Y. Unconventional heavy-fermion superconductor $CeCoIn_5$: dc magnetization study at temperatures down to 50 mK. *Phys. Rev. B 65*, 18 (2002), 180504.

[219] Tsuei, C., and Kirtley, J. Pairing symmetry in cuprate superconductors. *Rev. Mod. Phys. 72*, 4 (2000), 969.

[220] Ueda, K. Electrical resistivity of antiferromagnetic metals. *J. Phys. Soc. Japan 43* (1977), 1497–1508.

[221] Ueda, K., and Moriya, T. Contribution of spin fluctuations to the electrical and thermal resistivities of weakly and nearly ferromagnetic metals. *J. Phys. Soc. Japan 39* (1975), 605–615.

[222] Van Harlingen, D. Phase-sensitive tests of the symmetry of the pairing state in the high-temperature superconductors evidence for $d_{x^2-y^2}$ symmetry. *Rev. Mod. Phys. 67*, 2 (1995), 515–535.

[223] Vekhter, I., Hirschfeld, P., and Nicol, E. Thermodynamics of d-wave superconductors in a magnetic field. *Phys. Rev. B 64*, 6 (2001), 064513.

[224] Vekhter, I., and Houghton, A. Quasiparticle thermal conductivity in the vortex state of high- T_c cuprates. *Phys. Rev. Lett. 83*, 22 (1999), 4626–4629.

[225] Vekhter, I., and Vorontsov, A. Interplane and intraplane heat transport in quasi-two-dimensional nodal superconductors. *Phys. Rev. B 75*, 9 (2007), 094512.

[226] Volovik, G. Superconductivity with lines of GAP nodes: density of states in the vortex. *JETP Lett. 58* (1993), 469–73.

[227] Volovik, G., and Gorkov, L. Superconducting classes in heavy fermion systems. *Soviet Phys. JETP 61* (1985), 843.

[228] von Lohneysen, H. The superconducting phases of UPt_3. *Physica B 197* (1994), 551–62.

[229] VORONTSOV, A., AND VEKHTER, I. Nodal structure of quasi-two-dimensional superconductors probed by a magnetic field. *Phys. Rev. Lett. 96*, 23 (2006), 237001.

[230] WALKER, I., GROSCHE, F., FREYE, D., AND LONZARICH, G. The normal and superconducting states of CeIn$_3$ near the border of antiferromagnetic order. *Physica C 282-287* (1997), 303–306.

[231] WASTIN, F., P. BOULET, J.REBIZANT, E. C., AND LANDER, G. Advances in the preparation and characterization of transuranium systems. *J. Phys.: Condens. Matter 15* (2003), S2279–S2285.

[232] WATANABE, T., IZAWA, K., KASAHARA, Y., HAGA, Y., ONUKI, Y., THALMEIER, P., MAKI, K., AND MATSUDA, Y. Superconducting gap function in antiferromagnetic heavy-fermion UPd$_2$Al$_3$ probed by angle-resolved magnetothermal transport measurements. *Phys. Rev. B 70*, 18 (2004), 184502.

[233] WRIGHT, D., EMERSON, J., WOODFIELD, B., GORDON, J., FISHER, R., AND PHILLIPS, N. Low-temperature specific heat of $YBa_2Cu_3O_{7-\delta}$, $0 \leq \delta \leq 0.2$: evidence for d-wave pairing. *Phys. Rev. Lett. 82*, 7 (1999), 1550–1553.

[234] XU, D., YIP, S., AND SAULS, J. Nonlinear meissner effect in unconventional superconductors. *Phys. Rev. B 51*, 22 (1995), 16233–16253.

[235] YANASE, Y., JUJO, T., NOMURA, T., IKEDA, H., AND T. HOTTA, A. K. Y. Theory of superconductivity in strongly correlated electron systems. *Physics Reports 387* (2003), 1–149.

[236] YANG, G. *Theory of unconventional superconductors*. PhD thesis, University of Southern California, 2001.

[237] YANO, K., SAKAKIBARA, T., TAYAMA, T., YOKOYAMA, M., AMITSUKA, H., HOMMA, Y., MIRANOVIC, P., ICHIOKA, M., TSUTSUMI, Y., AND MACHIDA, K. Field-angle-dependent specific heat measurements and gap determination of a heavy fermion superconductor URu$_2$Si$_2$, 07121376.

[238] YAOUANC, A., DE RÉOTIER, P. D., HUXLEY, A., FLOUQUET, J., BONVILLE, P., GUBBENS, P., AND MULDERS, A. Strong axial anisotropy of the magnetic penetration length in superconducting. *J. Phys.: Condens. Matter 10* (1998), 9791–9798.

[239] YU, F., SALAMON, M., LEGGETT, A., LEE, W., AND GINSBERG, D. Tensor magnetothermal resistance in YBa$_2$Cu$_3$O$_{7-x}$ via Andreev scattering of quasiparticles. *Phys. Rev. Lett. 74*, 25 (1995), 5136–5139.

[240] YUAN, H. *Science 302* (2003), 2104.

[241] ZAPF, V., FREEMAN, E., BAUER, E., PETRICKA, J., SIRVENT, C., FREDER-ICK, N., DICKEY, R., AND MAPLE, M. Coexistence of superconductivity and antiferromagnetism in $CeRh_{1-x}Co_xIn_5$. *Phys. Rev. B 65*, 1 (2001), 014506.

[242] ÖZCAN, S., BROUN, D., MORGAN, B., HASELWIMMER, R., SARRAO, J., KAMAL, S., BIDINOSTI, C., TURNER, P., RAUDSEPP, M., AND WALDRAM, J. London penetration depth measurements of the heavy-fermion superconductor $CeCoIn_5$ near a magnetic quantum critical point. *Europhys. Lett. 62* (2003), 412.

[243] ZHENG, G.-Q., TANABE, K., MITO, T., KAWASAKI, S., KITAOKA, Y., AOKI, D., HAGA, Y., AND ONUKI, Y. Unique spin dynamics and unconventional superconductivity in the layered heavy fermion compound $CeIrIn_5$: NQR evidence. *Phys. Rev. Lett. 86*, 20 (2001), 4664–4667.

[244] ZHITOMIRSKY, M., AND UEDA, K. Phase diagram of the unconventional superconductor UPt_3 in the weak-crystal-field model. *Phys. Rev. B 53* (1996), 6591.

[245] ZHITOMIRSKY, M., AND WALKER, M. Thermal conductivity across a twin boundary in a d-wave superconductor. *Phys. Rev. B 57*, 14 (1998), 8560–8565.

FIGURE D.2: Louis Taillefer's group, May 2007. (L to R): (back) Nicolas Doiron-Leyraud, David Le Boeuf, Jean Philippe Reid, Louis Taillefer, Makariy Tanatar, (front) Jacques Corbin, Ramzy Daou, Hamideh Shakeripour, Doug Bonn.

FIGURE D.3: Mount *Damavand* in summer. The mount is a dormant volcano with the height 5,671 metres and the highest peak in Iran. It is a special place in the Persian mythology. Bottom: my friends and I are on the peak. *...with the hope of coming over the humanity peaks.*